



**HAL**  
open science

# Hydrogen flame acceleration in non-uniform mixtures

Luc Lecointre

► **To cite this version:**

Luc Lecointre. Hydrogen flame acceleration in non-uniform mixtures. Fluid Dynamics [physics.flu-dyn]. Université Paris-Saclay, 2022. English. NNT : 2022UPAST092 . tel-03879925v2

**HAL Id: tel-03879925**

**<https://theses.hal.science/tel-03879925v2>**

Submitted on 30 Nov 2022

**HAL** is a multi-disciplinary open access archive for the deposit and dissemination of scientific research documents, whether they are published or not. The documents may come from teaching and research institutions in France or abroad, or from public or private research centers.

L'archive ouverte pluridisciplinaire **HAL**, est destinée au dépôt et à la diffusion de documents scientifiques de niveau recherche, publiés ou non, émanant des établissements d'enseignement et de recherche français ou étrangers, des laboratoires publics ou privés.

# Hydrogen flame acceleration in non-uniform mixtures

*Accélération de flamme hydrogène en mélange non-uniforme*

Thèse de doctorat de l'université Paris-Saclay

École doctorale n° 579 : sciences mécaniques et énergétiques, matériaux et  
géosciences (SMEMAG)

Spécialité de doctorat: Combustion

Graduate School : Sciences de l'ingénierie et des systèmes,

Référent : Faculté des sciences d'Orsay

Thèse préparée dans les unités de recherche **STMF (Université Paris-Saclay, CEA)**,  
**EM2C (Université Paris-Saclay, CNRS, CentraleSupélec)**, **LISN (Université  
Paris-Saclay, CNRS)** sous la direction de **Christian TENAUD**, directeur de  
recherche, sous le co-encadrement de **Ronan VICQUELIN**, Professeur des Universités,  
**Etienne STUDER**, ingénieur de recherche CEA, et **Sergey KUDRIAKOV** ingénieur  
de recherche CEA.

Thèse soutenue à Paris-Saclay, le 07 juin 2022, par

**Luc LECOINTRE**

## Composition du jury

<b>Marc MASSOT</b> Professeur, Ecole Polytechnique	Président du jury
<b>Arnaud MURA</b> Directeur de recherche CNRS, INSIS	Rapporteur & Examineur
<b>Matei RADULESCU</b> Professeur, Université d'Ottawa	Rapporteur & Examineur
<b>Pascale DOMINGO</b> Directrice de recherche CNRS, CORIA	Examinatrice
<b>Christian TENAUD</b> Directeur de recherche CNRS, EM2C	Directeur de thèse

**Titre:** Accélération de flamme hydrogène en mélange non uniforme

**Mots clés:** Accélération de Flamme, Méthodes Haute Résolution, Combustion Hydrogène, Multi-résolution, Parois immergées, ISAT

**Résumé:** Cette thèse, effectuée en partenariat avec le CEA, présente le développement de méthodes numériques dédiées à la simulation du processus d'accélération d'une flamme hydrogène.

L'accélération et la transition de la déflagration à la détonation des flammes d'hydrogène/air sont des problèmes clés pour la sûreté nucléaire. Elles présentent également un intérêt croissant pour les domaines énergétiques et industriels impliquant de l'hydrogène. La connaissance de ces phénomènes doit permettre de se prémunir contre les conséquences d'une inflammation de l'hydrogène lors d'une fuite ou lors de sa production accidentelle dans une cuve de réacteur nucléaire comme observé lors des accidents de Three Mile Island en 1979 ou de Fukushima-Daiichi en 2011.

L'objectif de ce travail est de proposer des méthodes numériques de haute résolution capables de prédire les phénomènes intervenant dans le processus d'accélération de flamme.

Pour cela, un solveur numérique d'ordre élevé a été développé, il se base notamment sur un schéma de Lax-

Wendroff de haute résolution associée à une technique de capture de choc satisfaisant des contraintes de préservation de la monotonie. Ce schéma permet la simulation d'écoulements multi-espèces réactifs avec des équations d'état convexes.

Pour tenir compte de la variabilité des échelles spatiales, des outils de multi-résolution sont appliqués pour adapter localement le maillage. Des méthodes de paroi immergées ont également été intégrées pour permettre d'utiliser des configurations géométriques non triviales avec un maillage structuré.

La capacité du logiciel à reproduire les phénomènes fondamentaux en combustion et en détonation a été étudiée à travers une sélection de cas tests standards. Des dispositifs expérimentaux sont également simulés avec la transmission d'un front de détonation à travers un milieu poreux et la reproduction du tube d'accélération de flamme de l'université de Munich. Les résultats obtenus illustrent la capacité de nos méthodes à capturer avec précision les différentes étapes de l'accélération de flamme et la transition vers la détonation et à reproduire les observations expérimentales.

**Title:** Hydrogen flame acceleration in non-uniform mixtures

**Keywords:** Flame Acceleration, High-Resolution methods, Hydrogen Combustion, Multiresolution, Immersed Boundary, ISAT

**Abstract:** This thesis, carried out with the support of the CEA, presents the development of numerical methods dedicated to the simulation of the acceleration process of a hydrogen flame.

The acceleration and the transition from deflagration to the detonation of hydrogen/air flames are critical issues for nuclear safety. They are also of growing interest in energy and industrial fields involving hydrogen. The knowledge of these phenomena must allow protection against the consequences of hydrogen ignition during a leak or its accidental production in a nuclear reactor containment, as observed during the accidents of Three Mile Island in 1979 or Fukushima-Daiichi in 2011.

This work aims to propose high-resolution numerical methods capable of predicting the phenomena involved in the flame acceleration process.

For this purpose, a high-order numerical solver has been developed based on a high-resolution Lax-Wendroff scheme associated with a shock-capturing method sat-

isfying monotonicity preservation constraints. This scheme allows the simulation of reactive multi-species flows with convex equations of state.

To account for the variability of spatial scales, multiresolution techniques are applied to adapt the mesh locally. Immersed boundary methods have also been integrated to allow computing non-trivial geometrical configurations with a structured mesh.

The ability of the software to reproduce the fundamental phenomena in combustion and detonation has been studied through a selection of standard test cases. Experimental devices are also simulated with the transmission of a detonation front through a porous medium and the reproduction of the flame acceleration tube of the Technische of University Munich. The results illustrate the ability of our methods to accurately capture the different stages of the flame acceleration process and the transition to detonation and to reproduce the experimental observations.

# Remerciements

La fin de cette thèse représente pour moi l'aboutissement d'une période commencée il y a maintenant plus de 10 ans, lorsque je me suis lancé dans des études d'ingénieur avec petit à petit un rapprochement vers le monde de la recherche jusqu'à finir par me lancer dans un doctorat. C'est ainsi l'occasion de revenir sur tout le chemin parcouru, les différents choix d'orientations que j'ai pu faire pendant cette période et qui m'ont amené jusqu'ici. Toutes les étapes par lesquelles je suis passé m'ont façonné progressivement. Je suis heureux et fier de ce parcours plein de surprises, de difficultés parfois, mais aussi riche d'apprentissages, de rencontres et de grandes joies.

Cette section me permet donc de remercier toutes les personnes qui m'ont accompagné dans ces aventures.

Tout d'abord, je voudrais exprimer ma grande gratitude à mon équipe d'encadrants pendant ces trois dernières années. Tout d'abord à mon directeur de thèse Christian Tenaud, pour son soutien continu, son investissement et son extrême gentillesse ainsi qu'à mes autres encadrants Sergey Kudriakov, Ronan Vicquelin et Etienne Studer qui ont de même étaient toujours de bon conseil, à l'écoute et bienveillants pendant ces trois ans. Ils m'ont offert d'excellentes conditions pour réaliser ma thèse.

Je remercie également les membres du jury, les rapporteurs Arnaud Mura et Matei Radulescu, pour leurs retours et l'intérêt qu'ils ont porté à mes travaux, ainsi que Pascale Domingo et Marc Massot qui a accepté de présider le jury.

Je remercie toute ma famille, en particulier mes parents, qui m'ont plus vu qu'on pouvait le penser puisqu'ils m'ont notamment accueilli pendant le confinement de 2020. Ma sœur Claire et son mari Jean-Charles qui ont fait de même dans leur nouvelle maison en 2021. Je pense aussi à leurs trois enfants, Etienne, Agathe et la petite dernière Garance née durant l'été 2021 et devenue ma filleule. Je remercie également mon frère Louis, lui-même partit se lancer dans une thèse au Québec, mes deux derniers frères François et Benoît qui voleront bientôt de leurs propres ailes et enfin Hélène et son fiancé Louis, apparu pendant cette période de thèse.

Un grand merci à mes différents voisins de bureau, Mohamed et Omar au LIMSI, Aurelien, Erwan, Arthur, Nicolas et Roxane à l'EM2C qui m'ont accueilli dans les laboratoires ainsi que les nouveaux arrivants, Goeffrey, Valentin, Julien et Yuri. Ils ont tous participé à instaurer une ambiance stimulante et détendu dans les bureaux avec "toujours le mot pour rire". Merci également aux autres doctorants et acteurs au CEA, au LIMSI et au EM2C, en particulier Junghwa, Karl, Corentin, Victor, Victorien, Constantin, Jean, Ulysse, Alexandre, Kevin, Moisés, Pierre, Maxime, Gabriel, Antoine, Raksmy et tous les autres qui ont égayé la vie dans les laboratoires.

Merci aussi à ma nouvelle équipe que j'ai intégré en début d'année, Elie, Pierre, Anida et Adrien de l'équipe TRUST ainsi qu'Erwan et toute l'équipe du laboratoire LGLS qui m'ont accueilli et m'ont permis de finir sereinement la rédaction de ma thèse.

Enfin, merci à tous mes autres proches et amis de toujours, Thibault, Antonin, Raphaël, Pierre-Louis, Syrine, Thomas, Alexis et Eléonor ainsi que Guilhem, mon colocataire pendant ces trois ans, pour les soirées, les voyages et toutes les activités que l'on a partagés et que l'on partagera dans le futur.



# Résumé

Cette thèse, effectuée en partenariat avec le CEA, présente le développement de méthodes numériques dédiées à la simulation du processus d'accélération d'une flamme hydrogène.

L'accélération et la transition de la déflagration à la détonation des flammes d'hydrogène/air sont des problématiques clés pour la sûreté nucléaire. Elles présentent également un intérêt croissant pour les domaines énergétiques et industriels impliquant de l'hydrogène. La connaissance de ces phénomènes doit permettre de se prémunir contre les conséquences d'une inflammation de l'hydrogène lors d'une fuite ou lors de sa production accidentelle dans une cuve de réacteur nucléaire comme observé lors des accidents de Three Mile Island en 1979 ou de Fukushima-Daiichi en 2011.

Des expériences ont été conçues pour étudier les mécanismes d'accélération de la flamme d'hydrogène, mais leur capacité à identifier et à isoler les différents phénomènes impactant ce processus est limitée. De leur côté, les simulations numériques restent complexes à réaliser en raison des nombreux phénomènes multi-échelles impliqués et de la présence de discontinuités numériques induites par les ondes de choc et les fronts de détonation. L'objectif de ce travail est de proposer des méthodes numériques de haute résolution capables de répondre à ces problématiques.

Un solveur numérique d'ordre élevé a été développé, il se base sur des méthodes de splitting permettant d'utiliser des schémas numériques adaptés à chaque opérateur. En particulier, la résolution des équations d'Euler compressibles s'effectue avec un schéma de Lax-Wendroff de haute résolution (ordre 7) développé sur une base de schéma de Roe, associé une technique de capture de choc satisfaisant des contraintes de préservation de la monotonie. Ce schéma s'applique aux écoulements multi-composants réactifs utilisant des équations d'état convexes. Dans le cas des simulations de combustion hydrogène, des gaz parfaits avec des capacités thermiques dépendantes de la température sont considérés.

Pour tenir compte de la variabilité des échelles spatiales, des outils de multi-résolution sont appliqués pour adapter localement le maillage. Des méthodes de paroi immergées ont également été intégrées pour permettre d'utiliser des configurations géométriques non-triviales tout en conservant un maillage structuré.

La capacité du logiciel à reproduire les phénomènes fondamentaux en combustion et en détonation a été étudiée à travers une sélection de cas tests standards. Ceux-ci permettent d'évaluer les performances de nos méthodes numériques et des modèles utilisés ainsi que du mécanisme chimique sélectionné (H2 Mével). Des dispositifs expérimentaux sont également simulés avec la transmission d'un front de détonation à travers un milieu poreux et la reproduction du tube d'accélération de flamme de l'université de Munich. Les résultats obtenus illustrent la capacité de nos méthodes numériques à capturer avec précision les différentes étapes de l'accélération de flamme et la transition vers la détonation et à reproduire les observations expérimentales.



# Abstract

This thesis, carried out with the support of the CEA, presents the development of numerical methods dedicated to the simulation of the acceleration process of a hydrogen flame.

The acceleration and transition from deflagration to detonation of hydrogen/air flames are critical issues for nuclear safety. They are also of growing interest in energy and industrial fields involving hydrogen. The knowledge of these phenomena must allow protection against the consequences of hydrogen ignition during a leak or its accidental production in a nuclear reactor containment, as observed during the accidents of Three Mile Island in 1979 or Fukushima-Daiichi in 2011.

Experiments have been designed to study the mechanisms of hydrogen flame acceleration, but their ability to identify and isolate the phenomena impacting this process is limited. On the other hand, numerical simulations remain complex to perform due to the multi-scale phenomena involved and the presence of numerical discontinuities induced by shock waves and detonation fronts. This work aims to propose high-resolution numerical methods capable of addressing these issues.

A high-order numerical solver has been developed based on splitting methods, using numerical schemes adapted to each operator. In particular, the resolution of the compressible Euler equations is performed with a high-resolution Lax-Wendroff scheme (seventh-order) built from the Roe approximate Riemann solver, with a shock-capturing method satisfying monotonicity preservation constraints. This scheme applies to reactive multicomponent flows using convex equations of state. In the case of hydrogen combustion simulations, perfect gases with temperature-dependent heat capacities are considered.

To take into account the wide range of spatial scales involved, multiresolution tools are applied to locally adapt the mesh. Immersed boundary methods have also been integrated to allow the use of non-trivial geometric configurations while maintaining a structured mesh.

The ability of the software to reproduce the fundamental phenomena in combustion and detonation has been studied through a selection of standard test cases. These allow evaluating the performance of our numerical methods and the models used as well as the selected chemical mechanism (H2 Mevel). Experimental devices are also simulated with the transmission of a detonation front through a porous medium and the reproduction of the flame acceleration tube at the Technische University of Munich. The results illustrate the ability of our numerical methods to accurately capture the different stages of the flame acceleration and the transition to detonation and to reproduce the experimental observations.





# Contents

<b>Remerciements</b>	<b>i</b>
<b>Résumé</b>	<b>iii</b>
<b>Abstract</b>	<b>v</b>
<b>I Introduction</b>	<b>1</b>
<b>1 Context and motivations</b>	<b>3</b>
1.1 The hydrogen economy . . . . .	3
1.2 Safety challenges in this hydrogen economy . . . . .	4
1.3 Application in the context of nuclear safety . . . . .	5
<b>2 Detonation Phenomenon</b>	<b>7</b>
2.1 Subsonic and supersonic regimes : Deflagration and Detonation . . . . .	7
2.2 Detonation structure . . . . .	9
2.2.1 Steady one-dimensional ZND structure . . . . .	9
2.2.2 Unstable one-dimensional detonations . . . . .	12
2.2.3 Cellular detonation structure . . . . .	13
<b>3 Flame acceleration</b>	<b>17</b>
3.1 Deflagration regimes . . . . .	17
3.1.1 Ignition . . . . .	17
3.1.2 Laminar deflagration . . . . .	18
3.1.3 Cellular deflagration . . . . .	18
3.1.4 Premixed combustion turbulent regime . . . . .	21
3.1.5 Fast turbulent deflagration . . . . .	23
3.2 Transition to detonation . . . . .	24
3.2.1 Onset of Detonation . . . . .	24
3.2.2 Influence of boundary condition on flame acceleration . . . . .	26
3.2.3 Mixture Inhomogeneity . . . . .	27
<b>4 Objectives</b>	<b>29</b>
4.1 State of the art . . . . .	29
4.1.1 Experimental facilities . . . . .	29
4.1.2 Empirical criteria for Flame Acceleration and Deflagration to Detonation Transition Limits . . . . .	30
4.1.3 Numerical methods . . . . .	31
4.2 Starting point of Thesis . . . . .	32
4.2.1 MR_CHORUS solver . . . . .	32

4.2.2	AGATH solver . . . . .	32
4.3	Objectives and organization of Thesis . . . . .	33
<b>II</b>	<b>Numerical solver</b>	<b>35</b>
<b>5</b>	<b>Fluids dynamics of combustion</b>	<b>39</b>
5.1	Conservation equations for a compressible reactive mixture . . . . .	39
5.1.1	Navier-Stokes equation . . . . .	39
5.1.2	Diffusion of species . . . . .	40
5.1.3	Chemical kinetics . . . . .	41
5.2	Thermochemical Equilibrium Model . . . . .	42
5.2.1	Mixture of real gases . . . . .	43
5.2.2	Ideal gas mixture with temperature-dependent heat capacities . . . . .	45
<b>6</b>	<b>Numerical solution for multi-scale partial differential equations</b>	<b>49</b>
6.1	Finite Volume Method . . . . .	49
6.2	Time operator splitting . . . . .	51
6.3	Dedicated integration methods for combustion simulation . . . . .	52
6.3.1	Runge-Kutta Time Integration Methods . . . . .	52
6.3.2	Time integration of the viscous flux: Runge Kutta 2 . . . . .	54
6.3.3	Time integration of the Reaction: Radau5 Solver . . . . .	54
6.3.4	Integration of the convection flux: One-Step Monotonicity-Preserving (OSMP) scheme . . . . .	54
6.4	Multidimensional splitting . . . . .	55
<b>7</b>	<b>High Resolution Methods for mixtures of calorically perfect gases</b>	<b>57</b>
7.1	Approximate Riemann solver of Roe . . . . .	58
7.1.1	Roe averaged operator . . . . .	59
7.1.2	Entropy fix . . . . .	60
7.2	One-Step Monotonicity Preserving (OSMP) scheme . . . . .	61
7.2.1	Space-time discretization: Lax-Wendroff approach . . . . .	61
7.2.2	TVD and MP schemes . . . . .	63
7.3	Conclusion . . . . .	68
<b>8</b>	<b>Extension of the OSMP scheme to mixture of gases with convex equation of state</b>	<b>69</b>
8.1	1D Euler equations for mixture with convex equation of state . . . . .	70
8.1.1	Euler Hyperbolic conservation laws . . . . .	70
8.2	Approximate Riemann solver of Roe for mixture of gases with convex equation of state	71
8.3	High-order extension with modification of the total energy flux formulation . . . . .	73
8.4	Numerical results . . . . .	76
8.4.1	Convection of mass fraction and density waves . . . . .	76
8.4.2	One-dimensional shock-tube problem . . . . .	77
8.5	Conclusion . . . . .	78
<b>9</b>	<b>Carbuncle instability</b>	<b>83</b>
9.1	Evaluation of carbuncle correction . . . . .	84
9.1.1	Matrix stability analysis . . . . .	84
9.1.2	Detonation front test case . . . . .	86
9.2	Critical cells detection . . . . .	87
9.3	Cure carbuncle instability . . . . .	88
9.3.1	Rotated solver . . . . .	89
9.3.2	Specific additional dissipation . . . . .	89
9.3.3	Application to the OSMP7 scheme . . . . .	93
9.4	Conclusion . . . . .	94

<b>III</b>	<b>Algorithmic Description</b>	<b>97</b>
<b>10</b>	<b>Space adaptive Multiresolution</b>	<b>101</b>
10.1	Multiresolution analysis . . . . .	101
10.2	Local grid refinement . . . . .	104
10.2.1	Adaptive multiresolution algorithm . . . . .	105
10.3	Hydrodynamic instability . . . . .	105
10.4	Conclusion . . . . .	108
<b>11</b>	<b>Immersed Boundary Method</b>	<b>111</b>
11.1	Introduction . . . . .	111
11.2	State of the art . . . . .	111
11.3	Integration of fluid-solid interface inside numerical solver . . . . .	112
11.3.1	Geometrical configuration . . . . .	112
11.3.2	Implementation of ghost cells inside the flow . . . . .	113
11.3.3	Finite volume integration of the cut-cells . . . . .	115
11.4	Numerical results . . . . .	118
11.4.1	Flow around a cylinder at different Reynolds . . . . .	118
11.4.2	Shock wave interaction with two dimensional wedge . . . . .	123
11.5	Conclusion . . . . .	124
<b>12</b>	<b>In Situ Adaptive Tabulation (ISAT) for Multi-Scale Reaction Waves</b>	<b>127</b>
12.1	In Situ Adaptive Tabulation (ISAT) . . . . .	127
12.1.1	Description of the approximation . . . . .	128
12.1.2	Construction of the table . . . . .	129
12.2	Integration into the numerical scheme . . . . .	130
12.2.1	Adaptation of the time operator splitting . . . . .	130
12.2.2	Application to transient compressible phenomena . . . . .	130
12.3	Numerical simulation of gaseous detonation . . . . .	130
12.3.1	Ignition and creation of detonation front by a shock wave reflection . . . . .	131
12.3.2	Application without ISAT . . . . .	131
12.3.3	Application with ISAT . . . . .	132
12.3.4	Two dimensional detonation front . . . . .	134
12.4	Concluding remarks . . . . .	135
<b>IV</b>	<b>Applications Framework</b>	<b>137</b>
<b>13</b>	<b>Validation test cases</b>	<b>141</b>
13.1	Fundamental combustion properties of hydrogen flame . . . . .	141
13.1.1	Laminar flame characteristics . . . . .	141
13.1.2	Ignition delay . . . . .	143
13.2	Hydrodynamic and thermodiffusive instabilities . . . . .	144
13.3	Detonation simulation . . . . .	146
13.3.1	ZND detonation properties . . . . .	146
13.3.2	One-dimensional unstable detonation . . . . .	148
13.3.3	Two-dimensional unstable detonation . . . . .	149
13.4	Conclusion . . . . .	153
<b>14</b>	<b>Hydrogen flame acceleration simulations</b>	<b>155</b>
14.1	Attenuation and re-initiation of detonation front with porous medium . . . . .	155
14.1.1	Overview . . . . .	155
14.1.2	Numerical Results . . . . .	156
14.2	Acceleration tube configuration of the "GraVent" Technische University of Munich facility	158
14.2.1	Experimental and Numerical setup . . . . .	158

14.2.2 Numerical results . . . . .	161
14.3 Conclusion . . . . .	164
<b>General Conclusion and Prospects</b>	<b>167</b>
<b>V Appendix</b>	<b>171</b>
<b>Hyperbolic system of Conservation Laws</b>	<b>173</b>
A.1 Mathematical background . . . . .	173
A.1.1 One-dimensional Conservation Laws . . . . .	173
A.1.2 Scalar case . . . . .	174
A.1.3 Hyperbolic Systems of conservation laws . . . . .	176
A.2 Riemann problem and Godunov solver for 1D Euler equations with mixtures of ideal gases with temperature-dependent heat capacities . . . . .	180
A.2.1 Resolution of the Riemann problem . . . . .	180
A.2.2 Godunov solver . . . . .	182
<b>The HLLC Riemann solver</b>	<b>185</b>
B.3 HLL solver . . . . .	185
B.4 HLLC Approximate Riemann Solver . . . . .	186
<b>H2 Mével</b>	<b>189</b>
<b>Synthèse en français</b>	<b>191</b>
D.5 Introduction . . . . .	191
D.5.1 Contexte . . . . .	191
D.5.2 Accélération de flamme et transition vers la détonation . . . . .	191
D.6 Description du solveur numérique . . . . .	193
D.6.1 Equations et modèles . . . . .	193
D.6.2 Schéma OSMP . . . . .	193
D.6.3 Extension du schéma OSMP au mélanges de gaz avec un équations d'état convexe	194
D.6.4 Phénomène de carbuncle . . . . .	196
D.7 Algorithmie . . . . .	196
D.7.1 Méthode d'adaptation de maillage . . . . .	197
D.7.2 Méthode de paroi immergées . . . . .	197
D.7.3 In Situ Adaptive Tabulation . . . . .	197
D.8 Résultats . . . . .	197

# List of Figures

1.1	Global energy demand for H <sub>2</sub> by sector (left) and corresponding production technology (right) in 2020 [IEA21]	3
2.1	Balance of conservative variables around the flame front	8
2.2	Domains of detonation and deflagration solutions in the $p - 1/\rho$ plane	9
2.3	The Rayleigh line and the Hugoniot curve	10
2.4	Particular point in the ZND theory	11
2.5	ZND model sketch reproduced from [Lee08]	12
2.6	Schlieren image of a detonation front in 2H <sub>2</sub> -O <sub>2</sub> -12Ar, $P_1 = 20$ kPa [Aus03]	13
2.7	The cellular structure of a detonation wave. Detonation cells are traced out by the triple points composed of the incident shock, transverse shock, and Mach stem. $\lambda$ is the detonation cell width. Image taken from [LR05]	14
2.8	Soot foils in 2H <sub>2</sub> -O <sub>2</sub> -7Ar mixture (left) showing regular detonation cells, and 2H <sub>2</sub> -O <sub>2</sub> -1.33N <sub>2</sub> mixture (right) from [Aus03] showing irregular detonation cells	14
3.1	Expanding spherical hydrogen/air for lean and rich mixture with 5 atm pressure environment [LAW06]	19
3.2	Schematic of Darrieus Landau instability	19
3.3	Schematic of thermal-diffusive instability. Species diffusion (bold arrow) and heat diffusion (dashed arrow) respectively reinforce and reduce flame wrinkling	20
3.4	Dependence of growth rate $\omega$ for wavenumber $K$ for various values of Markstein length	20
3.5	Variation of Markstein length versus the equivalence ratio for H <sub>2</sub> -air mixtures initially at 100 kPa and ambient temperature. Data $\triangle$ Dowdy et al. [DSTW91], $\nabla$ Aung et al. [AHF97], $\circ$ Sun et al. [SSHL99], $\square$ Huang et al. [HZZ+06]	21
3.6	Borghini's diagram of combustion regimes [Bor85]	23
3.7	OH-PLIF of turbulent deflagration in obstructed channel with 12.5 vol. % (left), 15 vol % (middle) and 20 vol % (right) [Boe15]	24
3.8	Shadowgraph sequence of shock-flame interaction in GraVent experiments closed to a obstacle with 25% of hydrogen volume	24
4.1	Schematic of the combustion tube with obstacle. Instrumentation includes PMT, photomultiplier tube; PP, pressure sensor; CC, shock sensor [Sca17]	30
5.1	Variation of $c_p(T)$ , $\gamma(T)$ and $w(T)$ for main gases involved in H <sub>2</sub> combustion. Specific heat capacities are computed with polynomials described in [MZG02]	47
6.1	Geometrical illustration of the finite volume scheme on a integration cell	50
7.1	Second entropy fix of Harten and Hyman [HH83]	61
7.2	Sweby region in shaded region with flux limiter $\phi(r)$ . Regions in which function values $\phi(r)$ must lie in order to give TVD (a) and second-order TVD (b) methods. Two possible limiter functions: Roe's superbee (c) and van Leer's (d) limiter.	66

7.3	Reconstruction in the vicinity of a extremum. The TVD constraints alone clip the extremum (left) and identify a discontinuity (right), while the MP condition allows extending the flux limiting interval and including exact values. . . . .	67
8.1	Illustration with 2 species of the projection $\tilde{P}$ of the first approximation $\hat{P}$ on the hyperplane $\mathcal{H}$ defined by (8.5) . . . . .	72
8.2	Successive steps for building a stable OSMP scheme for multi-component real gas flow	75
8.3	Convergence curves using the OSMP7 scheme on a advection of mass fraction wave. Comparison with the initial formulation of the total energy flux and the new one with and without M-P limiter flux. . . . .	76
8.4	Distribution versus temperature of heat capacities at constant pressure ( $c_p$ ) following temperature polynomials found in [MZG02] for Nitrogen (N <sub>2</sub> ), Oxygen (O <sub>2</sub> ), and R22.	77
8.5	Distribution of the temperature, the velocity, the density, the pressure, the mass fraction of N <sub>2</sub> , O <sub>2</sub> and R22 and the heat capacity ratio $\gamma$ for a 1D Sod shock tube at $t = 30$ ms. Comparisons between the proposed corrected high-order OSMP scheme (blue bold line) with the original (uncorrected) OSMP scheme (green bold line) and the first-order Roe solver (black dashed line). . . . .	79
8.6	Comparison of the temperature, the velocity, the density, the pressure and the mass fraction distributions for the 1D Sod shock tube at $t = 30$ ms. Comparisons between results using calorically perfect gas (black dashed line) and Equilibrium real gas with complex thermodynamic (blue bold line) with the exact solution of the Riemann problem (red dashed line). . . . .	80
8.7	Comparison of the temperature, the velocity, the density, the pressure, the mass fraction and specific heat ratio distributions for the 1D Lax shock tube at $t = 15$ ms, obtained with (blue blod line) and without (green line) the modified OSMP scheme and with the exact solution however for ideal gases (black dashed line). . . . .	81
9.1	Pressure field with carbuncle instabilities generated from a perturbed two-dimensional ZND profile. . . . .	84
9.2	Distribution of the eigenvalues of $\mathbf{S}$ in the complex plane for Godunov scheme (top left), HLL scheme (top right), Roe scheme (bottom left) and HLLC (bottom right) . . . . .	86
9.3	Adimensional ZND profile with one-step reaction . . . . .	87
9.4	Computation of the detonation front (with OSMP7 solver and cure carbuncle method); Pressure field (left) and cells flagged by the carbuncle sensor (right). . . . .	88
9.5	Distribution of the eigenvalues of $\mathbf{S}$ in the complex plane for the Rotated Roe solver .	90
9.6	Simulation of Detonation front test case with Rotated Roe solver . . . . .	90
9.7	Distribution of the eigenvalues of $\mathbf{S}$ in the complex plane for the Roe solver without the pressure dissipative term without (left) and with (right) cell-detection . . . . .	91
9.8	Simulation of Detonation front test case for the D-Roe solver without the pressure dissipative term . . . . .	91
9.9	Distribution of the eigenvalues of $\mathbf{S}$ in the complex plane for the Roe solver with additional shear viscosity without (left) and with (right) cell-detection . . . . .	92
9.10	Simulation of Detonation front test case for the D-Roe solver with additional shear viscosity term . . . . .	92
9.11	Simulation of Detonation front test case for the D-OSMP7 solver hybridized with the rotated solver . . . . .	93
9.12	Distribution of the eigenvalues of $\mathbf{S}$ in the complex plane for the OSMP7 solver without the pressure dissipative term without (left) and with (right) cell-detection . . . . .	94
9.13	Simulation of Detonation front test case for the D-OSMP7 solver hybridized without the first-order pressure dissipative term. . . . .	94
9.14	Distribution of the eigenvalues of $\mathbf{S}$ in the complex plane for the OSMP7 solver with additional shear viscosity without (left) and with (right) cell-detection . . . . .	95
9.15	Simulation of Detonation front test case for the D-OSMP7 solver hybridized with the additional shear viscosity. . . . .	95

10.1	A graded tree data structure in 1D: dyadic tree in blue dashed line, leaves in bold black line, and virtual cells in red dashed line. . . . .	102
10.2	Left: set of a nested dyadic grid in 2D. Right: a sketch of a 2D tree structure with leaves in plain line and virtual leaves in red dashed line. . . . .	102
10.3	Sketch of the computational domain: initial configuration and boundary conditions. . . . .	106
10.4	Adapted grid obtained using 9 grid levels per tree and 10 trees distributed over the domain in the streamwise direction at a time $t = 287.5\mu s$ (dimensionless time $t c_{R22,I}/d_0 = 1.15$ ), colored by density values. . . . .	106
10.5	Schematic organization of flow patterns in shock wave/bubble interaction: UI = upstream bubble interface; DI = downstream bubble interface; RR = regular shock wave reflection on DI; INC = incident shock wave; TR = transmitted shock wave; DIF = wave diffraction, crossing of the two branches of the incident shock . . . . .	107
10.6	Temperature fields obtained with the 7 <sup>th</sup> -order OSMP scheme with (at the bottom), and without (at the top) the proposed modification of the OSMP scheme. . . . .	108
10.7	$x-t$ diagram of the shock wave / R22 bubble interaction. Black dots are for experiments and lines with colored dots for simulations. Symbols related to the different waves are given in Figure 10.5. . . . .	109
11.1	Illustration of cut-cells intersected by one solid face for the left panel and two solid faces for the right panel . . . . .	113
11.2	Schematic illustration of the interpolation of the symmetric point I of a ghost point A (left) in a general case (right) in the case of a sharp angle with distinction according to the integration direction . . . . .	114
11.3	Schematic view for implementation of zero normal gradient of velocity at the solid surface. . . . .	116
11.4	Small cut cells $\mathcal{C}_{i,j,k}$ and its two targeted cells $\mathcal{C}_{i,j+1,k}$ and $\mathcal{C}_{i+1,j,k}$ . . . . .	118
11.5	Sketch of the computational domain for subsonic flow around a cylinder . . . . .	119
11.6	Volume fraction of cut cells around immersed cylinder with initial mesh with seven levels of refinement. . . . .	120
11.7	Pressure field at the finest level and velocity component computed on the seven levels grid (dashed lines) and the eight levels grid (solid lines) for $Re = 40$ . . . . .	121
11.8	Physical parameters of the flow pattern for steady flow used in Table 11.1 . . . . .	121
11.9	Vorticity contours from left to right at $t = 5$ ms, $t = 10$ ms, $t = 15$ ms, $t = 20$ ms, $t = 25$ ms, $t = 30$ ms, $t = 40$ ms, and $t = 50$ ms . . . . .	122
11.10	Description of the various waves arising in the Schardin's problem. AW: accelerated wave, DW: decelerated shock-wave, EW: expansion wave, IS: incident shock-wave, MS: Mach stem, RS: reflected shock-wave, SL: slip layer, TP1 and TP2: triple points, V: vortex. (issued from [BEBM18]) . . . . .	123
11.11	Schematic diagram of Schardin's problem, all the dimension are in mm . . . . .	123
11.12	Comparison of triple point trajectory and locus of the vortex center . . . . .	124
11.13	Schlieren snapshots from top left to bottom right at $t = 60 \mu s$ , $t = 90 \mu s$ , $t = 120 \mu s$ , and $t = 150 \mu s$ . . . . .	125
11.14	Comparison of numerical shadowgraph (top-half) and experimental shadowgraph [CC00] (bottom-half) at $151 \mu s$ . . . . .	125
12.1	Schematic diagram of the region of accuracy and its growth . . . . .	129
12.2	binary tree . . . . .	129
12.3	Ignition by a reflected shock wave, test case configuration . . . . .	131
12.4	Isolines of temperature. Distinction of the different waves with the reflection wave, the transmission wave, the reflection and the detonation wave . . . . .	131
12.5	Schlieren photograph with relative times marked [OYBC82] . . . . .	132
12.6	Comparison with various parameters of tolerance and time-step using in the ISAT-CK7 algorithm. In black solid line: reference result without ISAT; in red dashed line on the left figure: $\epsilon_{tol} = 10^{-2}$ and $\Delta t_{reac} = 10^{-7}$ s; in green dashed line on right figure: $\epsilon_{tol} = 10^{-3}$ , $\Delta t_{reac} = 2 \cdot 10^{-7}$ s . . . . .	133



12.7	Isolines of temperature with ISAT-CK7 algorithm. Results are close to the reference results 12.4 . . . . .	133
12.8	Representation of the ISAT binary trees with the 38 759 recorded points. The cross correspond to the nodes and the bullets corresponds to the recorded points . . . . .	134
12.9	Vorticity inside a two-dimensional detonation front in 2H <sub>2</sub> /O <sub>2</sub> /7Ar initially at 6.67 kPa and 298 K at left (without ISAT), right (with ISAT) . . . . .	135
13.1	Laminar flame speed of H <sub>2</sub> /air at atmospheric condition ( $P = 1$ atm; $T = 298$ K) at different equivalence ratios . . . . .	142
13.2	Laminar flame speed of H <sub>2</sub> /air at atmospheric condition ( $P = 1$ atm; $T = 298$ K) at different equivalence ratios with various transport models . . . . .	143
13.3	Stoichiometric laminar flame H <sub>2</sub> /air profile with various resolution . . . . .	144
13.4	Comparison of the ignition delay time with Krejci et al. experimental results [KMV+13] for various pressures and for mixtures of H <sub>2</sub> /O <sub>2</sub> (98% dilution in Ar, equivalence ratio = 0.5) . . . . .	145
13.5	Evolution of the ignition delay time for stoichiometric H <sub>2</sub> /air mixture at $P = 1$ atm (left) and $P = 2$ atm (right) . . . . .	145
13.6	Schlieren image of expanding cylindrical H <sub>2</sub> /air flame at $P = 1$ atm and $T = 298$ K computed with $ \Delta\rho $ . . . . .	146
13.7	Computed Markstein lengths $L_M$ from present simulations versus the stoichiometric ratio for H <sub>2</sub> /air mixture at $P = 1$ atm and $T = 298$ K compared to experimental measurements from Dowdy et al. [DSTW91], Aung et al. [AHF97], Sun et al. [SSHL99] and Huang et al. [HZZ+06] . . . . .	147
13.8	Hydrogen detonation characteristic reaction scales and time (half reaction length at left, and half reaction time at right) versus equivalence ratio with initial conditions of 295K and 1 bar. . . . .	147
13.9	Hydrogen detonation effective activation energy parameter $\Theta$ versus equivalence ratio with initial conditions of 295K and 1 bar . . . . .	148
13.10	Maximum pressure histories for different Ar dilutions . . . . .	150
13.11	Maximum pressure histories for 25% Ar dilutions with Navier Stokes equations . . . . .	151
13.12	Pressure contours for detonation front with 2H <sub>2</sub> -O <sub>2</sub> mixture with 40% Ar dilution (left) and no dilution (right). . . . .	152
13.13	Numerical smoke foil records for 2H <sub>2</sub> -O <sub>2</sub> mixture with 40% Ar dilution (up) and no dilution (down). . . . .	152
13.14	Detonation cell size for 2H <sub>2</sub> -O <sub>2</sub> at various initial pressure measured experimentally by Barthel [Bar74] and Knystautas et al. [KLG82]. . . . .	153
14.1	Schematic representation of initial condition and boundaries for simulation of detonation interaction with porous medium . . . . .	156
14.2	Temperature field evolution illustrating the detonation re-initiation with $b = 30 l_{1/2}$ . Successive time at $t = 0, 2, 4, 6, 7, 8, 10, 12, 14 \mu\text{s}$ ; temperature scale is between 298 K (blue) and 3500 K (red). . . . .	157
14.3	Velocity of the precursor shock-wave recorded along the top and bottom boundaries for a pore size $b = 30l_{1/2}$ . . . . .	158
14.4	Temperature field obtained with Euler equations (at the top) and with Navier-Stokes equations (at the bottom) at $t = 9 \mu\text{s}$ . . . . .	158
14.5	Temperature field evolution illustrating the detonation re-initiation with $b = 15 l_{1/2}$ . Successive time at $t = 0, 2, 6, 8, 11, 15, 19, 24, 29, 32, 34, 35, 37, 42 \mu\text{s}$ ; temperature scale is between 298 K (blue) and 3500 K (red). . . . .	159
14.6	Velocity of the precursor shock-wave recorded along the top and bottom boundaries for a pore size $b = 15l_{1/2}$ . . . . .	159
14.7	Schematic of the explosion channel in the obstructed configuration (BR60); Dimensions in (mm) . . . . .	160
14.8	Transverse H <sub>2</sub> concentration profile in the inhomogeneous case at the initial condition . . . . .	161

14.9	Comparison of the flame velocities with experimental data for homogeneous mixture (left) and inhomogeneous mixture (right) . . . . .	162
14.10	Temperature field in between the left end plate and the first obstacle for the homogeneous mixture (left), with symmetry applied at $y = 0.03$ m, and inhomogeneous mixture (right) in the low Mach regime. Successive times at $t = 0, 1, 2, 3, 4, 5$ ms; temperature scale is between 293 K (blue) and 3000 K (red). . . . .	163
14.11	Temperature field in between the first two obstacles for homogeneous mixture (left), with symmetry applied at $y = 0.03$ m and inhomogeneous mixture (right) in the fast deflagration regime. Successive times at $t = 6, 6.25, 6.5, 6.75, 7, 7.25$ ms; temperature scale is between 293 K (blue) and 3000 K (red). . . . .	163
14.12	Density field through the second obstacle for inhomogeneous mixture $t = 7.34$ ms . . .	164
14.13	Vorticity field (top) and baroclinic production (bottom) through the second obstacle for inhomogeneous mixture $t = 7.34$ ms . . . . .	165
14.14	Temperature field (top) and pressure field (bottom) through the third obstacle for homogeneous mixture at $t = 8.68$ ms, with symmetry applied at $y = 0.03$ m . . . . .	165
14.15	Density field with mesh in the front flame for homogeneous mixture at $t = 8.68$ ms . .	166
14.16	Mass fraction of $\text{HO}_2$ in the front flame for homogeneous mixture at $t = 8.68$ ms . . .	166
17	Solution (left) and characteristic waves (right) for a shock wave . . . . .	176
18	Solution (left) and characteristic waves (right) for a rarefaction wave . . . . .	176
19	Schematic representation of the initial state in a shock tube. . . . .	180
20	Structure of the solution of the Riemann problem in the $x - t$ plane for the one-dimensional Euler equations in which the left wave is a shock wave and the right wave is a rarefaction wave. . . . .	180
21	Determination of the nature and intersection of the characteristic curves of shock wave $\lambda^-$ and rarefaction wave $\lambda^+$ in the $(u, p)$ plane . . . . .	183
22	Exemple de profils de densité, vitesse et température d'un tube de choc de Sod avec un mélange multi-composant avec et sans correction . . . . .	196
23	Champ de température illustrant un régime de quasi-détonation et la réinitiation de la détonation après un milieu poreux avec la superposition d'ondes transverses . . . . .	198
24	Champ de vorticité (haut) et de production barocline (bas) illustrant la perturbation du front de flamme et son accélération dans le tube d'accélération . . . . .	199



# List of Tables

1.1	Hydrogen physicochemical properties relevant for hydrogen safety (293.15 K/101.325 kPa) [XDS18]. . . . .	4
6.1	RaudauIIA method of order 5 . . . . .	54
8.1	Initial condition of pressure, density and species mass fraction for the Sod shock tube (left) and the Lax shock tube (right) problems . . . . .	77
10.1	Coefficients of centered linear polynomials interpolation [Har95] . . . . .	103
11.1	Physical parameters of the flow pattern around a circular cylinder at $Re = 40$ : wake length $L/d$ , location and recirculation centre (a,b), separation angle $\theta_s$ and drag coefficient $C_D$ . . . . .	120
11.2	Unsteady flow past at circular cylinder at $Re = 200$ : Strouhal number $St$ , drag coefficient $C_D$ , and lift coefficient $C_L$ . . . . .	122
13.1	Values of detonation parameters computed for mixture at $T_0 = 298$ K and $P_0 = 1$ atm with hydrogen chemical mechanism of Mével . . . . .	149
1	H <sub>2</sub> Mevel's detailed mechanism [MJL+09] . . . . .	190



# Nomenclature

## Acronyms

BR	Blockage Ratio
CJ	Chapman-Jouguet
DDT	Deflagration to Detonation Transition
DL	Darrieus-Landau
IBM	Immersed Boundary Method
ISAT	In Situ Adaptive Tabulation
LC	Large Curvature
LODI	Local associated One-Dimensional Inviscid problem
LTE	Local Thermodynamic Equilibrium
MD	Median
MP	Monotonicity Preserving
NSCBC	Navier-Stokes Characteristic Boundary Conditions
OSMP	One-Step Monotonicity Preserving
TVD	Total Variation Diminishing
UL	Upper Limit
VN	Von Neumann
ZND	Zeldovich-von Neumann-Döring

## List of main symbols

$\alpha$	Riemann invariants (SI units)
$\alpha_i$	Immersed volume fraction of cell $i$ (-)
$\beta$	temperature exponent (-)

$\chi$	stability parameter (-)
$\chi_j$	compressibility factor ( $\text{J kg}^{-1}$ )
$\Delta h_j^0$	enthalpy changes during the $j$ th reaction ( $\text{J mol}^{-1}$ )
$\Delta s_j^0$	entropy changes during the $j$ th reaction ( $\text{J K}^{-1} \text{mol}^{-1}$ )
$\Delta t$	time step (s)
$\Delta x$	space step (m)
$\Delta_I$	ZND induction length (m)
$\delta_l$	laminar flame thickness (m)
$\Delta_R$	ZND reaction length (m)
$\delta_R$	laminar flame reaction zone thickness (m)
$\dot{\omega}_i$	chemical production rate of the species $i$ ( $\text{s}^{-1}$ )
$\dot{\sigma}$	thermicity ( $\text{s}^{-1}$ )
$\dot{m}$	mass flux ( $\text{kg m s}^{-1}$ )
$\epsilon$	small number (-)
$\epsilon_I$	reduced activation energy (-)
$\eta_k$	Kolmogorov length microscale (m)
$\Gamma$	Grüneisen coefficient (-)
$\gamma$	heat capacity ratio (-)
$\kappa$	compressibility factor (-)
$\kappa_{i\pm 1/2}$	immersed side area fractions of cell $i$ (-)
$\lambda$	detonation cell size (m)
$\lambda$	thermal conductivity ( $\text{W m}^{-1} \text{K}^{-1}$ )
$\mathbb{K}$	stretch rate ( $\text{s}^{-1}$ )
$\mathbf{d}_k$	diffusion force of the $k$ th species (N)
$\mathbf{f}^E$	vector of Euler flux
$\mathbf{f}^V$	vector of viscous flux
$\mathbf{S}$	vector of source term
$\mathbf{u}$	velocity vector ( $\text{m s}^{-1}$ )
$\mathbf{V}_i$	diffusion velocity of the $i$ th species ( $\text{m s}^{-1}$ )
$\mathbf{w}$	vector of conservative variables

$\mathcal{D}_{ik}$	binary diffusion coefficient for species pair $i, k$ ( $\text{m}^2 \text{s}^{-1}$ )
$\mathcal{G}$	fundamental derivative (-)
$\mu_k$	electrochemical potential of species $k$ ( $\text{J kg}^{-1} \text{mol}^{-1}$ )
$\mu_l$	dynamic viscosity ( $\text{kg m}^{-1} \text{s}^{-1}$ )
$\nu$	CFL number
$\nu', \nu''$	stoichiometric coefficients (-)
$\nu_l$	kinematic viscosity ( $\text{m}^2 \text{s}^{-1}$ )
$\Omega$	volume of cell ( $\text{m}^3$ )
$\omega$	growth rate
$\bar{\mu}$	electrochemical potential ( $\text{J mol}^{-1}$ )
$\bar{W}$	mixture-averaged molar mass ( $\text{kg mol}^{-1}$ )
$\Phi$	equivalence ratio, premixed case (-)
$\Pi$	viscous strain rate tensor ( $\text{kg m}^{-1} \text{s}^{-2}$ )
$\Psi$	enthalpy conductive flux ( $\text{kg m}^{-1} \text{s}^{-3}$ )
$\rho$	density ( $\text{kg m}^{-3}$ )
$\sigma$	expansion ratio (-)
$\tau_I$	ZND induction time (s)
$\theta_k^*$	thermal diffusion ratio for species $k$ (-)
$\varepsilon$	turbulence dissipation rate (-)
$\varsigma$	Harten criterion (-)
$\Xi$	interface exchange term
$A$	pre-exponential kinetic factor (SI units)
$A_{\mathcal{F}}$	area of face $\mathcal{F}$ ( $\text{m}^2$ )
$C_D$	drag coefficient (-)
$C_i$	concentration of species $i$ ( $\text{mol m}^{-3}$ )
$C_L$	lift coefficient (-)
$c_p$	specific heat capacity at constant pressure ( $\text{J kg}^{-1} \text{K}^{-1}$ )
$c_s$	sound speed ( $\text{m s}^{-1}$ )
$c_v$	specific heat capacity at constant volume ( $\text{J kg}^{-1} \text{K}^{-1}$ )
$D$	ordinary multicomponent diffusion coefficient ( $\text{m}^2 \text{s}^{-1}$ )



$D$	tube diameter (m)
$d$	orifice diameter of roughness tube (m)
$D_k^*$	approximate diffusion coefficient for species $k$ ( $\text{m}^2 \text{s}^{-1}$ )
$D^T$	thermal diffusion coefficient ( $\text{m}^2 \text{s}^{-1}$ )
$E$	total energy per unit of mass ( $\text{J kg}^{-1}$ )
$E_a$	activation energy (J)
$H$	total enthalpy per unit of mass ( $\text{J kg}^{-1}$ )
$h$	specific enthalpy ( $\text{J kg}^{-1}$ )
$h_f^0$	formation enthalpy ( $\text{J mol}^{-1}$ )
$h_s$	sensible enthalpy ( $\text{J kg}^{-1}$ )
$K$	wavenumber
$k_f, k_b$	kinetic rate coefficients for the forward and backward reactions (SI units)
$K_{c,j}$	equilibrium constant for the $j$ th reaction (SI units)
$L_M$	Markstein length (m)
$l_r$	size of motion in turbulence flow (m)
$l_t$	integral scale (m)
$N_r$	number of elementary reactions (-)
$n_s$	number of chemical elements (-)
$N_{dim}$	space dimension (-)
$N_j$	amount of species $i$ (mol)
$p$	pressure (Pa)
$q$	heat of the reaction (J)
$q_j$	progress rate of the $j$ th reaction (-)
$q_r$	heat release of reaction ( $\text{J kg}^{-1}$ )
$r$	specific gas constant ( $\text{J K}^{-1} \text{kg}^{-1}$ )
$R_{gas}$	universal gas constant ( $\text{J K}^{-1} \text{mol}^{-1}$ )
$s$	specific entropy ( $\text{J K}^{-1} \text{kg}^{-1}$ )
$S_l$	flame velocity ( $\text{m s}^{-1}$ )
$S_l^0$	laminar flame velocity ( $\text{m s}^{-1}$ )
$T$	temperature (K)

$t$	time (s)
$t_F$	chemical time scale (s)
$t_r$	turbulence time scale (s)
$t_\eta$	Kolmogorov time microscale (s)
$u_i$	$i$ th-velocity component ( $\text{m s}^{-1}$ )
$u_{sp}$	gradient of induction ( $\text{m s}^{-1}$ )
$v$	particule velocity ( $\text{m s}^{-1}$ )
$v'$	velocity fluctuation ( $\text{m s}^{-1}$ )
$W_i$	molar mass of species $i$ ( $\text{kg mol}^{-1}$ )
$x, y, z$	spatial coordinates (m)
$x_i$	number of moles of the $i$ -th element (mol)
$Y_i$	mass fraction of the $i$ -th element (-)
$Ze$	Zeldovich number (-)

### **Nondimensional Parameters**

$Da$	Damköhler number
$Ka$	Karlovitz number
$Le$	Lewis number
$M$	Mach number (-)
$Re$	Reynolds number
$St$	Strouhal number



## Part I

# Introduction



# Context and motivations

The work presented here was carried out with the CEA in the context of hydrogen safety, an issue that has been studied extensively in nuclear safety and which is becoming increasingly important for other actors with the development and application of new uses, particularly in the production and storage of energy for the general public. We, therefore, present here the stakes of an economy turned towards hydrogen and those more applied explicitly to nuclear safety.

## 1.1 The hydrogen economy

Today, hydrogen is used as a chemical agent in many industrial domains. A large amount of hydrogen is required, for example, in the ammonia's production, generally intended for chemical fertilizer production, in the methanol's production, in the hydrogenation and the desulfurization of oil or biomass, and in the production of steel. For this last case, hydrogen is a reducing gas of the iron and is particularly required in the direct reduced iron process.

In 2020, its demand was about 90 Mt, with more than 70 Mt used as pure hydrogen and less than 20 Mt mixed with carbon-containing gases in methanol production and steel manufacturing. The distribution of uses and production means for the year 2020 are represented in figure 1.1 with data from the International Energy Agency report on hydrogen [IEA21].

In addition, hydrogen also has chemical characteristics that allow it to be considered as an energy carrier with applications in transportation and energy storage and production, or even as domestic

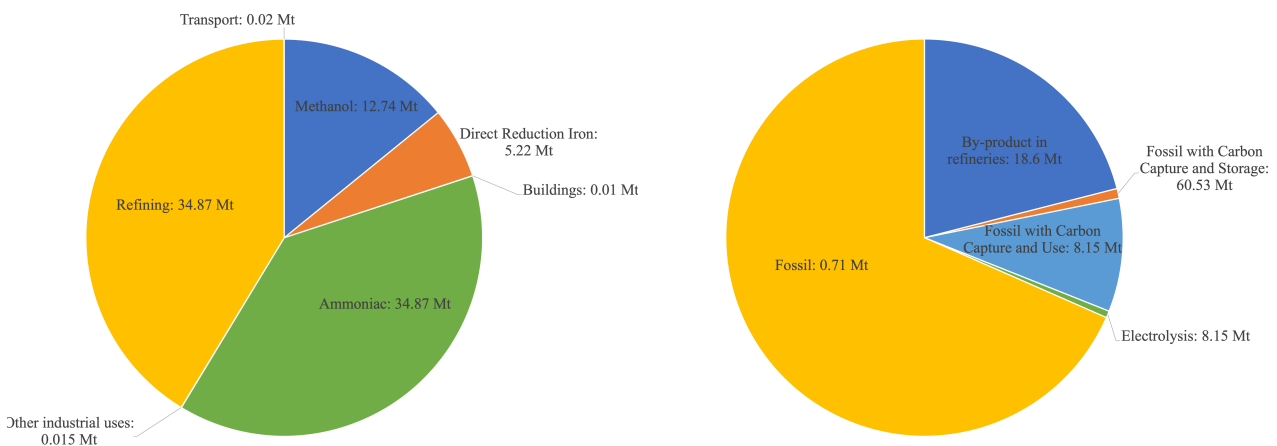


**Figure 1.1:** Global energy demand for  $H_2$  by sector (left) and corresponding production technology (right) in 2020 [IEA21]

	Hydrogen	Methane	Gasoline
Density (kg m <sup>-3</sup> )	0.089	0.67	-
Coefficient of diffusion in air (cm s <sup>-1</sup> )	0.61	0.16	0.05
Flammability limits (vol%)	4-75	5.3-15	1-7.6
Stoichiometric Ignition energy (mJ)	0.018	0.280	0.25
Energy density (MJ kg <sup>-1</sup> )	119.96	55.6	46.4
Auto-ignition temperature (K)	845	905	713
Deflagration index (bar m s <sup>-1</sup> )	550	55	100-150

**Table 1.1:** *Hydrogen physicochemical properties relevant for hydrogen safety (293.15 K/101.325 kPa) [XDS18].*

energy. It can indeed replace fossil fuels in virtually all applications. For several decades and in recent years, projects using hydrogen as an energy carrier on a large scale have been developed to meet emission reduction targets.

Hydrogen’s advantages are numerous for many of these uses because of its energy density (120 MJ/kg), its abundance (but unfortunately not naturally in the form of dihydrogen), and its wide variety of production methods potentially with low carbon and limited environmental impact. The main advantage of its use as an energy carrier is the absence of CO<sub>2</sub> emissions during its combustion or its use in a fuel cell. Hydrogen is also considered for energy storage for periods of up to a week in adapted structures [Wol15].

Implementing an economy based on hydrogen requires adapted infrastructures for storage, production, transport, and distribution and must respond to numerous technical, cost, and political issues that are not addressed here. The risks are relatively well controlled at the industrial level despite some major historical accidents with ammonium nitrate, but its flammable and explosive properties require strong reliability to deploy these technologies to the general public.

## 1.2 Safety challenges in this hydrogen economy

As mentioned before, hydrogen is not an energy source but an energy carrier, and consequently, it will be as clean as the method employed for its production.

Moreover, the intrinsic properties of this molecule imply some difficulties. First, dihydrogen is a very small molecule that imposes a low energy density on a volume. Its storage on the surface requires high pressure tanks (700 bar for Fuel Cell electrical vehicle’s) or its liquid form at a very low temperature (about 20 Kelvin). However, its density is still inferior to 0.1 kg/L in all cases compared to 0.7-0.8 kg/L for gasoline. Hydrogen is the substance with the smallest relative mass, and then it easily leaks from high-pressure environments. It also diffuses into steel and other metals, resulting in material strength reduction and embrittlement during its storage. Hydrogen gas is highly diffusive and buoyant; it rapidly mixes with the ambient air upon release and fills a confined space quickly.

Hydrogen is also characterized by a lack of odor and color which increases the difficulty of detection and its possibility of flaming with a wide range of flammability (when air is mixed with a hydrogen volume fraction of only 4% up to 75%) and low minimum ignition energy, which reinforces spontaneous ignition. Finally, its combustion produces high temperature and pressure during premixed flame propagation.

Table 1.1 gives the main properties of hydrogen in comparison to natural gas and gasoline. The deflagration index refers here to the maximum rate of pressure rise observed in a closed vessel without internal obstacles.

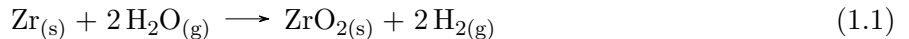
Those particular flammability properties make hydrogen a more sensitive gas than the other hydrocarbon fuels in confined space. Therefore, to ensure hydrogen’s safe and reliable use, its characteristics relevant in the phenomenon of leakage and diffusion, ignition, and explosion must be analyzed.

When hydrogen is ignited with low ignition energy, laminar combustion first occurs. Afterward, because of the inherent instability of the flame, the interaction with acoustic and pressure waves, and obstructions in the flow, the flame undergoes turbulent combustion, which increases the flame speed, and eventually shift to detonation. This work addresses both issues by the simulation of the flame acceleration phenomenon and the potential onset of detonation.

### 1.3 Application in the context of nuclear safety

Hydrogen safety issues have long been studied in the specific context of nuclear safety. Indeed, in case of a severe accident impacting the cooling system of a reactor containment, the high temperature can trigger some processes that produce hydrogen. The main sources are the zirconium-steam reaction, the water radiolysis, the reaction with boron carbide, or the reaction between the molten core with the concrete of containment.

In the historical accident of Three Miles Island (1979) and Fukushima-Daiichi (2020), the oxidation of zirconium by steam had led to massive hydrogen release when the core was no longer completely covered by liquid water and insufficiently cooled. Zirconium alloy has a very low absorption cross-section of thermal neutrons, a high hardness, ductility, and corrosion resistance. These properties are very interesting for nuclear technologies, and zirconium is used as cladding of fuel rods. There are several tons of this alloy around the fuel rods. However, when the temperature rises to about 1500 K, fuel claddings and other zircaloy structures will react with water vapor or steam and release a large amount of hydrogen and heat (Eq. 1.1), which causes the core to heat still faster. Moreover, the reaction between zircaloy and water increases with the temperature.



In order to prevent the development of hydrogen gas clouds, some mitigation measures are installed in the containment. In small volumes, such as in the Fukushima primary containment, the atmosphere is reduced in oxygen with the addition of nitrogen as inert gas. For larger volumes, Passive Autocatalytic Recombiners (PARs) are used to convert hydrogen and oxygen into water rapidly. However, the presence of recombiners does not eliminate the risk of flame acceleration in case of large production and can even provoke ignition of the mixture [GSv+15]. Spray systems mix the atmosphere and avoid stratification but reduce the water steam's diluent effect, which in turn reduces the explosion limits.

Accumulation of hydrogen inside the containment usually forms a heterogeneous and probably stratified semi-confined hydrogen-air or hydrogen-air-steam mixture layer. Depending upon factors such as geometry and local conditions such as mixture composition, temperature, pressure, and turbulence level, different combustion regimes are possible after the ignition of such layers. These regimes range from a laminar flame to a detonation; several phenomena described in chapter 3 take part in the flame acceleration phenomena until supersonic speed and the transition to the detonation. In the case of supersonic flame and especially with detonation front, high dynamic pressure loads are generated in the containment, which challenges the structural integrity of the containment wall.

During the partial core meltdown in the Three Mile Island Unit-2 accident, about 200 kg of hydrogen was released in the dome region of the containment. At about 10 hours from the initiating event (beginning of the accident), a pressure spike was observed within the containment. It was concluded that this was due to partial deflagration of hydrogen at 8 % concentration in the containment dome [R.E07]. Identical reactions occurred in boiling water reactors of the Fukushima Daiichi Nuclear Power Plant. Report of SANDIA [GKC+12] and TEPCO [TEP17] give an estimation of generation of between 660 kg and 880 kg of hydrogen in each unit in the first 24h after the beginning of the incident. The hydrogen was vented into the reactor maintenance halls and the resulting explosive mixture of hydrogen with air exploded in different sections, especially in the Unit 4 although it was de-fueled.

Flame acceleration phenomena and transition to detonation are significant for nuclear safety to prevent the loss of integrity of the last barrier between radioactive materials and the environment. The



influence of the local composition of the hydrogen/air reactive mixture on the premixed flame speed during its propagation is still an open problem both experimentally and numerically. Accurate prediction of the pressure loads is strongly related to the models' ability to predict the flame acceleration process. This work focuses on methods to simulate the flame behavior and characterize such risk numerically.

# Detonation Phenomenon

The detonation phenomenon is a specific regime of combustion involving supersonic velocity and significant overpressure, which can challenge the integrity of structures in confined environments. Detonations correspond to highly dynamic features structures of shock waves and reaction zone with however specific distributions in space in two or three dimensions. This chapter describes the main properties of a detonation front with the definition of, for instance, Chapman-Jouguet detonation, ZND profile, and cellular structure.

## 2.1 Subsonic and supersonic regimes : Deflagration and Detonation

For a free premixed flame, we distinguish two main combustion regimes: the deflagration regime, characterized by a subsonic propagation of the flame front related to the fresh gases; and the detonation regime, corresponding to the propagation of the flame front at a supersonic velocity.

The propagation mechanism of the flame front differs between the two regimes :

- For the detonation, a precursor shock increases the temperature before the flame front enough to auto-ignite the mixture and maintain the strength of this precursor shock in front of the reactive wave.
- For the deflagration, the flame progresses thanks to heat and species diffusion phenomena. In this regime, many phenomena interact with the flame front and accelerate it. Physical phenomena involved in this process are described more precisely in Chapter 3.

The two regimes of propagation can be differentiated using the conservation of mass, momentum, and total energy across a one-dimension flame front as illustrated in Figure 2.1. Considering the coordinate system attached to the flame front and a steady flow from each side of the front, these conservation laws correspond to:

$$\rho_u v_u = \rho_b v_b, \quad (2.1a)$$

$$p_u + \rho_u v_u^2 = p_b + \rho_b v_b^2, \quad (2.1b)$$

$$h_u + \frac{v_u^2}{2} = h_b + \frac{v_b^2}{2}, \quad (2.1c)$$

where the subscript  $u$  and  $b$  denote the unburnt and burnt gases, respectively.  $\rho$  is the density,  $v$  the velocity in the direction normal to the flame front,  $p$  the local pressure, and  $h$  the specific enthalpy.

To highlight the reaction of the front, the specific enthalpy term can be split into the enthalpy formation and the sensible enthalpy (2.1c) to obtain:

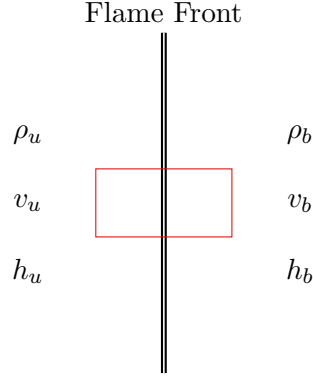


**Figure 2.1:** Balance of conservative variables around the flame front

$$h_{s,u} + q_r + \frac{v_u^2}{2} = h_{s,b} + \frac{v_b^2}{2}, \quad (2.2)$$

where  $q_r$  corresponds to the variation of the enthalpy formation between the unburnt gas and the burnt gas.

$$q_r = \sum_i^{\text{reactants}} Y_i h_{f_i}^o - \sum_i^{\text{products}} Y_i h_{f_i}^o, \quad (2.3)$$

where  $h_f^o$  are the formation enthalpy of each specie and  $Y_i$  the mass fraction of each specie involved in the chemical reaction.

Using the first two equations of conservation (2.1a) and (2.1b) we express the mass flux per unit area  $\dot{m} = \rho u$  with:

$$\dot{m} = \rho_u v_u = \rho_b v_b = \sqrt{\frac{p_b - p_u}{1/\rho_b - 1/\rho_u}}. \quad (2.4)$$

Since  $\dot{m}$  must be a real number, there is only two regions suitable with physical solution in the  $p - 1/\rho$  plane illustrated in Figure 2.2. The region with  $\rho_u < \rho_b$  and  $p_u < p_b$  corresponds to the detonation regime with compression across the detonation flame and the region with  $\rho_u > \rho_b$  and  $p_u > p_b$  corresponds to the deflagration wave with expansion of the gas across the front flame that slightly reduces the pressure.

Moreover, from the initial unburnt gas condition, the steady state solution of the burnt gas evolves along the straight line called the *Rayleigh line* with a slope  $-\dot{m}^2$ .

Using the relation (2.4) and the conservation of energy relation (2.2), we obtain:

$$h_{s,b} - (h_{s,u} + q_r) = \frac{1}{2}(p_b - p_u) \left( \frac{1}{\rho_u} + \frac{1}{\rho_b} \right). \quad (2.5)$$

At this step, we assume that the mixture of gases follows a perfect gas equation of state and is calorically perfect, which means that the heat capacities  $c_p$  of the burnt gas and the unburnt gas are constant with temperature. The validity of the following analysis for real gases, and especially the hypothesis on the equation of state, are reviewed in Chapter 5. A perfect equation of state  $p = \rho r T$  ( $r$  is the specific gas constant and  $T$  the local temperature) implies:

$$h_s = c_p T = \frac{\gamma}{\gamma - 1} \frac{p}{\rho}, \quad (2.6)$$

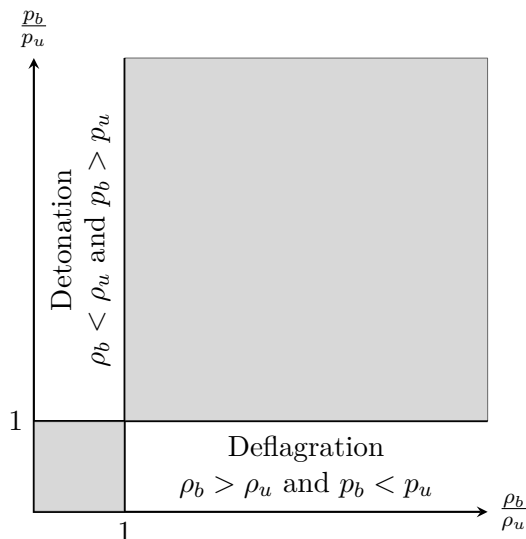


**Figure 2.2:** Domains of detonation and deflagration solutions in the  $p - 1/\rho$  plane

where  $\gamma$  is the heat capacity ratio of the gas. Introducing this relation into (2.5), we obtain the equation of an hyperbole in the  $p - 1/\rho$  plane called the *Hugoniot curve* parametrized by:

$$y = \frac{\frac{\gamma_u + 1}{\gamma_u - 1} - x + 2\frac{\rho_u q_r}{p_u}}{\frac{\gamma_b + 1}{\gamma_b - 1}x - 1}. \quad (2.7)$$

The conservation laws (2.1) then imply that the burnt gas must simultaneously satisfy the Rayleigh line and the Hugoniot curve. This situation is illustrated in Figure 2.3.

If the Rayleigh line does not intersect the Hugoniot curve, there is no solution. Otherwise, there are two distinct points in the same regime with a strong and a weak solution for a given mass flux. Chapman and Jouguet [Oxo99, Jou05] postulate that the detonation solution will converge to the minimum velocity and minimum entropy variation that correspond to the point where the Rayleigh line is tangent to the Hugoniot curve. Experiments confirm this hypothesis, and this specific point is called the Chapman-Jouguet point. The velocity of the detonation front is named the Chapman-Jouguet velocity.

In the deflagration case, the Chapman-Jouguet point corresponds to the maximum possible deflagration speed, which is approximately one-half the Chapman-Jouguet detonation Mach number in the explosive mixture. Contrary to the Chapman-Jouguet detonation, there is no stability consideration in the deflagration case, and a wide range of solutions are possible, allowing flame acceleration mechanisms.

## 2.2 Detonation structure

After gas dynamics analysis based on conservation equations between equilibrium states, we consider in this section the structure of the detonation front in more detail. The one-dimensional model has been formally described by Zeldovich, von Neumann, and Döring and referred to as the ZND model.

### 2.2.1 Steady one-dimensional ZND structure

The ZND structure describes various steps in the evolution of the detonation front. This model considers the chemical kinetics and detailed reactions of the mechanism, distinguishing between the

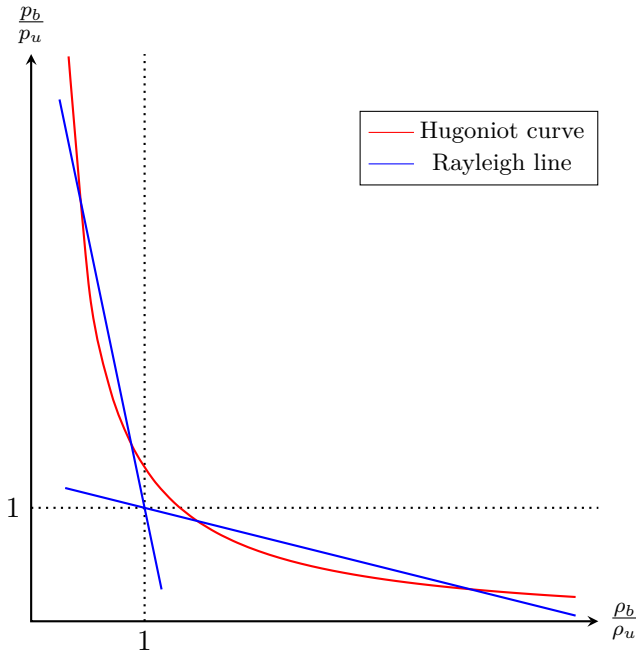


**Figure 2.3:** *The Rayleigh line and the Hugoniot curve*

initiation reactions with limited heat production and the chain-branching exothermic reactions that significantly increase the temperature.

The ZND structure consists of a leading front that adiabatically compresses and heats the reactants up to the ignition temperature. This precursor shock is followed by an induction zone where active radical species are generated in the initiation reaction. This zone is globally thermally neutral. The rapid chain reaction zone finally increases the temperature and reduces local pressure until the final Chapman-Jouguet state. An example of the successive zone of the ZND structure is illustrated in Figure 2.5. Concerning the evolution in the  $p - 1/\rho$  diagram, the transition through the detonation front first stays on the Hugoniot curve without heat release by reaction (Crussard curve) that corresponds to the precursor shock to get the Von Neuman point and then returns to the Chapman-Jouguet point along the reaction zone (Figure 2.4) that releases heat.

The ZND structure and especially the length of the induction zone is controlled by various chemical parameters with, for example, the activation energy present in the Arrhenius law described in Chapter 5 that measures the temperature sensitivity of the chemical reaction. The induction length is correlated with the properties of the detonation waves and has an impact on the grid resolution needed to capture the detonation structure properly, as discussed in § 13.3.2.

Considering the steady-state ZND model for detonation structures in the reference frame attached to the moving shock wave, with  $n_s$  species, we obtain the set of equations:

$$\frac{d}{dx'}(\rho v' Y_i) = \rho \dot{\omega}_i; \quad (i = 1, \dots, n_s) \quad (2.8a)$$

$$\frac{d}{dx'}(\rho v'^2 + p) = 0; \quad (2.8b)$$

$$\frac{d}{dx'}(\rho v' H) = 0, \quad (2.8c)$$

where  $x'$  and  $v'$  are respectively the distance to the shock wave and the particle velocity in the reference frame of the shock wave.  $Y_i$  and  $\dot{\omega}_i$  are the mass fraction and the chemical production rate of the species  $i$ , respectively.  $H$  is the total enthalpy corresponding to the sum of the specific enthalpy and the kinetic energy of the gas:

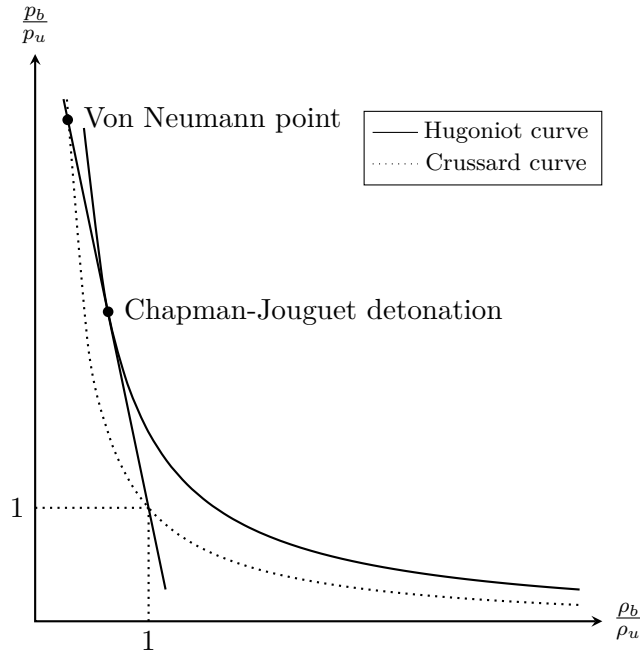


**Figure 2.4:** Particular point in the ZND theory

$$H = h + \frac{1}{2}u^2. \quad (2.9)$$

It is possible to express equations (2.8) in a more convenient form for integration which is given by:

$$\frac{dp}{dt'} = -\rho v'^2 \frac{\dot{\sigma}}{1 - M^2}; \quad (2.10a)$$

$$\frac{d\rho}{dt'} = -\rho \frac{\dot{\sigma}}{1 - M^2}; \quad (2.10b)$$

$$\frac{dv'}{dt'} = v' \frac{\dot{\sigma}}{1 - M^2}; \quad (2.10c)$$

$$\frac{dY_i}{dt'} = \dot{\omega}_i \quad (i = 1, \dots, n_s), \quad (2.10d)$$

with  $M$  the flow Mach number ( $M = v'/c_s$  where  $c_s$  is the local sound speed) and  $t' = x'/v'$ .  $\dot{\sigma}$  is the thermicity, used to denote the non-dimensional energy release rate, defined by:

$$\dot{\sigma} = \sum_{i=1}^{n_s} \left( \frac{\bar{W}}{W_i} - \frac{h_i}{c_p T} \right) \dot{\omega}_i, \quad (2.11)$$

where  $\bar{W}$  is the mean molar mass of the mixture, and  $h_i$  the specific enthalpy of specie  $i$ .

The transformation of the set of equations (2.8) to (2.10) is described in Appendix B of [Ng05].

For a ZND detonation wave traveling at the Chapman-Jouguet velocity, the equilibrium state is reached when  $v'$  reaches the sound speed value in the burnt gas. By conservation laws described in (2.1), we obtain the value of the Chapman-Jouguet velocity, the strength of the precursor shock wave, and the composition of the Von Neuman state. Knowing the initial and final condition, (2.10) can be solved to compute the ZND profile entirely. The computation of this profile will often be used to initiate numerical simulations.

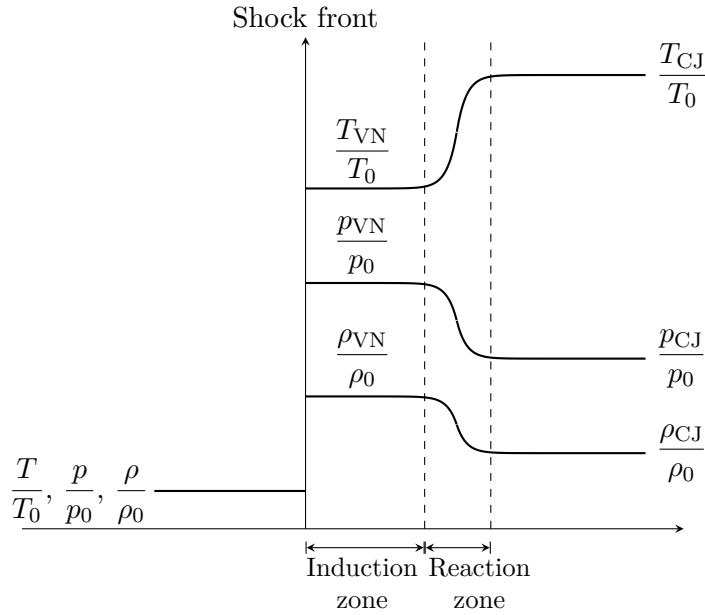


**Figure 2.5:** ZND model sketch reproduced from [Lee08]

### 2.2.2 Unstable one-dimensional detonations

Steady ZND profiles are difficult to observe experimentally. Indeed, depending on the initial conditions and mixture properties, the detonation front is inherently unstable. In one dimension, this instability property can generate pulsations on the post-shock pressure and variation of the shock velocity.

Many theoretical and numerical studies of the one-dimensional pulsating detonation have been carried out in the past [Erp62, BMR91, SQ97, NRH+05]. Linear stability analyses performed by Erpenbeck [Erp62, Erp64] show that laminar ZND structures are sensitive to hydrodynamic perturbations, especially for detonation with strong shock waves. In the following decades, other critical parameters have been identified as influencing the pulsating structures with the specific heat ratio, the activation energy, the heat release and the order of the reaction, and the degree of the detonation overdrive (characterizing detonation faster than the Chapman-Jouguet velocity called pathological detonation [Lee08]). Bifurcations in the pulsations are also observed with a structure that changes from harmonic oscillations to chaotic structures [BMR91].

Most of these studies have been realized with one single-step Arrhenius law; however, using multi-step reaction highlights the influence of the chain-branching kinetics on the pulsating structure. Based on a three-step reaction model with initiation reactions, chain branching reaction, and chain termination, Short & Quirk [SQ97] linked the stability properties to the ratio between the induction zone length and the reaction zone length, i.e., the distance from the main reaction to the location where all the radicals are consumed.

The reason invoked for the instability is the presence of small fluctuations in the shock temperature, which results in large fluctuations in the induction delay time that destabilize the detonation front. Meyer and Oppenheim [MO71a, MO71b] then made a distinction between a strong regime with uniformly distributed ignition and a mild regime with exothermic spots. The strong regime gives detonation free of instability; it requires that neighboring particles initially at slightly different shock strength release their chemical energy with similar delays. In that case, the power pulses overlap and give a single gas-dynamic effect. They related irregular cells to the sensitivity of the chemical induction time  $\tau_i$  to changes of shock temperature.

Using hypothesis that induction time has Arrhenius form:

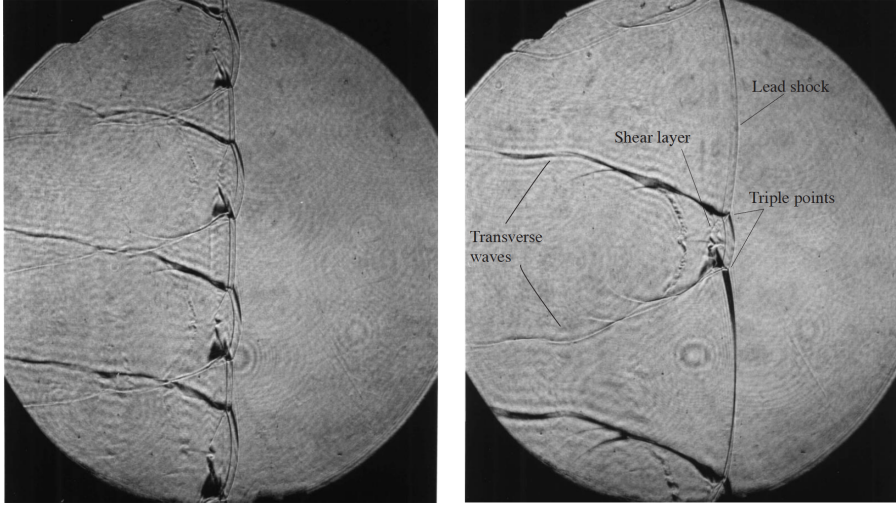


**Figure 2.6:** Schlieren image of a detonation front in  $2H_2-O_2-12Ar$ ,  $P_1 = 20$  kPa [Aus03]

$$\tau_I \sim \exp\left(\frac{E_a}{R_{gas}T_{VN}}\right), \quad (2.12)$$

with  $E_a$  the global activation energy, and  $R_{gas}$  the universal gas constant, Radulescu [Rad03] construct criteria between stable and unstable ignition using the normalized activation energy  $\epsilon_I = \frac{E_a}{R_{gas}T_{VN}}$ . Since a long time for energy release still leads to quasi-simultaneous energy deposit and coherence between time and space even if the changes of induction times are important. Radulescu and Ng [NRH+05] also consider the ratio between the induction length  $\Delta I$  and reaction length  $\Delta R$  to construct a stability parameter  $\chi$  such as:

$$\chi = \left| \frac{T}{\Delta R} \frac{\partial \Delta I}{\partial T} \right| = \epsilon_I \frac{\Delta I}{\Delta R}. \quad (2.13)$$

The values of  $\chi$  are used to compare stability between different mixtures, Ng et al. [NRH+05] create a neutral stability curve from analytical analyses to distinguish stable from unstable one-dimensional detonation. Similar numerical tests with pulsation instability generated in a one-dimensional hydrogen detonation front with stabilizing effect of argon dilution are presented in § 13.3.2.

### 2.2.3 Cellular detonation structure

In one dimension, instability is expressed with longitudinal oscillations in the direction of detonation propagation. In two or three dimensions, transverse oscillations normal to the direction of propagation are superimposed to the longitudinal pulsations. The leading front of the detonation is then deformed by a triple shock configuration, in which transverse shock waves propagate perpendicularly to the main direction of detonation propagation. This configuration is visible in the Schlieren images of Austin [Aus03] in Figure 2.6.

Transverse shock wave propagation will collide periodically as the detonation propagates with time. During those collisions, high temperature and pressure regions are generated and accelerate the local leading shock. Local gas expands as the front moves forward, and shock strength finally decays until the next collision. The trajectory of the triple point forms scale-like structures called *detonation cells*. Detonation front with cells is schematically represented in Figure 2.7.

Detonation cell size is a characteristic dynamic parameter of the detonability of a mixture and can be used to estimate another dynamic parameter as the limited diameter of a tube for the propagation of a detonation front described in § 4.1.2. Detonation cells can be observed experimentally with a thin



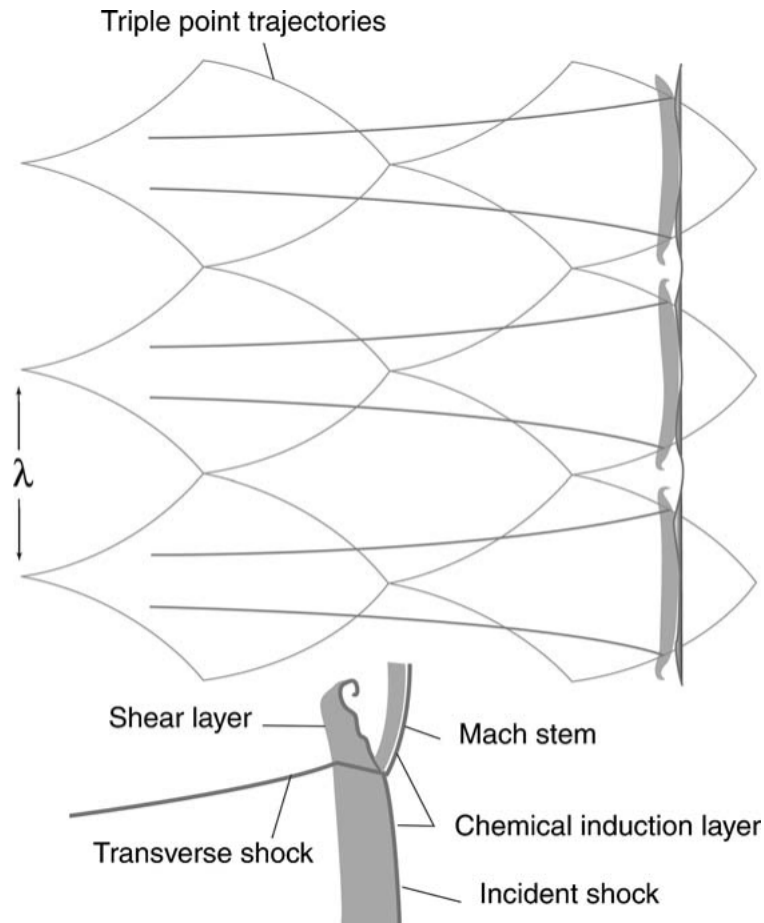


**Figure 2.7:** *The cellular structure of a detonation wave. Detonation cells are traced out by the triple points composed of the incident shock, transverse shock, and Mach stem.  $\lambda$  is the detonation cell width. Image taken from [LR05]*

layer of soot or smoke foil that records local overpressure created by transverse waves and collision (Figure 2.8). Quantitative theories have been developed to predict the cell size with, for example, linear proportionality relationship between the cell size and the ZND chemical length scale proposed by Shchelkin and Troshin [ST64]. Estimation of the proportionality coefficient and its relation with the mixture composition and its equivalent ratio has been investigated by Shepherd et al. [SMMT88]. Finally, the semi-empirical method has been developed by Gavrikov et al. [GED00] that described this coefficient with a relation with the stability parameter of the detonation structure. Following this work, Ng et al. [NJL07] also established an empirical relation based on the stability parameter  $\chi$  for the one-dimensional ZND structure described previously.

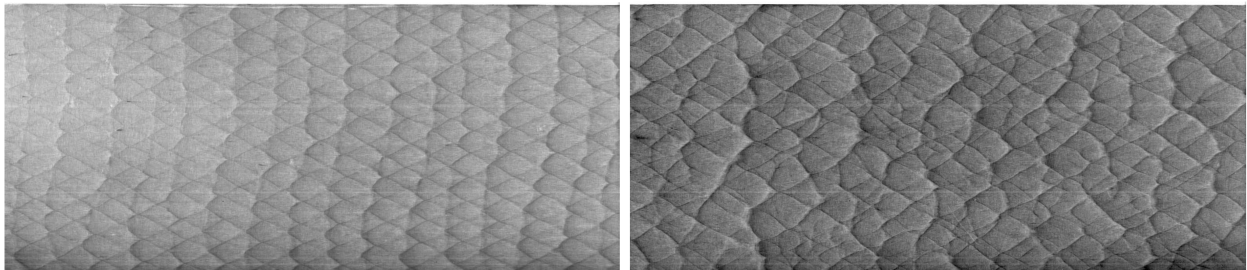


**Figure 2.8:** *Soot foils in  $2H_2-O_2-7Ar$  mixture (left) showing regular detonation cells, and  $2H_2-O_2-1.33N_2$  mixture (right) from [Aus03] showing irregular detonation cells*

Indeed, in relation to the instability displayed by one-dimensional detonation waves, multi-dimension structures form more or less regular structures that characterize the degree of stability of the det-

onation front. In the case of a weak detonation, detonation cells are regular, and their size is well determined. With more unstable detonation, the transverse wave strength is much more important. Large detonation cells length ratios can be observed [APS05].

Regularity property will have a significant impact on the behavior of the detonation front, especially on the critical conditions necessary for the existence of a quasi-steady ZND detonation. The classical ZND model can well approximate the propagation of the detonation front with weak transverse waves. However, for detonation fronts with strong transverse waves and sensitivity to instabilities, 2D and 3D effects with shock compression and compressible turbulence interactions can maintain sufficiently high burning rates necessary for the self-sustenance even with velocity below Chapman-Jouguet velocity. From a numerical consideration, the grid resolution needed to capture instabilities on irregular detonation front correctly is also higher [CMY08]. Test in this regard are carried out in § 13.3.3.



## Flame acceleration

This chapter summarizes the main mechanisms associated with flame acceleration and the Deflagration to Detonation Transition (DDT). The detonation regime induces shock waves and flame front that converge to the Chapman-Jouguet (CJ) velocity. During the deflagration regime, the flame front speed varies from laminar speed, of the order of a few meters per second, to speeds close to the speed of sound in the burnt gas. The acceleration is due mainly to the increase of the flame surface area induced by different phenomena acting more or less dominantly according to the deflagration phase. Three successive phases, characterized by the speed of the flame, can be distinguished during a continuous flame acceleration.

1. The laminar and cellular flame propagation, introduced in § 3.1.2 with an exponential acceleration due to gas expansion and hydrodynamic instabilities intrinsic to the flame sometimes called autoturbulence.
2. The slow turbulent deflagration regime, described in § 3.1.4 with a prevalence of the impact of turbulence on the flame.
3. The fast deflagration regime, described in § 3.1.5 with the impact of compressible effects on the flame.

Finally, the flame acceleration process can eventually lead to a DDT because of various phenomena influencing the local reactivity of the mixture described in § 3.2.

### 3.1 Deflagration regimes

#### 3.1.1 Ignition

Two ignition modes are possible in a premixed mixture depending on the ignition energy involved. With moderate ignition energy, deflagration will be created. This ignition scenario is encountered in accidents in industrial environments, especially with H<sub>2</sub>-air mixture, which requires low ignition energy, as we saw in the Chapter 1.

With high ignition energy, a detonation can be directly initiated if H<sub>2</sub> concentration is sufficiently high. In that case, the onset of detonation is initiated with the generation of high local temperature and pressure. Critical energy is required to produce a blast wave which will decay to the Chapman-Jouguet strength with sufficient radius to establish the induction-zone thickness [HC94]. This direct ignition generally requires the use of an explosive system. However, Yoshikawa and Lee [LKY78, Yos80] have investigated other mechanisms of direct initiation by photolysis and turbulent mixing to create the critical chemical conditions required for the onset of detonation.

Mechanisms of direct initiation of detonation are similar to those allowing transition from deflagration mode to the detonation mode described in § 3.2 where the critical conditions are achieved via flame

acceleration and compressible effects.

### 3.1.2 Laminar deflagration

After the ignition of the mixture, the flame is close to a laminar deflagration mode. This laminar regime is impacted by three fundamental mechanisms: thermal diffusion, species diffusion, and chemical reaction.

When the flame front has a slow velocity, gases are dilated in an isobaric process, expanding the fresh gas in front of the reaction zone and putting them in motion. This expansion is combined with propagation of the flame front characterized by a laminar velocity  $S_l^0$  in the fresh gas frame. This fundamental velocity depends on the diffusion effects.

Such laminar flame is also characterized by their expansion ratio  $\sigma = \rho_u/\rho_b$ , (where subscripts  $u$  and  $b$  designed the unburnt gas and burnt gas, respectively) and the laminar flame thickness  $\delta_l$  corresponding in this work to the thermal thickness computed with temperature gradient:

$$\delta_l = (T_b - T_u) / \max \left( \left| \frac{\partial T}{\partial x} \right| \right). \quad (3.1)$$

According to the theory of Mallard and Le Chatelier, the flame thickness is split into two distinct zones: the preheat zone, where the thermal diffusion effect heats the mixture until auto-ignition temperature is reached, and the reaction zone, where chemical heat release takes place. The thickness of the reaction zone  $\delta_R$  is approximated with  $\delta_R = \delta_l / Ze$ .  $Ze = E_a \frac{T_b - T_u}{R_{gas} T_b^2}$  is the Zeldovich number, computed with the overall activation energy  $E_a$ .

Computation of the laminar flame using the numerical methods developed in this study and comparison with experimental data is performed in § 13.1.

### 3.1.3 Cellular deflagration

In the classical theoretical description, the laminar flame front is assumed to have a stable structure and propagate while conserving a planar one-dimensional shape. However, premixed flame fronts are affected by hydrodynamic and thermodiffusive instabilities that distort its surface and accelerate the flame front creating cellular structure. Figure 3.1 shows an example of the expansion of a spherical lean hydrogen/air flame and the corrugated flame surface observed in a spherical bomb. Rich hydrogen/air flame does not show the same propensity to be cellularly unstable with the same experimental condition.

The first analyses of the destabilizing effect during the thermal expansion of a flat front flame have been realized by Darrieus [Dar38], and Landau [Lan44] in the 1940s. Considering small perturbations in the velocity and pressure component, they performed a linear stability analysis to establish a dispersion relation between the instability's growth rate  $\omega$  and the wavenumber  $K$ :

$$\omega_{DL} = \frac{K S_l^0 \sigma}{\sigma + 1} \left[ \sqrt{\frac{\sigma^2 + \sigma - 1}{\sigma}} - 1 \right]. \quad (3.2)$$

This relation indicates that all the wavelengths along an infinitely thin plane flame front grow exponentially. According to this analysis, short-wavelength perturbations grow more rapidly than longer ones, and the growth rate becomes infinite as the wavelength approaches zero. Indeed, if a flame is slightly curved, streamlines in the burnt gas converge behind the convex part of the front and diverge behind the concave part as illustrated in Figure 3.2, which continuously reinforce the wrinkling.

Moreover, non infinitely thin flame and thermo-diffusive effects also impact the laminar flame front with stabilizing or destabilizing effects on the instabilities depending on the Lewis number. If the heat flux prevails over the diffusive flux, which means that the effective Lewis number  $Le_{eff} > 1$ , then the

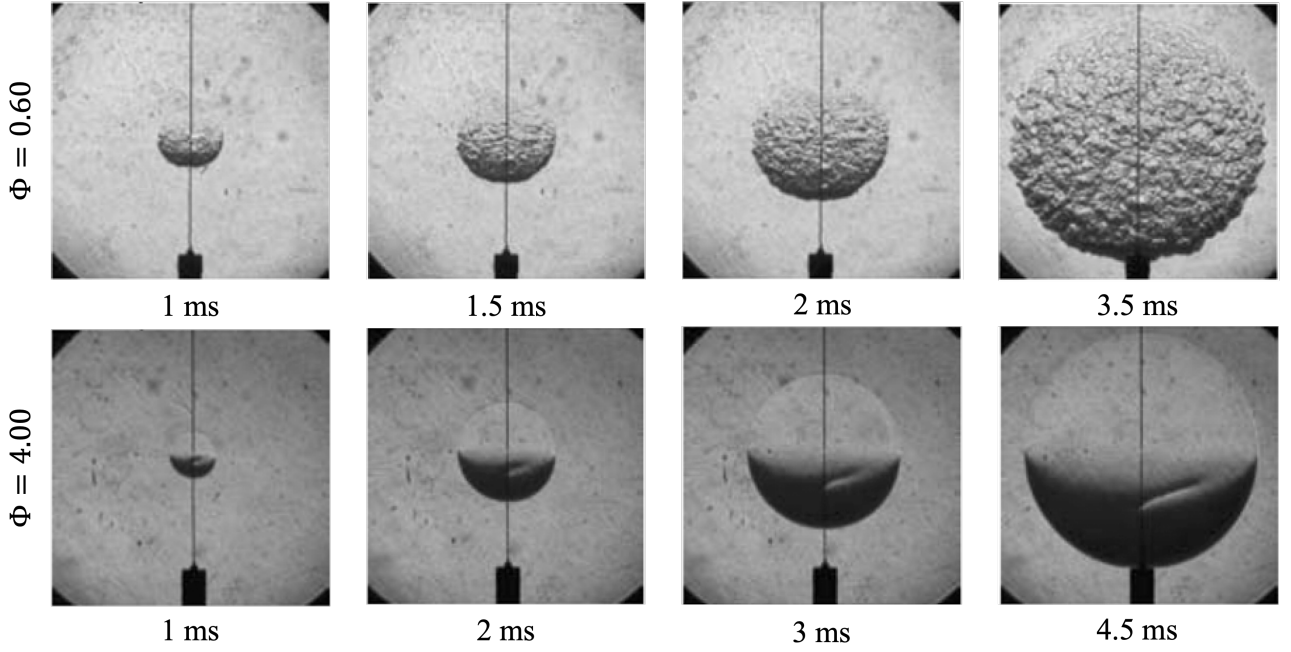


**Figure 3.1:** Expanding spherical hydrogen/air for lean and rich mixture with 5 atm pressure environment [LAW06]

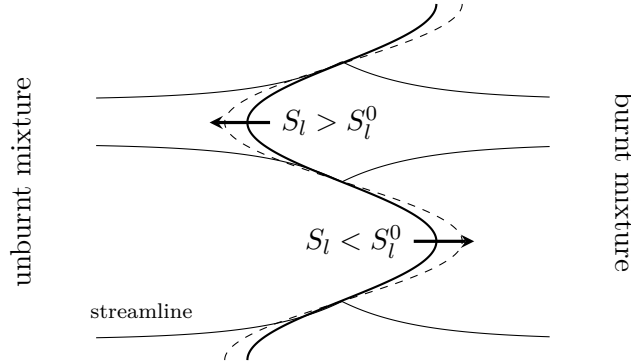


**Figure 3.2:** Schematic of Darrieus Landau instability

velocity at the concave part of the flame front will increase, and the flame wrinkling is thus reduced. However, when the thermal diffusivity is slow ( $Le_{eff} < 1$ ), limiting species concentration with weak heat flux in the convex sections will increase velocity and enforce the flame wrinkling. Those two configurations are illustrated in Figure 3.3.

In order to include the diffusive effect, Markstein [MAR51] introduced the definition of the Markstein length  $L_M$  to express the flame velocity as a function of the strain rate  $\mathbb{K}$  of the flame:

$$S_l = S_l^0(1 - L_M \mathbb{K}). \quad (3.3)$$

With this formulation, linear relation evolves depending on the value sign of the Markstein length:

$$\omega = \frac{K S_l^0 \sigma}{\sigma + 1} \left[ \sqrt{\frac{\sigma^2 + \sigma - 1}{\sigma} + L_M K (L_M K - 2\sigma) - L_M K - 1} \right]. \quad (3.4)$$

If  $L_M = 0$ , same relation (3.2) is found than with Darrieus-Landau analysis. If  $L_M < 0$ , hydrodynamics instability are reinforced. Finally, if  $L_M > 0$ , small wavelength becomes stable and a stability limits  $K_n = \frac{1}{2} \frac{\sigma-1}{\sigma L_M}$  appear (Figure 3.4).

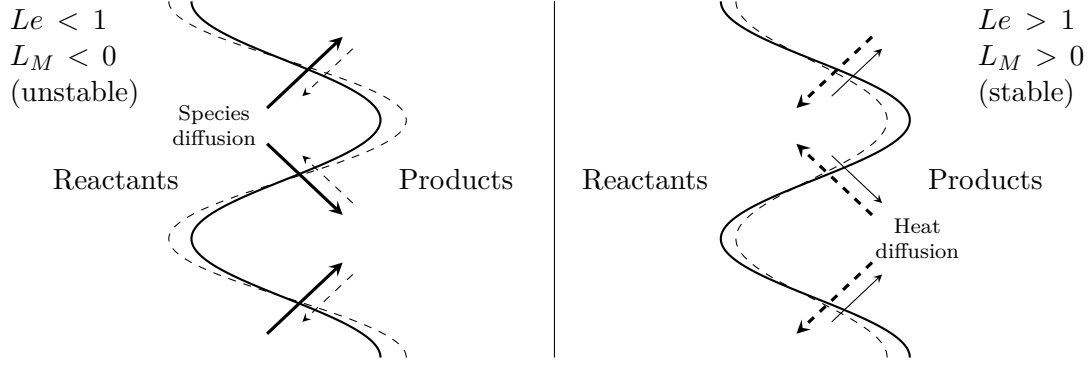


**Figure 3.3:** Schematic of thermal-diffusive instability. Species diffusion (bold arrow) and heat diffusion (dashed arrow) respectively reinforce and reduce flame wrinkling

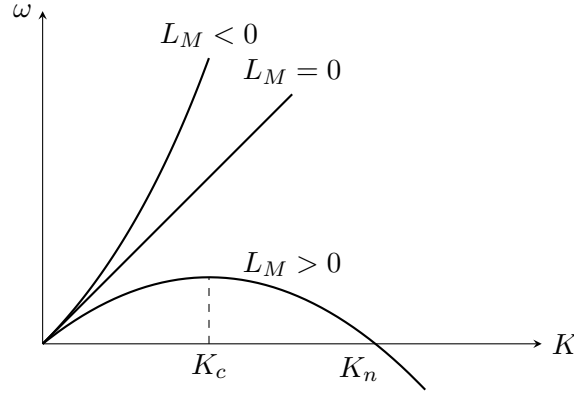


**Figure 3.4:** Dependence of growth rate  $\omega$  for wavenumber  $K$  for various values of Markstein length

The Markstein length is usually determined experimentally. Considering a one-step reaction with a large activation energy, constant properties, and heat capacity  $c_p$ , Pelcé and Clavin [CW82, PC88] and Matalon [MM82] have obtained asymptotic expressions for the Markstein number  $Ma$ :

$$Ma = \frac{L_M}{\delta_l} = \frac{\sigma}{\sigma - 1} \left[ \ln \sigma + \frac{Ze(Le_{eff} - 1)}{2} \int_1^\sigma \frac{\ln(x)}{x - 1} dx \right]. \quad (3.5)$$

An analytical expression for the effective Lewis number  $Le_{eff}$  is defined by Addabbo et al. [ABM02] as:

$$Le_{eff} = 1 + \frac{(Le_E - 1) + (Le_D - 1)\mathcal{A}}{1 + \mathcal{A}}, \quad (3.6)$$

where  $Le_E$  and  $Le_D$  correspond respectively to the reactant relatively in excess or deficient.  $\mathcal{A} = 1 + Ze(\varphi - 1)$  with  $\varphi$  the ratio of mass excess-to-deficient reactants in the fresh mixture.  $\varphi$  correspond to the equivalence ratio  $\Phi$  for rich mixtures and its reciprocal  $1/\Phi$  for fuel-lean mixtures.

Experimental measurements of the Markstein length and effective Lewis number are usually realized on spherical expanding flame. Measurement is realized with a small stretch ratio. As the flame is not stationary, only instabilities growing fast enough can develop. A spherical flame, initially stable, becomes cellular starting from a specific size, defined by its radius  $R_0$  from the ignition point, and expressed by a critical Peclet number, corresponding to the appearance of the first unstable wavelengths. Peclet number depends on the thermal expansion coefficient, and the Lewis number [BM87].

Experimental results based on the relation between flame velocity and stretching according to the definition of the Markstein number are given Figure 3.5 for  $H_2$ -air mixture with various equivalence

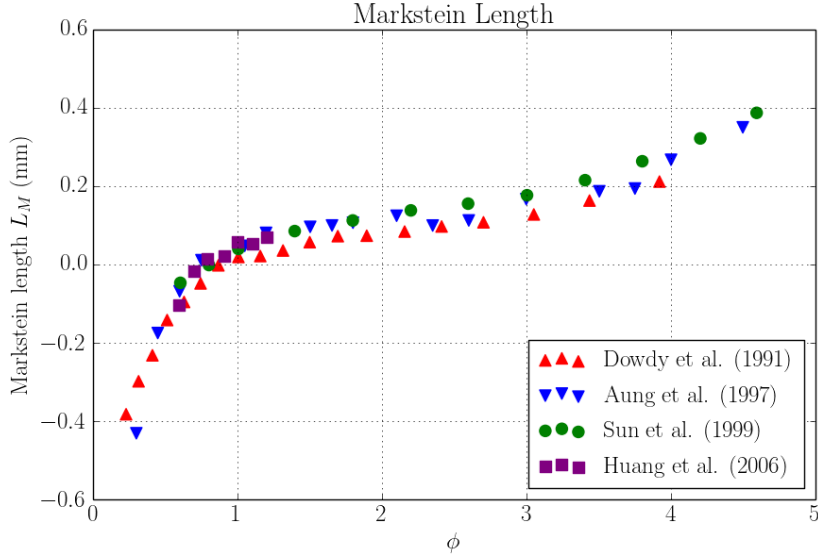


**Figure 3.5:** Variation of Markstein length versus the equivalence ratio for  $H_2$ -air mixtures initially at 100 kPa and ambient temperature. Data  $\triangle$  Dowdy et al. [DSTW91],  $\nabla$  Aung et al. [AHF97],  $\circ$  Sun et al. [SSHL99],  $\square$  Huang et al. [HZZ<sup>+</sup>06]

ratios. Such results on the Markstein length indicate that lean hydrogen flames are very unstable. For a mixture of hydrogen/air, the transition from unstable to stable propagation is located between 24% and 26% of  $H_2$ .

Reproduction of such results is performed with our numerical solver on a two-dimensional flame expanding cylinder § 13.2 to characterize the capability to reproduce properties of stability of the flame front with our chemical mechanism and diffusive models.

### 3.1.4 Premixed combustion turbulent regime

The diffusive and instability processes induce the laminar flame's effective velocity. In the case of local ignition, the laminar front flame is developed spherically around the ignition point. The lower density of the burnt gases causes volume expansion, creating a flow in the fresh gas ahead of the flame front (piston effect). Flow instabilities can be triggered at sufficiently high induced flow velocity and create turbulence. Obstructions in the flow also increase turbulence generation in the wake of obstacles. Through the formation of eddies structure, the turbulence will interact with the flame front.

Turbulence is characterized by fluctuations of the local properties and especially by the velocity fluctuations. Turbulence is characterized by the RMS velocity  $v'$  and its integral scale  $l_t$ .

A Reynolds number  $Re(l_r)$  is associated for each turbulent scale  $l_r$  as:

$$Re(l_r) = \frac{v'(l_r)l_r}{\nu_l}, \quad (3.7)$$

where  $v'(l_r)$  is the characteristic velocity of the motion of size  $l_r$ , and  $\nu_l$  the kinematic viscosity.

If turbulence is homogeneous and isotropic, the energy flux is transferred from large scales of motion to the small scales and kept constant along this energy cascade. The turbulence dissipation rate  $\varepsilon$  is given by the ratio of the kinetic energy  $v'(l_r)^2(l_r)$  divided by the time scale  $l_r/v'(l_r)$ :

$$\varepsilon = \frac{v'(l_r)^3}{l_r}. \quad (3.8)$$



Scales of turbulence  $l_r$  go down from the integral scales  $l_t$ , corresponding to the order of the confining geometry dimensions, to the Kolmogorov microscale  $\eta_k$  corresponding to the size where viscosity dominates, and turbulent kinetic energy is dissipated into heat with a Reynolds number close to unity.

$$Re(\eta_k) = \frac{v'_k \eta_k}{\nu_l} = \frac{\varepsilon^{1/3} \eta_k^{4/3}}{\nu_l} = 1. \quad (3.9)$$

Thus, the Kolmogorov microscales of length  $\eta_k$  and time  $t_\eta$  correspond to

$$\eta_k = \left( \frac{\nu_l^3}{\varepsilon} \right)^{1/4}, \quad t_\eta = \left( \frac{\nu_l}{\varepsilon} \right)^{1/2}. \quad (3.10)$$

Interaction between the turbulence and the flame is presented as an interaction between flame and vortex corresponding to turbulent eddies. Some dimensionless parameters are used to characterize the impact of eddy turbulence on the flame front:

- The Karlovitz number  $Ka$  defined as the ratio of chemical time scale  $t_F$  and to Kolmogorov time scale  $t_\eta$ ,

$$Ka = \frac{t_F}{t_\eta} = \frac{v'(\eta_k)/\eta_k}{S_l^0/\delta_l} = \left( \frac{\delta}{\eta_k} \right)^2. \quad (3.11)$$

- The eddy Damköhler number  $Da(l_r)$  defined as the ratio between the time scale  $t_r$  and the chemical time scale  $t_F$ .

$$Da = \frac{t_r}{t_F} = \frac{l_t/v'(l_t)}{\delta_l/S_l^0}. \quad (3.12)$$

These two numbers are related with  $Ka = 1/Da(\eta_k)$  and with the turbulent Reynolds number at the integral scales  $Re_t = Da^2 Ka^2$

The impact of the turbulence on the flame front depends on the combustion regimes. Those regime are presented in Borghi diagram (Figure 3.6) identified in terms of length ( $l_t/\delta$ ) and velocity ( $v'/S_l^0$ ) ratio.

In the case of a small value of Reynolds number  $Re_t$ , turbulence is too weak to interfere with the combustion process, and the flame propagates in a laminar regime. In the other case, distinct regions are identified:

- $Re_t < 1$ :  
Turbulence is too weak to interfere with the combustion process; thus, the flame is in a laminar regime;
- $Ka < 1$  ( $Da > 1$ ):  
The flame thickness is smaller than the Kolmogorov microscale. The inner structure of the front flame is preserved and close to the laminar flame. This regime is called the "flamelet regime", it is split into two distinct sub-regimes related to the impact of the turbulent motion on the flame front.
  - $v' < S_l^0$ : The velocity fluctuation is too low to wrinkle the flame front significantly. This regime is called the "wrinkled flamelet regime";
  - $v' > S_l^0$ : The fluctuation amplitude is significant compared to the flame speed, and the turbulent motion wrinkles the flame front. This regime is called the "corrugated flamelet regime".
- $Ka > 1$  and  $Da(l_t) > 1$ :  
In that case, the turbulent integral time scale is larger than the chemical time scale, but the Kolmogorov scale is smaller than the flame thickness. The small eddies impact the inner flame

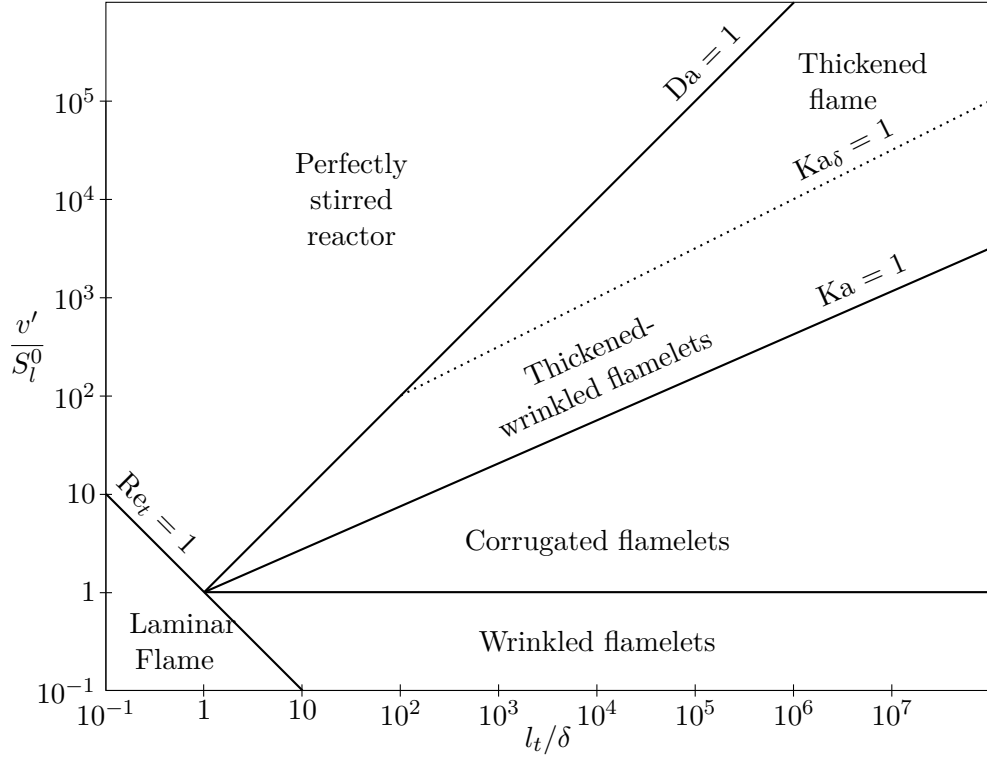


**Figure 3.6:** Borghi's diagram of combustion regimes [Bor85]

structure. This regime is called the "thickened flame regime". A second Karlovitz number  $Ka_\delta = \delta_r/\eta_k$  related to the thickness of the reaction zone of the flame is also introduced to distinguish the effects on the inner flame structure.

- $Ka_\delta < 1$  : turbulent motions modify the flame preheated but not the reaction zone. The regime is called the "thickened-wrinkled flame regime";
- $Ka_\delta > 1$  : both diffusion and reaction zone are affected by the turbulent motion. There is no laminar structure anymore in the flame structure. This regime is called the "thickened flame regime".
- $Da(l_t) < 1$ :  
The integral time scale is shorter than the chemical time scale, and the mixing is fast. This regime is called the "perfectly stirred reactor".

Experimental shadowgraph and OH-PLIF sequences of hydrogen flame acceleration presented by Boeck [Boe15] allow characterizing the deformation of the flame front through an obstructed tube (Figure 3.7). By increasing the equivalence ratio of the mixture with  $H_2$  volume concentration from 12.5 to 20%, the averaged flame tip velocity increases, impacting the Karlovitz number. At 12.5%, the regime of the flame corresponds to a wrinkled flamelet. At 15%, the flame is corrugated with a velocity that rises 120m/s. Close to the stoichiometric mixture, with 20%  $H_2$  concentration and flame tip velocity at 300m/s, the turbulence interacts with the front flame with a reaction zone that is spatially extended, suggesting a thickened flame regime. For this last concentration, velocity close to the supersonic value introduced compressible effects that induced a transition from slow to fast deflagration regime.

### 3.1.5 Fast turbulent deflagration

Above a velocity of the flame front higher than half of the sound speed in the fresh gas, the compressible effect impacts the behavior of the front flame. When the velocity reaches the sound speed, the compressible effects and their interaction with the flame become the predominant mechanism of the acceleration.

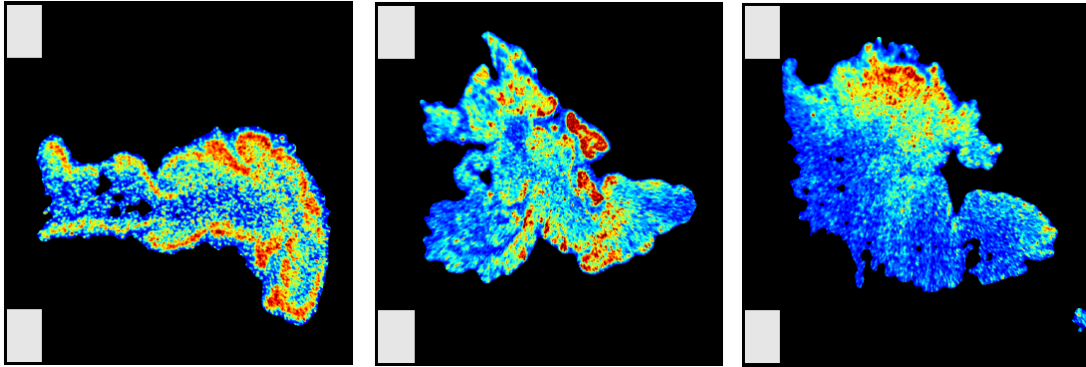


**Figure 3.7:** *OH-PLIF of turbulent deflagration in obstructed channel with 12.5 vol. % (left), 15 vol % (middle) and 20 vol % (right) [Boe15]*

The generation of a pressure wave with the fluctuation of the heat release rate in the reaction flame preheats the fresh gas. The reflection on the boundary returns this pressure wave that interacts with the flame with a positive feedback mechanism that increases instability. The shock-flame interaction produces Richmeyer-Meshkov instability induced by a non-parallel gradient of density and pressure. Chemical reactions generate a strong variation of pressure fluctuations, and acoustic-flame interaction is repeated continuously, resulting in a continuous generation of small turbulence scales that will increase the burning rate.

With the presence of geometric components in the flow, the compression waves close to the obstacle are reinforced and modified thermodynamic conditions in front of the flame. The thermodynamic state does not reach the auto-ignition limit but increases the temperature and the burning rate (Figure 3.8).

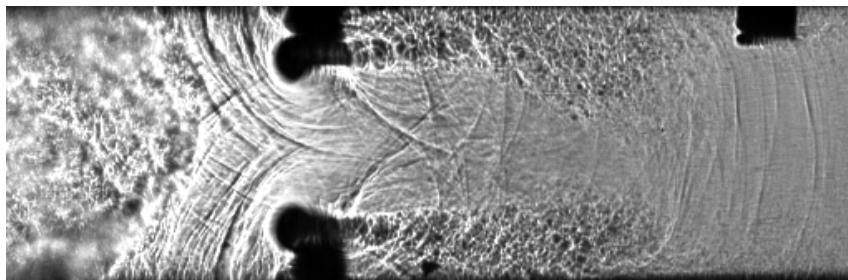


**Figure 3.8:** *Shadowgraph sequence of shock-flame interaction in GraVent experiments closed to a obstacle with 25% of hydrogen volume*

These phenomena progressively accelerate the flame front until the maximum Chapman-Jouguet deflagration velocity is reached. This regime, dependent on the thermodynamic properties of the mixture, is called *choking* regime. At those velocities, the front flames generally transit to a detonation. However, with specific obstacle-laden tubes, turbulence can sustain the flame in this regime [CL03].

## 3.2 Transition to detonation

### 3.2.1 Onset of Detonation

As described with the representation of the balance equation in the  $p - 1/\rho$  plane in 2.1, there is no possible continuous transition from the deflagration zone to the detonation zone. The Deflagration to Detonation Transition (DDT) is then a discontinuous process. The velocity of the flame generally accelerates until a maximum close to the Chapman-Jouguet deflagration velocity before an abrupt transition to reach the CJ detonation velocity.

There are two identified onset mechanisms of detonation observed numerically and experimentally:

- Direct initiation of detonation resulting from shock wave reflection or local shock wave focusing. In that case, the shock strength creates pressure and temperature conditions sufficient to auto-ignite the mixture and create a local explosion.
- Initiation of a detonation by the setting up of a favorable situation through the instabilities and mixing process.

The first category corresponds to a shock wave strong enough to cause rapid auto-ignition to create a blast wave similar to direct initiation. Such transitions have been experimentally and numerically observed [GS66, ST95, CdW06]. Those transitions are much more probable with interaction with obstacles and walls that can produce strong reflected shock. Combustion is initiated if the temperature rises above the auto-ignition temperature. Two distinct modes of ignition are distinct behind the reflected shock, weak (mild) ignition showing distributed ignition kernels between the wall and the reflected shock wave, and strong (sharp) ignition leading to homogeneous reaction along the reflected wall producing a blast wave that can decay in a detonation wave. Various models to predict ignition modes have been described. Voevodsky and Soloukhin [VS65] attributed this distinction to the dominant reaction mechanism in the chemical chain reaction. Meyer and Oppenheim [MO71a, MO71b] described criteria based on the temperature sensitivity of the ignition delay time. A review of the models is available in [BMS17].

The second mechanism involves multiple varieties of instabilities and mixing processes resulting in the formation of hot spots in the unreacted mixture ahead of the flame brush leading to spontaneous detonation initiation. Those onsets of detonation can occur inside the flame brush [OG07], in the boundary layer between the flame and a precursor shock wave [KAMD05], or after a shock-flame interaction, [TBB01].

The first explanation of this onset of detonation is proposed by Zeldovich et al. [ZLMS70] with the propagation of spontaneous reaction waves through a gradient of reactivity computed with the spatial evolution of the gradient of induction time with  $u_{sp} = (d\tau_i/dx)^{-1}$ . Propagation regimes of the ignition wave created inside a hot spot are delineated by the magnitude of  $u_{sp}$  [Zel80]. The spontaneous reaction wave propagates through the reactive mixture transition to a detonation wave when  $u_{sp} > c_{s,u}$  the fresh gas speed of sound.

In addition to this, Lee [LKY78] also explained transition to detonation with a mechanism of self-reinforcement called SWACER mechanism for "shock wave amplification by coherent energy release" analogous to a resonance phenomenon. For example, if  $S_l^0 < u_{sp} < c_{s,u}$ , the spontaneous reaction wave is subsonic and propagated through the hot spot without modification of the regime. However, the creation of a hot spot also triggers a thermodynamical response of the surrounding gas forming an acoustic wave independent of the reaction wave. If the downstream pressure due to the heat release of the reaction wave allows it to propagate faster than the acoustic wave, the subsonic reaction wave can amplify the leading acoustic wave. Modification of the initial condition will create an ignition delay time gradient between acoustic and ignition waves. Synchronization between the chemical energy heat release and the acoustic shock wave then eventually accelerate the reactive wave to supersonic speeds. At this point, reactive wave and acoustic wave will coalesce and transition to a detonation wave. Description of such phenomena is available in [KSQH02].

Multiple numerical analyses and simulations have been performed to reproduce gradients of reactivity. Various numerical simulations in the previous decades performed such an onset of detonation: He and Clavin [HC92] highlighted a critical gradient of temperature, Kryuchkov et al. [KDE96] tested the influence of the Arrhenius law on the onset of density, Khokhlov et al. [KOT99] observed hot spots generation induced by a highly turbulent flame brush after a shock-flame interaction. Radulescu et al. [RSB13] proposed to use the  $\chi$  parameter described in § 2.2.2 to characterize the detonability of reactive mixture through amplification of gas-dynamic disturbance. Gu et al. [GEB03] established a parameter using the characteristic time scale of exothermic heat release within the hot spot as a sensitive measure of the coupling between reactive and acoustic waves. Moreover, Thomas et al. [TBB01] found that turbulent mixing between burned and unburned gases can increase combustion

rate near compression waves. The onset of detonation in the shock-flame experiments is observed to occur near the turbulent combustion front, which indicates that turbulent mixing plays an important role in Deflagration to Detonation Transition. Towery et al. [TPH20] then complete the criterion of Gu et al. considering the influence of the flow turbulence on the reactive and acoustic wave coupling.

### 3.2.2 Influence of boundary condition on flame acceleration

Interaction with geometry and boundary conditions influence the mechanisms of supersonic combustion waves. They can have both positive and negative effects on the propagation of detonations.

The obstacles reduce the run-up distance before the transition to detonation compared to a smooth tube. This strong acceleration was initially attributed by Shchelkin [Shc40] to the no-slip condition of the boundary that increases turbulence and distorts the flame front, which increases the burning rate. To this phenomenon, Bychkov and Valiev [BAVL10, VBA<sup>+</sup>10] add another mechanism, independent of the Reynolds number, where flame propagation in obstructed channel creates pockets of fresh gas leading to strong gas expansion due to delayed burning in the pocket and accelerates flame front. Positive feedback along the obstacle is produced by this mechanism until supersonic speed, leading to suitable conditions for a transition to detonation. A tube filled with periodically spaced orifice plates acts like interconnected explosion chambers.

Conversely, interactions with the boundary condition and obstacles also result in a velocity deficit compared to the theoretical Chapman-Jouguet detonation velocity. When the detonation front is lower but still maintained with significant overpressure, the regime is called *quasi-detonation*. In smooth wall detonation tubes, detonation failed when tube diameter has a diameter comparable with the detonation cell size  $\lambda$  with a velocity deficit of about 15%. In obstacle-filled tubes, velocity deficits of about 50% are reported in [Shc40] without quenching.

The velocity deficit compared to CJ velocity is attributed to the heat and momentum losses at the wall but also to the transverse wave interaction of the multi-dimensional structures. Through experiments with absorbing walls, Dupré et al. [Dup] and Radulescu [RL02] observed abrupt change in the detonation dynamics corresponding to the boundary between stable and unstable detonation. So they distinguish two distinct failure mechanisms considering mixture with regular or irregular cellular structures:

- For regular structure, with weak transverse waves, the structure of the cells does impact the attenuation process, and detonations fail by the mass divergence at the wall and the attenuation of the transverse wave. Radulescu [RL02] observe that limits before detonation are similar to the theoretical limit of existence of curved ZND;
- For irregular-cell detonations, the structure developed transverses waves of significant strength that influence the reinitiation mechanism of detonations near the limits and overcome the attenuation of the transverse waves at the porous walls. In that case, the steady ZND model cannot approximate the propagation velocity, and multi-dimensional effects must be considered.

Detailed studies of detonation propagation have been carried out in rough tube [TLK91]. The diffraction of the shock around an obstacle decouples the reaction front and the shock. However, reflected shock produces an overdriven detonation that reinitiates the detonation front. Turbulent mixing between products and reactants could also permit the reaction front to be coupled to the shock even for a reflected shock temperature too low. Detonation in rough tubes is then generally quite robust in resisting velocity deficit.

Conditions for the detonation propagation through an orifice of diameter  $d$  have been conducted. For detonation, the cell size of the order of the orifice opening ( $\lambda \approx d$ ) abrupt transition to choking regime or subsonic deflagration is observed. In experiments with porous medium conducted by Makris et al. [Mak93], similar velocity deficits are measured. However, such obstacles allow a continuous transition between the quasi-detonation and choking regimes.

A numerical calculation representing diffraction through a wall of obstacles and the reinitiation at the Mach stems in the wake of the obstacles is presented in § 14.1.

### 3.2.3 Mixture Inhomogeneity

As seen in the introduction, hydrogen is very light and highly diffusive. With production realized at a local point, like, for example, with the oxidation of Zircaloy, the accumulation of hydrogen in a confined space usually forms a heterogeneous mixture. Spatial gradients in  $H_2$  concentrations will then prevail in real-world scenarios.

Conditions explored in numerical and experimental test cases are often specific to a single mixture gas. Many parameters are kept constant, although they can impact the flame acceleration. With an inhomogeneous mixture, as observed in nuclear safety, ignition can happen in local higher fuel concentration regions and propagate towards lower concentration regions. Flame acceleration is also impacting. The variation of flammability limits stretches the flame front, and modification of the Lewis number along the composition gradient influences the instabilities.

Considering an inhomogeneous mixture, a first situation corresponds to the fuel concentration gradient parallel to the propagation direction. In that case, the detonation front 'sees' a uniform mixture as it propagates through the gradient. The behavior of the detonation then depends on the steepness of the concentration gradient, governed by the reactivity gradient. Thus smooth concentration gradients can facilitate the transition to detonation [TSE91]. Conversely, a sharper gradient can provoke detonation decay by creating dissociation between the precursor shock and the reactive front [KAD<sup>+</sup>98].

A second possible situation corresponds to a gradient of concentration perpendicular to the direction of explosion propagation. Experimental investigations with such transverse concentration gradients [KJG11, GSH<sup>+</sup>13] reported that deflagration to detonation transition is mainly governed by the maximum local  $H_2$  concentration. However, this simple criterion of maximum concentration is not always valid. Vollmer [VES12], and Boeck [Boe15] showed that transverse concentration gradients could significantly promote the deflagration to detonation transition in an unobstructed channel with the reinforcement of the flame acceleration by flame elongation. Stronger flame acceleration and increase of the transition to detonation probability are measured. Inversely, in highly obstructed channels, the propensity for DDT with high  $H_2$  concentration can also be reduced with a transverse concentration gradient.

The structure of the detonation wave is also impacted by the transverse concentration gradients resulting in a curved detonation front. Detonation cell width generally increases both in the lean and rich parts of the mixture compared to the homogeneous mixture. Kessler et al. [KGO12] presents simulations of detonation front in channel with transverse gradients. They highlight the significant impact of the activation energy of the mixture: complex curved detonation front structures for weakly unstable detonation show that detonation can survive and propagate through a mixture of which a significant portion is not sufficiently reactive to support detonation on its own. Such a situation allows a get more important velocity deficit without detonation failure. For unstable detonation waves, fluctuations in the local temperature caused by transverse waves drop the local reaction rate and decouple the shock and the reaction zone leading to failure of the detonation wave for important concentration gradients. With a large concentration gradient, Boeck et al. [BBHS16] observed experimentally a specific detonation regime called "single-headed propagation" with one single strong transverse wave that sustains the detonation. Song et al. [SHC20] reproduce such regime with even an alternative regime between the single-head mode and the multi-head mode using variations of the concentration gradient.



# Chapter 4

## Objectives

### 4.1 State of the art

The flame acceleration and the transition from deflagration to detonation involve multiple phenomena that have been observed experimentally and numerically in the last decades.

#### 4.1.1 Experimental facilities

Different experimental facilities with metrological devices for combustion diagnostics are devoted to the study of flame acceleration.

One of the fundamental input data to model flame propagation is the laminar velocity of the mixture and its intrinsic instability. Different facilities are used to characterize flame propagation at low speed, from stabilized burner to spherical bombs. Such devices allow to observe laminar flame and, following some post-processing, to obtain characteristic properties of laminar flame such as the unstretched laminar velocity of the front flame and the Markstein length [LCP03, Dah05]. Numerical simulations of spherical bomb and treatment to obtain laminar flame velocity and Markstein length are performed and discussed in § 13.2.

Experimental facilities of many different scales have been set up to observe the behavior of the hydrogen and the propagation of hydrogen flame. There is, for example, experiments in small diameter tubes [LJN13], or the observation of condensation and stratification of hydrogen/Air mixture in large volumes like the HDR facilities [MDK85], or the CEA test facilities called MISTRA [SBT+12] where  $H_2$  is substituted by He.

The flame acceleration phenomenon and the DDT are generally studied in flame acceleration tubes. The CEA Paris Saclay has designed, for example, the SSEXHY facility (Structure Submitted to an EXplosion of HYdrogen) with a combustion tube used to characterize the flame propagation mechanisms. This acceleration tube allows any mixture and uses gas-chromatographic analysis to set the initial and boundary conditions of the experiments correctly. A series of sensors are distributed along the combustion tube in Figure 4.1 to perform combustion diagnostics with piezoelectric sensors used as a pressure sensor, shock-sensor, and photomultiplier tubes to detect UV light emitted by  $OH^\bullet$  radicals located in the reaction front. Finally, annular obstacles are positioned inside the tube to reinforce the flame acceleration. A complete description of this experimental facility is available in [Sca17].

In this work, we will present in Chapter 14 the simulation of the Gradients and Venting ("GraVent") facility [BKH+16], a similar acceleration tube from the Technische Universität of München. An extensive open-source database of experiments on the flame acceleration (<https://www.mw.tum.de/td/forschung/ddt/>) is proposed for this facility, and it also has already been used for numerical studies [EVS14, KHBW19]. This facility has an explosion channel with a rectangular cross-section and allows optical measurements. Flat plate obstacles are installed along the channel with variable blockage



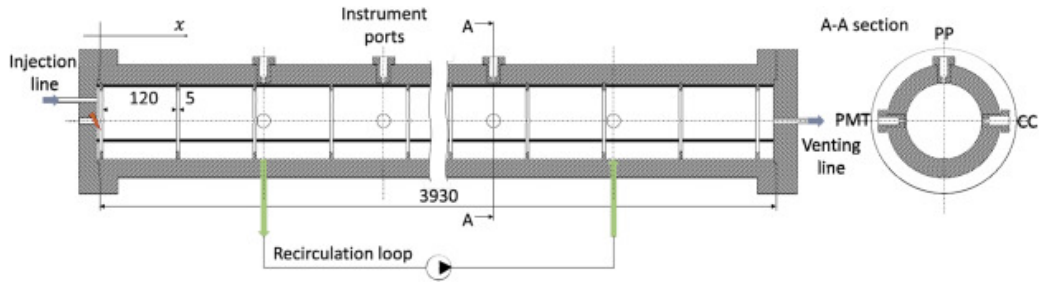


**Figure 4.1:** Schematic of the combustion tube with obstacle. Instrumentation includes PMT, photo-multiplier tube; PP, pressure sensor; CC, shock sensor [Sca17]

ratios. Concentration profiles of hydrogen are initially generated with specific diffusion time to characterize the effect of transverse concentration gradients on the flame acceleration. § 14.2 described more precisely the initial conditions and the geometrical configuration used in our simulations.

The various experimental devices dedicated to the flame acceleration observations study the impact of mixture composition, geometrical configuration, wall roughness, the porosity of the interfaces... The resulting data allows formulating empirical criteria to characterize the flame acceleration and the onset of detonation.

#### 4.1.2 Empirical criteria for Flame Acceleration and Deflagration to Detonation Transition Limits

Empirical laws are built to anticipate the behavior of the flame in a confined environment considering fundamental parameters like the flame speed, the Zeldovich number, the Lewis number, the sigma expansion coefficient, the mixture's activation energy of the mixture...

For example, critical expansion ratio  $\sigma^*$  is used to determine the capability to produce fast deflagration, a necessary condition to have DDT process. For  $H_2$ -air mixtures, Dorofeev et al. [DKA<sup>+</sup>01] tested correlations with various flow parameter and especially determined a formulation of a  $\sigma^*$  function of the dimensionless activation energy  $\epsilon_I = E_a/R_{gas}T_u$  as:

$$\sigma^* = f(\epsilon_I) = 0.910^{-5}\epsilon_I^3 - 0.0019\epsilon_I^2 + 0.1807\epsilon_I + 0.2314. \quad (4.1)$$

Malet [Mal05] also derived other formulations with specific blockage ratio  $BR = 1 - (d/D)^2$ , where  $d$  and  $D$  denote the orifice and tube diameters, respectively, corresponding to 0.63:

$$\sigma^* = 0.075Ze(Le_{H_2} - 1) + 4.38. \quad (4.2)$$

Studies of Kuznetsov et al. [KAMD05], Vesper et al. [AWS02], and Dorofeev [Dor09] show experimentally significant effects of the mixture, the initial level of turbulence, the tube size, and the roughness on the run-up distance, defined as the flame propagation distance where the flame speed reaches the sound speed in the combustion products.

In orifice plate filled tube, Peraldi et al. [PKL88] proposed a detonation propagation limit  $d/\lambda = 1$  for the quasi-detonation regime. Dorofeev et al. [DSK<sup>+</sup>00] extends this deflagration to detonation criterion by considering the obstacle spacing  $S$  with  $L/\lambda > 7$  with  $L$  a macroscopic length-scale defined by  $L = (S + D)/2/(1 - d/D)$ . Later, Dorofeev [Dor09] extract an analytical expression to estimate the run-up distance depending on the blockage ratio, [Ahm16] correlates run-up distance with the  $\chi$  stability parameter highlighting the importance of unstability that increase ability to generate hot spots and shorter the run-up distance.

However, many questions remain open concerning flame acceleration. Since there is a complex coupling of multiple physical and chemical processes, interpretation of the experimental studies is complex,

and empirical criteria are limited. Initial conditions like turbulence, concentration gradient, or the detonation's intrinsic properties, like its stability, significantly impact the propagation limit. Thus, the conditions causing the transition to detonation, the role of induction time on this transition, and the influence of geometry and wall conditions are still not well understood. Numerical simulations are then essential to address these issues.

### 4.1.3 Numerical methods

To investigate the complex situations induced by the flame acceleration and DDT phenomena, numerical solvers must meet various numerical challenges. They need to be accurate and robust to handle compressible computations with reactive multi-components.

Methods applied to the case of flame acceleration are generally Godunov-based methods, which are conservative methods capable of capturing discontinuities properly. To increase the time and spatial order, methods are usually associated with interpolation methods such as the Weighted Essentially Non-Oscillatory (WENO) and Monotone Upstream-centered Schemes for Conservation Laws (MUSCL). Thus, different solvers have been used in the literature to propose simulations of flame acceleration. First numerical simulations of transition to detonation in [KOT99], and various studies of flame acceleration [MMR12, TKGO13] used a second-order Godunov solver of Colella and Glaz [CG85]. The solver "Flame Acceleration Simulation Tool" (FAST), found in many works studying detonation front and effects of geometrical configuration on flame acceleration [GOO07, GOO08, GHO16, GBO21], uses an HLLC scheme (described in Appendix A.2.2) and a WENO method to increase the spatial order until the 5th order. The HLLC scheme has also been implemented in an OpenFoam library available on <https://sourceforge.net/projects/ddtfoam> with slope limiters called "cellMDLimited" [EVS14] used in the studies of Khodadadi et al. [KHBW19, KHW20] that reproduced the GraVent acceleration tube and the effects of the inhomogeneous mixture. This solver has the specificity to use an auto-ignition sub-grid model separating each computational cell into a "shocked" and an "unshocked" part and treat the low Mach number flow with the PISO scheme.

Another OpenFoam library called *RhoCentralFoam* based on the central-upwind schemes of Kurganov and Tadmor [KT02] is used in [ZZZ21]. Large Eddy Simulation (LES) methods have been applied for flame acceleration at subsonic velocity in [JC13], but also with detonation front simulations using the Linear Eddy Model formulation Compressible Linear Eddy Model (CLEM-LES) approach developed in [Max16] that adapt the subgrid models for the model reaction rates to respond accordingly to strong shocks and rapid expansions.

However, interpolation methods like the WENO scheme are overly dissipative near material interfaces and shear waves. Various implementations of the WENO scheme to reduce the dissipation have been tempted to apply them to detonation and flame acceleration simulations like the WENO-CD [CDLM17] or TENO [FHA16] schemes. Other interpolation methods based on the Total Variation Diminishing criterion (described in § 7.2.2) used in the MUSCL type scheme can also be dissipative at the material interface and tend to clip local extrema. Houim [HK11] then attempts to hybridize numerical method combined double-flux multi-component model [BA03], WENO and adaptive TVD slope limiters to calculate compressible multi-component flows with low dissipation accurately.

The reaction model must also be very accurate because of its significant impact on the behavior of the flame front. Indeed, the first steps of the acceleration depend on the laminar flame velocity and the thermo-diffusive instabilities. Moreover, the transition to detonation is strongly related to the ignition delay time and the reactive gradient, and the stability of the detonation front has a significant influence on the propagation limit. Some simulations introduced a detailed chemistry model [EVS14, ZZZ21] but many of the previous simulations used in the literature are based on a one-step Arrhenius law. Lu et al. [LKO22] chosen to use the Chemical Diffusive Model (CDM) to construct a single-step Arrhenius law calibrated with a genetic algorithm model to reproduce detonation properties such as the induction length or the detonation cell size [KOO19]. However, not all properties of the flame can be recovered with so few parameters.

Another numerical challenge to overcome in these simulations is the extensive spatial scale range involved. Indeed, compressible flows induce local regions with high activity such as shock waves, flame front, and turbulence. In the large experiments we want to reproduce, many areas have a relatively low activity that imposes adapting the mesh dynamically to avoid inefficient grid resolutions. Such adaptations are generally applied in the different studies using adaptive mesh refinement methods [DDG<sup>+</sup>09] with structured meshes.

## 4.2 Starting point of Thesis

In this work, we developed and tested our own numerical solver that addresses all these numerical issues. We have based this solver on two existing tools, the MR\_CHORUS solver, dedicated to the simulation of highly compressible flow, and AGATH, a one-dimensional flamelet solver library.

### 4.2.1 MR\_CHORUS solver

The MR\_CHORUS<sup>1</sup> solver described in [TRB15] is developed to solve the compressible Navier Stokes equations. It provides numerical methods adapted to high compressible flow coupled to adaptive multiresolution grid refinement strategy.

The compressible fluxes are solved using a One-Step Monotonicity Preserving scheme (OSMP scheme) developed in [DT04] and described in § 7.2. This scheme is based on the Roe solver associated with a Lax Wendroff procedure to increase the scheme's order and improvement of the classical TVD flux limiter to keep monotonicity condition without clipping extrema. The OSMP scheme properly captures discontinuities and compressible effects with a very low numerical dissipation. Moreover, the Lax Wendroff procedure increases the Roe solver's order in time and space and no longer needs multi-staged Runge Kutta time integrations.

The MR\_CHORUS code also provides adaptive multiresolution procedure described in Chapter 10 based on techniques developed by Harten [Har95] and Cohen [CKMP03], which allow a high data compression rate.

Additional developments are integrated to this solver in this work to adapt these existing numerical methods in the case of flame acceleration with reactive terms with the extension to the OSMP scheme for non-ideal multicomponent gases described in Chapter 8.

Integration of complex thermodynamic and reactive terms will also use the AGATH library.

### 4.2.2 AGATH solver

AGATH is a flamelet solver library similar to CHEMKIN or Cantera. This one-dimensional solver is used to evaluate thermodynamical and transport properties and chemical sources terms that appear in the Navier Stokes equation and give flexibility for the kinetics and transport description. It is compatible with the chemkin standard format file.

In this work, AGATH is used to compute thermodynamic values like pressure and temperature starting from a set of conservative values like density, mixture composition, or internal energy. Different thermodynamic models are available. In our application cases, we use a model with fitted polynomials to transcript temperature-dependent heat capacity as described in § 5.2.2.

AGATH solver computes the diffusion operators, thermal conductivity, or dynamic viscosity for every local mixture according to the model required. It also provides chemical source terms thanks to integrated numerical methods to resolve non-linear systems like Radau5 or LSODE.

Finally, the AGATH solver is used to obtain one-dimensional reference results with, for example, the computation of laminar flame or ZND profiles or specific flame properties like laminar flame velocity, ignition delay time...

---

<sup>1</sup>Declaration d'Invention DI 03760-01

### 4.3 Objectives and organization of Thesis

We present in this work the development of a numerical solver capable of accurately capturing the behavior of the flame during its evolution from laminar deflagration to detonation regimes. The objective is to analyze and address the numerical issues raised by such a simulation.

Our scheme is based on the numerical tools proposed by the MR\_CHORUS solver with specific adaptation to use them with multicomponent non-ideal gas and reactive flows. The AGATH library is used for thermodynamics models, viscous and diffusive terms, and computation of the chemical source terms.

Part II describes the implementation of the numerical solver. We detail the Navier-Stokes model and the assumptions on the thermodynamic model in Chapter 5. The finite volume method and splitting strategy are described in Chapter 6. Chapter 7 presents the OSMP scheme used for monocomponent ideal gases. Its extension to multicomponent mixtures with non-calorically perfect gases is developed in Chapter 8.

Part III describes algorithmic strategies associated with the numerical solver: the adaptive multiresolution methods in Chapter 10, the Immersed Boundary Method (IBM) used to integrate obstacles in structured mesh in Chapter 11, and ISAT methods used to accelerate the computation of the reactive source term in Chapter 12.

The last Part IV is dedicated to the simulation of reactive test cases. Chapter 13 presents one-dimensional and two-dimensional validation cases to evaluate the performance of the solver to capture the phenomena involved in the successive steps of flame acceleration. Finally, Chapter 14 presents extensive simulations: first, the propagation of detonation waves inside porous medium with attenuation and re-initiation of the detonation front; then, the reproduction of the GraVent acceleration tube experiment with and without concentration gradient.



## Part II

# Numerical solver



# Introduction

This part presents the numerical strategy we used in our simulations of flame acceleration and transition to detonation. To perform such simulations, various physical phenomena must be captured from the thermodiffusive instability to the advection of compressible waves. A compressible solver with high accuracy is needed, and the use of non-ideal gas flow is necessary to deal with the physical behavior of the species in a wide temperature range.

Chapter 5 presents the governing equations of reactive flows based on the Navier-Stokes equations with chemical source terms and species transport equations. Specific attention is given to the thermodynamic model employed. We describe the properties allowing to obtain a convex equation of state which will be necessary for the numerical solver to treat the hyperbolic parts of the equations properly.

Chapter 6 describes the time operator splitting techniques to integrate time-dependent PDEs numerically. The splitting approach is used to deal with the multiple time scales related to the various phenomenon. In particular, an implicit Radau5 solver is applied to compute the stiff reactive source term, and an explicit centered second-order Runge Kutta solver approximates the viscous flux.

Specific development is necessary to describe the numerical methods used to approximate the Euler flux. Chapter 7 introduced the classical Roe solver and the OSMP scheme, a high-resolution scheme with specific monotonicity preserving conditions in the case of polytropic gases mixture. Chapter 8 describes the methods we developed to extend the Roe solver and the OSMP scheme to the case of mixtures of gases with convex equations of state. It consists in approximating the compressibility factors at the Roe average state with a first estimation based on the method developed by Vinokur and Montagné [VM90]. Then a new formulation of the Energy flux selects a new combination to correct inconsistencies with the mass flux introduced by this approximation in the OSMP scheme. Application of this complete solver shows in 1D case very high accuracy on a smooth solution and good behavior close to discontinuities with very low dissipation.

Finally, in multidimensional detonation cases, the OSMP solver, unfortunately, produces shock instability called "carbuncle". Such numerical instability usually appears with Riemann solvers like the Godunov or Roe solvers. Chapter 9 describes the methods used to analyze stability and to cure this carbuncle. Based on various tests, we chose to add an additional shear viscosity term to the numerical flux associated with a critical cell sensor to cure this instability with minimal impact on the physical phenomena.





# Fluids dynamics of combustion

This chapter introduces the governing equations for reactive flows based on the Navier-Stokes equations coupled with species transport equations to describe the diffusion of species and associated source terms to incorporate reaction phenomena.

First, conservation equations and thermodynamic models are written for a general real gases mixture at a local equilibrium state. The convexity of the equation of state is an essential property for the characteristic solution of the Riemann problem used in the numerical schemes described in Chapter 7. The description of the thermodynamic model and the hypothesis made on the equation of state to obtain the convex property are discussed in § 5.2. We finally present the ideal gas mixture model with temperature-dependent heat capacities that integrate the vibrational and rotational energy of the molecules in the equation of state. This thermodynamic model is usually used in the combustion simulation since it approximates the internal energy of the species at a wide range of temperatures.

## 5.1 Conservation equations for a compressible reactive mixture

### 5.1.1 Navier-Stokes equation

Let us consider a mixture of gases with  $n_s$  chemical species.

$$\mathbf{w} = (\rho Y_1, \dots, \rho Y_{n_s}, \rho \mathbf{u}, \rho E)^T, \quad (5.1)$$

is the vector of the conservative variables.  $\rho$  is the density,  $\rho_i = \rho Y_i$ , where  $Y_i$  is the mass fraction of the  $i^{\text{th}}$  species.  $\mathbf{u}$  is the velocity vector, and  $E$  is the total energy per unit of mass corresponding to the sum of formation enthalpy, sensible energy, and kinetic energy.

The reactive system is described by the Navier-Stokes transport equations:

$$\frac{\partial \mathbf{w}}{\partial t} + \nabla \cdot (\mathbf{f}^E(\mathbf{w}) - \mathbf{f}^V(\mathbf{w}, \nabla \mathbf{w})) = \mathbf{S}(\mathbf{w}), \quad (5.2)$$

where  $\mathbf{S}(\mathbf{w})$  corresponds to the source term due to the reactive mixture and  $\mathbf{f}^E(\mathbf{w})$  and  $\mathbf{f}^V(\mathbf{w}, \nabla \mathbf{w})$  are the Euler and the viscous fluxes respectively:

$$\mathbf{f}^E = \begin{pmatrix} \rho \mathbf{u} Y_1 \\ \vdots \\ \rho \mathbf{u} Y_{n_s} \\ \rho \mathbf{u} \otimes \mathbf{u} + p \mathbb{I} \\ \rho \mathbf{u} H \end{pmatrix}, \quad \mathbf{f}^V = \begin{pmatrix} \rho Y_1 \mathbf{V}_1 \\ \vdots \\ \rho Y_{n_s} \mathbf{V}_{n_s} \\ \Pi \\ \mathbf{u} \cdot \Pi + \Psi \end{pmatrix}, \quad \mathbf{S} = \begin{pmatrix} \rho \dot{\omega}_1 \\ \vdots \\ \rho \dot{\omega}_{n_s} \\ 0 \\ 0 \end{pmatrix}, \quad (5.3)$$

with  $p$  the local static pressure of the flow and  $H = E + p/\rho$  the total specific enthalpy.  $\mathbf{V}_k$  is the diffusion velocity of the  $k^{\text{th}}$  species described more precisely in § 5.1.2 and  $\dot{\omega}_k$  its net chemical production rate.  $\mathbb{I}$  is the  $N_{dim} \times N_{dim}$  identity matrix, with  $N_{dim}$  the space dimension.

$\Pi$  is the viscous strain rate tensor modeled for a Newtonian fluid as:

$$\Pi = \mu_l \left( \nabla \mathbf{u} + \nabla^t \mathbf{u} - \frac{2}{3} (\nabla \cdot \mathbf{u}) \mathbb{I} \right), \quad (5.4)$$

where  $\mu_l$  is the dynamic viscosity and the bulk (or volume) viscosity was neglected. In the following, the value of the dynamic viscosity will be computed using Sutherland's law.

The sum of the  $n_s$  species transport equations leads to the mass balance equation:

$$\frac{\partial \rho}{\partial t} + \nabla \cdot (\rho \mathbf{u}) = 0. \quad (5.5)$$

Consequently, following conditions on species diffusion velocities and reaction rates must recover the following relationships:

$$\sum_{k=1}^{n_s} V_{k,j} Y_k = 0 \quad \text{and} \quad \sum_{k=1}^{n_s} \dot{\omega}_k = 0. \quad (5.6)$$

Finally, the enthalpy conductive flux  $\Psi$  in the viscous term is composed of heat and species diffusion flux:

$$\Psi = -\lambda \nabla T + \sum_{k=1}^N (\rho h_k Y_k \mathbf{V}_k) - p \sum_{k=1}^N (D_k^T \mathbf{d}_k), \quad (5.7)$$

with  $\lambda$  the thermal conductivity,  $T$  the local static temperature of the flow.  $h_k$  is the specific enthalpy of the  $k^{\text{th}}$  species. The last term is the Dufour heat flux corresponding to the heat flux induced by concentration gradient with  $D_k^T$  the thermal diffusion coefficient of species  $k$ . In most cases and in the following of this work, the Dufour effect is neglected because it is very small compared to the other diffusive effects.

### 5.1.2 Diffusion of species

Various models are possible to express diffusion velocities in a multi-component system. Complete models are generally too expensive in terms of CPU cost. However, solving numerical combustion problems, especially combustion with hydrogen, requires considering molecular diffusion. A review of the models is available in [HTERT04].

The general expression of the diffusion velocity of a specie  $i$  in the mixture is expressed by:

$$\mathbf{V}_i = \frac{1}{X_i \bar{W}} \sum_{k \neq i}^N W_i D_{ik} \nabla X_k - \frac{D_i^T}{\rho Y_i} \nabla (\ln T) \quad (5.8)$$

with the diffusion force of the specie  $k$ ,  $\mathbf{d}_k$ :

$$\mathbf{d}_k = \nabla X_k + (X_k - Y_k) \nabla \ln p. \quad (5.9)$$

$D_{ij}$  are the ordinary multi-component diffusion coefficients, and  $D_i^T$  the thermal diffusion coefficient of the  $i^{\text{th}}$  species. The second term in the equation (5.8) corresponds to the thermodiffusion effect

or Soret effect. This effect accounts for the diffusion of mass due to temperature gradients. The light molecules are driven towards hot regions and heavy molecules towards cold regions. The Soret effect is often neglected but can be important in the case of combustion of hydrogen because of the light radicals that impact locally on the flame structure [dCE02]. Impact on the Soret effect on the computation of the hydrogen laminar flame speed in § 13.1 confirms the importance of this term.

The values of the diffusion coefficients  $D_{ij}$  and  $D_i^T$  are computed using a system of equations defined by a  $\mathbf{L}$  matrix. This matrix is filled using collision integrals derived from the generalized Boltzmann equation [MM61]. Resolution of the terms of the matrix is then obtained using the procedure described by Dixon-Lewis [DLC68] by using the reduced dipole moment, collision diameter, and rotational specific heat of each component. The computation of the multi-component diffusion terms is realized by the AGATH library using the transport table provided by the chemkin formalism.

Evaluation of the multi-component diffusion coefficients is expensive in terms of CPU time, some approximation using a zeroth-order approximation like in the so-called *mixture-averaged* formulation:

$$\mathbf{V}_i^* = -D_i^* \mathbf{d}_k - D_i^* \theta_i^* \frac{\nabla T}{T} \quad \text{with} \quad D_k^* = \frac{1 - Y_k}{\sum_{j \neq k} X_j / \mathcal{D}_{jk}}, \quad (5.10)$$

where  $\theta_i^*$  is the thermal diffusion ratio.  $\mathcal{D}_{jk}$  are the binary diffusion coefficient of the two species  $j$  and  $k$  depending only on species pair properties.

However, as illustrated with the computation of the laminar flame speed in § 13.1, the mixture-averaged expression gives significant differences which impose to use initial multi-component formulation to obtain correct properties in the flame acceleration process.

Finally, an additional term is applied to guarantee the conservation of the mass (5.6) that can be no longer satisfied after approximations in the diffusion velocities. To impose this one, the diffusion velocities  $\mathbf{V}_i$  of each specie  $i$  is split into a predictor term  $\mathbf{V}_i^*$  and a corrector term  $\mathbf{V}_c$ :

$$\mathbf{V}_i = \mathbf{V}_i^* + \mathbf{V}_c. \quad (5.11)$$

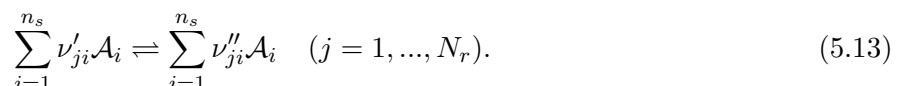
The correction velocity  $\mathbf{V}_c$  allows to recover mass conservation:

$$\mathbf{V}_c = - \sum_{k=1}^{n_s} Y_k \mathbf{V}_k^*. \quad (5.12)$$

### 5.1.3 Chemical kinetics

The hydrogen combustion process is modeled by a detailed reaction mechanism describing a list of elementary reactions involved in the global reaction. A numerous list of mechanisms has been developed in the last decades ([LZKD04, HDH11, Kon19, OCCS+04]). Hydrogen mechanisms generally involve about ten species and several tens of elementary reactions. These mechanisms are built using a large set of experimental data like flame velocity measurements, ignition in shock tubes, concentration in flow reactors... Recent evaluations of hydrogen combustion mechanism are available in [OZP+14].

The computation of the source terms  $\dot{\omega}_k$  is made from the list of elementary reactions. Considering a chemical system involving  $n_s$  species  $\mathcal{A}_i$  and  $N_r$  elementary reactions. Each elementary reaction is written in the form:



The progress rate  $q_j$  of the  $j$ -th reaction is defined as:

$$q_j = k_{f,j} \prod_{i=1}^{n_s} C_i^{\nu'_{ji}} - k_{b,j} \prod_{i=1}^{n_s} C_i^{\nu''_{ji}}, \quad (5.14)$$

where  $C_i$  denotes the molar concentration of the species  $i$ . The forward constants  $k_f$  are generally expressed using the Arrhenius law which takes the form:

$$k_j = A_j T^{\beta_j} \exp\left(-\frac{E_{a,j}}{R_{gas}T}\right), \quad (5.15)$$

with  $A_j$  the pre-exponential constant,  $\beta_j$  the temperature exponent.

The backward constants  $k_b$  are obtained from equilibrium constant  $K_{c,j}$ :

$$K_{c,j} = \frac{k_{fi}}{k_{bj}} = \left(\frac{p_{atm}}{R_{gas}T}\right)^{\sum_{k=1}^{n_s} \nu_{kj}} \exp\left[\frac{\Delta s_j^0}{R_{gas}} - \frac{\Delta h_j^0}{R_{gas}T}\right], \quad (5.16)$$

where the parameters  $\Delta s_j^0$  and  $\Delta h_j^0$  correspond, respectively, to entropy and enthalpy changes during the transition from reactants to products for the  $j$ th reaction.

For some reactions like the dissociation of recombination, third-body collision must be required to provide the energy necessary for the reaction to proceed. This dependence to a third body evolves with the pressure, and correction on rate coefficients is provided with, for example, the fall-off modeling of Troe [Tro79].

Finally, the net chemical production  $\dot{\omega}_k$  of the species  $k$  then corresponds to the sum of all contribution of the elementary reactions.

$$\dot{\omega}_k = W_k \sum_{j=1}^{N_r} (\nu''_{jk} - \nu'_{jk}) q_j, \quad (5.17)$$

where  $W_k$  is the mass molar of the specie  $k$ .

The list of the values of  $A_j$ ,  $\beta_j$ ,  $E_{a,j}$ ,  $\Delta h_j^0$ ,  $\Delta s_j^0$ , and other coefficients involved in the description of the chemical mechanism are available in the literature with a standardized format CHEMKIN [KRM+05].

In the flame acceleration and detonation simulation, we choose to use the hydrogen chemical mechanism of Rémi Mével [MJL+09]. It is composed of 38 reactions on nine reactive species and  $N_2$  and Ar supplementary inert species with third body contribution. This mechanism is based on the Konnov model (which seems to have relevant properties for detonation case [CPLP07]) and Mueller et al. [MKYD99] model. Reactions of the model are listed in Annexe B.4.

Validation cases on laminar flame, hydrodynamic instability and detonation front have been conducted, and are provided in § 13.1.

## 5.2 Thermochemical Equilibrium Model

We suppose the gases are in Local Thermodynamic Equilibrium (LTE), a state where thermodynamic values are considered to have been relaxed to a local equilibrium with only one local temperature. This approximation is implicitly made by using reaction mechanisms described previously, but the validity of the LTE assumption is discussed in [TKGO13] for the case of detonation simulation. In those cases, the time scales associated with relaxation to thermodynamic equilibrium  $\tau_{H_2-H_2}^{vib}$  can be close to the ignition delay time  $\tau_{ign}$  behind the precursor shock wave, and some dissociation reactions can be inhibited. Research on the vibrational nonequilibrium effects in detonations is available in [SSZ+17], for  $H_2$ /air detonation at initial atmospheric condition, we have  $\tau_{ign} \approx 5\tau_{H_2-H_2}^{vib}$ . In this

work, we always consider the LTE assumption despite a potential underestimation of the detonation cell size.

### 5.2.1 Mixture of real gases

The basic form of the equation of state links the internal energy  $e = E - \frac{1}{2} \sum_{i=1}^{N_{dim}} u_i^2$  of a system with the specific entropy of the system  $s$ , the composition  $N_1, \dots, N_{n_s}$  corresponding of the amount of substance of each specie, and the density  $\rho$ .

$$e = e(s, \rho, N_1, \dots, N_{n_s}). \quad (5.18)$$

The equation of state contains all the thermodynamic information about the system, and by definition, the intensive parameters  $T$ ,  $p$  and  $\bar{\mu}_{i,i=1,\dots,n_s}$  corresponding to the temperature, the pressure and the electrochemical potential, respectively:

$$T = \left. \frac{\partial e}{\partial s} \right|_{\rho, N_i}, \quad -p = \left. \frac{\partial e}{\partial(1/\rho)} \right|_{s, N_i}, \quad \text{and} \quad \bar{\mu}_j = \left. \frac{\partial e}{\partial N_j} \right|_{s, \rho, N_k, k \neq j}. \quad (5.19)$$

In the differentiable form, the equation of state (5.18) becomes:

$$de = T ds - p d\left(\frac{1}{\rho}\right) + \sum_{i=1}^{n_s} \bar{\mu}_i dN_i. \quad (5.20)$$

Then the equation of state is equivalent to the formulation expressing intensive parameter  $p$  with the extensive parameters:

$$p = p(\rho, s, N_1, \dots, N_{n_s}). \quad (5.21)$$

Since  $e$  is a monotonically increasing function of  $s$  as  $T > 0$ , we choose to express the equation of state in a equivalent form with:

$$p = p(\rho_1, \dots, \rho_{n_s}, \tilde{e}), \quad (5.22)$$

with  $\tilde{e} = \rho e$ , the internal energy per unit of volume.

We introduce the compressibility factors  $\{\kappa, (\chi_i, i = 1, \dots, n_s)\}$  corresponding to the differential of  $p$ :

$$dp = \sum_i \chi_i d\rho_i + \kappa d\tilde{e}, \quad (5.23)$$

where

$$\chi_i = \left. \frac{\partial p}{\partial \rho_i} \right|_{\rho_k, k \neq i, \tilde{e}}, \quad \text{and} \quad \kappa = \left. \frac{\partial p}{\partial \tilde{e}} \right|_{\rho_i, i=1, \dots, n_s}. \quad (5.24)$$

The differentiable form (5.20) implies that

$$d\tilde{e} = \rho de + e d\rho = \rho T ds + \left(e + \frac{p}{\rho}\right) d\rho + \rho \sum_{i=1}^{n_s} \bar{\mu}_i dN_i. \quad (5.25)$$

Introducing the specific enthalpy  $h = e + p/\rho$  we have

$$\left. \frac{\partial \tilde{e}(\rho, s)}{\partial \rho} \right|_{s, N_{i,i=1,\dots,n_s}} = h. \quad (5.26)$$

Then, combining (5.23) and (5.26), the speed of sound can then be expressed with the pressure derivatives:

$$c_s^2 = \left. \frac{\partial p}{\partial \rho} \right|_{s, N_{i,i=1,\dots,n_s}} = \sum_{i=1}^{n_s} \chi_i Y_i + \kappa h. \quad (5.27)$$

In the following, others specific thermodynamic variables will be useful such as the *specific heats* at constant volume  $c_v$  and constant pressure  $c_p$ :

$$c_v = \left. \frac{\partial e}{\partial T} \right|_{\rho, Y_{i,i=1,\dots,n_s}} = T \left. \frac{\partial s}{\partial T} \right|_{\rho, Y_{i,i=1,\dots,n_s}}, \quad \text{and} \quad c_p = \left. \frac{\partial h}{\partial T} \right|_{\rho, Y_{i,i=1,\dots,n_s}} = T \left. \frac{\partial s}{\partial T} \right|_p, \quad (5.28)$$

and the *adiabatic exponent*  $\gamma$ :

$$\gamma = - \frac{1}{\rho p} \left. \frac{\partial p}{\partial(1/\rho)} \right|_s = - \left. \frac{\partial \log p}{\partial \log(1/\rho)} \right|_s. \quad (5.29)$$

The adiabatic exponent is the negative slope of the isentrope as drawn in the  $(\log p, \log 1/\rho)$  plane. It is also related with the sound speed with the relation:

$$c_s = \sqrt{\left. \frac{\partial p}{\partial \rho} \right|_s} = \sqrt{\frac{\gamma p}{\rho}}. \quad (5.30)$$

The pressure  $p$  and the temperature  $T$  are assumed to be non-negative, consequently,  $e$  is monotonic in  $\frac{1}{\rho}$  and  $s$ . Thermodynamic stability conditions described in [MP89] considering physical allowed states requires  $\gamma > 0$ . In that case, the sound speed is real, and the Euler system of equations is hyperbolic.

The fundamental derivative

$$\mathcal{G} = - \frac{1}{2} \frac{1}{\rho} \frac{\partial^3 e / \partial(1/\rho)^3}{\partial^2 e / \partial(1/\rho)^2} \Big|_s = \frac{1}{2} \frac{1}{\gamma \rho^2 p} \left. \frac{\partial^2 p}{\partial(1/\rho)^2} \right|_s, \quad (5.31)$$

measures the convexity of the isentropes in the  $p - (1/\rho)$  plane. In particular, if  $\mathcal{G} > 0$ , the isentropes are convex. Using the positivity of  $\gamma$ ,  $\mathcal{G} > 0$  if and only if:

$$\left. \frac{\partial^2 p}{\partial \rho^2} \right|_s > 0. \quad (5.32)$$

By definition, we consider that an equation of state is convex if its fundamental derivative is strictly positive.

Finally the Grüneisen coefficient  $\Gamma$  allows measuring the spacing of the isentropes in the  $(\log p, \log(1/\rho))$  plane.

$$\Gamma = - \frac{1}{\rho T} \frac{\partial^2 e}{\partial s \partial(1/\rho)} = \frac{1}{\rho} \left. \frac{\partial p}{\partial e} \right|_{1/\rho} = \frac{p}{\rho T} \left. \frac{\partial \log p}{\partial s} \right|_{\log(1/\rho)}. \quad (5.33)$$

When  $\Gamma > 0$ , isentropes do not cross each other in this plane, in this case the Hugoniot curve introduced in §2.1 is well defined.

## 5.2.2 Ideal gas mixture with temperature-dependent heat capacities

In hydrogen flame simulation, we consider a mixture of ideal gases with temperature-dependent heat capacities. The ideal gas law corresponds to:

$$p = \rho r T, \quad \text{with} \quad r = \frac{R_{gas}}{W_{mean}}, \quad (5.34)$$

where  $R_{gas}$  is the universal constant of ideal gas and  $W_{mean}$  the molar weight of the gas.

For an ideal gas,  $e$  is independent of  $\rho$  at fixed  $T$ . In this case:

$$de = c_v dT, \quad dh = c_p dT. \quad (5.35)$$

The adiabatic exponent  $\gamma$  reduces to the ratio of the specific heats and the Grüneisen coefficient  $\Gamma$  to the compressibility factor  $\kappa$ :

$$\gamma = \frac{c_p}{c_v}, \quad \Gamma = \kappa, \quad (5.36)$$

and the specific heat capacities verify:

$$c_p = \frac{\gamma r}{\gamma - 1}, \quad c_v = \frac{r}{\gamma - 1}, \quad c_p = c_v + r. \quad (5.37)$$

In the case of polytropic ideal gases, the heat capacities are constant. However, as the vibrational and rotational energy of the molecular species increases with temperature, we consider that the specific heat capacities varies with respect to the temperature and the composition of the mixture.

$$c_p(T, \mathbf{Y}) = \sum_{k=1}^{n_s} c_{pk}(T) Y_k, \quad c_v(T, \mathbf{Y}) = \sum_{k=1}^{n_s} c_{vk}(T) Y_k, \quad (5.38)$$

with the specific heat capacities  $c_{vk}$  and  $c_{pk}$  of the  $k^{th}$  specie. Adiabatic exponent is a function of the temperature and the composition  $\gamma = \gamma(T, \mathbf{Y})$ .

Then, the specific enthalpy  $h$  is defined by the sum of the contribution of the specific enthalpy of each species  $h_k$ :

$$h = \sum_{k=1}^{n_s} h_k Y_k = \sum_{k=1}^{n_s} \left( \int_{T_0}^T c_{pk} dT' + \Delta h_{f,k}^0 \right) Y_k, \quad (5.39)$$

where  $\Delta h_{f,k}^0$  are the species standard enthalpies of formation at the reference temperature  $T_0$ . The corresponding specific energy is

$$e = \sum_{k=1}^{n_s} \left( \int_{T_0}^T c_{vk} dT' - \frac{R_{gas} T_0}{W_k} + \Delta h_{f,k}^0 \right) Y_k = h - \frac{p}{\rho}. \quad (5.40)$$

Finally, the compressibility factors correspond to:

$$\kappa = \frac{r}{c_v} = \gamma - 1, \quad \text{and} \quad \chi_k = \frac{R_{gas}}{W_k} T - e_k \kappa, \quad \text{for } k = 1, \dots, n_s, \quad (5.41)$$

with  $W_k$  the molar mass of the  $k^{th}$  species.



In the following, dependence on the temperature of the heat capacities is implemented using the NASA polynomials model [Bur84]. Thus, specific heat capacities  $C_{pk}$  of each species  $k$  are approximated with polynomials. This model is usual in combustion simulations involving large variations of temperature and species. Specific data for coefficients of polynomials are available in the literature with the CHEMKIN format [MZG02].

### Convexity of the equation of state

In the case of a mixture of ideal gases with temperature-dependent heat capacities, according to (5.41), positivity of both  $\Gamma$  and the sound speed  $c_s$  are always guaranteed. Then the sufficient condition to have a convex hyperbolic system of equation is  $\mathcal{G} > 0$  which is equivalent to  $\frac{\partial^2 p}{\partial \rho^2} \Big|_{\rho} \geq 0$ . In that case with development used in [Bec00] and with the fact that the sound speed  $c_s$  depends only on both  $T$  and the composition  $\mathbf{Y}$ , we obtain:

$$\begin{aligned} \frac{\partial^2}{\partial \rho^2} p(\rho, s, \mathbf{Y}) &= \frac{\partial}{\partial \rho} c_s^2(\rho, s, \mathbf{Y}) \\ &= \frac{\partial}{\partial \rho} c_s^2(\rho, e, \mathbf{Y}) + \frac{\partial}{\partial \rho} e(\rho, s, \mathbf{Y}) \frac{\partial}{\partial e} c_s^2(\rho, e, \mathbf{Y}) \\ &= 0 + \frac{p}{\rho^2} \frac{1}{c_v(T, \mathbf{Y})} \frac{\partial}{\partial T} c_s^2(\rho, T, \mathbf{Y}). \end{aligned} \quad (5.42)$$

Then the convex condition is verified if and only if the sound speed is a non-decreasing function of the temperature.

$$\frac{\partial}{\partial T} c_s(T, \mathbf{Y}) \geq 0. \quad (5.43)$$

By developing the derivatives of the sound speed we obtain:

$$\begin{aligned} \frac{\partial}{\partial T} c_s(T, \mathbf{Y}) &= \frac{\partial}{\partial T} \sqrt{\gamma(T, \mathbf{Y}) r(\mathbf{Y}) T} \\ &= \frac{1}{2} \sqrt{\frac{\gamma(T, \mathbf{Y}) r(\mathbf{Y})}{T}} \left( \frac{T}{\gamma(T, \mathbf{Y})} \frac{\partial \gamma(T, \mathbf{Y})}{\partial T} + 1 \right). \end{aligned}$$

So the convex condition (5.43) is equivalent to:

$$w(T) = \frac{T}{\gamma(T, \mathbf{Y})} \frac{\partial \gamma(T, \mathbf{Y})}{\partial T} = \frac{\partial}{\partial \log(T)} \log(\gamma(T, \mathbf{Y})) \geq -1. \quad (5.44)$$

For the species involved in the hydrogen combustion and with the polynomials described in [MZG02] this condition is always recovered. The figure 5.1 represents the evolution with  $T$  of the specific heat capacity  $c_p(T)$ , the heat capacity ratio  $\gamma(T)$  for the main gases involved in  $\text{H}_2$  combustion. We note that the condition 5.44 on the function  $w(T)$  is strongly satisfied <sup>1</sup>.

---

<sup>1</sup>Discontinuity appear around  $T = 1000$  K because two different polynomials are used in our thermodynamic model before and after 1000 K and that the continuity of their derivative is not guaranteed

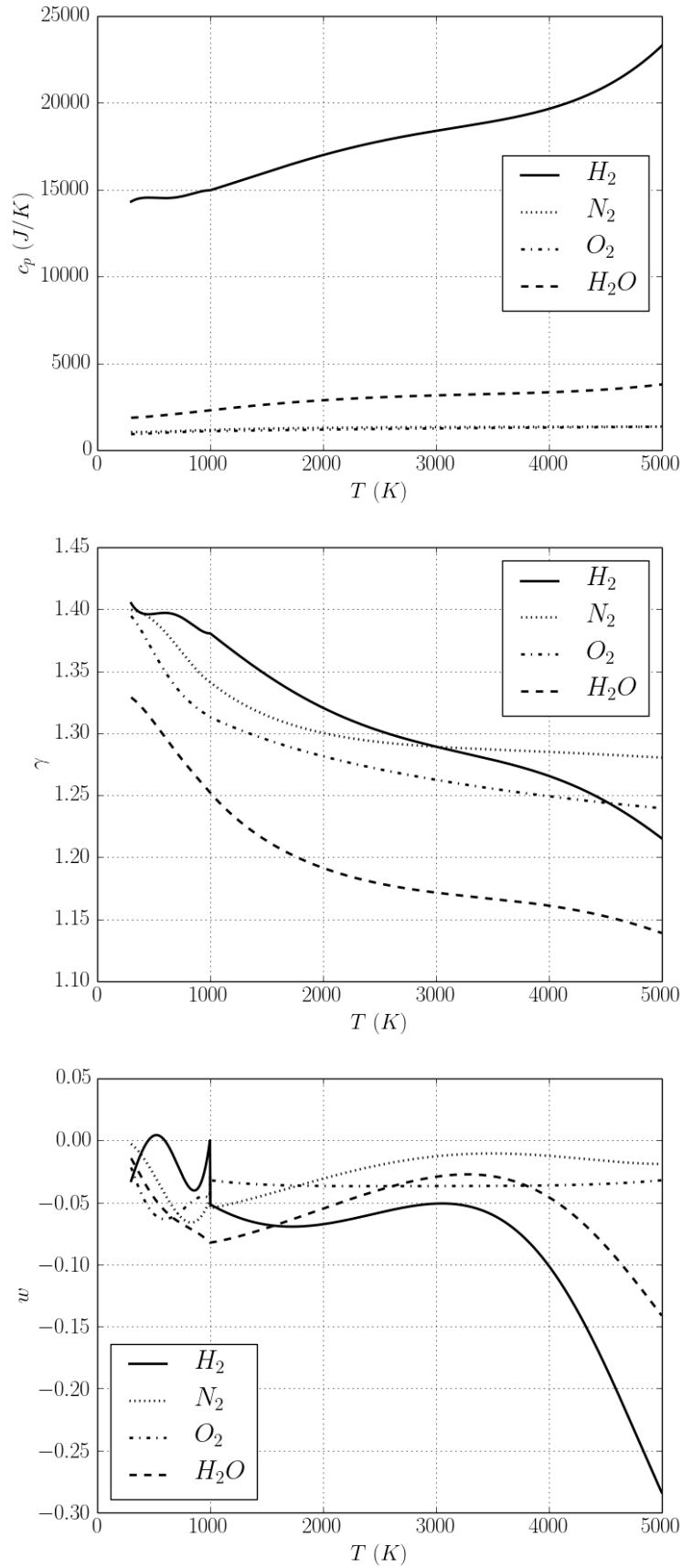


**Figure 5.1:** Variation of  $c_p(T)$ ,  $\gamma(T)$  and  $w(T)$  for main gases involved in  $H_2$  combustion. Specific heat capacities are computed with polynomials described in [MZG02]



# Numerical solution for multi-scale partial differential equations

Simulation of flame acceleration from initial hydrodynamic instabilities to transition to detonation front involves a broad spectrum of time and space scales. Those large scales appear in the operators of the reactive Navier-Stokes equations 5.2. The non-linear convection with compressible effects is described by the Euler operator  $\mathbf{f}^E$ , the diffusion and the viscous phenomena by  $\mathbf{f}^V$  and the reactive solution by the computation of the source term  $\mathbf{S}$ . Each operator has specific time and space characteristic scales. Particularly, detailed chemistry will involve fast time scales compared to the convection and the characteristic diffusion times. To face these multi-scales phenomena, dedicated time integration schemes are needed.

There are two approaches for the numerical approximation of Partial Differential Equations (PDE):

- Explicit methods are easier to implement but involve significant stability restriction, which induces very long computation for solving the fastest physical or numerical time scales.
- Implicit methods generally require extra computation with some inversion method but are able to cope with numerical stiffness because time steps are determined by the targeted accuracy instead of numerical stability.

Although different types of high-order implicit schemes have been conceived to properly handle the entire time scale spectrum of the problem while ensuring accurate numerical approximation [NS05, DS10], the usual strategy is using hybrid implicit/explicit time discretization with especially time operator splitting methods. In this approach, the different subproblems associated with each operator are decoupled and solved independently with dedicated methods during a prescribed splitting time step. This method reduces computational resources and guarantees stability as long as the inner numerical solvers are stable themselves. However, specific attention is given to the resulting splitting errors in the case of stiff PDEs. Once this splitting error is properly controlled, the operators have dedicated high-order methods so that the splitting scheme determines the global accuracy of the time integration scheme.

## 6.1 Finite Volume Method

In our simulations, Navier Stokes equations are solved using a *Finite volume approach* on a Cartesian grids. We denote  $\Omega_j$  the cell of the computational volume indexed by  $j$  with a control volume  $|\Omega_j| = \int_{\Omega_j} d\mathbf{x}$ .  $U_j(t)$  is the cell-averaged value of the discrete quantity  $U(\mathbf{x}, t)$  on  $\Omega_j$ :

$$U_j(t) = \frac{1}{|\Omega_j|} \int_{\Omega_j} U(\mathbf{x}, t) d\mathbf{x}. \quad (6.1)$$

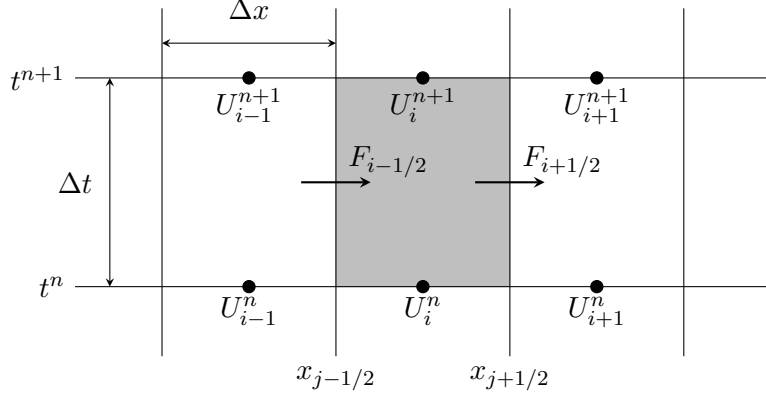


**Figure 6.1:** Geometrical illustration of the finite volume scheme on a integration cell

We consider a hyperbolic system of conservation law with one space dimension of the form:

$$\frac{\partial}{\partial t} \mathbf{U}(x, t) + \frac{\partial}{\partial x} \mathbf{F}(\mathbf{U}(x, t)) = 0. \quad (6.2)$$

with  $\mathbf{U} : \mathbb{R} \times \mathbb{R}^+ \rightarrow \Omega$  with  $\Omega$  an open subset of  $\mathbb{R}^m$  with  $m$  the number of equations in this system.  $\mathbf{U}$  is then a vector with  $m$  components composed by conserved quantities or state variable corresponding to (5.1) in the case of fluids dynamics problem.  $F : \Omega \rightarrow \mathbb{R}^m$  is the flux function.

In the finite volume framework the one-dimensional conservation law (6.2) reads:

$$U_j^{n+1} = U_j^n - \frac{\Delta t}{|\Omega_j|} (F_{j+1/2}^n \cdot \mathbf{n}_{j+1/2} - F_{j-1/2}^n \cdot \mathbf{n}_{j-1/2}), \quad (6.3)$$

where  $U_j^n = U_j(t_n)$  is the value of the discretized conservative variable at time  $t^n = n\Delta t$  with  $\Delta t = t^{n+1} - t^n$  the time step.  $\mathbf{n}_{j+1/2}$  is the normal to the face located at  $x_{j+1/2}$  and  $F_{j+1/2}^n$  the numerical flux of the scheme at this cell interface defined as  $\Delta t$  average with:

$$F_{j+1/2}^n = \int_{t^n}^{t^{n+1}} F(x_{j+1/2}, t) dt. \quad (6.4)$$

Finite volume on a integration cell is schematically represented on figure 6.1.

Approximation of the numerical flux  $F_{j+1/2}^n$  is realized considering a Riemann problem at the interface of two adjacent cells  $\Omega_j$  and  $\Omega_{j+1}$  with the cell-averaged values  $U_j^n$  and  $U_{j+1}^n$  inside each cell respectively. Then we have  $F_{j+1/2}^n = F_{j+1/2}^n(U_i^n, U_{i+1}^n)$ .

Description of the Riemann problem and exact resolution with Euler equation for convex hyperbolic system is realized in Appendix V.

The time step of the integration is constraint by the domain of dependence. Courant, Friedrichs and Lewy (CFL) condition based on  $\nu = \max(|\lambda|) \frac{\Delta t}{\Delta x}$  gives the limit of the time-step  $\Delta t$  to keep stable numerical method without interaction between characteristic waves.

The total variation of  $U$  corresponds to:

$$TV(U) = \lim_{\epsilon \rightarrow 0} \frac{1}{\epsilon} \int_{-\infty}^{\infty} |U(x + \epsilon) - U(x)| dx. \quad (6.5)$$

Since the function  $U^n(x, t)$  is approximated by a piecewise constant function, this definition of TV reduces to:

$$TV(U^n) = \sum_{i=-\infty}^{\infty} |U_{i+1}^n - U_i^n|. \quad (6.6)$$

The numerical method is said *consistent* with the original conservation law if the numerical flux  $F_{i+1/2}^n$  reduces to the true flux  $F$  for the case of constant flow. If  $U(x, t) = \bar{U}$  with  $\bar{U}$  a constant, then:

$$F_{i+1/2}(\bar{U}, \bar{U}) = F(\bar{U}). \quad (6.7)$$

Lax-Wendroff theorem [LW60] proved in the case of finite volume methods that if a conservative and consistent scheme converges to some function  $U(x, t)$  as the grid is refined, this one corresponds to a weak solution of the conservation law. Definition of the convergence here however requires two conditions:

1. Over every bounded set  $\Omega = [a, b] \times [0, T]$  in x-t space,

$$\int_0^T \int_a^b |U^{(k)}(x, t) - U(x, t)| dx dt \rightarrow 0 \text{ as } k \rightarrow \infty, \quad (6.8)$$

with  $U^{(k)}(x, t)$  the piecewise constant function that takes the value  $U_j^n$  on the space time mesh cell  $(x_{j-1/2}, x_{j+1/2}) \times (t_n, t_{n+1})$ .  $k$  corresponding to the mesh used with  $\Delta x^{(k)}$  and  $\Delta t^{(k)}$  approaching zero as  $k \rightarrow \infty$ .

2. For each time  $\tau$ , there is a real constant  $R > 0$  such that for all  $k$

$$TV(U^{(k)}(\cdot, t)) < R \text{ for all } 0 \leq t \leq \tau. \quad (6.9)$$

## 6.2 Time operator splitting

We describe here two classical first and second order, respectively Lie and Strang, splitting schemes. Let consider two operators  $\mathcal{L}^1$  and  $\mathcal{L}^2$ , Lie scheme consists in successively solving each time operator:

$$w_j^{n+1} = \mathcal{L}_{\Delta t}^2 \mathcal{L}_{\Delta t}^1 w_j^n. \quad (6.10)$$

This method is only first order accurate in time and operators do not act symmetrically on the solution that could lead to numerical issues. Strang schemes is usually preferred since it ensures a second order accurate time integration and give a symmetrical solution with respect to the operators:

$$w_j^{n+1} = \mathcal{L}_{\Delta t/2}^2 \mathcal{L}_{\Delta t}^1 \mathcal{L}_{\Delta t/2}^2 w_j^n. \quad (6.11)$$

The difficulty with the stiff equations is to avoid some numerical order reduction in the presence of scales much faster than the splitting time step, this could be the case for the convection and the diffusion process compared to the fast reaction time scales. The splitting procedure we used here is based on the analysis of the splitting error for a reaction/diffusion/convection systems described in literature [Dua11, LV99, DM04]. To avoid important splitting errors, better performances are expected while ending the splitting scheme by the time integration of the reaction part [DM04] in a Strang scheme. A Lie scheme is applied with the convection and diffusion operators to limit the restitution time:

$$w_j^{n+1} = \mathcal{L}_{\Delta t/2}^R \mathcal{L}_{\Delta t}^V \mathcal{L}_{\Delta t}^E \mathcal{L}_{\Delta t/2}^R w_j^n, \quad (6.12)$$

where  $\mathcal{L}^E$  is the discrete approximation of the operator of convection;  $\mathcal{L}_{\Delta t}^E : \mathbf{w}_t = -\nabla \cdot (\mathbf{f}^E(\mathbf{w}))$  and  $\mathcal{L}_{\Delta t}^V$  the discrete approximation of the diffusion operator  $\mathcal{L}_{\Delta t}^V : \mathbf{w}_t = -\nabla \cdot (\mathbf{f}^V(\mathbf{w}, \nabla \mathbf{w}))$ .

The splitting method considers high-order dedicated integration methods for each operator so that the splitting scheme rules the control of accuracy.

If the fastest time scales play a leading role in the global physics of the phenomenon, splitting time scales must be small enough to capture the global dynamics. In the opposite case, larger splitting time scales can be used, but order reductions may appear due to short-life transients associated with the fastest variables.

We choose to apply an implicit integration scheme to solve the reaction operator, since it represents the fastest time scales. The convection and diffusion operator are solved by explicit approaches. In the simulation of flame acceleration and transition to the detonation, the explicit stability constraints applied to the convection, and the diffusion will impose a splitting time step that is not excessive compared to the chemical characteristic time especially when velocity are important. Then we avoid order reduction and guarantee stable results with explicit stability restrictions.

## 6.3 Dedicated integration methods for combustion simulation

We present here the dedicated integration methods used in the splitting procedure 6.12.

### 6.3.1 Runge-Kutta Time Integration Methods

We describe in this section some one-step Runge-Kutta methods that give implicit and stabilized explicit techniques that have shown to be very efficient for the numerical solution of reactions and diffusion problems.

Let us consider the scalar initial value problem:

$$\begin{cases} d_t U = F(t, U(t)), \\ U(0) = U_0, \end{cases} \quad (6.13)$$

with  $U_0 \in \mathbb{R}$  and  $U : \mathbb{R} \rightarrow \mathbb{R}$ ,  $F : \mathbb{R} \times \mathbb{R} \rightarrow \mathbb{R}$ . The objective is to obtain an approximation  $U_n$  of the exact solution  $U(t_n)$  for a time discretization given by  $t_0 = 0 < t_1 < \dots < t_n$ .

The exact solution of 6.13 at  $t_1 = t_0 + \Delta t$  is given by:

$$U(t_1) = U_0 + \int_{t_0}^{t_1} f(t, U(t)) dt. \quad (6.14)$$

The first order explicit Euler method approximate this solution by:

$$U_1 = U_0 + \Delta t f(t_0, U_0). \quad (6.15)$$

By approximating the integral in 6.14 by a higher-order quadrature formula, we can build higher-order one-step methods. The Runge method of second-order is then constructed with the mid-point approximation and the Euler method.

$$U_1 = U_0 + \Delta t f\left(t_0 + \frac{\Delta t}{2}, U_0 + \frac{\Delta t}{2} f(U_0)\right). \quad (6.16)$$

A generalization to high order-quadrature formulae given  $s$ -stage Runge-Kutta methods is possible:

$$\begin{cases} g_i = U_0 + \Delta t \sum_{j=1}^s a_{ij} f(t_0 + c_j \Delta t, g_j), \quad i = 1, \dots, s, \\ U_1 = U_0 + \Delta t \sum_{j=1}^s b_j f(t_0 + c_j \Delta t, g_j). \end{cases} \quad (6.17)$$

When  $a_{ij} = 0$  for  $j \leq i$ , the scheme is explicit in time. Otherwise it describes implicit Runge-Kutta methods. The arrays  $b, c \in \mathbb{R}^s$  and the matrix  $A = (a_{ij})_{1 \leq i, j \leq s} \in \mathcal{M}_s(\mathbb{R})$  are usually described using the Butcher tableau:

$$\begin{array}{c|cccc}
 c_1 & a_{11} & a_{12} & \cdots & a_{1s} \\
 c_2 & a_{21} & a_{22} & \cdots & a_{2s} \\
 \vdots & \vdots & & \ddots & \vdots \\
 c_s & a_{s1} & a_{s2} & \cdots & a_{ss} \\
 \hline
 & b_1 & b_2 & \cdots & b_s
 \end{array} \tag{6.18}$$

The Butcher tableau for the Runge method of second order 6.16 is then:

$$\begin{array}{c|cc}
 0 & & \\
 \frac{1}{2} & \frac{1}{2} & \\
 \hline
 & 0 & 1
 \end{array} \tag{6.19}$$

The stability and order analysis of such scheme are realized using the Dahlquist test equation [Dah63]:

$$\begin{cases} d_t U = \lambda U, \\ U(0) = 1, \end{cases} \tag{6.20}$$

with  $\lambda \in \mathbb{C}$ . For any numerical scheme we obtain:

$$U_1 = R(z)U_0, \quad z = \Delta t \lambda. \tag{6.21}$$

$R : \mathbb{C} \rightarrow \mathbb{C}$  is the stability function of the method and  $R(z)$  correspond to the numerical solution of 6.20 given after one time step  $\Delta t$ . The numerical scheme is of order  $p$  if  $R(z)$  satisfy:

$$e^z - R(z) = \mathcal{O}(\Delta t^{p+1}) = \mathcal{O}(z^{p+1}), \tag{6.22}$$

The numerical solution recursively computed can be written as:

$$U_n = (R(z))^n U_0, \tag{6.23}$$

the stability domain of the method is given by the set of  $z$  for which  $U_n$  remains bounded for  $n \rightarrow \infty$ :

$$S = \{z \in \mathbb{C}; |R(z)| \leq 1\}. \tag{6.24}$$

A Runge-Kutta methods is said to be A-stable if:

$$\{z \in \mathbb{C}, \operatorname{Re}(z) \leq 0\} \subset S. \tag{6.25}$$

The implicit Runge-Kutta schemes are A-stable. For eigenvalues with large real part, characteristic of stiff equations, a stability function  $R(z)$  much smaller than 1 is also necessary, a property corresponding to the L-stability. A method is L-stable if it is A-stable and  $R(z) \rightarrow 0$  as  $z \rightarrow \infty$ . L-stable methods are then dedicated for integrating stiff equations.



$\frac{4 - \sqrt{6}}{10}$	$\frac{88 - 7\sqrt{6}}{360}$	$\frac{296 - 169\sqrt{6}}{1800}$	$\frac{-2 + 3\sqrt{6}}{225}$
$\frac{4 + \sqrt{6}}{10}$	$\frac{296 + 169\sqrt{6}}{1800}$	$\frac{88 + 7\sqrt{6}}{360}$	$\frac{-2 - 3\sqrt{6}}{225}$
1	$\frac{16 - \sqrt{6}}{36}$	$\frac{16 + \sqrt{6}}{36}$	$\frac{1}{9}$
	$\frac{16 - \sqrt{6}}{36}$	$\frac{16 + \sqrt{6}}{36}$	$\frac{1}{9}$

**Table 6.1:** *RadauIIA method of order 5*

### 6.3.2 Time integration of the viscous flux: Runge Kutta 2

We consider a Runge-Kutta method of second-order 6.16 to capture diffusion phenomena.

The numerical integration of  $\mathbf{f}^V(\mathbf{w}, \nabla \mathbf{w})$  described in 5.3 requires the approximation of the divergence of the viscous flux. In particular, temperature, velocity and mass fraction gradients evaluated at the cell interface are involved in its expression. In the normal direction to the cell interface  $\xi$ , the gradient is computed by a second-order approximation:

$$\left. \frac{\partial \phi}{\partial \xi} \right|_{i+1/2,j,k} = \frac{1}{\delta \xi} (\phi_{i+1,j,k} - \phi_{i,j,k}) + \mathcal{O}(\delta \xi^2). \quad (6.26)$$

In the tangential direction  $\eta$ , lying in the plane of the cell interface, the gradient is expressed as:

$$\left. \frac{\partial \phi}{\partial \eta} \right|_{i+1/2,j,k} = \frac{1}{4\delta \eta} (\phi_{i+1,j+1,k} + \phi_{i,j+1,k} - \phi_{i+1,j-1,k} - \phi_{i,j-1,k}) + \mathcal{O}(\delta \eta^2). \quad (6.27)$$

### 6.3.3 Time integration of the Reaction: Radau5 Solver

The reaction operator usually has the fastest time scales of the numerical solver, and an implicit integration scheme is then chosen. The Radau5 solver is an implicit Runge Kutta scheme developed by Hairer & Wanner [HW96]. This solver uses the 3-stage Ehle's method RadauIIA [Ehl69] to implement coefficients of the implicit schemes whose coefficients are given in Table 6.1. This method allows to get a fifth-order resolution and guarantee stability properties (A-stable and L-stable). This method is known to be very suitable for highly stiff problems.

Another specificity of the Radau5 solver is the adaptive time-stepping strategy that guarantees a prescribed accuracy. Radau5 solver uses a lower order embedded method to numerically estimate the local error and adapt the time step  $\Delta t_{new}$  associated with prescribed absolute and relative tolerances. This adaptive time-stepping strategy saves computing time since it can discriminate stiff zones from regular ones. By default, the absolute and relative tolerance values will be set to  $1 \times 10^{-3}$  and  $1 \times 10^{-10}$  respectively in our simulations.

Efficient algorithmic methods dedicated to matrix inversion, Newton iterative method, etc., are also implemented to solve the intermediate evaluation  $g_i$  in 6.17 and save computational time despite the non-linear system and the numerical difficulties imposed by the implicit properties. All these algorithmic methods are discussed in detail in [HW96].

### 6.3.4 Integration of the convection flux: One-Step Monotonicity-Preserving (OSMP) scheme

The numerical Euler flux  $\mathbf{f}^E(\mathbf{w})$  is approximated by an explicit time and space  $p^{\text{th}}$ -order One-Step scheme developed in [DT04] that will be described in the next chapters. This integration scheme method is based on the Approximated Riemann solver of Roe combined with shock-capturing methods

to prevent spurious oscillations while increasing the order of the scheme with a Lax-Wendroff approach described in the Chapter 7. Specific treatment of those schemes to extend it to a mixture of real gases is presented in the Chapter 8. Compressible and large gradients effects impose a high-order of accuracy for this operator to avoid numerical dissipation. We generally used seventh order of accuracy in our simulations.

## 6.4 Multidimensional splitting

To extend these numerical schemes in the multidimensional case, splitting strategy is also used to couple time and space approaches. The difficulty is to consider non-linear cross derivative terms that appear in the second and high-order terms of the subproblems with the dedicated schemes of each operator. We also need to guarantee that the resulting scheme will be non-oscillatory. The simplest way to avoid the problem of cross derivatives is to use a Strang directional splitting strategy which is only second-order accurate.

In two dimensions, since the directional operators  $\mathbf{L}_{\delta_x}$  and  $\mathbf{L}_{\delta_y}$  in each space direction do not commute, the second order accuracy is recovered every two time step with the symmetric solution:

$$w_j^{n+2} = \mathbf{L}_{\delta_x} \mathbf{L}_{\delta_y} \mathbf{L}_{\delta_y} \mathbf{L}_{\delta_x} w_j^n. \quad (6.28)$$

In the same way, the three dimensional splitting is constructed with a second order accuracy recovered every six time steps:

$$w_j^{n+6} = (\mathbf{L}_{\delta_x} \mathbf{L}_{\delta_y} \mathbf{L}_{\delta_z})(\mathbf{L}_{\delta_x} \mathbf{L}_{\delta_z} \mathbf{L}_{\delta_y})(\mathbf{L}_{\delta_y} \mathbf{L}_{\delta_z} \mathbf{L}_{\delta_x}) \\ (\mathbf{L}_{\delta_y} \mathbf{L}_{\delta_x} \mathbf{L}_{\delta_z})(\mathbf{L}_{\delta_z} \mathbf{L}_{\delta_y} \mathbf{L}_{\delta_x})(\mathbf{L}_{\delta_z} \mathbf{L}_{\delta_x} \mathbf{L}_{\delta_y}) w_j^n. \quad (6.29)$$

with  $\mathbf{L}_{\delta_z}$  the operator discrete approximation in the third space direction.



# High Resolution Methods for mixtures of calorically perfect gases

This chapter describes the numerical methods used to approximate the solution of the Euler hyperbolic conservation laws with discretization on a single grid using convexity property defined in the Chapter V. The objective is to solve multicomponent compressible flows with multiple potential discontinuities correctly.

The numerical scheme applied to these equations then must possess some features:

- sharp resolution of the discontinuities with the absence of spurious oscillation in the vicinity of them,
- consistent with the weak form of the conservation law and convergence,
- verifies a discrete form entropy condition to select a physically correct weak solution.

An additional requirement is a high-order accuracy with low numerical diffusion to track discontinuities properly. Such methods are referred to as high-resolution methods.

The Godunov solver corresponds to the full resolution of the Riemann problem at the intersection of each finite volume cell. This approach is both robust and accurate but is CPU time-consuming. Indeed, the Riemann problem involves expensive iterative procedures like the Newton-Raphson procedure combined with computations of numerical integrals. The complete resolution of the Riemann problem and the description of the Godunov solver in the case of species with temperature-dependent heat capacities is described in the Appendix A.2. Non-iterative solutions to approximate numerical fluxes at the intermediary state in the Riemann problem have been developed to reduce CPU time. The MR\_CHORUS solver used in this work considers the approximate solver of Roe presented in § 7.1 which is a low diffusive Riemann solver.

However, the Godunov solver and the Roe solver are only first-order accurate. A high-order extension is then necessary to satisfy the high resolution desired. The One-Step Monotonicity Preserving (OSMP) dedicated to this extension to high-order scheme is described in § 7.2. The main idea of this scheme is to increase the order of accuracy in time and space of the Roe scheme by using a Lax-Wendroff approach associated with a flux limiter to keep high-resolution of the smooth solution and well-resolved nonoscillatory discontinuities.

In this chapter, we consider only calorically perfect gases. Indeed, the initial Roe solver and OSMP scheme are built for gas with constant adiabatic ratio  $\gamma$  and heat capacities  $c_p$ . The extension to the case of multicomponent mixtures with a convex equation of state will be found in Chapter 8.

## 7.1 Approximate Riemann solver of Roe

Exact solution of the Riemann problem, such as realized by the Godunov solver described in Appendix A.2.2 is too expensive to use in a large computational domain. Approximate Riemann solvers have been developed in the last decades to approximate the intermediary state of the Riemann problem without using an exact resolution of the Riemann problem, such as in the two-shocks Riemann solver, the two rarefactions Riemann solver, the Osher Solomon solver, the HLL/HLLC solvers which are solvers commonly used. Description of those methods is available in [Tor09, Bec00]. The HLLC solver is one of the most usual and appears in several studies of flame acceleration computations; this particular solver is described more precisely in Appendix A.2.2.

We choose in this work to use the Roe solver, which is the less diffusive scheme among the complete Riemann solver<sup>1</sup>.

This approximate Riemann solver of Roe has been described for the first time by Roe in [Roe81]. Some improvements have been made to solve entropy issues with a slight modification of the flux expression and extension to non-ideal gas described more precisely in the next chapter. We describe the scheme with only one space dimension. In that case, the size of the conservative variable vector  $\mathbf{w}$  corresponds to  $N = n_s + 2$ .

We consider here a mixture of calorically perfect gas, in this case, the adiabatic ratio  $\gamma$  and the heat capacity  $c_p$  are constant for each temperature and pressure. With this assumption, the Jacobian matrix of the Euler flux  $\mathbf{A}(\mathbf{w}) = \frac{\partial \mathbf{f}^E(\mathbf{w})}{\partial \mathbf{w}}$  becomes:

$$\mathbf{A}(\mathbf{w}) = \begin{pmatrix} u(1 - Y_1) & -uY_1 & \cdots & -uY_1 & Y_1 & 0 \\ -uY_2 & u(1 - Y_2) & \cdots & -uY_2 & Y_2 & 0 \\ \vdots & \ddots & \ddots & \vdots & \vdots & \vdots \\ \vdots & \ddots & \ddots & -uY_{N-1} & Y_{N-1} & 0 \\ -uY_N & \cdots & \cdots & u(1 - Y_N) & Y_N & 0 \\ (\frac{1}{2}(\gamma - 1) - 1)u^2 & \cdots & \cdots & (\frac{1}{2}(\gamma - 1) - 1)u^2 & (3 - \gamma)u & \gamma - 1 \\ u(\frac{1}{2}(\gamma - 1)u^2 - H) & \cdots & \cdots & u(\frac{1}{2}(\gamma - 1)u^2 - H) & H - (\gamma - 1)u^2 & (1 + (\gamma - 1))u \end{pmatrix}, \quad (7.1)$$

with the  $N$  size eigenvalues  $(u, \dots, u, u + c_s, u - c_s)$

The corresponding eigenvectors are given by:

$$\begin{aligned} \mathbf{K}^{(1)} &= \left[ 1, 0, \dots, \dots, 0, u, \frac{1}{2}u^2 \right]^T; \\ \mathbf{K}^{(i)} &= \left[ 0, \dots, 1, \dots, 0, u, \frac{1}{2}u^2 \right]^T; \\ \mathbf{K}^{(n_s)} &= \left[ 0, \dots, \dots, 0, 1, u, \frac{1}{2}u^2 \right]^T; \\ \mathbf{K}^{(N-1)} &= [Y_1, \dots, Y_i, \dots, Y_{n_s}, u + c_s, H + uc_s]^T; \\ \mathbf{K}^{(N)} &= [Y_1, \dots, Y_i, \dots, Y_{n_s}, u - c_s, H - uc_s]^T. \end{aligned} \quad (7.2)$$

Roe's initial approach consists in replacing the Jacobian matrix in the Riemann problem (30) with a constant Jacobian matrix and then operating a linear version of the Euler hyperbolic system at each cell interface. We then obtain a linear hyperbolic system just as described in §A.1.3.

<sup>1</sup>refers to the approximate Riemann solver that considers the three characteristic fields present in the exact solution of the Riemann problem (a shock wave, a contact discontinuity, and an expansion fan) as described in Appendix A.2.2

$$\tilde{\mathbf{A}} = \tilde{\mathbf{A}}(\mathbf{w}_L, \mathbf{w}_R), \quad (7.3)$$

where  $\mathbf{w}_L$  and  $\mathbf{w}_R$  are the conservative vectors at, respectively, the left and right part of the interface. To converge to a weak solution, the matrix  $\tilde{\mathbf{A}}$  must satisfy the following list of properties :

1. The system must be hyperbolic. It means that  $\tilde{\mathbf{A}}$  has real eigenvalues  $\tilde{\lambda}_i = \tilde{\lambda}_i(\mathbf{w}_L, \mathbf{w}_R)$  and linearly independent eigenvectors  $\tilde{\mathbf{K}}^{(i)} = \tilde{\mathbf{K}}^{(i)}(\mathbf{w}_L, \mathbf{w}_R)$ ;
2. The approximation is consistent with the jacobian matrix i.e. as  $\mathbf{w}_L, \mathbf{w}_R$  smoothly tends to  $\mathbf{w}$ ,  $\tilde{\mathbf{A}}(\mathbf{w}_L, \mathbf{w}_R)$  smoothly tends to the jacobian  $\mathbf{A}(\mathbf{w})$ ;
3. The conservation must be satisfy across discontinuities  $\tilde{\mathbf{A}}(\mathbf{w}_L, \mathbf{w}_R)(\mathbf{w}_L - \mathbf{w}_R) = \mathbf{f}^E(\mathbf{w}_L) - \mathbf{f}^E(\mathbf{w}_R)$ .

With such a Jacobian matrix, the numerical flux  $\tilde{\mathbf{f}}^E(\mathbf{U}_L, \mathbf{U}_R)$  at the interface between two consecutive cells then becomes:

$$\tilde{\mathbf{f}}^E(\mathbf{U}_L, \mathbf{U}_R) = \frac{1}{2}(\mathbf{f}^E(\mathbf{U}_L) + \mathbf{f}^E(\mathbf{U}_R)) - \frac{1}{2} \sum_{k=1}^N \tilde{\alpha}_k \cdot |\tilde{\lambda}_k| \tilde{\mathbf{K}}^{(k)}, \quad (7.4)$$

The  $\tilde{\alpha}_k$  are the characteristic variables corresponding to the  $k^{th}$  component of  $(\mathbf{U}_R - \mathbf{U}_L)$  in the eigenvector basis. With the linearization of the Jacobian matrix, they correspond to some Riemann invariants of the other characteristic fields.

$$\mathbf{U}_R - \mathbf{U}_L = \sum_{k=1}^N \tilde{\alpha}_k \cdot \tilde{\mathbf{K}}^{(k)}, \quad \text{or equivalently} \quad \begin{pmatrix} \tilde{\alpha}_1 \\ \vdots \\ \tilde{\alpha}_N \end{pmatrix} = \left( \tilde{\mathbf{K}}^{(k)} \right)^{-1} \cdot (\mathbf{U}_R - \mathbf{U}_L), \quad (7.5)$$

with  $\tilde{\mathbf{K}}^{-1}$  the inverse matrix of  $\tilde{\mathbf{K}}$

### 7.1.1 Roe averaged operator

Linearization of the matrix  $\tilde{\mathbf{A}}$  requires a consistent expression of the different terms. To be able to respect the last two properties Roe [Roe81] suggested to use a parameter vector  $\mathbf{Q}$  such that components of  $\mathbf{U}$  and of the Euler flux vector  $\mathbf{F}(\mathbf{U})$  can be expressed as quadratic compositions of the  $\mathbf{Q}$  components. In the case of multi-component flow, this corresponds to:

$$\mathbf{Q} = (q_1, q_2, \dots, q_N)^T = \sqrt{\rho}(Y_1, \dots, Y_{n_s}, u, H)^T. \quad (7.6)$$

The averaged vector  $\tilde{\mathbf{Q}}$  is obtained with a simple arithmetic averaging  $\tilde{\mathbf{Q}} = \frac{1}{2}(\mathbf{Q}_R + \mathbf{Q}_L)$ . The corresponding variable of mass fraction  $\tilde{Y}_1, \dots, \tilde{Y}_{n_s}$ , velocity  $\tilde{u}$  and enthalpy  $\tilde{H}$  at the Roe averaged state are then computed with the Roe averaged operator, where  $r$  stands for each component of  $(Y_1, \dots, Y_{n_s}, u, H)^T$ :

$$\tilde{r} = \theta r_L + (1 - \theta) r_R, \quad (7.7)$$

with

$$\theta = \frac{\sqrt{\rho_L}}{\sqrt{\rho_L} + \sqrt{\rho_R}}, \quad (7.8)$$

and the value of the density at the interface becomes:

$$\tilde{\rho} = \sqrt{\rho_L \rho_R}. \quad (7.9)$$

Let us consider  $\phi$  and  $\psi$  two arbitrary variables. The Roe averaged operator respects the following identities for the variation across interface  $\Delta(\cdot) = (\cdot)_R - (\cdot)_L$  :

$$\Delta(\rho\phi) = \tilde{\rho} \Delta\phi + \tilde{\phi} \Delta\rho; \quad (7.10a)$$

$$\Delta(\rho\psi\phi) = \tilde{\rho} \tilde{\phi} \Delta\psi + \tilde{\rho} \tilde{\psi} \Delta\phi + \tilde{\phi} \tilde{\psi} \Delta\rho. \quad (7.10b)$$

### 7.1.2 Entropy fix

The weak solution obtained by the original Godunov method satisfies the entropy condition. However, it can be violated by using the Roe solver. In order to make this scheme satisfy this condition, correction is usually added to its formulation, referred to as entropy fix.

Entropy fix generally intends to cure failure of Roe's scheme in case of transonic rarefactions. Indeed, representation of a rarefaction fan by a single discontinuity with respect of the jump relation defined by the last properties (iv) of the Roe solver leads to a nonentropy consistent solution [Lev92].

The entropy fix must then replaces such discontinuities with an alternative description.

To identify the occurrence of such transonic rarefaction, each  $k$ -th elementary wave is associated to two propagation velocity  $\lambda_{k,L}$  and  $\lambda_{k,R}$  corresponding in the case of a rarefaction wave, the first and the last waves of the fan. Rarefaction waves will then have an impact on entropy condition if

$$\lambda_{k,L} < 0 < \lambda_{k,R}. \quad (7.11)$$

Inside the rarefaction wave, different approximation can be made by considering a constant intermediary state or linear variable intermediary state between the two side of the wave. It results in a modification of the formulation of the Roe solver (7.4) when the eigenvalue  $\tilde{\lambda}_k$  is close to zero.

$$\mathbf{f}_{(e.f.)}^E(U_L, U_R) = \frac{1}{2}[\mathbf{f}^E(U_L) + \mathbf{f}^E(U_R)] - \frac{1}{2} \sum_{k=1}^p q(\tilde{\lambda}_k) \tilde{\alpha}_k \tilde{\mathbf{K}}^{(k)}, \quad (7.12)$$

where the function  $q(\tilde{\lambda}_k)$  is a suitable modification of the function  $|\tilde{\lambda}_k|$ .

Review of correction entropy solution are available in [PQVV00]. We choose in our simulations to use the second entropy fix of Harten and Hyman [HH83] that consider a linear transition between the state  $u_{k,L}$  and  $u_{k,R}$  for  $\lambda_{k,L} < \frac{x}{t} < \lambda_{k,R}$ :

$$u_k^1\left(\frac{x}{t}\right) = u_{k,L} + \frac{\frac{x}{t} - \lambda_{k,L}}{\lambda_{k,R} - \lambda_{k,L}}(u_{k,R} - u_{k,L}). \quad (7.13)$$

The limiting velocity is defined by

$$\lambda_{k,L} = \tilde{\lambda}_k - \delta_k, \quad \text{and} \quad \lambda_{k,R} = \tilde{\lambda}_k + \delta_k, \quad (7.14)$$

with  $\delta_k = \max[0, \tilde{\lambda}_k - \lambda_k(u_L), \lambda_k(u_R) - \tilde{\lambda}_k]$ .

This linear expression results in the following expression of  $q(\tilde{\lambda}_k)$ :

$$q^{\text{HH2}}(\tilde{\lambda}_k) = \begin{cases} \frac{1}{2} \left( \frac{\tilde{\lambda}_k^2}{\delta_k} + \delta_k \right) & \text{if } |\tilde{\lambda}_k| < \delta_k, \\ |\tilde{\lambda}_k| & \text{if } |\tilde{\lambda}_k| \geq \delta_k. \end{cases} \quad (7.15)$$

For  $|\tilde{\lambda}_k| < \delta_k$ , the function  $|\tilde{\lambda}_k|$  is replaced by a parabolic function with vertex in  $(0, \delta_k/2)$ , as seen in Figure 7.1.

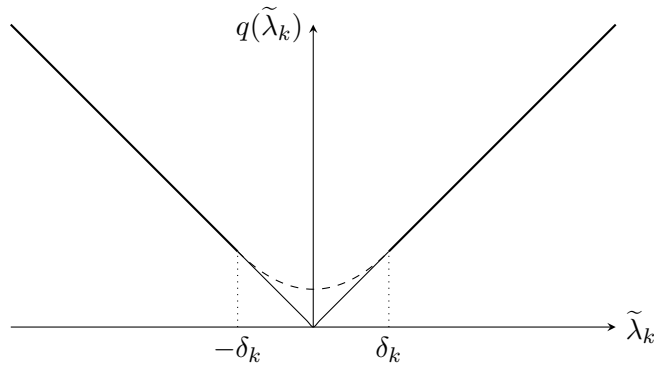


**Figure 7.1:** *Second entropy fix of Harten and Hyman [HH83]*

## 7.2 One-Step Monotonicity Preserving (OSMP) scheme

The Godunov solver and the approximate Riemann solver of Roe described previously are only first-order accurate in time and space. In the vicinity of a large gradient, they produce numerical viscosity that smoothes the solution. The objective of this section is to increase the order of accuracy of the basic numerical scheme. In order to satisfy conditions of the Lax-Wendroff theorem described in § 6.1 and obtain convergent entropy-satisfying solution, a specific attention have to be brought to the oscillation phenomena near the discontinuities.

There are two classical approaches to obtain non-oscillatory high-order numerical schemes we call the TVD approach and the ENO/WENO approach. The class of *essentially non-oscillatory* (ENO) methods initially developed in [HO87] consists in reconstructing a non-oscillatory global piecewise approximation with high-order polynomials to interpolate values at the intersection of two cells. The reconstruction without spurious oscillation is made on adapted support that avoids discontinuities. Based on the ENO methods, *weighted ENO* (WENO) methods have been developed, which combine the results on all the possible stencils with a weight associated with each of them rather than choosing only one. The smoother approximations will then receive greater weight [LOC94]. Multiple formulations derived from the WENO scheme are also available in the literature (with schemes like WENO-Z [CCD11], TENO, [FHA16], embedded WENO [vtI17]...) in order to reduce numerical dissipation of such scheme. Hybrid methods are also developed in order to reconstruct interpolation function as in Boundary Variation Diminishing (BVD) reconstruction [DXL<sup>+</sup>18] with the selection of the most appropriate reconstruction operator from different possibilities, including hyperbolic tangent function and piecewise polynomials.

In this work, we choose to use the One-Step Monotonicity Preserving (OSMP) scheme presents in the MR\_CHORUS solver. It is a high-order numerical scheme with flux limiter based on the work of Daru and Tenaud [DT04]. This solution uses a one-step approach with high-order accuracy in time and space with very low numerical dissipation allowing to capture efficiently hydrodynamic instabilities as illustrated in § 10.3. Moreover, this numerical scheme is less CPU time consuming than multistage schemes like the WENO scheme needing multi-stage Runge-Kutta time integration to increase the order of accuracy in time.

### 7.2.1 Space-time discretization: Lax-Wendroff approach

We first consider scalar transport equation:

$$\frac{\partial u}{\partial t} + \frac{\partial f(u)}{\partial x} = 0. \quad (7.16)$$

A one-step finite volume scheme reads:



$$u_j^{n+1} = u_j^n - \frac{\Delta t}{\Delta x} (F_{j+1/2} - F_{j-1/2}). \quad (7.17)$$

It is possible to increase the order of accuracy simultaneously in time and space using for example the Lax-Wendroff scheme [LeV02] based on the Taylor series expansion.

$$u(x, t_{n+1}) = u(x, t_n) + \Delta t u_t(x, t_n) + \frac{1}{2} \Delta t^2 u_{tt}(x, t_n) + \mathcal{O}(\Delta t^3). \quad (7.18)$$

Using the conservation law, as  $x, t$  are independent variables, we have:

$$\begin{cases} u_t &= -f_x, \\ u_{tt} &= -(f_x)_t = -(f_t)_x = -(au_t)_x = (af_x)_x, \\ u_{ttt} &= (a(u)f_x)_{xt} = (a_t f_x + a f_{xt})_x, \\ &= (a_t f_x - a(a f_x)_x)_x, \\ &= ((a_t + a a_x) f_x - (a^2 f_x)_x)_x, \\ &= -(a^3 u_x)_{xx}. \end{cases} \quad (7.19)$$

where  $a(u) = df/du$  is the Jacobian of the flux. Similarly, for the general case, the  $m$ -th time derivative correspond to:

$$u_{mt} = ((-a)^m u_x)_{(m-1)x}. \quad (7.20)$$

With discretization of the derivatives with central finite difference approximations, we obtain the second order in time and space Lax-Wendroff numerical scheme:

$$u_j^{n+1} = u_j^n - \frac{\Delta t}{2\Delta x} (f_{i+1}^n - f_{i-1}^n) + \frac{1}{2} \left( \frac{\Delta t}{\Delta x} \right)^2 (a_{j+1/2}^n (f_{j+1}^n - f_j^n) - a_{j-1/2}^n (f_j^n - f_{j-1}^n)). \quad (7.21)$$

The Lax-Wendroff numerical flux is then written:

$$F_{j+1/2}^{lw} = f_j^n + \frac{(1-\nu)_{j+1/2}}{2} (f_{j+1}^n - f_j^n), \quad (7.22)$$

with  $\nu = a \frac{\Delta t}{\Delta x}$  the CFL number. This flux is written for the case where  $a(u) > 0$ , but can be generalized to the negative case by symmetry of the dimensional indices with reference to the interface  $(i + 1/2)$ .

Lax Wendroff's approach can be extended further to increase the order in a space and time coupled manner. Following the relation (7.20) a linear advection equation of the third-order accuracy scheme in time and space is:

$$F_{j+1/2}^3 = F_{j+1/2}^{lw} - \left( \frac{(1-\nu^2)_{j+1/2}}{6} (f_{j+1}^n - f_j^n) - \frac{(1-\nu^2)_{j-1/2}}{6} (f_j^n - f_{j-1}^n) \right). \quad (7.23)$$

The numerical flux can be recast in the following form:

$$F_{j+1/2}^3 = f_j^n + \Phi_{j+1/2}^3 \frac{(1-\nu)_{j+1/2}}{2} (f_{j+1}^n - f_j^n), \quad (7.24)$$

with

$$\Phi_{j+1/2}^3 = 1 - \frac{1}{3} \frac{(1 + \nu^2)_{j+1/2} - (1 - \nu^2)_{j-1/2} r_{j+1/2}}{(1 - \nu)_{j+1/2}}, \quad (7.25)$$

where  $r_{j+1/2}$  is the ratio of consecutive gradients:

$$r_{j+\frac{1}{2}} = \frac{f_j^n - f_{j-1}^n}{f_{j+1}^n - f_j^n}. \quad (7.26)$$

Following successive corrections of the higher order error terms, a relation of recurrence can be established to construct schemes of arbitrarily high  $p$ -th order of accuracy, whose numerical flux can be written in the generic form:

$$F_{j+1/2}^{p+1} = F_{j+1/2}^p + \theta_{p+1} \sum_{l=0}^p (-1)^l C_p^l f_{j+m-l}^n, \quad (7.27)$$

where  $m = \lfloor \frac{(p-1)}{2} \rfloor$  ( $\lfloor \cdot \rfloor$  is the integer division symbol),  $C_r^l = \frac{r!}{(r-s)!s!}$ , and:

$$\theta_l = \prod_{k=2}^l (-1)^k \frac{\lfloor k/2 \rfloor - (-1)^k \nu}{k}. \quad (7.28)$$

All those schemes are stable with the CFL condition  $\nu \leq 1$ . As previously we can write the  $p$ -th flux order using an accuracy function  $\Phi_{j+1/2}^p$  with the formalism:

$$F_{j+1/2}^{p+1} = f_j^n + \Phi_{j+1/2}^p \frac{(1 - \nu)_{j+1/2}}{2} (f_{j+1}^n - f_j^n). \quad (7.29)$$

Expression of the corresponding accuracy function until the seventh order expressed with the ratio of consecutive gradients  $r_{j+1/2}$  can be found in [DT04].

In the case of the Euler equations, the linearization of the jacobian matrix  $\tilde{\mathbf{A}}_{j+1/2}$  (7.3) allows to transform the initial equation into characteristic form (19) corresponding to a combination of advection equations applied to the characteristic variables  $\tilde{\alpha}_k$  associated to eigenvalues  $\tilde{\lambda}_k$ . Using the Lax-Wendroff approach on these advection equations with attention to the sign of the eigenvalues, the one-step numerical flux with  $p$ -th order of accuracy in time and space is given by:

$$\tilde{\mathbf{f}}_{j+1/2}^E = \tilde{\mathbf{f}}_{j+1/2}^{\text{Roe}} + \frac{1}{2} \sum_{k=1}^N \left( \Phi_k^p (1 - |\nu_k|) |\tilde{\lambda}_k| \tilde{\alpha}_k \tilde{\mathbf{K}}^{(k)} \right)_{j+1/2}, \quad (7.30)$$

with  $\nu_k = \tilde{\lambda}_k \Delta t / \Delta x$ .

## 7.2.2 TVD and MP schemes

However, numerical schemes with order higher than one, such as the Lax-Wendroff method, generally produce spurious (unphysical) oscillations, called the Gibbs phenomenon, especially in the vicinity of large gradients. In this case, hypothesis of the Lax theorem [LW60] described in § 6.1 are not completed and finite volume scheme is no longer ensured to converge towards the weak solution.

A property of the entropy-satisfying weak solution of a conservation law is the monotonicity preserving across time. If we consider two sets of initial data  $u_0$  and  $v_0$  with  $v_0(x) \geq u_0(x)$  for all  $x \in \mathbb{R}$  then the respective entropy solution  $u(x, t)$  and  $v(x, t)$  satisfy:

$$v(x, t) \geq u(x, t), \quad x \in \mathbb{R}, \quad t \in \mathbb{R}^+. \quad (7.31)$$

A numerical method  $U_j^{n+1} = \mathcal{H}(u^n, j)$  is called a *monotone method* if the analogous discrete property holds:

$$V_j^n \geq U_j^n \quad \forall j \quad \Rightarrow \quad V_j^{n+1} \geq U_j^{n+1} \quad \forall j. \quad (7.32)$$

Such a monotone method guarantees non-physical oscillations close to the discontinuities. However, a monotone method is proved to be at most first-order accurate [HHLK76].

A numerical method computed with a consistent monotone method with  $\Delta t/\Delta x$  fixed then converges to the entropy solution as the grid is refined.

### Total Variation Diminishing property

The exact solution of the local Riemann problem for non-linear scalar conservation law when the initial data  $u(x, 0)$  has bounded total variation, is that

- No new local extrema in  $x$  may be created,
- Value of a local minimum increases and value of a local maximum decreases.

So the total variation  $TV(u(t))$  is a decreasing function of time

A numerical scheme is said to be Total Variation Diminishing (TVD) if:

$$TV(u^{n+1}) \leq TV(u^n), \quad \forall n. \quad (7.33)$$

Any TVD method is monotonicity preserving.

Moreover, in the case of non-linear schemes with a conservative form as:

$$u_i^{n+1} = u_i^n - C_{i-\frac{1}{2}} \Delta u_{i-\frac{1}{2}} + D_{i+\frac{1}{2}} \Delta u_{i+\frac{1}{2}}, \quad (7.34)$$

where  $\Delta u_{i+\frac{1}{2}} = u_{i+1} - u_i$  and  $C_{i-\frac{1}{2}}, D_{i+\frac{1}{2}}$  are coefficients of the scheme.

Harten [Har83] proved that a sufficient condition for the scheme to be TVD is that the coefficients satisfy:

$$\begin{cases} C_{i+\frac{1}{2}} \geq 0, \\ D_{i+\frac{1}{2}} \geq 0, \\ 0 \leq C_{i+\frac{1}{2}} + D_{i+\frac{1}{2}} \leq 1. \end{cases} \quad (7.35)$$

A way to obtain high-resolution methods is then to combine high-order numerical methods where it is possible and conserve monotonicity solutions with low order methods close to discontinuities. The selection is then done using flux limiter method.

### Flux limiter

The objective of the flux limiter method is to hybridize low-order numerical flux and high-order numerical flux according to the TVD condition. In order to keep a TVD scheme with high order simulation and then guarantee convergence of the scheme to a weak solution, we start applying a high-order numerical scheme and locally reduced the order in regions with production of spurious oscillations. We called  $F_H(U)$  the high order flux we must consider in the smooth regions and  $F_L(U)$  the low order flux that behaves well near discontinuities. We built a TVD flux  $F^{TVD}(U)$  with:

$$F^{TVD}(U) = F_L(U) + (1 - \phi(U))[F_H(U) - F_L(U)], \quad (7.36)$$

where  $\phi(U)$  is called the flux limiter,  $\phi(U) \in [0, 1]$ . Integration scheme in the cell  $j$  becomes:

$$U_j^{n+1} = U_j^n + \frac{\Delta t}{\Delta x} (F_{j+1/2}^{TVD}(U) - F_{j-1/2}^{TVD}(U)). \quad (7.37)$$

The one-step  $p$ -th order numerical flux (7.29) can be written in the format of (7.34) with the coefficient  $C_{j-1/2}$  and  $D_{j+1/2}$  corresponding to (for  $a(u) > 0$ ):

$$\begin{aligned} C_{j-1/2} &= \nu_{j-1/2} \left( 1 - \frac{1}{2}(1 - \nu)_{j-1/2} \right) \Phi_{j-1/2}^p, \\ D_{j+1/2} &= -\frac{1}{2} \nu_{j+1/2} \left( 1 - \nu_{j+1/2} \right) \Phi_{j+1/2}^p. \end{aligned} \quad (7.38)$$

Using the criteria developed by Harten (7.35) to guarantee TVD properties of the numerical scheme, we obtain:

$$\begin{cases} 0 \leq \Phi_{j+1/2}^{p-TVD} \leq \frac{2}{1 - \nu_{j+1/2}}, \\ 0 \leq \Phi_{j+1/2}^{p-TVD} \leq \frac{2r_{j+1/2}}{\nu_{j+1/2}} \frac{1 - \nu_{j-1/2}}{1 - \nu_{j+1/2}}. \end{cases} \quad (7.39)$$

Then we obtain a region for the TVD scheme in the  $r - \phi$  plane called the Sweby region [Swe84] illustrated in Figure 7.2. Moreover, for any accurate second-order method, we must have  $\phi = 1$  for  $r = 1$ , and Sweby found that it is best to take  $\phi$  as a convex combination of  $\phi = 1$  (Lax-Wendroff method) and  $\phi = r$  (Beam-Warming method) which define the second-order TVD region.

Several limiters have been developed to impose limiter function and avoid spurious oscillation while conserving solutions in the TVD regions.

$$\begin{aligned} \text{minmod:} \quad & \phi(r) = \text{minmod}(1, r), \\ \text{Superbee:} \quad & \phi(r) = \max(0, \min(1, 2r), \min(2, r)), \\ \text{van Leer:} \quad & \phi(r) = \frac{r + |r|}{1 + |r|}. \end{aligned} \quad (7.40)$$

We choose to use here the suberbee limiter of Roe [Roe85] taking the upper boundary for  $\phi_{j+1/2}^{TVD}$ :

$$\Phi_{j+1/2}^{p-TVD} = \max \left( 0, \min \left( \frac{2}{1 - |\nu_{j+1/2}|}, \Phi_{j+1/2}^p, 2 \frac{r_{j+1/2}}{|\nu_{j+1/2}|} \frac{1 - |\nu_{j-1/2}|}{1 - |\nu_{j+1/2}|} \right) \right). \quad (7.41)$$

### Monotonicity Preserving (MP) condition

TVD flux limiter allows avoiding spurious oscillations with a high-order numerical scheme. However, these schemes may clip extrema of the solution. Indeed, evaluated with only two points, the TVD flux limiter cannot differentiate an extremum from a discontinuity.

The TVD conditions described in 7.39 can be interpreted as a geometrical restriction for a flux with the form:

$$F_{j+1/2} = f_j^n + \Phi_{j+1/2}^{p-TVD} \frac{(1 - \nu)}{2} (f_{j+1}^n - f_j^n). \quad (7.42)$$

The first TVD constraint geometrically means the numerical flux  $F_{j+1/2}$  must belong to the interval  $[f_j^n, f_{j+1}^n]$  and the second TVD constraint means that the numerical flux  $F_{j+1/2}$  must belong to the interval  $[f_j^n, f_j^{ul}]$  where:

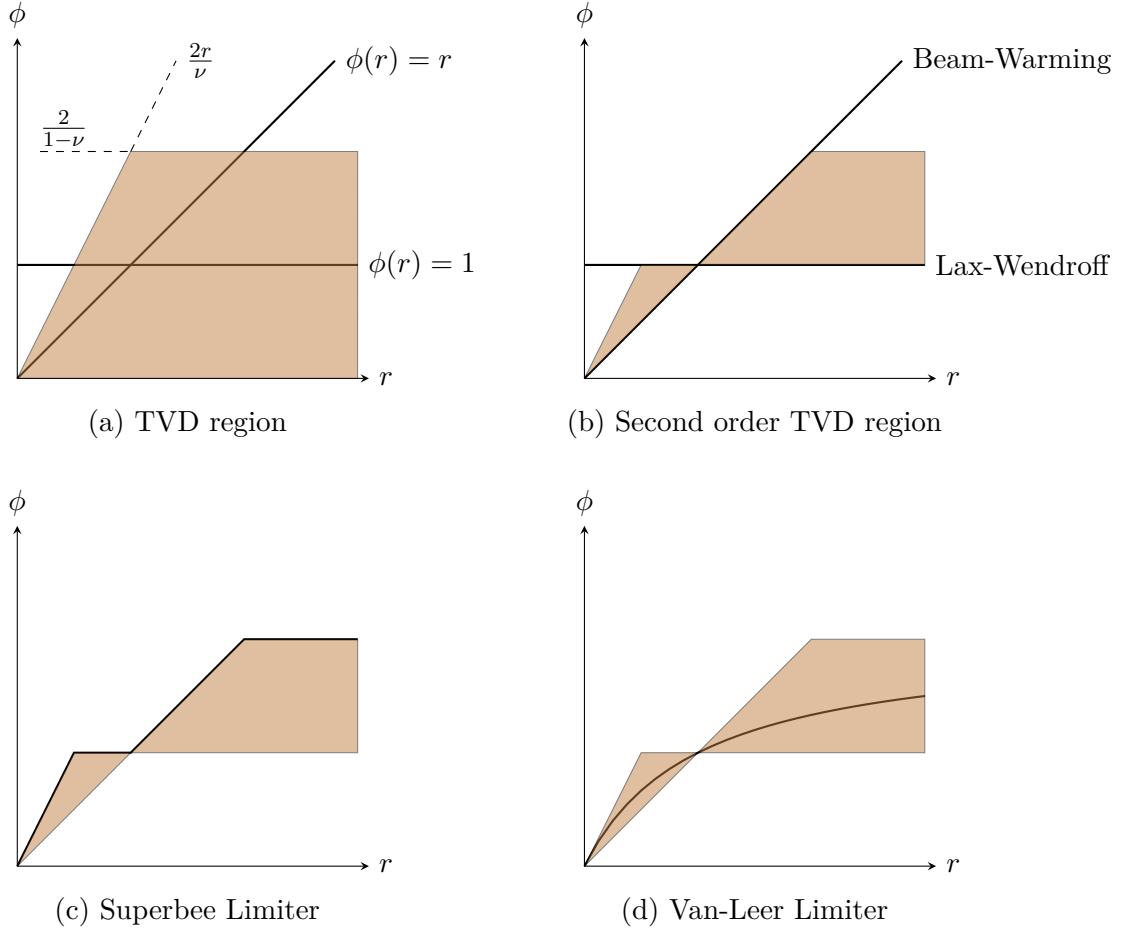


**Figure 7.2:** Sweby region in shaded region with flux limiter  $\phi(r)$ . Regions in which function values  $\phi(r)$  must lie in order to give TVD (a) and second-order TVD (b) methods. Two possible limiter functions: Roe's superbee (c) and van Leer's (d) limiter.

$$f_j^{\text{ul}} = f_j^n + \frac{1-\nu}{\nu}(f_j^n - f_{j-1}^n). \quad (7.43)$$

To avoid the loss of accuracy near extrema, Suresh and Huynh [SH97] has developed an improved flux limiter by introducing an approximation of the curvature of the solution at the intersection  $j + 1/2$  with:

$$d_{j+1/2} = \text{minmod}(d_j, d_{j+1}) \quad \text{with} \quad d_j = f_{j+1}^n - 2f_j^n + f_{j-1}^n. \quad (7.44)$$

From a geometric point of view, it consists in enlarging the previous intervals. In the following, we note  $[f^1, f^2, \dots, f^k]$  the interval  $[\min(f^1, f^2, \dots, f^k), \max(f^1, f^2, \dots, f^k)]$ .

The first interval  $[f_j^n, f_{j+1}^n]$  is enlarged to  $[f_j^n, f_{j+1}^n, f_j^{\text{md}}]$  (MD stands for median), with:

$$f_j^{\text{md}} = \frac{1}{2}(f_j^n + f_{j+1}^n) - \frac{1}{2}d_{j+1/2}, \quad (7.45)$$

and the second interval  $[f_j^n, f_j^{\text{ul}}]$  is enlarged to  $[f_j^n, f_j^{\text{ul}}, f_j^{\text{lc}}]$  (LC stands for large curvature and UL for upper limit), with

$$f_j^{\text{lc}} = f_j^n + \frac{1}{2} \left( 1 + \frac{d_{j-1/2}}{f_j^n - f_{j-1}^n} \right) (f_j^{\text{ul}} - f_j^n). \quad (7.46)$$

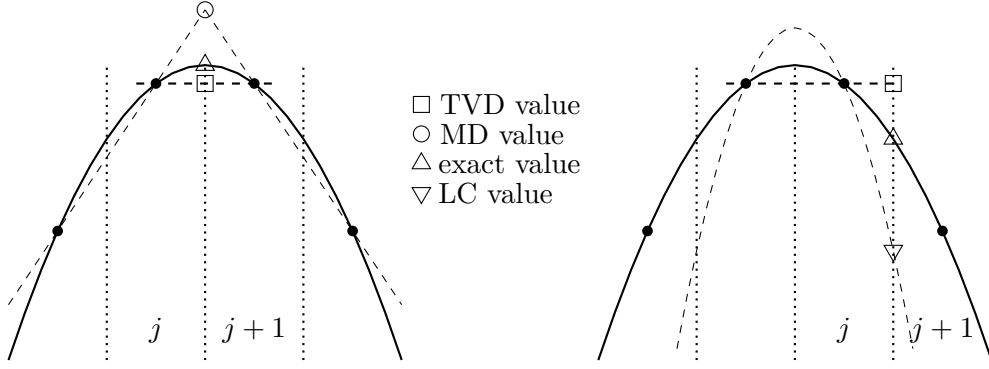


**Figure 7.3:** Reconstruction in the vicinity of an extremum. The TVD constraints alone clip the extremum (left) and identify a discontinuity (right), while the MP condition allows extending the flux limiting interval and including exact values.

These new intervals  $[f_j^n, f_{j+1}^n, f_j^{\text{md}}]$  and  $[f_j^n, f_j^{\text{ul}}, f_j^{\text{lc}}]$  allow to differentiate extremum from discontinuities and include the exact values of the flux around the extremum as illustrated in Figure 7.3.

Express this condition with constraints on  $\Phi^{MP}$  is equivalent to have:

$$\begin{cases} \min\left(0, \Phi_{j+1/2}^{\text{md}}\right) \leq \Phi_{j+1/2}^{p-MP} \leq \max\left(\frac{1}{1-\nu_{j+1/2}}, \Phi_{j+1/2}^{\text{md}}\right), \\ \min\left(0, \frac{2r_{j+1/2}}{\nu_{j+1/2}} \frac{1-\nu_{j-1/2}}{1-\nu_{j+1/2}}, \Phi_{j+1/2}^{\text{lc}}\right) \leq \Phi_{j+1/2}^{p-MP} \leq \max\left(0, \frac{2r_{j+1/2}}{\nu_{j+1/2}} \frac{1-\nu_{j-1/2}}{1-\nu_{j+1/2}}, \Phi_{j+1/2}^{\text{lc}}\right). \end{cases} \quad (7.47)$$

with

$$\Phi_{j+1/2}^{\text{md}} = \left(\frac{2}{1-\nu_{j+1/2}}\right) \frac{f_j^{\text{md}} - f_j^n}{f_{j+1}^n - f_j^n} \quad \text{and} \quad \Phi_{j+1/2}^{\text{lc}} = \left(\frac{2r_{j+1/2}}{\nu_{j+1/2}} \frac{1-\nu_{j-1/2}}{1-\nu_{j+1/2}}\right) \frac{f_j^{\text{lc}} - f_j^n}{f_j^{\text{ul}} - f_j^n}. \quad (7.48)$$

Finally, the MP constraint which preserves accuracy is computed with

$$\Phi_{j+1/2}^{p,MP} = \max\left(\Phi_{j+1/2}^{\min}, \min\left(\Phi_{j+1/2}^p, \Phi_{j+1/2}^{\max}\right)\right), \quad (7.49)$$

where

$$\Phi_{j+1/2}^{\min} = \max\left(\min\left(0, \Phi_{j+1/2}^{\text{md}}\right), \min\left(0, \frac{2r_{j+1/2}}{\nu_{j+1/2}} \frac{1-\nu_{j-1/2}}{1-\nu_{j+1/2}}, \Phi_{j+1/2}^{\text{lc}}\right)\right), \quad (7.50)$$

and

$$\Phi_{j+1/2}^{\max} = \min\left(\max\left(\frac{2}{1-\nu_{j+1/2}}, \Phi_{j+1/2}^{\text{md}}\right), \max\left(0, \frac{2r_{j+1/2}}{\nu_{j+1/2}} \frac{1-\nu_{j-1/2}}{1-\nu_{j+1/2}}, \Phi_{j+1/2}^{\text{lc}}\right)\right). \quad (7.51)$$

Finally, associating the equation (7.30) with the monotonicity preserving flux limiter, the OSMP flux at the  $p$ -th order corresponds to:

$$\tilde{\mathbf{f}}_{j+1/2}^E = \frac{1}{2} (\mathbf{f}_{j+1}^E + \mathbf{f}_j^E) - \frac{1}{2} \sum_{k=1}^N \left(\tilde{\alpha}_k^{M-P} \left|\tilde{\lambda}_k\right| \cdot \tilde{\mathbf{K}}^{(k)}\right)_{j+1/2}, \quad (7.52)$$

where  $\tilde{\alpha}_k^{M-P}$  are functions associated with flux limiter MP:

$$\tilde{\alpha}_k^{M-P} = \left[ \left( 1 - \phi_k^{p_{M-P}} (1 - |\nu_k|) \right) \tilde{\alpha}_k \right]_{j+1/2}, \quad k \in [1, N]. \quad (7.53)$$

### 7.3 Conclusion

This chapter presented the construction of the OSMP solver for monocomponent ideal gas. This scheme was implemented in this configuration in the initial MR\_CHORUS solver. It is based on the approximated Riemann Roe solver. A Lax-Wendroff procedure allows increasing the order of the simulation. In order to avoid spurious oscillation in the vicinity of discontinuities and guarantee the convergence to the entropic solution, a Monotonicity Preserving (MP) flux limiter constrained the value of the reconstructed flux. This MP flux limiter is based on the classical TVD limiter with some improvement using the reconstructed curvature of the solution to differentiate a local extremum from a discontinuity.

We usually consider the seventh order of accuracy OSMP7 scheme in our simulation. According to numerical test cases with the advection of a strong vortex realized in [TRB15], OSMP7 recovers a fifth-order of accuracy in the  $L_1$  norm, with small order reduction induced by linearization error of the flux reconstruction and a magnitude error much lower than the one recovered by the MPWENO. Test cases presented in Chapter 8 and 10 confirm the performance of this solver to capture hydrodynamic instability with minimum diffusion.

In order to apply this scheme using a more complex thermodynamic model as required by the computation of reactive mixtures, some adaptation of the Roe and the OSMP solvers have to be made. This extension to general convex equation of state is the purpose of the following chapter.

## Extension of the OSMP scheme to mixture of gases with convex equation of state

In the previous chapter, Riemann solvers and high-resolution methods described like the OSMP solver are built for perfect polytropic gas. As discussed in 5.2 we consider here gases at Local Thermodynamic Equilibrium, and we supposed that the equation of state is convex to be able to solve the Riemann problem with the classical three-waves model described in Appendix A.2.2. With these assumptions, several generalizations of the Roe approximate Riemann solver have been proposed in cases with mono-component real gases [Abg91, Gla88, VM90, LLS90, CC94, ATC17]. Difficulties usually encountered in developing such generalizations come from the non-uniqueness of the Roe averaged state at the interface between right and left states of the Riemann problem when applied to a non-ideal gas or a non-perfect equation of state. Indeed, the Roe averaged state requires additional approximations for the compressibility factors, which are pressure derivatives with respect to the independent variables (the density and the internal energy, for instance). Several methods to approximate those pressure derivatives have already been formulated in the literature. A solution proposed in [Gla88] consists in considering arithmetic averages of the pressure derivatives of fictitious intermediary states corresponding to the different possible paths between the left and right states.

Recent methods of generalization of the Roe solver to real gases are based on the projection of approximated pressure derivatives onto a subspace defined by the jump relationships across the interface [VM90, LLS90, CC94]. A Roe averaged speed of sound is then deduced from the Roe average of pressure derivatives. Mottura et al. [MVZ97] have evaluated such methods and concluded that similar results with the different methods are obtained with, however, a better numerical efficiency with the methods proposed by Vinokur & Montagné [VM90] and Liou, Van Leer and Shuen [LLS90]. More recently, contrary to the usual strategy, Arabi et al. [ATC17] proposed to first approximate the speed of sound before computing interface averages of the corresponding compressibility factors. Later on, Arabi et al. [ATC19] extended the proposed Roe scheme for multi-component real gas flows by treating the mixture as a single equilibrium gas to define the contact discontinuity and thus the density jump. Knowing that the mass fractions are constant on both sides of the contact discontinuity, the jump of the partial convective masses can be calculated using the classical resolution of a Riemann problem. The advantage of this formulation is to guarantee the positivity of the mass fractions, but the mass flux computation is only first-order accurate. Extension to a higher-order numerical scheme with quadratic reconstruction or MUSCL scheme [Lar91] are evoked, but the successive Roe average states can then become inconsistent with the thermodynamic properties evolution on a large stencil, and the sum of mass fractions can differ from unity when using more than two species. Besides, a solution to compute a real gas mixture with two distinct species was also proposed in [Abg96] with an extension to high-order approximations. Nevertheless, this is only applicable to mixtures with only two distinct species.



We here follow the strategy introduced by Vinokur and Montagné [VM90] to evaluate a Roe averaged value of compressibility factors in a non-thermally perfect single gas. We first propose extending this technique to multi-component real gas flows based on a similar prediction from an integration between the left and the right states of the Riemann problem, followed by an orthogonal projection onto a well-chosen subspace. It allows us to define an accurate Roe averaged value of the speed of sound. We secondly introduce the proposed averaged state of the compressibility factors into the One-Step Monotonicity-Preserving (OSMP) scheme to obtain an extension towards real gas flows. However, numerical artifacts appear in the vicinity of contact discontinuity (interface between species), and potential low order of convergence is observed in smooth solutions with a large variation of composition and temperature. Those issues come from the proposed compressibility factor averaged states of the Riemann problem that do not seem consistent over the large stencil when using a high-order scheme. By analyzing Riemann invariants, we propose a reformulation of the discrete total energy flux using a linear combination of Riemann invariants associated with the same characteristic wave to recover high-order accuracy. An additional Monotonicity-Preserving constraint is applied to this linear combination to deal with discontinuities. Knowing the averaged speed of sound evaluated by our proposed extension of the Vinokur and Montagné method [VM90], this new formulation gives an additional relation between compressibility factors that satisfied the jump relationships across the interface between the left and right states of the Riemann problem.

## 8.1 1D Euler equations for mixture with convex equation of state

In this section, we consider the mixture with a convex equation of state, such as described in chapter 5. With such mixture, formulation of the Jacobian matrix of the Euler flux will be modified from 7.1 with the integration of non-constant pressure derivatives.

### 8.1.1 Euler Hyperbolic conservation laws

We consider the Euler part of the Navier Stokes equation introduced in (5.2), the Euler equations form a hyperbolic system of equations:

$$\frac{\partial \mathbf{w}}{\partial t} + \frac{\partial}{\partial x} \mathbf{f}^E(\mathbf{w}) = 0. \quad (8.1)$$

The set of possible states for the conservative vector is by definition:

$$T \geq 0; \quad P \geq 0; \quad 0 \leq Y_i \leq 1; \quad \sum_{i=1}^m Y_i = 1, \quad (8.2)$$

which is a convex open subset of  $\mathbb{R}^N$

With a mixture of  $n_s$  real gases, the Jacobian matrix  $\mathbf{A}(\mathbf{w}) = \frac{\partial \mathbf{f}^E(\mathbf{w})}{\partial \mathbf{w}}$  corresponds to:

$$\mathbf{A}(\mathbf{w}) = \begin{pmatrix} u(1 - Y_1) & -uY_1 & \cdots & -uY_1 & Y_1 & 0 \\ -uY_2 & u(1 - Y_2) & \cdots & -uY_2 & Y_2 & 0 \\ \vdots & \ddots & \ddots & \vdots & \vdots & \vdots \\ \vdots & \ddots & \ddots & -uY_{N-1} & Y_{N-1} & 0 \\ -uY_N & \cdots & \cdots & u(1 - Y_N) & Y_N & 0 \\ \chi_1 + (\frac{1}{2}\kappa - 1)u^2 & \chi_2 + (\frac{1}{2}\kappa - 1)u^2 & \cdots & \chi_N + (\frac{1}{2}\kappa - 1)u^2 & (2 - \kappa)u & \kappa \\ (\chi_1 - H)u + \frac{1}{2}\kappa u^3 & (\chi_2 - H)u + \frac{1}{2}\kappa u^3 & \cdots & (\chi_N - H)u + \frac{1}{2}\kappa u^3 & H - \kappa u^2 & (1 + \kappa)u \end{pmatrix}, \quad (8.3)$$

with the compressibility factors  $\{\kappa, (\chi_i, i = 1, \dots, n_s)\}$  defined in (5.24). It corresponds to the calorifically perfect variant (eq. (7.1)) where  $\kappa = (\gamma - 1)$  and  $\chi_k = 0$ .

The corresponding eigenvectors are given by:

$$\begin{aligned}
\mathbf{K}^{(1)} &= \left[ 1, 0, \dots, \dots, 0, u, \frac{1}{2}u^2 - \frac{\chi_1}{\kappa} \right]^T ; \\
\mathbf{K}^{(i)} &= \left[ 0, \dots, 1, \dots, 0, u, \frac{1}{2}u^2 - \frac{\chi_i}{\kappa} \right]^T ; \\
\mathbf{K}^{(n_s)} &= \left[ 0, \dots, \dots, 0, 1, u, \frac{1}{2}u^2 - \frac{\chi_{n_s}}{\kappa} \right]^T ; \\
\mathbf{K}^{(N-1)} &= [Y_1, \dots, Y_i, \dots, Y_{n_s}, u + c_s, H + uc_s]^T ; \\
\mathbf{K}^{(N)} &= [Y_1, \dots, Y_i, \dots, Y_{n_s}, u - c_s, H - uc_s]^T ;
\end{aligned} \tag{8.4}$$

and the eigenvalues are  $(u, \dots, u, u + c_s, u - c_s)$ .

According to the general description of the equation of state in § 5.2, thermodynamic stability requires that  $\gamma > 0$  and thus  $c_s$  is a real number. With this property, the Euler equations are always a hyperbolic equation system.

Moreover, according to Bethe [Bet42], if the fundamental derivative is positive  $\mathcal{G} > 0$ , the eigenvalues  $u \pm c_s$  does not vanish and the characteristic field are GNL (see A.1.3). The theorem of Bethe also demonstrated that a sufficient condition for adiabatic compression shocks to be entropy increasing is to have  $\Gamma > -2$  when the EOS obeyed the convexity constraint.

In the case of a mixture of ideal gases with temperature-dependent heat capacities, we have seen in 5.2.2 that the polynomials used to describe the relationship between the heat capacities and the temperature allows keeping the sound speed as a non-decreasing function of the temperature. The convexity of the Euler equations then allows having a classic resolution of the Riemann problem with distinct characteristic waves.

## 8.2 Approximate Riemann solver of Roe for mixture of gases with convex equation of state

We want to apply the Roe solver presented in 7.1 based on a constant approximation of the Jacobian matrix 8.3 express at the Roe averaged state. However, this Roe average matrix then involves expressions of the compressibility factors  $\{\kappa, (\chi_i, i = 1, \dots, n_s)\}$  that must be evaluated at the Roe average state.

Combining the property (3) of the Roe solver and identities (7.10) of the Roe average operator, a new relationship between the variation of conservative variables and the compressibility factors is established:

$$\Delta p = \sum_{i=1}^{n_s} \tilde{\chi}_i \Delta \rho_i + \tilde{\kappa} \Delta \epsilon. \tag{8.5}$$

We extend the procedure introduced by Montagné et al. [MYV89] and Liou et al. [LLS90] to the case of multi-component real gas flow. It consists of a first prediction of the values of the compressibility factors by using the left and right thermodynamic states. Then correct these predictions by the projection of the predictions onto the  $(n_s - 1)$  hyperplane defined by the relationship (8.5).

Following Vinokur and Montagné, the prediction  $(\hat{\chi}_i, \hat{\kappa})$  of the compressibility factors is fulfilled by integrating themselves along a straight line path between the two left and right thermodynamic states:

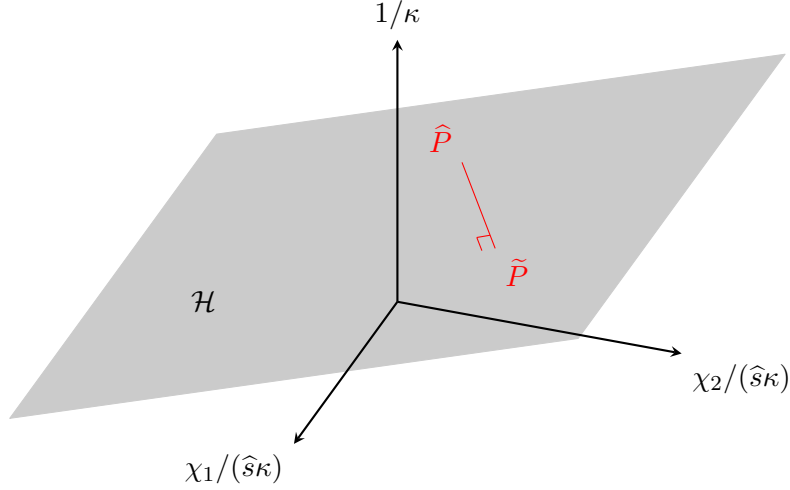


**Figure 8.1:** Illustration with 2 species of the projection  $\tilde{P}$  of the first approximation  $\hat{P}$  on the hyperplane  $\mathcal{H}$  defined by (8.5)

$$\hat{\chi}_i = \int_0^1 \chi_i[\epsilon(\zeta), \rho_1(\zeta), \dots, \rho_{n_s}(\zeta)] d\zeta, \quad (8.6a)$$

$$\hat{\kappa} = \int_0^1 \kappa[\epsilon(\zeta), \rho_1(\zeta), \dots, \rho_{n_s}(\zeta)] d\zeta, \quad (8.6b)$$

where the parameter  $\zeta$  is normalized to have  $\zeta_L = 0$  for the left state and  $\zeta_R = 1$  for the right state. The straight-line path is defined with:

$$\rho_i(\zeta) = \rho_{i,L} + \zeta \Delta\rho_i, \quad i = 1, \dots, n_s; \quad (8.7a)$$

$$\epsilon(\zeta) = \epsilon_L + \zeta \Delta\epsilon. \quad (8.7b)$$

Depending on the gap magnitude between the left and right states, several approximate quadrature formulae can be used for evaluating integrals. We privileged the Simpson rule here, which is mainly adapted for large variation between two states. For the approximation of  $\kappa$ , this gives:

$$\hat{\kappa} = \frac{1}{6} (\kappa_L + 4\kappa(\epsilon_M, \rho_{1,M}, \dots, \rho_{n_s,M}) + \kappa_R), \quad (8.8)$$

with  $\epsilon_M = \frac{1}{2}(\epsilon_L + \epsilon_R)$  and  $\rho_{i,M} = \frac{1}{2}(\rho_{i,L} + \rho_{i,R})$ . The value of  $\kappa(\epsilon_M, \rho_{i,M})$  is computed using the equation of state (5.21) and the definition of the pressure derivative  $\kappa$  (5.24).

Finally, in order to satisfy the properties (3) of the Roe solver, an orthogonal projection is carried out from the predicted values  $\hat{\kappa}$  and  $\hat{\chi}_i, i = 1, \dots, n_s$  on the  $n_s - 1$  hyperplane defined by the equation (8.5). In order to be independent of the arbitrary constant present in the definition of  $\epsilon$  and to be close to a dimensionless orthonormal framework, we perform the orthogonal projection in the following system of coordinates:

$$\left( \frac{1}{\hat{\kappa}}, \left\{ \frac{\chi_i}{\hat{s}\hat{\kappa}}, i = 1, \dots, n_s \right\} \right), \quad (8.9)$$

$\hat{s}$  is a normalization factor with the dimension of  $\chi_i$  chosen as  $\hat{s} = \hat{c}^2 = \sum_{i=1}^{n_s} \chi_i \hat{Y}_i + \hat{\kappa} \hat{h}$ , where the symbol

( $\hat{\cdot}$ ) corresponds in this last expression to the Simpson rule (8.8). The configuration with two species where the hyperplane (8.5) is a 2D plane is illustrated Figure 8.1.

The orthogonal projection in the space of coordinates (8.9) from the predicted values  $\hat{\kappa}$  and  $\hat{\chi}_i, i = 1, \dots, n_s$  on the hyperplane defined by (8.5) gives the following compressibility factors:

$$\tilde{\kappa} = \frac{D\hat{\kappa}}{D - \Delta p \delta p} \quad \tilde{\chi}_i = \frac{D\hat{\chi}_i + \hat{s}^2 \Delta\rho_i \delta p}{D - \Delta p \delta p}, \quad (8.10)$$

with

$$D = \hat{s}^2 \sum_{i=1}^N (\Delta \rho_i^2) + \Delta p^2, \quad (8.11)$$

and the error on pressure ( $\delta p$ ) that, finally by construction, satisfies the precision up to machine accuracy after the projection step:

$$\delta p = \Delta p - \hat{\kappa} \Delta \epsilon - \sum_{i=1}^N \hat{\chi}_i \Delta \rho_i. \quad (8.12)$$

The celerity of sound at the Roe averaged state then becomes:

$$\tilde{c}_s = \sqrt{\sum_{i=1}^{n_s} \tilde{\chi}_i \tilde{Y}_i + \tilde{\kappa} \tilde{h}}. \quad (8.13)$$

This procedure allows us to obtain a combination of the compressibility factors and an approximation of the speed of sound that is coherent with the Roe properties at the intermediate state. The present procedure generalizes the Roe scheme for multi-component gas flow with an arbitrary convex equation of state. We notice that contrary to the case with calorically perfect gases, the solution obtained here is no longer unique. This non-unicity might have a significant impact on the extension at high-order accuracy discussed in the next section.

It can be noted that the existence of  $\tilde{c}_s$  from (8.13) is not guaranteed since nothing prevents the variation of the compressibility factors to avoid negative value of the sum inside the square root. However, this numerical scheme is robust enough in cases studied here with non-calorically perfect gas. Indeed, the Simpson rule accurately estimates the compressibility factors, so their variations are limited during the projection. Moreover, the normalization factor  $\hat{s}$  brings the basis used for the projection (8.9) close to an orthonormal basis which prevents significant variation of one factor compared to the other during the orthogonal projection. The final value for the sound speed is then generally close to the initial left and right values. Some additional constraints may be necessary in very low density cases, but this aspect has not been investigated here.

### 8.3 High-order extension with modification of the total energy flux formulation

We introduced in the previous section a method to compute an averaged state of the compressibility factors that respects the properties of the Jacobian matrix of the Euler flux. This is carried out through an orthogonal projection on the  $n_s - 1$  hyperplane defined by (8.5). However, through the use of several test cases, numerical artifacts close to discontinuities and poor order of convergence may be observed (some examples will be provided in the section devoted to results; see § 8.4).

Indeed, in some configurations, despite the orthogonal projection procedure, an infinite number of solutions respect the Roe solver properties, especially when the dimension of the problem is high with multi-component mixture. Thus, most of the time, the Roe averaged state obtained does not necessarily correspond to a realistic thermodynamic state. This problem does not appear using the first-order scheme, *i.e.* the original Roe scheme, but only occurs with a high-order scheme because of the large extent of the stencil. When a wide stencil is required, the evolution of the averaged compressibility factors become inconsistent with the evolution of the mass fraction. Thus, inaccurate approximation of the compressibility factors at the Roe average state can reduce the effective order of convergence of the scheme around significant variations of composition and/or thermodynamic variables in a smooth solution. In the same way, numerical artifacts are also introduced when significant species variations occur in the vicinity of contact discontinuities.

By analyzing the problem, we found that inconsistency coming from the relationship used to reconstruct the numerical flux related to the total energy (7.4). The ratio of compressibility factors explicitly

appears through a linear combination of the Riemann invariants associated to the same eigenvalue  $u$  attributed to contact waves:

$$\begin{aligned} \Delta F_{\rho E} = \Delta(\rho u H) = & \sum_{i=1}^{n_s} \tilde{\alpha}_i \left( \tilde{E}_c - \frac{\tilde{\chi}_i}{\tilde{\kappa}} \right) |\tilde{u}| + \tilde{\alpha}_{N-1} \left( \tilde{H} + \tilde{u} \tilde{c}_s \right) |\tilde{u} + \tilde{c}_s| \\ & + \tilde{\alpha}_N \left( \tilde{H} - \tilde{u} \tilde{c}_s \right) |\tilde{u} - \tilde{c}_s|. \end{aligned} \quad (8.14)$$

Considering the definition of the speed of sound, given by (8.13), and the relationship (8.5) linking the pressure jump to the density and the internal energy jumps through the compressibility factors, the first term of the total energy flux (8.14), noted  $\tilde{\alpha}_{N+1}$ , can be expressed using variations of several variables:

$$\tilde{\alpha}_{N+1} = \sum_{i=1}^{n_s} \tilde{\alpha}_i \left( \tilde{E}_c - \frac{\tilde{\chi}_i}{\tilde{\kappa}} \right) = \Delta(\rho E) - \tilde{H} \frac{\Delta p}{\tilde{c}_s^2} - \tilde{\rho} \tilde{u} \Delta u, \quad (8.15)$$

Let us note that the proposed term ( $\tilde{\alpha}_{N+1}$ ) follows an advection equation similarly to the classical Riemann invariants ( $\tilde{\alpha}_k$ ,  $k \in [1, N]$ ). This additional advection equation is then solved using a specific accuracy function  $\Phi_{\alpha_{N+1}}^p$  as described in § 7.2. Then, the total energy flux is expressed without being explicitly connected to the independent values of the compressibility factors but only with the value of the sound speed obtained from the combination (8.13). We apply an MP condition on the supplementary accuracy function  $\Phi_{\alpha_{N+1}}^p$  to avoid spurious oscillations. The total energy component of the high-order M-P limited Euler flux then reads:

$$\begin{aligned} \tilde{F}_{\rho E}^{p-MP} = & \frac{1}{2} (F_L(\rho E) + F_R(\rho E)) - \frac{1}{2} \left( \tilde{\alpha}_{N+1}^{M-P} |\tilde{u}| + \tilde{\alpha}_{N-1}^{M-P} (\tilde{H} + \tilde{u} \tilde{c}_s) |\tilde{u} + \tilde{c}_s| + \right. \\ & \left. \tilde{\alpha}_N^{M-P} (\tilde{H} - \tilde{u} \tilde{c}_s) |\tilde{u} - \tilde{c}_s| \right), \end{aligned} \quad (8.16)$$

with  $\tilde{\alpha}_{N-1}$ , and  $\tilde{\alpha}_N$  given by (7.53).

From a mathematical point of view, applying the OSMP scheme on  $\tilde{\alpha}_{N+1}$  independently of the  $n_s$  first  $\tilde{\alpha}_i$  is actually equivalent to define a constraint on the compressibility factors which results in corrected effective values  $\bar{\chi}_i$ ,  $i = 1, \dots, n_s$  and  $\bar{\kappa}$  that are solutions of the set of equations:

$$\begin{cases} \Delta p = \sum_{i=1}^{n_s} \bar{\chi}_{i,j+1/2} \Delta \rho_i + \bar{\kappa}_{j+1/2} \Delta \epsilon, \\ \tilde{c}_{s,j+1/2}^2 = \sum_{i=1}^{n_s} \bar{\chi}_{i,j+1/2} \tilde{Y}_{i,j+1/2} + \bar{\kappa}_{j+1/2} \tilde{h}_{j+1/2}, \\ \tilde{\alpha}_{N+1,j+1/2}^{M-P} = \sum_{i=1}^{n_s} \tilde{\alpha}_{i,j+1/2}^{M-P} \left( \tilde{E}_{c,j+1/2} - \frac{\bar{\chi}_{i,j+1/2}}{\bar{\kappa}_{j+1/2}} \right). \end{cases} \quad (8.17)$$

The first two relationships correspond to the properties that must be preserved to fulfill the jump relationships of the Riemann problem and the definition of the sound speed predicted by our proposed extension of the Vinokur and Montagné algorithm (8.10). The third one corresponds to the relation that must be verified once applied the OSMP scheme on the additional Riemann invariant  $\tilde{\alpha}_{N+1}$ . Since the expression of the flux (8.16) no longer requires explicit values for the compressibility factors, then we simply have to guarantee the existence of the solution.

Equations (8.17) correspond to a linear system with  $n_s + 1$  unknowns and three equations. The existence of a set of compressibility factors consistent with the Roe solver properties and the  $N + 1$  accuracy functions and their associated M-P constraints is then guaranteed. In the case of two species, there is even a unique solution corresponding to the value of the sound speed previously predicted.

Thus, we obtain a stable high-order scheme based on a Roe solver for multi-component real gases that preserves conservation through jump relations and adequately capture discontinuities on the mass fraction of species. An overview of the different steps leading to the final high-order Euler flux is proposed in the following algorithm 8.2.

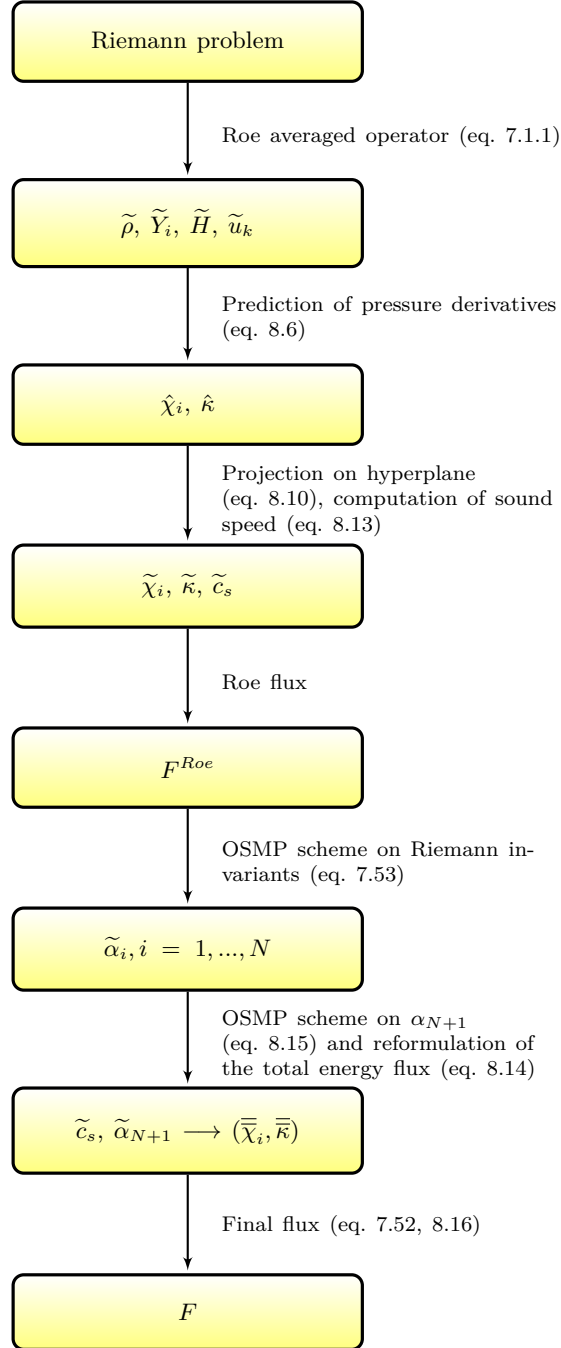


**Figure 8.2:** *Successive steps for building a stable OSMP scheme for multi-component real gas flow*

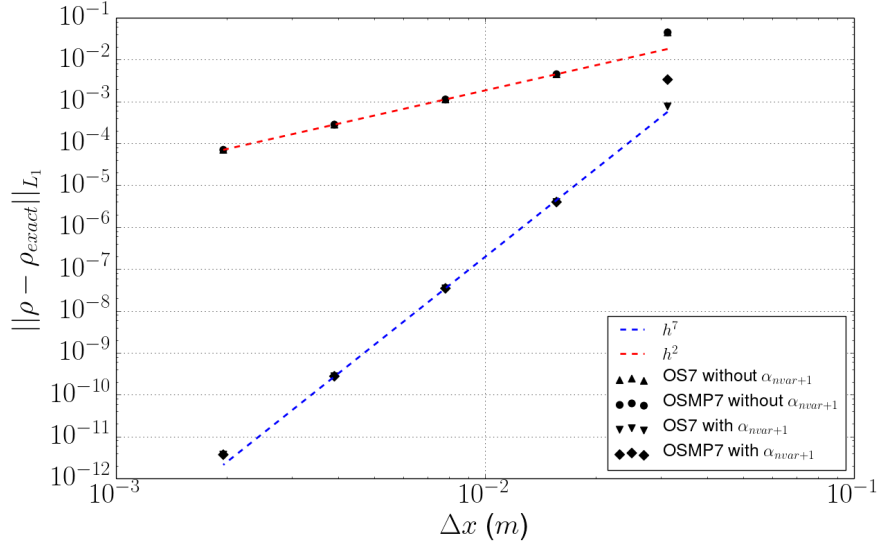


**Figure 8.3:** Convergence curves using the OSMP7 scheme on a advection of mass fraction wave. Comparison with the initial formulation of the total energy flux and the new one with and without M-P limiter flux.

## 8.4 Numerical results

In the following simulations, mixtures of non-calorically perfect gases with temperature-dependant heat capacities are considered.

### 8.4.1 Convection of mass fraction and density waves

This first case performs a grid-convergence analysis. The high-order scheme is applied on a smooth case of convection of mass fraction and density waves in a flow with uniform pressure. This case has previously been treated in [CMRR21]. We consider a mass fraction wave in a flow with uniform velocity  $u_0 = 100$  m/s and pressure  $p_0 = 1$  Bar. The mixture is composed of two gases with specific heat ratio of  $\gamma_1 = 1.6$  and  $\gamma_2 = 1.4$ . The specific isochore heat capacity is set in order to have  $c_{v,1} = 2c_{v,2}$ . The computational domain corresponds to  $\Omega = [0, 1]$  with periodic conditions. The initial mass fraction of the first species and the initial density are:

$$Y_1(x) = \frac{1}{2} + \frac{1}{4} \sin(4\pi x), \quad \rho_0(x) = 1 + \frac{1}{2} \sin(2\pi x) \quad \forall x \in \Omega. \quad (8.18)$$

Computation is performed using the OSMP scheme of 7<sup>th</sup>-order with and without the modification on the discrete total energy flux using the  $\alpha_{N+1}$  term described in (8.15) and (8.16). The exact solution is the passive convection of the waves. Errors in the  $L_1$ -norm relative to the exact solution are reported in Figure 8.3 for the density at  $t = 0.05$  s after five periods of convection.

It is found that in this case, with significant variations in composition and temperature leading to relevant variation of sound speed, the initial estimation of the compressibility factors with the extension of Vinokur and Montagné method described with (8.10) provides a scheme which is only second-order accurate. Their successive values are inadequate with the physical mixture, and pressure variations are generated, impacting the flow velocity and the density profile. The introduction of  $\tilde{\alpha}_{N+1}$  in the first term of the total energy flux (8.14) avoids the influence of the different compressibility factors and allows to recover the seventh-order accuracy of the OSMP scheme. Since computations have been undertaken with both the unlimited OS7 scheme and the Monotonicity Preserving constraint OSMP7 scheme, we could notice that the M-P condition does not influence results in this smooth test case except in low resolution with only 32 grid points by differentiating extrema from discontinuities.

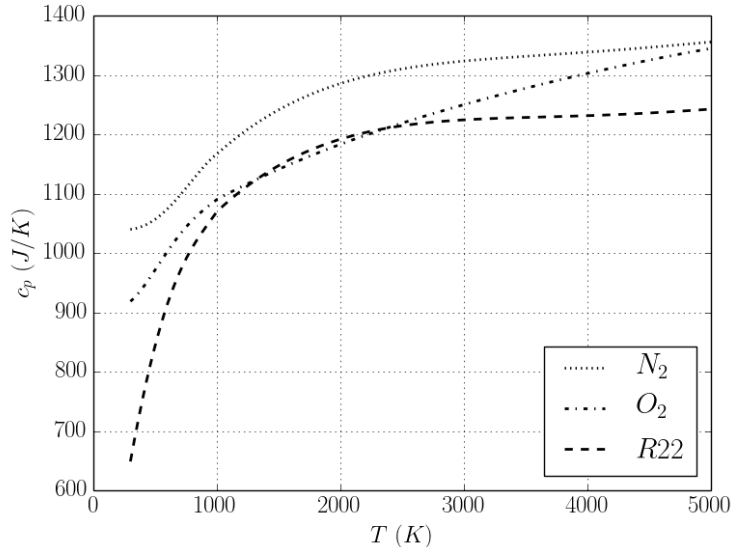


**Figure 8.4:** Distribution versus temperature of heat capacities at constant pressure ( $c_p$ ) following temperature polynomials found in [MZG02] for Nitrogen ( $N_2$ ), Oxygen ( $O_2$ ), and R22.

	Sod shock tube		Lax shock tube	
	Left	Right	Left	Right
$N_2$ (%)	70	20	70	20
$R_{22}$ (%)	20	70	20	70
$O_2$ (%)	10	10	10	10
$P$ (bar)	1	0.1	10	1
$\rho$ (kg/m <sup>3</sup> )	1.	0.125	1.602	1.222
$\gamma$	1.35	1.20	1.26	1.19

**Table 8.1:** Initial condition of pressure, density and species mass fraction for the Sod shock tube (left) and the Lax shock tube (right) problems

### 8.4.2 One-dimensional shock-tube problem

We consider classical cases of shock tube problems corresponding to exact Riemann problems. The tube length is  $L_x = 50$  m, and the computational domain extent is  $x \in [0, L_x]$ . We initially consider two states of different mixtures, separated by a diaphragm located at the middle of the tube ( $x = 25$  m). At the initial time ( $t = 0$ ), the diaphragm is broken. Classically, a shock wave moves towards the low-pressure side while a rarefaction fan goes to the high-pressure side. In between, a contact discontinuity associated with the three species moves at the fluid velocity.

The initial conditions at the left state  $\mathcal{U}_L$  and right state  $\mathcal{U}_R$  are given in table 8.1. The first one corresponds to the classical Sod shock tube test case and the second corresponds to the Lax shock tube test case that is generally subjected to more spurious oscillations. Each mixture is composed of three species, with  $N_2$ ,  $O_2$  and R22 gas with thermodynamic properties and the polynomial coefficients for the computation of the heat capacities available in Appendix D of [MZG02]. The use of three species is significant to test the robustness of our method because this additional dimension increases the possible solutions at the Roe intermediate state. The species  $O_2$  stays constant across the shock wave, a constant value sensitive to the numerical error with high-order simulation illustrates the accuracy of the estimation and the correction around the contact wave. Figure 8.4 shows the variation of the heat capacities with the temperature of the three species involved in the simulation.

In the following, simulations are performed with 640 grid cells with a CFL number  $CFL=0.9$ . The final times are chosen so that extreme waves do not have time to reach the domain boundaries and keep the values of conservative variables unchanged at the computational domain limits.



Results of the Sod shock tube obtained after 30 ms are presented in Figure 8.5. The solution obtained with the proposed corrected high-order OSMP scheme is compared to the original (uncorrected) OSMP solution and the first-order Roe solver. As usual, these distributions clearly show, from right to left, the shock wave, the contact discontinuity and the rarefaction fan, separated with constant solution values. The use of a high-order scheme with a monotonicity preserving feature significantly reduces the numerical diffusion and more properly captures discontinuities and rarefaction waves compared to a classic first-order Roe solver, as illustrated in Figure 8.5. However, when the original (uncorrected) OSMP scheme is applied, numerical artifacts appear in the contact discontinuity mainly due to the evaluation of compressibility factors that do not necessarily correspond to a realistic thermodynamic state. Using the additional M-P criteria on the combination of Riemann invariants (7.53), the resulting intermediary state is closer to a physically realistic state, and the mass fraction contact discontinuity is captured with robustness (see Figure 8.5).

To validate the solution obtained with the proposed modified OSMP scheme, we compare it (Figure 8.6) to the exact solution of the Riemann problem obtained with the same thermodynamic data with Godunov solver presented in Annexe V. These solutions are also compared to the exact solution with constant heat capacities for each species corresponding to the ideal gas problem. Thus, we could judge the high quality of the real gas solution obtained since it perfectly fits the exact solution. Discrepancies are clearly registered with the exact solution for an ideal gas, with differences in the wave speeds and the intermediary states between these waves. These discrepancies are coming from the variation of heat capacities of the species and then the difference of predicted speed of sound with the real gas treatment. These are mainly visible in the high-temperature region where the thermodynamics coefficient for R22 exhibits drastic variations (See Figure 8.4). These results justify the proposed approach for real gas flow predictions.

Similar results for the Lax shock tube are presented after 15 ms in Figure 8.7. A comparison with and without the corrected OSMP scheme illustrates the method's efficiency in reducing numerical artifact and capturing contact waves with minimal numerical diffusion. We notice that pressure and velocity are constant within the contact discontinuity.

## 8.5 Conclusion

With a non-ideal equation of state, the Roe average state is not unique. A physically consistent estimation is then necessary to apply the Roe solver and the OSMP scheme described in Chapter 7. We developed the extension of the OSMP scheme for mixtures of gases with an arbitrary convex equation of state based on two steps:

- A first prediction of the compressibility factors at the Roe average state is performed with an integration on the straight line between the left and the right state. This solution is orthogonally projected onto the hyperplane defined by the relationship (8.5), which corresponds to a direct implication of the properties of the Roe solver. The speed of sound is computed at the Roe average state from this first approximation of the compressibility factors.
- A new formulation of the total energy flux based on a combination of the Riemann invariants relative to the multispecies has been expressed in (8.14). A new MP constraint is applied to the combination of Riemann invariants. This condition is equivalent to selecting a new set of Riemann invariants that are still fulfilled the jump relationships of the Riemann problem and the previously computed sound speed and are more consistent thermodynamically with the composition of the mixture.

This numerical method allows preserving a high order of accuracy for regular solutions with non-calorically perfect gas mixture, such as used in reactive simulation, despite significant composition and temperature variations. It also efficiently captures the mass fraction contact discontinuities with robustness and avoids numerical artifacts.

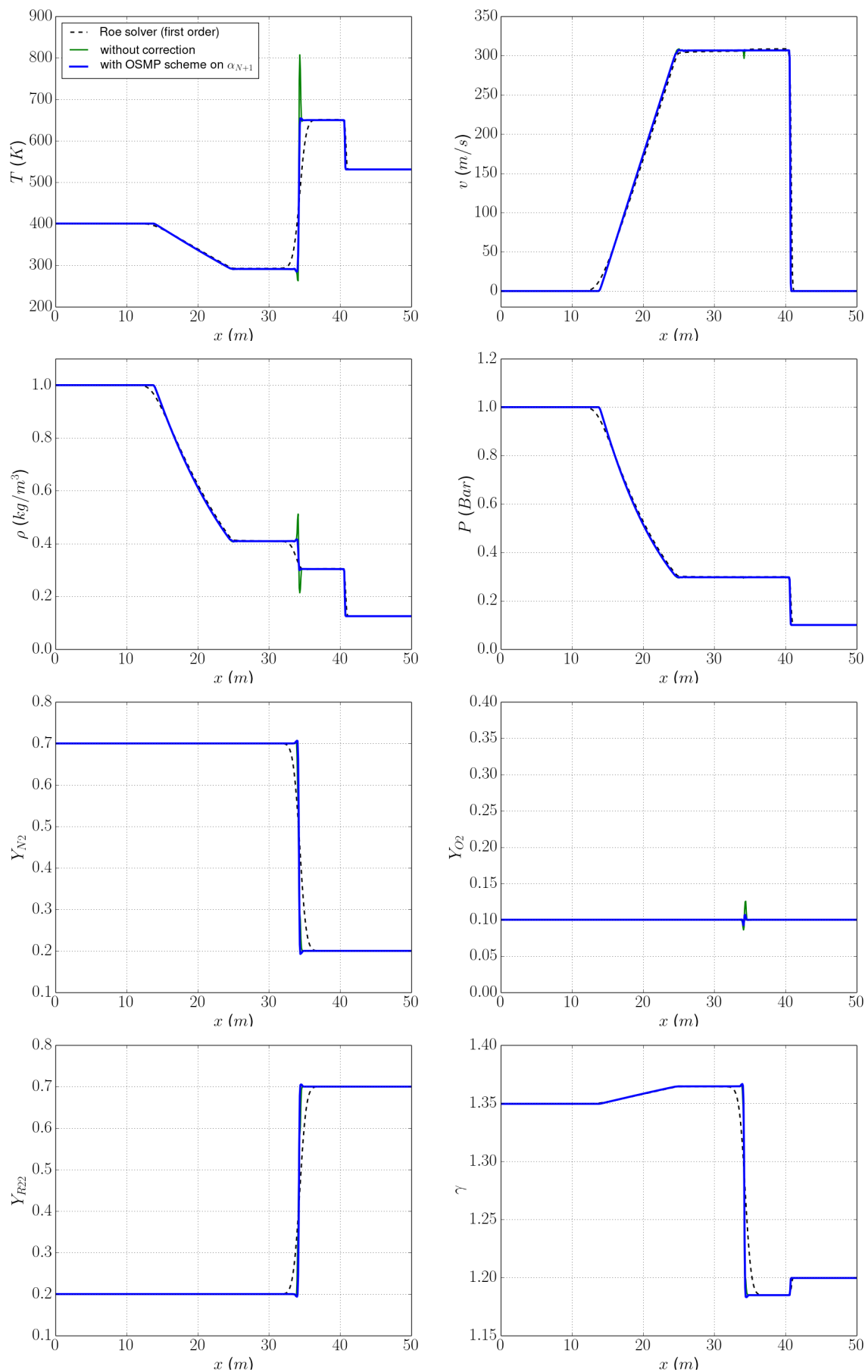


**Figure 8.5:** Distribution of the temperature, the velocity, the density, the pressure, the mass fraction of  $N_2$ ,  $O_2$  and  $R22$  and the heat capacity ratio  $\gamma$  for a 1D Sod shock tube at  $t = 30$  ms. Comparisons between the proposed corrected high-order OSMP scheme (blue bold line) with the original (uncorrected) OSMP scheme (green bold line) and the first-order Roe solver (black dashed line).

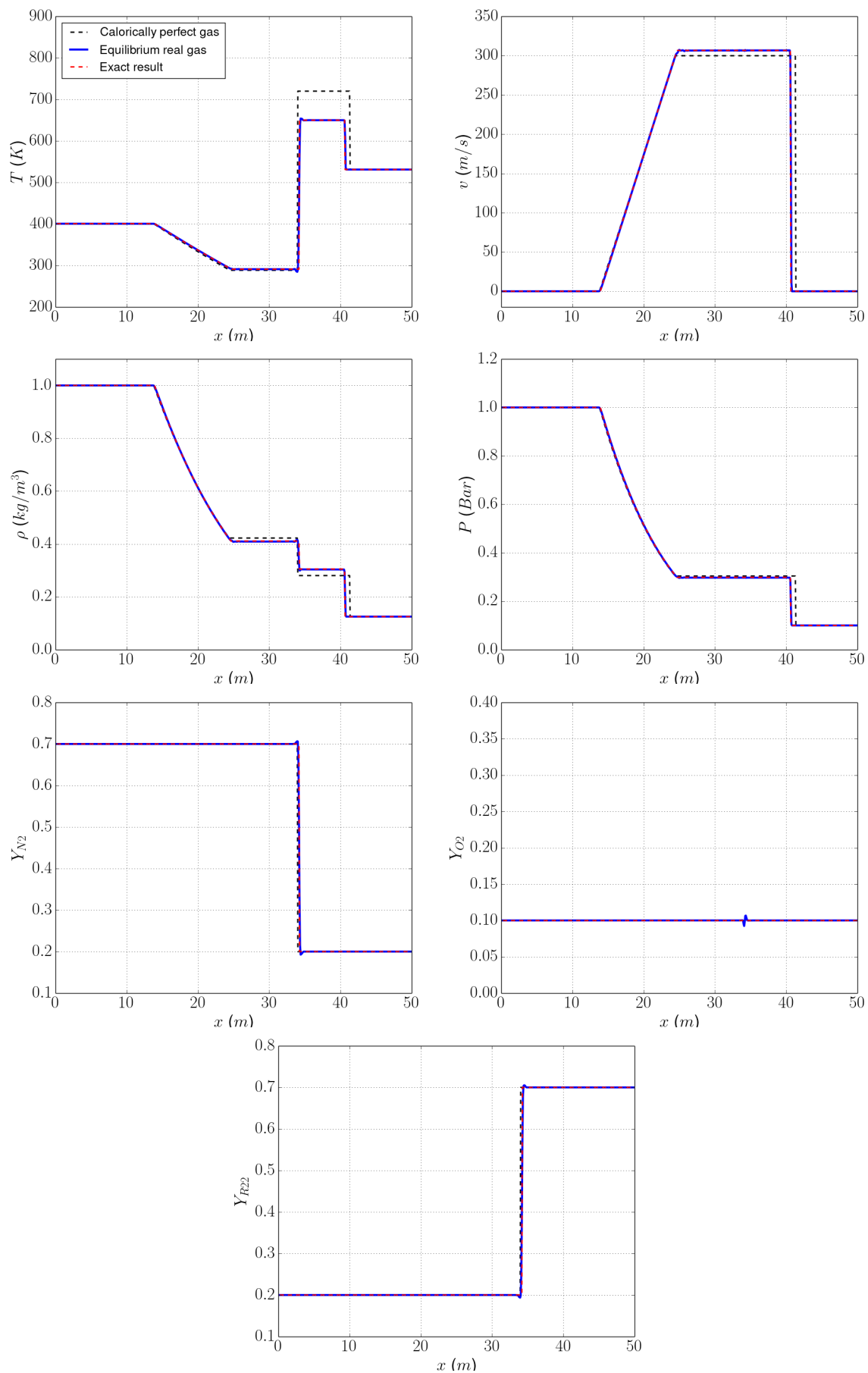


**Figure 8.6:** Comparison of the temperature, the velocity, the density, the pressure and the mass fraction distributions for the 1D Sod shock tube at  $t = 30$  ms. Comparisons between results using calorically perfect gas (black dashed line) and Equilibrium real gas with complex thermodynamic (blue bold line) with the exact solution of the Riemann problem (red dashed line).

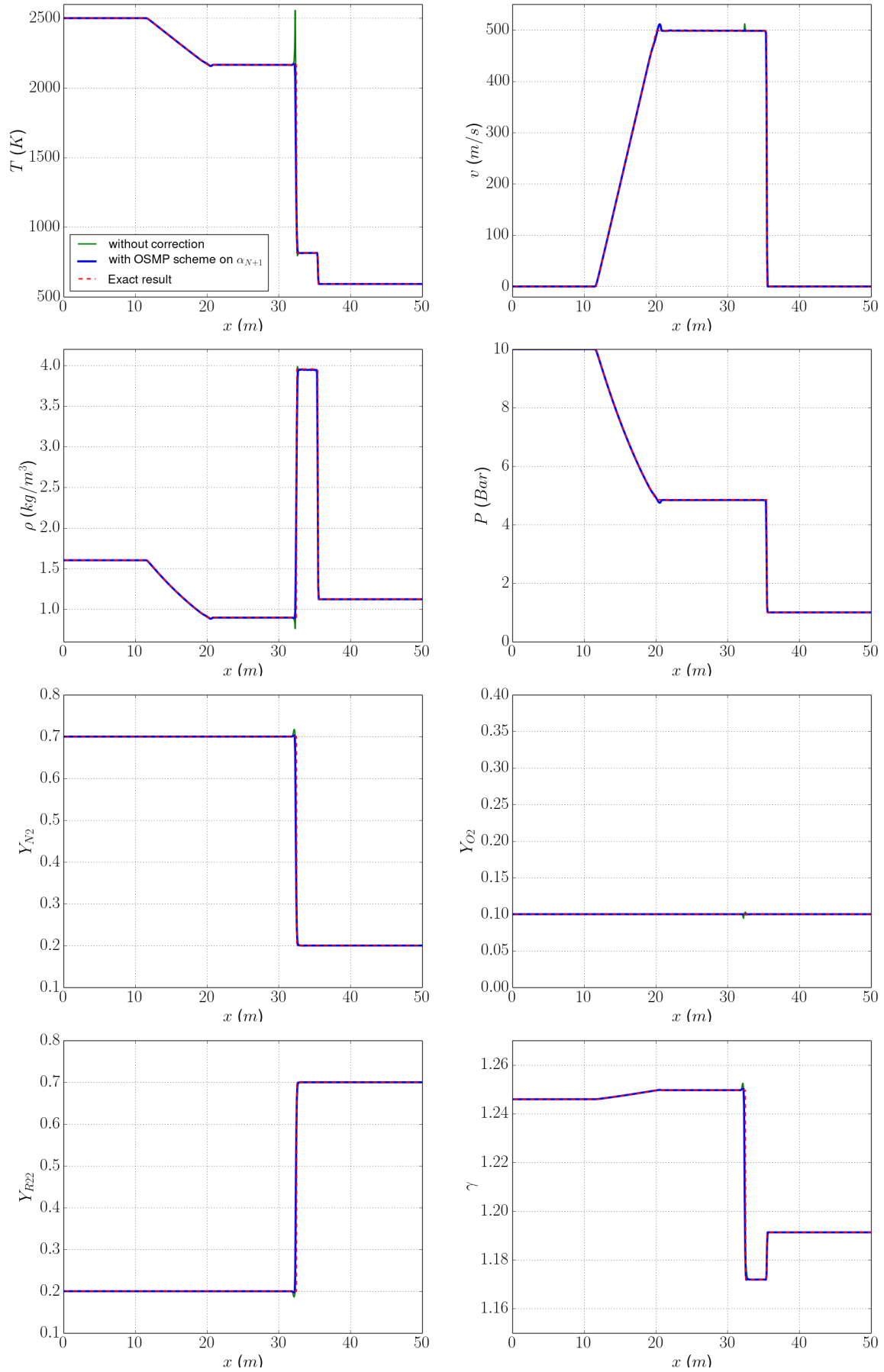


**Figure 8.7:** Comparison of the temperature, the velocity, the density, the pressure, the mass fraction and specific heat ratio distributions for the 1D Lax shock tube at  $t = 15$  ms, obtained with (blue solid line) and without (green line) the modified OSMP scheme and with the exact solution however for ideal gases (black dashed line).



## Carbuncle instability

Applied with more than one dimension, the low dissipative numerical schemes such as the approximated Riemann solvers described previously may create some instabilities leading to the appearance of the so-called *carbuncle phenomenon*. This phenomenon appears when dealing with strong shocks, as we meet in detonation cases. An example of such carbuncle phenomena is illustrated in Figure 9.1 in the case of perturbation of a 2D ZND profile achieved with one-step virtual chemistry. This carbuncle instability takes the form of "sawtooth perturbation" close to the shock wave.

This phenomenon has been studied in the literature in the last decades. Since the first description by Peery and Imlay [PI88] on the classical application of a supersonic flow around a blunt body, multiple analyses have detailed hypotheses and suggested solutions to cure this carbuncle phenomenon. Quirk [Qui94], and Pandolfi [PD01] listed the upwind Riemann solver affected by that instability. The numerical parameters which favor the carbuncle structure have then been identified. Carbuncle phenomenon happens when a strong normal shock is well aligned with grid coordinates (actually in the normal direction of the shock), and it occurs with Riemann solvers using three waves model like for example, the Godunov solver or, for our case with the Roe solver and more generally with numerous numerical methods that preserve the steady contact wave.

In two dimensions, the linearly degenerate characteristic wave is associated with an entropy wave already present in one dimension and a vorticity wave which seems to be responsible for the instability [RGCM00]. Indeed, this instability seems to come from an insufficient dissipation in the transverse direction. In [Lio00], Liou also pointed out that the carbuncle phenomenon is also connected to the pressure term in the mass flux expression.

A possible explanation of this phenomenon in [Qui94] described an odd-even decoupling of the pressure and density fields that provokes variation in the sound speed along with the shock wave and produces the characteristic sawtooth perturbation. Analysis of Dumbser et al. [DMG04] shows that the instability arises from the upstream side of the cells, directly adjacent to the shock. An unstable mode is then convected through the shock wave and generates the visible carbuncle downstream of the shock.

Stability analysis for two-dimensional steady shock waves on structured mesh have been performed in the literature using linear stability theory [RGCM00], and matrix stability analysis [DMG04] providing some clues to understand better and control the phenomenon. In the following, the analysis of [DMG04] will be used to illustrate methods and difficulties encountered, especially in the case of multicomponent flow with OSMP scheme.

Based on these observations, a wide range of possibilities have been developed to cure carbuncle instability. All these solutions have in common to increase the dissipation of the solver. The main ones are listed here:

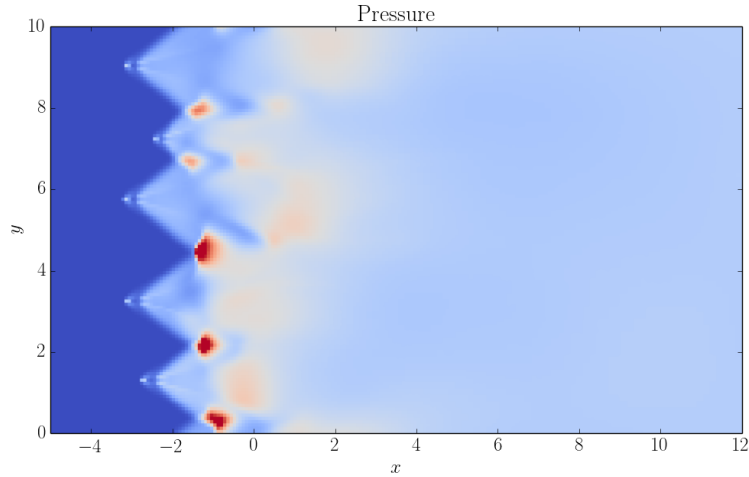


**Figure 9.1:** *Pressure field with carbuncle instabilities generated from a perturbed two-dimensional ZND profile.*

- Replacing the high-resolution solver with a lower-resolution solver in the vicinity of a strong shock with, for example, hybridization with HLL [sKKRK03, SYY14],
- Addition of artificial viscosity [Rod17],
- Using rotated scheme or multidimensional scheme [Ren03, ZLCZ16],
- Addition of transverse viscosity with modifying the Harten entropy fix or with additional viscosity term into the momentum flux [CYBL18]
- Remove pressure dependency in the original mass flux [CHR<sup>+</sup>18b]

These solutions have been implemented and tested in our work. Until now, we did not succeed for now to build a fully satisfying solution. That is why we present here three solutions we retained using rotated Roe solver proposed by [Ren03] and two different ways to introduce additional dissipation term proposed by [CYBL18] and [CHR<sup>+</sup>18b].

## 9.1 Evaluation of carbuncle correction

We present two methods to evaluate the proposed carbuncle correction. First, a matrix stability analysis as described by Dumbser et al. in [DMG04] to observe unstable modes. However, this analysis does not evaluate the quality of the solution and seems not to be relevant for all solvers, in particular for the case with high-order schemes. A standard test with the simulation of a detonation front is also proposed to compare cure carbuncle solutions.

### 9.1.1 Matrix stability analysis

In order to evaluate the risk of carbuncle instability with specific numerical methods, matrix stability analysis is performed based on the method described by Dumbser in [DMG04]. We separated the conservative variables between a steady mean value and an error value:

$$Q_k = Q_k^0 + \delta Q_k. \quad (9.1)$$

The numerical flux function between a cell  $k$  and a neighbouring cell  $m$  is linearized around steady mean value.

$$F_{km}(Q_L, Q_R) = F_{km}(Q_L^0, Q_R^0) + \frac{\partial F_{km}}{\partial Q_L} \delta Q_L + \frac{\partial F_{km}}{\partial Q_R} \delta Q_R. \quad (9.2)$$

Based on the finite volume description we used in our simulation, the semi-discretized governing equation combined with this linearization gives the linear error evolution model.

$$\frac{d\delta Q_k}{dt} = -\frac{1}{|\Omega_k|} \sum_{m=1}^{2^{N_{dim}}} \frac{\partial F_{km}}{\partial Q_k} \delta Q_k \Delta S_{km} - \frac{1}{|\Omega_k|} \sum_{m=1}^{2^{N_{dim}}} \frac{\partial F_{km}}{\partial Q_m} \delta Q_m \Delta S_{km}, \quad (9.3)$$

where  $\Omega_m$  is the volume of the cell  $m$ , and  $\Delta S_{km}$  the surface of the intersection between the cell  $k$  and its neighbor  $m$ . Then the first part corresponds to the influence of the error in the cell  $k$  itself, and the second part corresponds to the influence of the errors in the neighbor's cells  $m$ .

This relation is written for the  $N_{tot}$  cells present in the computational domain:

$$\frac{d}{dt} \begin{pmatrix} \delta Q_1 \\ \vdots \\ \delta Q_{N_{tot}} \end{pmatrix} = \mathbf{S} \cdot \begin{pmatrix} \delta Q_1 \\ \vdots \\ \delta Q_{N_{tot}} \end{pmatrix}. \quad (9.4)$$

$\mathbf{S}$  is called the "stability matrix". Based on the initial error the resolution of the equation 9.4 is:

$$\frac{d}{dt} \begin{pmatrix} \delta Q_1 \\ \vdots \\ \delta Q_{N_{tot}} \end{pmatrix} = \exp(\mathbf{S}t) \cdot \begin{pmatrix} \delta Q_1 \\ \vdots \\ \delta Q_{N_{tot}} \end{pmatrix}_{t=0}. \quad (9.5)$$

This solution then remains bounded if all the real part of the eigenvalues ( $\lambda(\mathbf{S})$ ) of the stability matrix  $\mathbf{S}$  are negative:

$$\max(\text{Re}(\lambda(\mathbf{S}))) \leq 0. \quad (9.6)$$

Given the semi-discretized formalism, we notice that this stability analysis is independent of the CFL number and even independent of the time discretization.

In the same way, as in [DMG04], we compute the stability matrix on a stable shock wave with a Cartesian mesh containing  $11 \times 11$  cells as computational domain. The shock wave is located between the fifth and the sixth cell. The initial upstream values and downstream values are provided by the exact Rankine-Hugoniot relationships in  $x$ -direction. These relationships are computed using a Newton-Raphson procedure to consider various thermodynamic models, especially temperature-dependent heat capacities.

The computation of the term of the gradients of numerical flux involved in the coefficients of the stability matrix ( $\mathbf{S}$ ) are computed using centered difference approximation:

$$\frac{\partial F_{km}}{\partial Q_k} = \frac{F_{km}(Q_k + \Delta Q_k, Q_m) - F_{km}(Q_k - \Delta Q_k, Q_m)}{2\Delta Q_k}. \quad (9.7)$$

The variation  $\Delta Q_k$  are adapted to the conservative variable using an adimensional vector to balance the influence of each variable with the reference values  $Q^{\text{ref}}$ :

$$\Delta Q_k = Q_k^{\text{ref}} \Delta Q^*. \quad (9.8)$$

with



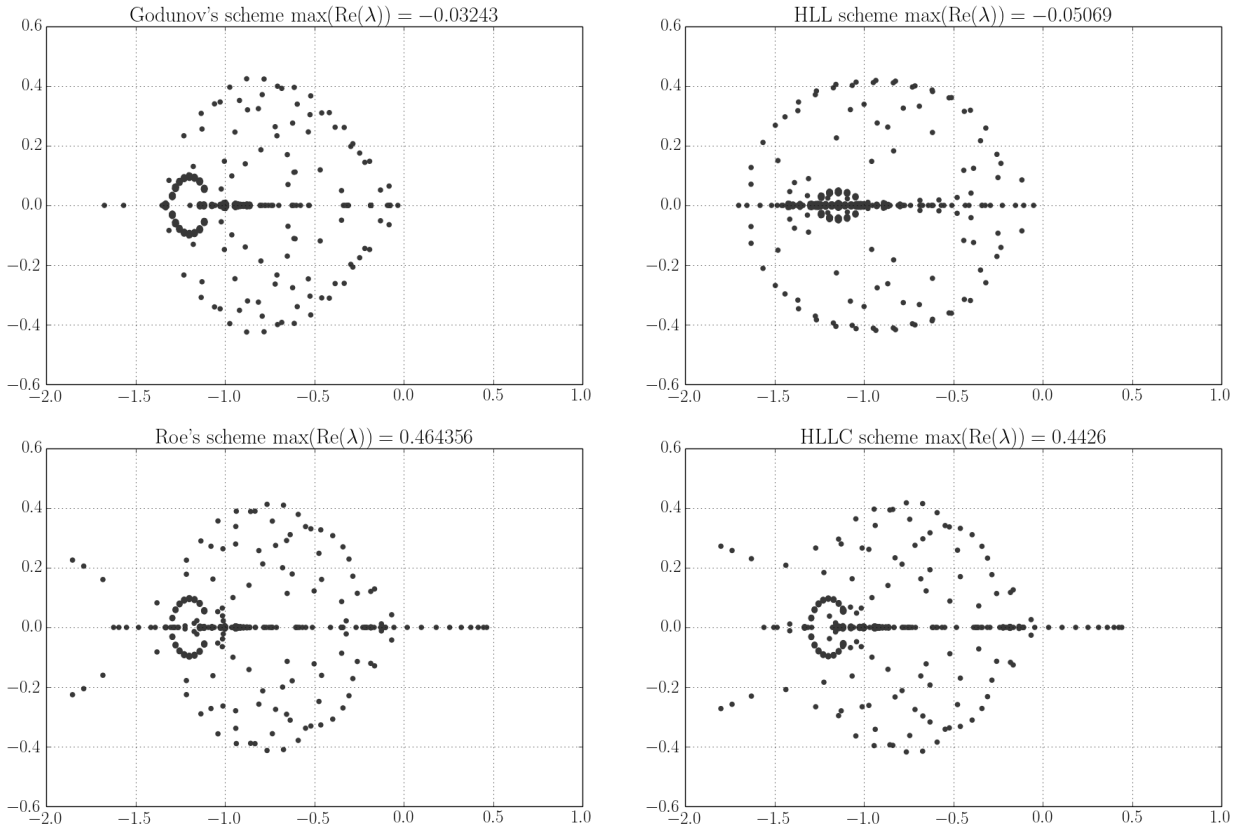


**Figure 9.2:** *Distribution of the eigenvalues of  $\mathbf{S}$  in the complex plane for Godunov scheme (top left), HLL scheme (top right), Roe scheme (bottom left) and HLLC (bottom right)*

$$Q^{\text{ref}} = \left( \rho_L, \dots, \rho_L, \rho_L M_0 c_L, \rho_L (M_0 c_L)^2 \right)^2. \quad (9.9)$$

Using sufficiently small variation  $\Delta Q^*$ , the approximations of (9.7) will be correct despite the non-linearity of the function. The numerical test indicates that a variation of  $\Delta Q^* = 10^{-9}$  allows obtaining converged and stabilized results for our Approximated Riemann solver.

The Figure 9.2 gives values of the eigenvalues of the stability matrix  $\mathbf{S}$  with a shock wave at a Mach  $M_0 = 7$  for a monospecies gas with a constant heat capacity ratio of 1.4 with Godunov, Roe, HLL, and HLLC solvers. The HLL solver, which is an incomplete Riemann solver, gives stable results. Using sufficiently small variation  $\Delta Q^*$  give stable results for the Godunov scheme also with  $M_0 = 7$  but we have however unstable results with other mach number as for instance with  $M_0 = 5$  which gives a maximum eigenvalues of 0.74. With the Roe solver, that we used to build our OSMP scheme, unstable eigenvalues are visible with a maximum eigenvalue with real part of  $Re(\lambda) = 0.46$ .

### 9.1.2 Detonation front test case

Carbuncle issues are highlighted with a detonation front simulation using the simplest model used in the two-dimensional detonation analysis of Bourlioux et al. [BM92].

We neglected all dissipation terms and used only Euler equations for reacting gas. The reaction involved one reactant species  $F$  and a product species  $P$  with source term computed by Arrhenius law:

$$\dot{\omega}_P = A^* Y_F \exp(-E_a^*/T), \quad (9.10)$$

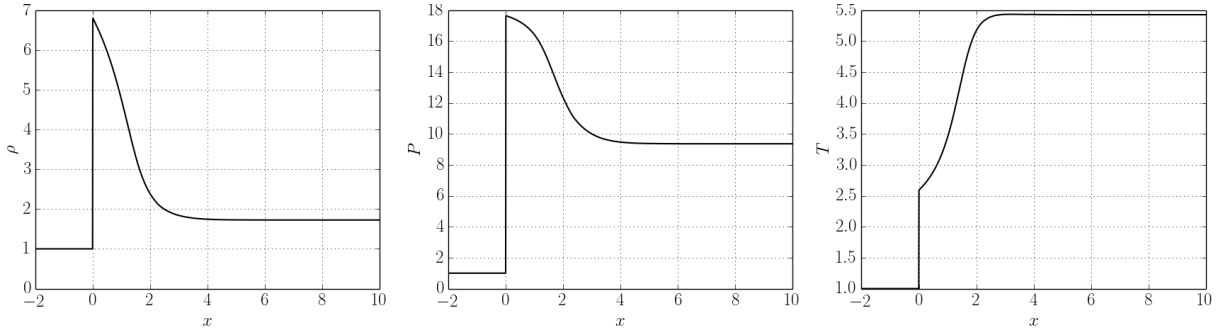


**Figure 9.3:** *Adimensional ZND profile with one-step reaction*

with  $A^*$  and  $E_a^*$  respectively the adimensional pre-exponential factor and adimensional activation energy.

We performed the simulation with  $\gamma = 1.2$ ,  $E_a^* = 20$  and a adimensional heat release produced by the reaction  $Q = 20$ . The pre-exponential factor  $A^* = 200$  is chosen to impose important auto-ignition time. Figure 9.3 presents the corresponding ZND profile.

The simulation is initialized with the steady ZND profile. Perturbation is added to the downstream velocity to disturb the front. Periodic boundary conditions are imposed in the transverse direction of the detonation.

With the production of detonation cells that distort the front and the strong involved, the detonation front is very sensitive to carbuncle instability, as illustrated with a first-order Roe solver in Figure 9.1. Such simulation is then an efficient way to test correction methods.

## 9.2 Critical cells detection

The different methods to cure the carbuncle correspond to the addition of dissipation in the numerical solver. It is then preferable to isolate critical cells with "carbuncle danger" to avoid global scheme modifications in all the computational volume.

Various cells detectors have been proposed in the literature based on the analysis of the vicinity of the cells and empirical observation on the carbuncle danger situation. Thus, Quirk [Qui94] proposed a pressure-based sensing function before computing the flux between two cells  $k$  and  $m$  using:

$$\frac{|p_{R,h} - p_{L,h}|}{\min(p_{L,h}, p_{R,h})} > \beta, \quad (9.11)$$

where the subscript  $h$  is the index for all the adjacent interfaces of both cells  $k$  and  $l$ . The threshold parameter  $\beta$  is generally taken as 1.

In our simulation, we consider a more precise analysis derived from this test with the method described by Chen et al. [CHR<sup>+</sup>18a]. This method uses the evaluation of the pressure gradient  $\nabla p_{km}$  at the intersection of two adjacent cells  $k$  and  $m$  to indicate shock wave direction and its strength.

We note  $\nabla p_{km}^t$  the pressure gradient in the transverse direction to the interface  $I_{km}$  between the cell  $k$  and  $m$  and with normal direction  $\mathbf{n}_{km}$ :

$$\nabla p_{km}^t = \nabla p_{km} - (\nabla p_{km} \cdot \mathbf{n}_{km}) \mathbf{n}_{km}. \quad (9.12)$$

A transverse face is near vertical to a shock if the projected pressure gradient corresponds to the main contribution to the pressure gradient, and this gradient is larger than a certain value:

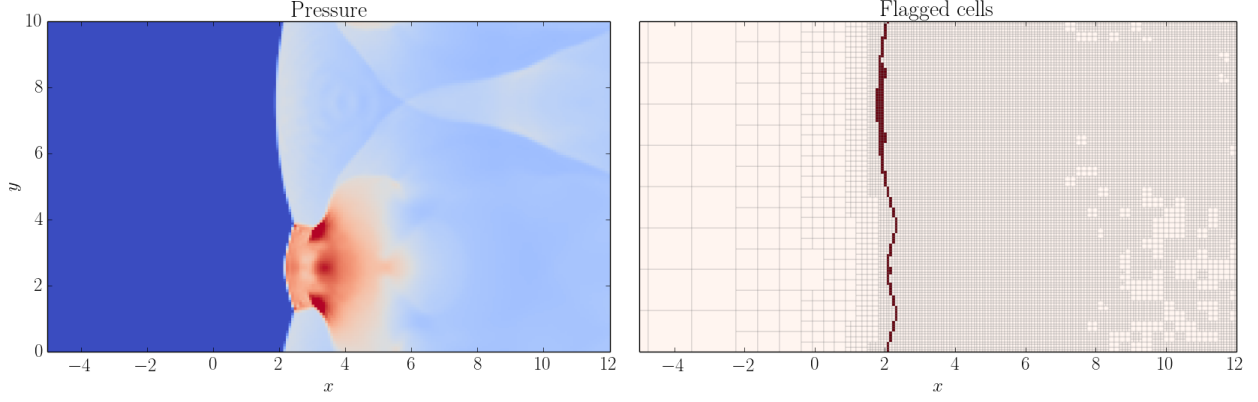


**Figure 9.4:** *Computation of the detonation front (with OSMP7 solver and cure carbuncle method); Pressure field (left) and cells flagged by the carbuncle sensor (right).*

$$\frac{|\nabla p_{km}^t|}{\max(|\nabla p_{km}, \beta_1 \tilde{\rho} \tilde{c}_s^2 / \Delta l)} > \beta_2, \quad (9.13)$$

where  $\beta_1$  is the threshold of the shock strength chosen to be 0.2 in our simulation and  $\beta_2$  to identify vertical shock chosen to be 0.95. The notation  $\tilde{\cdot}$  correspond to the value in the Roe averaged state.

Moreover, in order to discriminate more precisely if the shock is aligned with the mesh, comparison between direction of the pressure gradient and the velocity are added:

$$\frac{|\tilde{\mathbf{u}} \cdot \nabla p|}{\sqrt{(\tilde{\mathbf{u}} \cdot \mathbf{n})^2 |\nabla p|^2 + |\tilde{\mathbf{u}} \cdot \nabla p|^2}} > \beta_3, \quad (9.14)$$

where  $\beta_3$  is chosen to be 0.95.

Figure 9.4 presents an example of the cells flagged by the carbuncle sensor on the detonation test case. We must also notice that these cells are flagged only during the computation of the flux in the transverse direction of the shock wave.

This carbuncle sensor is used in the simulation presented in Chapter 13 and Chapter 14, which correspond to effective applications of flame acceleration and involve strong shock, especially with the presence of detonations front.

In the case of a high-order scheme as the OSMP7 scheme, a cure carbuncle method will be used if the carbuncle sensor flags one cell of the stencil.

In the following simulations of this chapter, a suffix "D" is added to the solver name to signify the use of the sensor.

### 9.3 Cure carbuncle instability

Several possibilities to cure the carbuncle have been studied in the literature. In our simulation, we have implemented three of them, including a rotated solver of Roe, the suppression of the pressure dissipation term of the mass flux, and the addition of shear viscosity. All these methods give similar results and cure the carbuncle efficiently for the first order Roe solver. However, transcription of this additional dissipation to the high-order OSMP scheme is not as efficient as for the first-order Roe scheme.

### 9.3.1 Rotated solver

The first method proposed by Ren [Ren03] uses a scheme with a rotated solver to avoid grid alignment between the computation of the flux and the vertical shock.

The rotated upwind scheme is based on the decomposition of direction  $\mathbf{n}$  into two orthogonal directions  $\mathbf{n}_1$  and  $\mathbf{n}_2$

$$\mathbf{n} = C^1 \mathbf{n}_1 + C^2 \mathbf{n}_2, \quad (9.15)$$

where  $C_1 = \mathbf{n}_1 \cdot \mathbf{n}$  and  $C_2 = \mathbf{n}_2 \cdot \mathbf{n}$  must be positive scalar in order to keep the same left and right states in both directions  $\mathbf{n}_1$  and  $\mathbf{n}_2$ . The rotational invariance property of the Euler equations implies that numerical flux can be decomposed into the computation of the flux into two orthogonal directions.

$$\mathbf{f}^E(\mathbf{n}) = C^1 \mathbf{f}^E(\mathbf{n}_1) + C^2 \mathbf{f}^E(\mathbf{n}_2). \quad (9.16)$$

Therefore the expression of the total flux function of the Roe solver 7.4 becomes:

$$\mathbf{F}_{i+\frac{1}{2}}^{Roe} = \frac{1}{2}(\mathbf{F}_L + \mathbf{F}_R) - \frac{1}{2} \left[ \sum_{m=1}^2 C_{i+1/2}^m \sum_{k=1}^N \tilde{\alpha}_k \cdot |\tilde{\lambda}_k| \tilde{\mathbf{K}}^{(k)} \right]. \quad (9.17)$$

Following the computation of the orthogonal directions proposed by Zhang et al. [ZLCZ16] which must avoid a maximum of additional dissipation, we have:

$$\mathbf{n}_1 = \mathbf{T}_1 \mathbf{n}, \quad \mathbf{n}_2 = \mathbf{T}_2 \mathbf{n}, \quad (9.18)$$

with

$$\mathbf{T}_1 = \begin{bmatrix} \cos(\alpha) & \sin(\alpha) \\ -\sin(\alpha) & \cos(\alpha) \end{bmatrix} \quad \mathbf{T}_2 = \begin{bmatrix} \sin(\alpha) & -\cos(\alpha) \\ \cos(\alpha) & \sin(\alpha) \end{bmatrix}, \quad (9.19)$$

where  $\alpha$  is the rotation angle at each interface which is deduced from:

$$\alpha = \frac{\pi}{4} \max_i \left( 1 - \min \left( \frac{p_L}{p_R}, \frac{p_R}{p_L} \right)^3 \right), \quad (9.20)$$

with  $i$  denoting the interface of the two adjacent cells  $k$  and  $m$

This method adapts the rotation angle to the strength of the local pressure ratio and increases dissipation only close to the region with strong pressure discontinuity. Coefficient  $C^1$  and  $C^2$  are also always positive. Therefore the left and right states are still the same in both directions  $\mathbf{n}_1$  and  $\mathbf{n}_2$ .

Despite this modification of the dissipative terms, the stability matrix analysis still does not respect the stability criterion 9.6 as illustrated in Figure 9.5 for the  $M_0 = 7$  case. However, in our numerical tests using the rotated Roe solver presented in Figure 9.6, no carbuncle instability occurred. This result suggests that the main reason for the effective cure of the instability comes from the computed directions rather than the dissipation itself.

### 9.3.2 Specific additional dissipation

Pressure dissipation term and vorticity mode have both been identified as impacting the apparition of carbuncle instabilities. It results in the addition of a specific dissipation term in the numerical flux formulation associated respectively to the pressure dissipation term [Lio00] and vorticity term [CYBL18].

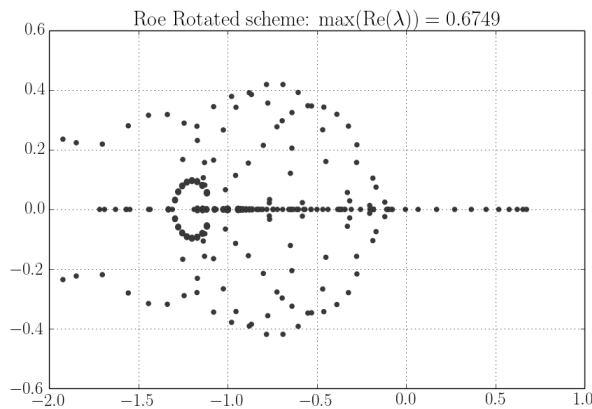


**Figure 9.5:** *Distribution of the eigenvalues of  $\mathbf{S}$  in the complex plane for the Rotated Roe solver*

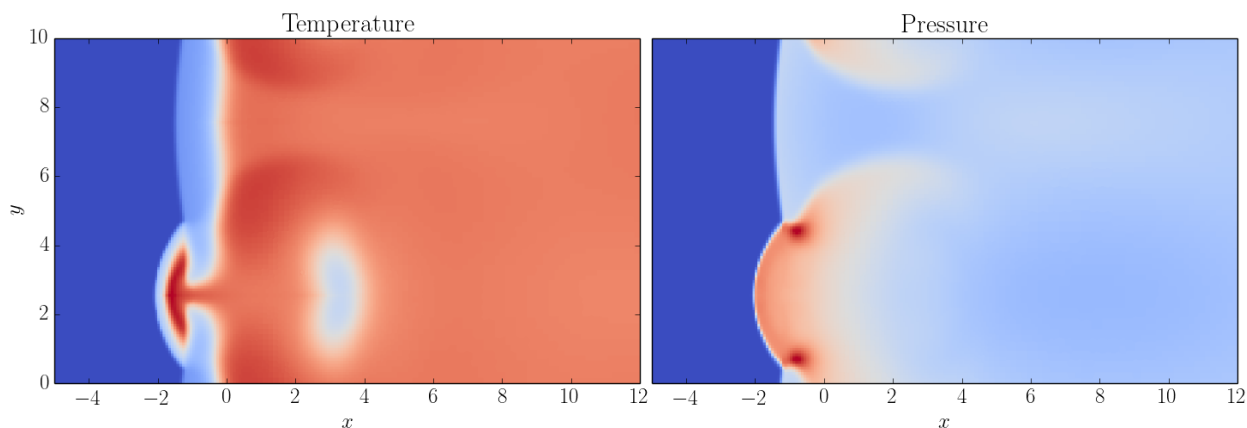


**Figure 9.6:** *Simulation of Detonation front test case with Rotated Roe solver*

### Remove pressure dissipation term

This first method uses the fundamental cure developed in [CHR<sup>+</sup>18b] that consists in the addition in the flux of the pressure dissipative term that appears in the mass flux. This method is based on the work of [Lio00] that highlights the connection between the pressure dissipative term in the mass flux and the production of shock wave instability. For the Roe solver, the formulation of the mass flux corresponds to:

$$F_{Roe}(1) = \frac{1}{2} [(\rho u)_L + (\rho u)_R] - \frac{1}{2} [D^{(\rho)} \Delta \rho + D^{(u)} \Delta u + D^{(p)} \Delta p], \quad (9.21)$$

with  $D^{(\rho)}$ ,  $D^{(u)}$  and  $D^{(p)}$  the dissipative term extract of the formulation of the Roe solver (7.4) by putting in factor the variation of density, velocity and pressure.

The dissipative pressure term  $D^{(p)}$  then corresponds to:

$$D^{(p)} = \frac{|\tilde{u} + \tilde{c}| + |\tilde{u} - \tilde{c}| - 2|\tilde{u}|}{2\tilde{c}^2} [1, \tilde{\mathbf{u}}, \tilde{E}c]^T. \quad (9.22)$$

Analysis of the stability matrix with on a system of two cells intersecting by a shock wave in [CHR<sup>+</sup>18b] expressed with primitives variables highlights the contribution of this pressure dissipative term on the positive eigenvalues.

This carbuncle cure method consists in the suppression of the dissipative term in the expression with the addition of the flux  $\Delta \mathbf{H}_{ij}$  at the global flux formulation:

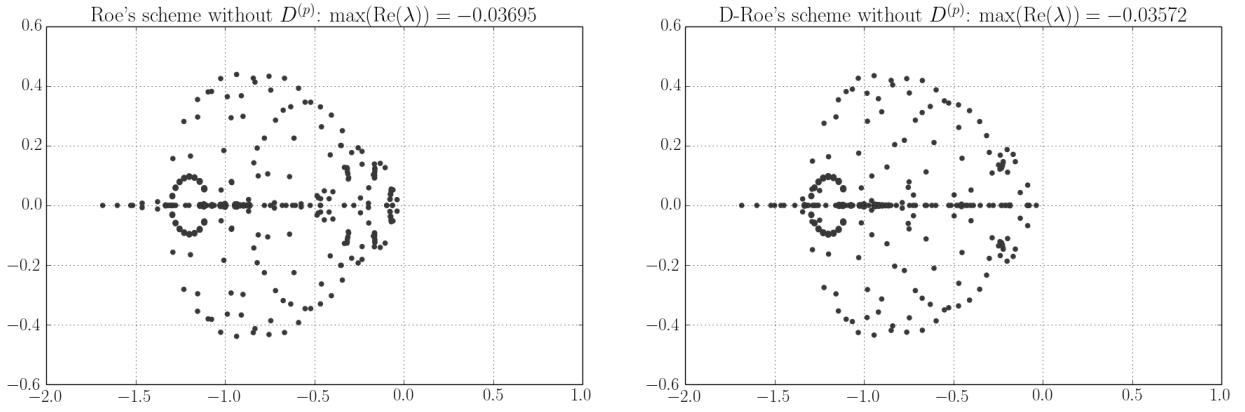


**Figure 9.7:** Distribution of the eigenvalues of  $\mathbf{S}$  in the complex plane for the Roe solver without the pressure dissipative term without (left) and with (right) cell-detection

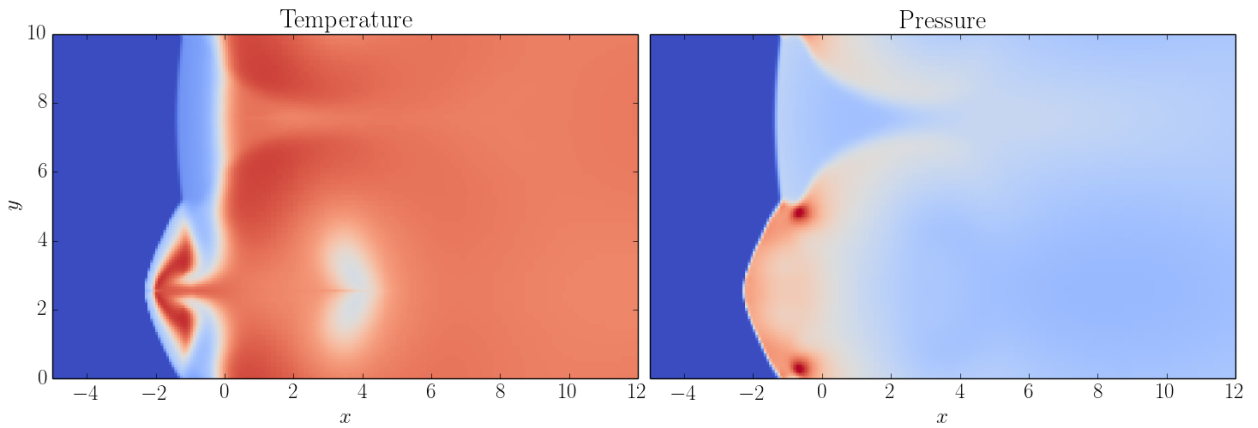


**Figure 9.8:** Simulation of Detonation front test case for the D-Roe solver without the pressure dissipative term

$$\Delta \mathbf{H}_{ij} = \frac{1}{2} \frac{\Delta p}{2\tilde{c}^2} (|\tilde{u} + \tilde{c}_s| + |\tilde{u} - \tilde{c}_s| - 2|\tilde{u}|) \begin{bmatrix} 1 \\ \tilde{u} \\ \tilde{v} \\ \tilde{E}c \end{bmatrix}. \quad (9.23)$$

When removing this term from the numerical flux formulation of the Roe solver, the stability criterion (9.6) is recovered. Eigenvalues of the corresponding stability matrix with and without the carbuncle detection for  $M_0 = 7$  are represented in Figure 9.7 and results for the simulation of the detonation front in Figure 9.8.

This method precisely targets the pressure dissipative term. If we apply this framework to the Rotated solver case, we notice that this one introduces dissipation on all the terms of (9.21). For example, considering the density dissipative term  $D^{(\rho)} = |u_{\mathbf{n}}|$ , we have:

$$\begin{aligned} D_{Roe}^{(\rho)} &= |C_1 u_{\mathbf{n}_1} + C_2 u_{\mathbf{n}_2}|, \\ &\leq C_1 |u_{\mathbf{n}_1}| + C_2 |u_{\mathbf{n}_2}| = D_{Rotated}^{(\rho)}. \end{aligned} \quad (9.24)$$

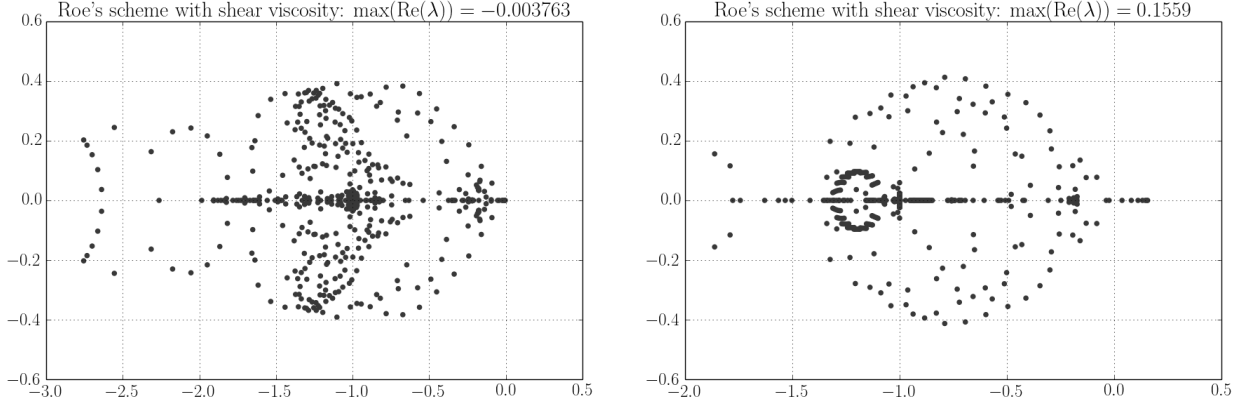


**Figure 9.9:** Distribution of the eigenvalues of  $\mathbf{S}$  in the complex plane for the Roe solver with additional shear viscosity without (left) and with (right) cell-detection

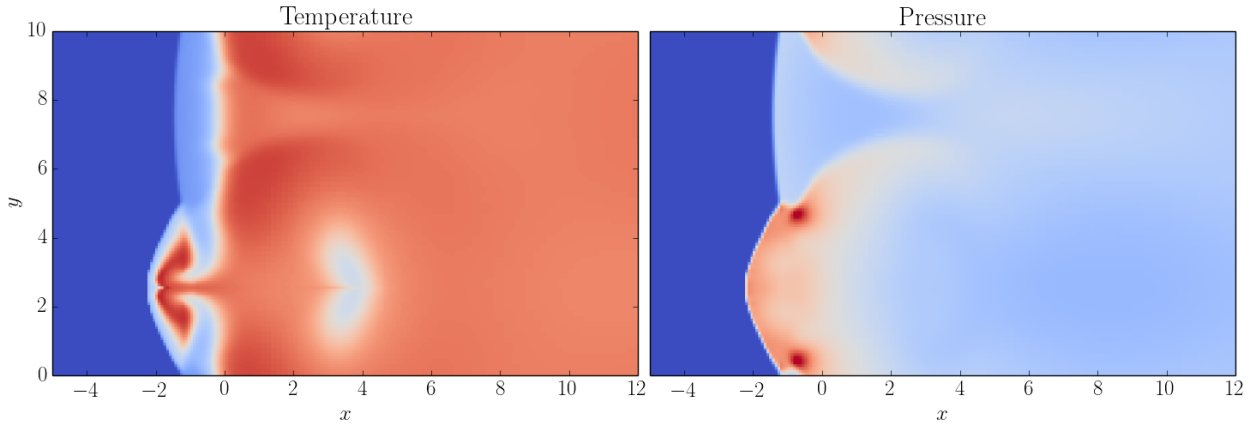


**Figure 9.10:** Simulation of Detonation front test case for the D-Roe solver with additional shear viscosity term

### Additional shear viscosity

An alternative dissipation term is proposed in [CYBL18]. It is based on an analogy between the vorticity mode of the Roe solver and the momentum flux of the carbuncle-free HLL solver. An additional shear viscosity to prevent unstable vorticity mode is then developed with the form:

$$\Delta H_{mk} = -\frac{1}{2} \tilde{\rho} \tilde{c}_s \begin{bmatrix} 0 \\ -\Delta v + \varphi \cdot \Delta u \\ -\Delta v + \varphi \cdot \Delta u \\ 0 \end{bmatrix}. \quad (9.25)$$

with  $\varphi = \frac{|c_R - c_L|}{\max(c_R, c_L)}$  the acoustic speed difference rate use to reduce and scale the normal viscosity.

Results using the stability matrix analysis are presented in Figure 9.9 and the detonation front simulation in Figure 9.10.

The method seems to be stable when applied everywhere in the computational domain but gives positive real eigenvalues when applying the cell detection. However, the simulation we performed with the Roe solver does not make appear carbuncle phenomenon despite those positive eigenvalues.

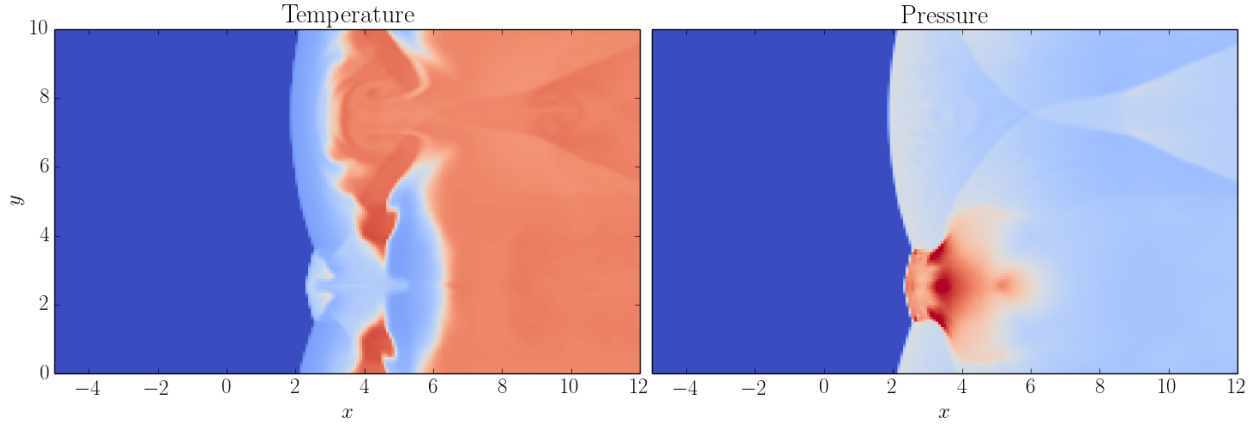


**Figure 9.11:** *Simulation of Detonation front test case for the D-OSMP7 solver hybridized with the rotated solver*

### 9.3.3 Application to the OSMP7 scheme

This section aims to extend methods previously described to fix shock wave instability using the OSMP scheme with the multicomponent flux described previously in Chapter 8. This high-order scheme allows better resolution of the detonation front with less diffusion than the previous first-order solver. However, applying the three cure carbuncle methods faces some additional difficulties.

First of all, contrary to the first order Roe solver, the local CFL number ( $\nu$ ) is explicitly integrated into the formulation of the OSMP scheme (7.52) through the accuracy function  $\Phi^{p,MP}$ . Therefore, the generalized methods will no longer be independent of the time discretization. However, although it impacts the value of the positive real eigenvalues of the stability matrix, variation of the time step does not modify the properties of the stability matrix.

A hybrid scheme must be employed to use the rotated Roe scheme with no impact on the OSMP scheme in the regions with no risk of instability. A rotated solver is then used for cells detected by the carbuncle sensor, and the OSMP scheme is used elsewhere. This solution is working but modifies the numerical solution behavior since the shock-capturing method based on the monotonicity preserving scheme is not used anymore close to the shock wave and implies numerical order reduction of the scheme. Figure 9.11 presents results obtained for the simulation of the detonation front with the hybrid rotated/OSMP7 scheme.

Adapting the dissipative pressure terms to the OSMP7 formulation in the previous carbuncle method does not give satisfying results. Indeed, with the OSMP scheme, the pressure dissipative term  $D^{(p)}$  of the mass flux expression evolves with the stencil of the numerical scheme:

$$D^{(p)} = \alpha \left[ \tilde{Y}_1, \dots, \tilde{Y}_{n_s}, u, v, \frac{1}{2}(u^2 + v^2) \right]^T, \quad (9.26)$$

where

$$\alpha = \frac{1}{\tilde{c}^2} \left[ \left( (1 - \phi_{N-1}^{o,MP} (1 - \nu_{N-1})) |\tilde{U} + \tilde{c}| + (1 - \phi_N^{o,MP} (1 - \nu_N)) |\tilde{U} - \tilde{c}| \right) - 2 \sum_{k=1}^{n_s} \tilde{Y}_k (1 - \phi_k^{o,MP} (1 - \nu_k)) |\tilde{U}| \right].$$

However, this formulation seems to degrade stability in areas without carbuncle danger. This phenomenon is visible on the stability matrix Figure 9.12 with significant positive eigenvalues when this



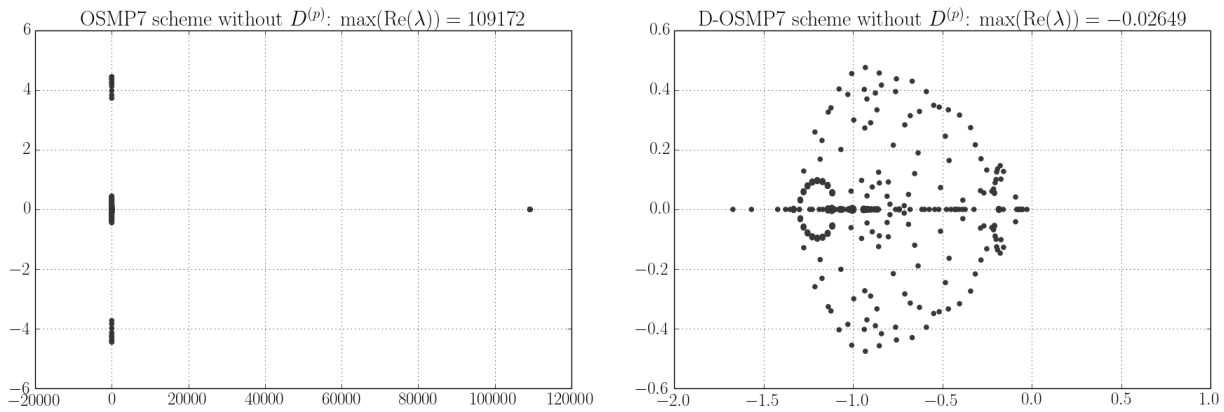


**Figure 9.12:** *Distribution of the eigenvalues of  $\mathbf{S}$  in the complex plane for the OSMP7 solver without the pressure dissipative term without (left) and with (right) cell-detection*

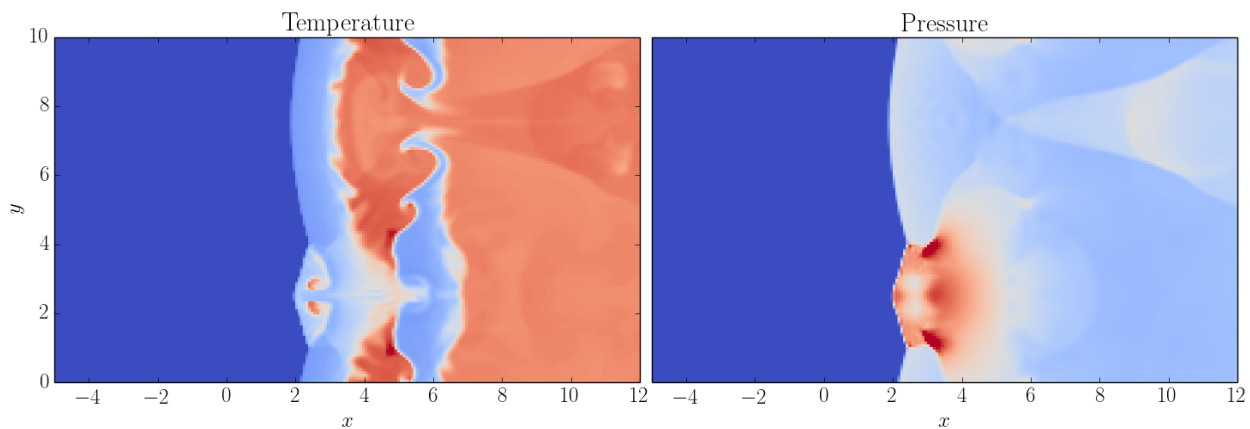


**Figure 9.13:** *Simulation of Detonation front test case for the D-OSMP7 solver hybridized without the first-order pressure dissipative term.*

additional dissipative term is applied on all the computational volume. Using this definition, numerical simulations of the detonation front have proven to be very unstable.

The pressure dissipative term can be used with the Roe solver initial formulation 9.23 to cure carbuncle by removing only the first-order dissipative term. Corresponding matrix stability analysis and results for the simulation of the detonation front are respectively presented in Figure 9.12 and in Figure 9.13.

No modification is made to adapt the vorticity dissipation term to the OSMP scheme. Unfortunately, with the current formulation, we still have slight positive eigenvalues when using with OSMP scheme (Figure 9.14). However, no carbuncle instability occurred in the detonation front simulation (Figure 9.15), nor in the numerical simulations presented in the next chapters by applying this method until now.

## 9.4 Conclusion

We have presented an exploration of different methods to cure carbuncle instabilities we observe in the simulation of strong shock as involved in the detonation front. Three approaches have been tested on the Roe solver, and their extension to the OSMP scheme applies to multicomponent flow is intended. A stability analysis described by Dumbser et al. [DMG04], and a simulation of a detonation wave are used to evaluate the performance of the methods.

None of the explored methods gave complete satisfaction to treat these phenomena properly. The

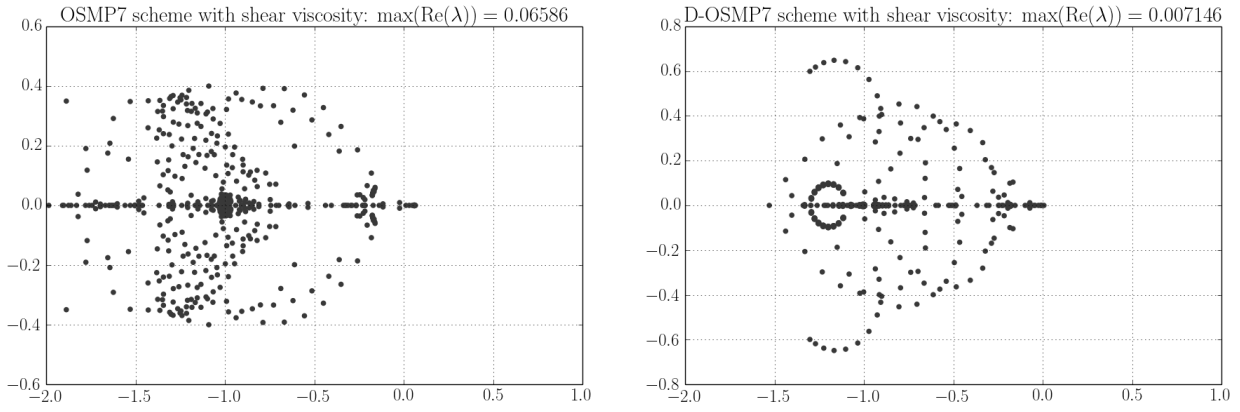


**Figure 9.14:** Distribution of the eigenvalues of  $\mathbf{S}$  in the complex plane for the OSMP7 solver with additional shear viscosity without (left) and with (right) cell-detection

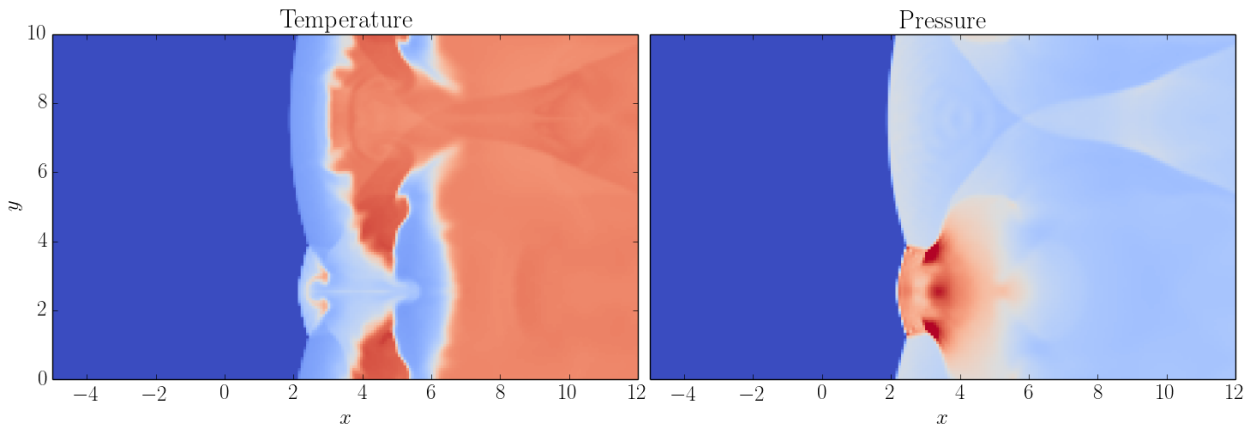


**Figure 9.15:** Simulation of Detonation front test case for the D-OSMP7 solver hybridized with the additional shear viscosity.

use of the rotating solver guarantees to converge to the weak solution of the Euler equations, but it interferes with the flux limiter of the OSMP scheme because it does not integrate with the large stencil. The two other solutions may not fulfill the stability conditions with a large stencil and may integrate numerical perturbations due to the modification of the flux expression. In the following, the simulations presented will be obtained with the additional vorticity dissipation term, which seems to be the more robust cure carbuncle method. This correction is applied on specific cells flagged with a carbuncle sensor. This method seems to work with no significant impact on the propagation of the strong shock waves, but additional investigation on its real impact is probably still necessary. Indeed, the distinction between the physical and pure numerical instabilities in the detonation front example is not easy.



## Part III

# Algorithmic Description



# Introduction

The last part has described the numerical solver and the numerical solution applied to solve the Navier Stokes operators. In this part, additional algorithms are presented to address some of the issues raised by the simulation of flame acceleration.

First, the simulation of reactive compressible multi-component flows exhibits spatial multi-scales that need to be resolved in the DNS approach. To obtain gains in both CPU time and memory usage, we employ a grid refinement technique to tighten grid points in regions where physical phenomena occur and coarsen them elsewhere. Chapter 10 presents the grid refinement strategy based on a Multiresolution Analysis (MRA) initially developed by A. Harten [Har95] and theoretically formalized by Cohen et al. [Coh00]. It has been used here to properly resolve discontinuities and interfaces while optimizing the number of numerical cells properly.

Chapter 11 addresses the problem of integration of immersed boundaries in Cartesian meshes. Such methods are necessary to reproduce the phenomena observed in experimental configurations such as the flame acceleration tubes presented in § 4.1.1 with our high-order numerical solver. The algorithm chosen to implement such a method and its combination with the high-order schemes is presented.

Finally, chapter 12 presents the In Situ Adaptive Tabulation (ISAT) method initially developed by Pope [Pop97] and its application to detonation cases. This algorithm creates a dynamic tabulation of the thermodynamic regions encountered during the computation to save CPU consumption time in the detailed chemistry calculation. We attempt to apply ISAT tabulation to the case of transient phenomena involving detonation waves and discuss this method's gains and disadvantages for our simulation cases.



## Space adaptive Multiresolution

We saw in chapter 6 how to deal with stiff problems using splitting procedure with dedicated high-order time integration for each operator. However, to simulate flame acceleration, we also have to deal with multi-scale structures in space. The modeling equations need a high spatial discretization to capture the small structures of the problem. A necessary condition to guarantee the efficiency of previous schemes relies on a sufficiently accurate spatial mesh representation. In the case of a deflagration or detonation flame front, we saw that the characteristic lengths of reactions are generally less than a millimeter. It is then necessary to have a sufficient resolution to capture the flame profile properly at these scales to not degrade the accuracy of the results allowed by the high-order time integration. However, a uniform mesh is rapidly too expensive in terms of computational resources to capture the finest scales, and the accuracy obtained with such a resolution in the smoothest areas is excessive in comparison. Then we are using adaptive discretization methods to reduce the computing requirements and concentrate the significant computational effort on local dominant phenomena.

We use in this work an *adaptive multiresolution* method, based on the work of Harten [Har95] and the fully adaptive algorithm of Cohen et al. [CKMP03]. This method is based on the use of nested dyadic grids. The Multiresolution method represents a set of function data as values on a coarse grid with a series of local estimations called *details* at the different levels of nested grids. Details give information on the local smoothness of the solution. Multiresolution methods have a rigorous and accurate regularity analysis and give better compression rates and gain in CPU time than the classical Adaptive Mesh Refinement methods based on iterative local refinement patch on the computational volume [DDG<sup>+</sup>09]. Multiresolution techniques described here are largely based on the multiresolution kernel of MR\_CHORUS code (see § 4.2.1) developed by Christian Tenaud.

### 10.1 Multiresolution analysis

The cell-averaged multiresolution of Harten [Har95] uses the same values of the conservative variables on univariate dyadic intervals as the finite-volume scheme. We denote by  $l = 0, 1, \dots, L$  the grid level from the coarsest ( $l = 0$ ) to the finest ( $l = L$ ). Dyadic intervals in three dimensions at level  $l$  are written:

$$\Omega_{i,j,k}^l = [2^{-l}i, 2^{-l}(i+1)] \times [2^{-l}j, 2^{-l}(j+1)] \times [2^{-l}k, 2^{-l}(k+1)] \text{ with } i, j, k \in \{0, \dots, 2^{l-1}\}, \quad (10.1)$$

A tree data structure is used to encode the multiresolution analysis technique. The *root* referred to the basis of the tree, the *nodes* are elements of the tree, and the *leaves* are the upper elements. In  $N_{dim}$  dimension, a parent-cell at a level  $l$  has always  $2^{N_{dim}}$  children cells at the level  $l+1$ . Tree data structures in one and two dimensions are illustrated in Figures 10.1 and 10.2 respectively.



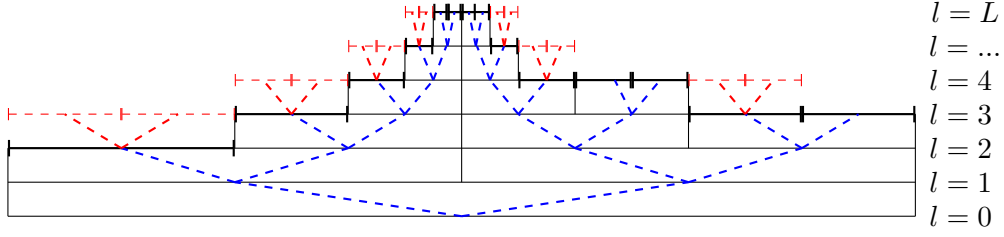


**Figure 10.1:** A graded tree data structure in 1D: dyadic tree in blue dashed line, leaves in bold black line, and virtual cells in red dashed line.

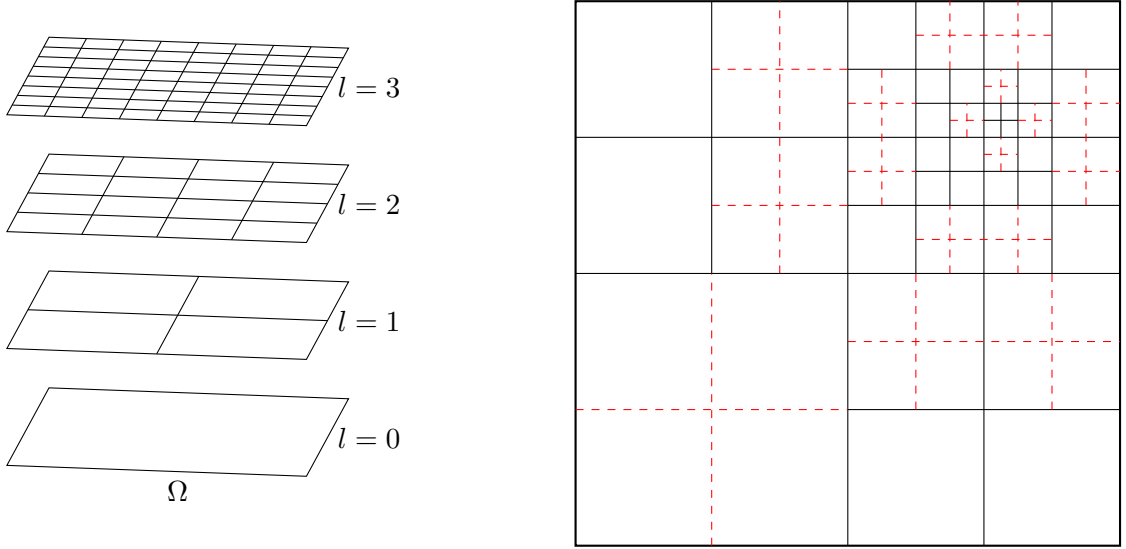


**Figure 10.2:** Left: set of a nested dyadic grid in 2D. Right: a sketch of a 2D tree structure with leaves in plain line and virtual leaves in red dashed line.

The projection and the prediction operators are used for relating consecutive levels. The projection operator noted  $P_{l+1 \rightarrow l}$  compute the cell-average value of the solution on a node at grid level  $l$  from the cell-average values of the children of this node at grid level  $l+1$ .

$$\mathbf{w}_j^l = \sum_{p \in \mathcal{C}_j^l} \frac{|\Omega_j^{l+1}|}{|\Omega_j^l|} \mathbf{w}_p^{l+1}, \quad (10.2)$$

where  $\mathcal{C}_j^l$  denotes the  $2^{N_{dim}}$  children at grid level  $l+1$ .  $|\Omega_j^l|$  correspond to the volume of an interval  $\Omega_j^l$  of the dyadic grid at the level  $l$ .

The projection then corresponds to the exact averages computed at the finer level. So, as far as grids are nested, this projection operator is exact and unique when using a finite volume approach.

The prediction operator noted  $P_{l \rightarrow l+1}$  uses cell-average values at the grid level  $l$  for approximate the values at the grid level  $l+1$ . Contrary to the projection operator, there is an infinite number of approximation choices. However, Cohen et al. [CKMP03] impose two constraints:

- The prediction is *local*, i.e. that the approximation of  $\mathbf{w}^{l+1}$ , that is noted  $\hat{\mathbf{w}}^{l+1}$ , is computed using the cell-average values  $\mathbf{w}^l$  on a stencil surrounding the cell  $\Omega_j^{l+1}$
- The prediction is *consistent* with the projection in the sense that

$$P_{l \rightarrow l+1} \circ P_{l+1 \rightarrow l} = \text{Id}. \quad (10.3)$$

In this work, the approximation is realized with a centered linear polynomial interpolation. In one dimension, the approximated values of the two childrens are:

**Table 10.1:** *Coefficients of centered linear polynomials interpolation [Har95]*

Order ( $r$ )	$s$	$\xi_1$	$\xi_2$	$\xi_3$
1	0	0	0	0
3	1	$-\frac{1}{8}$	0	0
5	2	$-\frac{22}{128}$	$\frac{3}{128}$	0
7	3	$-\frac{201}{1024}$	$\frac{11}{256}$	$-\frac{5}{1024}$

$$\begin{cases} \hat{\mathbf{w}}_{2j}^{l+1} = \mathbf{w}_j^l + \sum_{p=1}^s \xi_p (\mathbf{w}_{j+p}^l - \mathbf{w}_{j-p}^l), \\ \hat{\mathbf{w}}_{2j+1}^{l+1} = \mathbf{w}_j^l - \sum_{p=1}^s \xi_p (\mathbf{w}_{j+p}^l - \mathbf{w}_{j-p}^l). \end{cases} \quad (10.4)$$

where  $\xi_p$  are the coefficients of the linear polynomial interpolation of order  $r = 2s + 1$  given in Table 10.1 for  $s \leq 3$ . In future simulations, we generally choose to use  $s = 1$ .

On a cartesian mesh, multidimensional polynomial interpolations are obtained by the tensor product of the 1D operator [BH97]. If we define the polynomial interpolation  $Q^s$  as:

$$Q^s(j; \mathbf{w}^l) = \sum_{p=1}^s \xi_p (\mathbf{w}_{j+p}^l - \mathbf{w}_{j-p}^l). \quad (10.5)$$

the tensor product of the polynomial interpolation in two dimensions, proposed by Bihari and Harten [BH97] reads:

$$\hat{\mathbf{w}}_{2j+p, 2k+q}^{l+1} = \mathbf{w}_{j,k}^l + (-1)^p Q^s(j; \mathbf{w}_{\cdot, k}^l) + (-1)^q Q^s(k; \mathbf{w}_{j, \cdot}^l) - (-1)^{p+q} Q_2^s(j, k; \mathbf{w}^l), \quad (10.6)$$

where the operator  $Q_2^s$ , derived from a tensor product, reads:

$$Q_2^s(j, k; \mathbf{w}^l) = \sum_{a=1}^s \xi_a \sum_{b=1}^s \xi_b (v_{j+a, k+b}^l - c_{j-a, k+b}^l - v_{j+a, k-b}^l + v_{j-a, k-b}^l). \quad (10.7)$$

In the same way, polynomial interpolations are also extended to 3-dimensions with the equivalent tensor-product described in [TD11].

The error of prediction at a level  $l$  is estimated using the detail  $\mathbf{d}_j^l$  defined as the difference between the exact and the predicted values obtained with projection:

$$\mathbf{d}_j^l = \mathbf{w}_j^l - \hat{\mathbf{w}}_j^l. \quad (10.8)$$

Because of the consistency property, the sum of details on children of a node satisfies:

$$\sum_{p \in \mathcal{C}_j^p} |\Omega_j^{l+1}| \mathbf{d}_p^{l+1} = 0. \quad (10.9)$$

If we note  $\mathbf{D}^l$  the vector of all details at a grid level  $l$ , and  $\mathbf{W}^l$  the vector of the solution at a grid level  $l$ . we observe that the knowledge of  $(\mathbf{D}^{l+1}, \mathbf{W}^l)$  is equivalent to the knowledge of  $\mathbf{W}^{l+1}$ .

$$\mathbf{W}^{l+1} \longleftrightarrow (\mathbf{W}^l, \mathbf{D}^{l+1}). \quad (10.10)$$

Recursively, from the finest grid level  $L$  down to the root, we can implement the multiresolution transformation:

$$\mathcal{M} : \mathbf{W}^L \mapsto (\mathbf{W}^0, \mathbf{D}^1, \dots, \mathbf{D}^L). \quad (10.11)$$

The multiresolution transform  $\mathcal{M}$  is a linear operator seen as a change of basis that can be used for encoding  $\mathbf{W}^L = \mathcal{M}\mathbf{W}^0$  or for decoding  $\mathbf{W}^0 = \mathcal{M}^{-1}\mathbf{W}^L$ .

Details give information on the regularity of the solution. They decay with the grid level on smooth solutions and even recover null values for solutions with local bounded  $r$ th order derivatives. Let us recall that this bounded order is related to the width of the prediction polynomials  $r = 2s + 1$ . The multiresolution format is then convenient for data compression. Moreover, they can be used for adapting the mesh locally to the behavior of the solution through the use of a local grid refinement, which should decrease CPU time and memory requirements.

## 10.2 Local grid refinement

The details decay on regular solutions and recover large values in discontinuous regions [Coh00]. Then, they are convenient to adapt the grid locally, i.e., refine the grid in zones where driving phenomena occur while coarsening the grid elsewhere. The local grid refinement is then based on a threshold operation consisting of setting to zero details with normalized  $L_1$ -norm lower than a threshold parameter  $\varsigma_l$  on each grid level  $l$ :

$$\forall j \frac{|\mathbf{d}_j^l|}{\max |\mathbf{d}|} < \varsigma_l \Rightarrow \mathbf{d}_j^l = 0, \quad (10.12)$$

with  $\max |\mathbf{d}|$  correspond to the maximum detail met in all the leaf of all the graded tree on the computational domain.

Leaves with details set to zero are then discarded from the tree-data structure.

The threshold parameter  $\varsigma_l$  allows setting a prescribed tolerance on the *detail* corresponding to the difference between the finite-volume solution  $\mathbf{w}_j^l$  evaluated on the finest grid and the solution obtained on the refined grid  $\hat{\mathbf{w}}_j^l$ . To obtain the same order magnitude  $\varsigma$  on each grid level  $l$ , following Harten [Har95], the threshold parameter  $\varsigma_l$  must be prescribed at:

$$\varsigma_l = 2^{N_{dim}(l-L)} \varsigma. \quad (10.13)$$

The user chooses the value of  $\varsigma$  to drive the solution accuracy and the efficiency of the grid refinement. Moreover, an additional criterion is added to the condition (10.8) to anticipate the formation of discontinuities from a regular solution which can appear with hyperbolic conservation laws. We assume that the forthcoming loss of regularity can be detected by detail values estimated on coarser grids. So, following a heuristic criterion of Harten [Har95], children at a grid level  $l + 1$  are added to the tree if the following criterion is true:

$$\frac{|\mathbf{d}_j^l|}{\max |\mathbf{d}|} \geq 2^{2s-1} \varsigma_l. \quad (10.14)$$

To be able to apply prediction operator  $P_{l-1 \rightarrow l}$  for a cell at grid level  $l$ , adjacent cell at the grid level  $l - 1$  included in the stencil of the polynomial interpolation must stay in the tree. Moreover, numerical fluxes are always computed on the highest grid level. The stencil of the OSMP scheme is then completed using virtual ghost cells computed with a prediction operator when the grid does not exist at the same level. This also requires additional cells to apply the projection at the refined

level. For instance, using the OSMP7 scheme,  $s + 2$  nearest neighbor cells must be added in each direction. When these supplementary constraints are met, the obtained tree is said *graded* as shown on Figures 10.1 and 10.2.

Let us recall that the fluxes at grid interfaces are calculated at the highest level between two adjacent cells. Therefore to ensure strict conservation in the flux computation between cells at different grid levels, the ingoing flux on the leaf at the grid level  $l$  is set with the sum of the outgoing fluxes on the leaves at the grid level  $l + 1$ .

### 10.2.1 Adaptive multiresolution algorithm

Based on the previous description of the method, we represent here the different steps of the dynamic adaptation method. This algorithm is run at the beginning of each time step.

---

#### Algorithm 1 Adaptive Multiresolution scheme

---

**Input :** Threshold value  $\varsigma$ , values of the conservative variables  $\mathbf{w}_j^l$  on the leaves  $\Omega_j^l$  of the trees.

- 1: Encode values on fathers of the leaves  $\Omega_j^{l-1}$  using the projection operator (10.2) (at the initialization, all the levels of the tree are encoding).
  - 2: Compute the approximated values  $\hat{\mathbf{w}}_j^l$  on the leaves using the prediction operator based on linear interpolation (10.4) and compare it to the initial value  $\mathbf{w}_j^l$  to obtain detail  $\mathbf{d}_j^l$  with (10.8).
  - 3: Flag the mesh that should be leaves or should be nodes based on the values of the detail and the threshold  $\varsigma$  with (10.12) and (10.14).
  - 4: Add children to the leaves flagged as nodes by created new leaf  $\Omega_j^{l+1}$ , compute the values  $\mathbf{w}_j^{l+1}$  with prediction operator. Then propagate this information to the neighbors of the leaf and create cells  $\mathbf{w}_{j+k}^l$  if necessary the tree graded.
  - 5: Delete superfluous cells with a small detail compared to the threshold value.
  - 6: Create fictive cells compute with prediction (10.4) in order to keep the same level and same grid refinement for the operators' stencil on each leaf.
- 

In order to browse the tree structures efficiently, all the routines call by this program are recursive and start from the roots of each tree and call themselves on the successive childrens if necessary.

The values  $\mathbf{w}_j^l$  of the fictive cells are also updated by the prediction operator after each change in the values of the leaves during the integration scheme.

Further details on this multiresolution implementation are available in [TD11].

## 10.3 Hydrodynamic instability

In order to illustrate the application of the multiresolution, we present here a test case of a bubble of gases interacting with a shock wave propagating in the air. This test case also presents elementary physical mechanisms as the production of acoustic waves and vorticity through the baroclinic process and the creation of hydrodynamic instabilities, which will be involved in the process of flame acceleration. This test case also illustrates the interest of the modified OSMP scheme described in Chapter 8 for multicomponent with non-calorically perfect gases.

The test case consists of a cylindrical bubble filled with a dense hydrochlorofluorocarbon refrigerant R22 gas, initially located in ambient air at atmospheric pressure. A planar shock wave moving in ambient air at a Mach number  $M_s = 1.22$  towards the R22 bubble interacts with it. This configuration has been chosen because it has been studied experimentally [HS87], and numerically [DvW19, KD19] usually to validate numerical approaches. The sketch of the initial configuration is given in Figure 10.3 where the computational domain is also illustrated. Only the upper half of the experimental configuration is simulated. A symmetric boundary condition is applied at the lower bound of the domain. At inlet and outlet boundaries, non-reflecting boundary conditions based on the work of Poinot and Lele [PL92] are prescribed, although extreme waves do not reach these boundaries at the final simulation

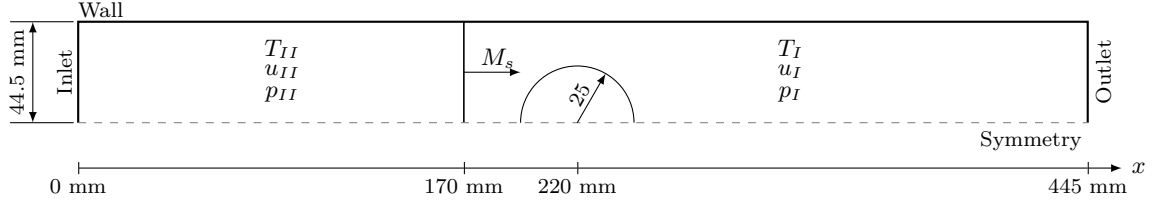


**Figure 10.3:** Sketch of the computational domain: initial configuration and boundary conditions.

time. A solid wall is located at the top boundary, where slip condition is prescribed ( $\mathbf{u} \cdot \mathbf{n}_{wall} = 0$ , with  $\mathbf{n}_{wall}$  the wall-normal vector) as well as symmetry condition for scalars.

The computational domain length is  $L_x = 445 \times 10^{-3}$  m and its height is  $L_y = 44.5 \times 10^{-3}$  m. The R22 cylindrical bubble which initially has a diameter of  $d_0 = 25 \times 10^{-3}$  m, is initially centered on the bottom symmetry line at  $x = 220 \times 10^{-3}$  m from the inlet. The shock wave is initially located at  $x = 170 \times 10^{-3}$  m, and the state in front of the moving shock wave (noted region I, Figure 10.3) is prescribed to be at the atmospheric conditions with  $T_I = 298$  K, and  $P_I = 101325$  Pa. The fluid is initially at rest, so we have  $u_I = 0$  m.s $^{-1}$

Simulations is performed for a real gas configuration with a mixture of 79 % of N $_2$  and 21 % of O $_2$  in Air leading to, respectively, mass fraction  $Y_{Air} = 0.767$  and  $Y_{O_2} = 0.233$ , while the bubble is filled with pure R22 dense gas. Heat capacity ratio ( $\gamma_{Air}$  and  $\gamma_{R22}$ ) as well as compressibility factors are calculated through polynomials found in [MZG02] like in the shock tube test case of § 8.4.2. At the initial state, heat capacity ratios in the region I corresponds to  $\gamma_{Air,I} = 1.399$  and  $\gamma_{R22,I} = 1.175$ . The post-shock conditions are computed with the resolution of the Rankine Hugoniot relation with a Newton-Raphson procedure given  $T_{II} = 339.74$  K,  $u_{II} = 115.85$  m/s and  $p_{II} = 159117$  Pa.

Simulation is performed on a structured grid using the adaptive mesh refinement. To obtain cells with an aspect ratio of unity, the computational domain is composed of 10 roots of tree data structure along the streamwise direction. Each tree comprises nine grid levels that lead to  $5120 \times 512$  grid points in  $(x \times y)$  directions if the solution is coded at the finest grid level. This finest grid resolution is equivalent to have 575 grid points along the initial bubble diameter  $d_0$  ( $\delta x = d_0/575$ ). Denner and Wachem [DvW19] performed a grid convergence study on the ideal gas configuration and showed that grid convergence is obtained on the finest grid they used with  $\delta x = d_0/500$ .

Only the Euler operator is involved in the simulation, there is no reaction and no viscous term apply. The OSMP7 solver described in the chapters 7 and 8 is apply. Simulations are performed with a CFL number of 0.5, and a threshold MRA parameter  $\zeta = 10^{-3}$ .

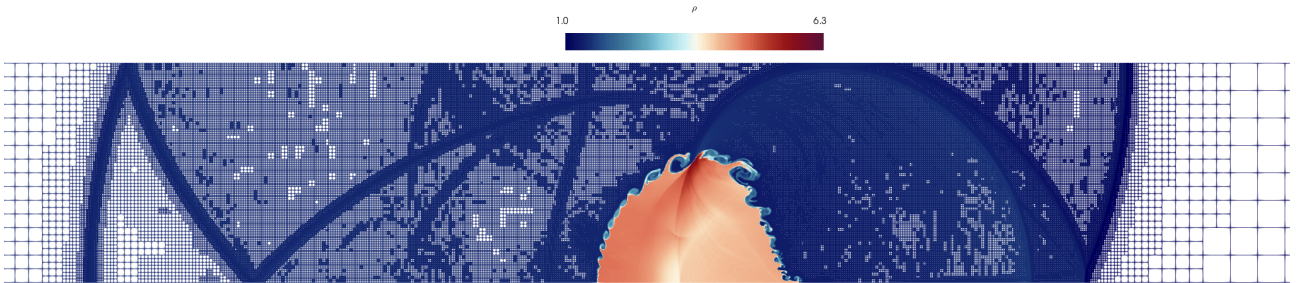


**Figure 10.4:** Adapted grid obtained using 9 grid levels per tree and 10 trees distributed over the domain in the streamwise direction at a time  $t = 287.5 \mu\text{s}$  (dimensionless time  $t c_{R22,I}/d_0 = 1.15$ ), colored by density values.

The solution at a time  $t = 287.5 \times 10^{-6}$  s (corresponding to a dimensionless time based on the R22 initial speed of sound  $c_{R22,I}$  of  $t c_{R22,I}/d_0 = 1.15$ ) is presented in Figure 10.4 where we can see the adapted grid colored by the density field. Regions where high gradients occur are clearly evidenced by the presence of a high grid level. On the opposite, in regions where a regular solution occurs, the grid

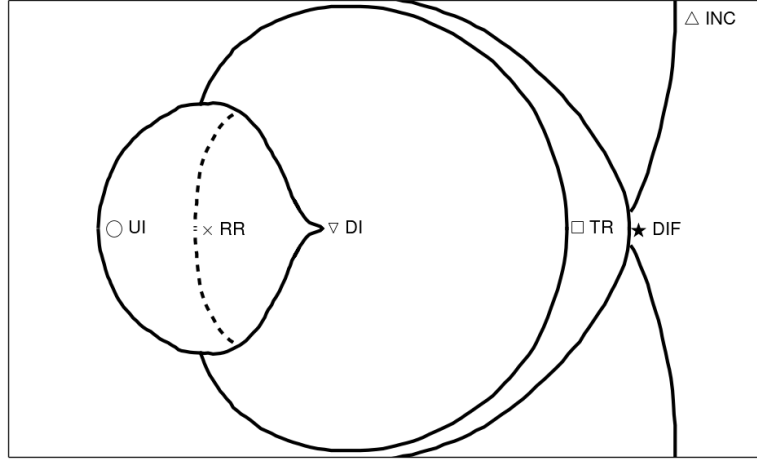


**Figure 10.5:** Schematic organization of flow patterns in shock wave/bubble interaction: *UI* = upstream bubble interface; *DI* = downstream bubble interface; *RR* = regular shock wave reflection on *DI*; *INC* = incident shock wave; *TR* = transmitted shock wave; *DIF* = wave diffraction, crossing of the two branches of the incident shock

is coarsened, and cells are discarded from the graded tree, leading to a drastic memory compression compared to the finest unique grid, with a reduction of 85 % of the number of cells compared to the finest mesh at the final dimensionless time  $t c_{R22,I}/d_0 = 1.15$ .

When the incident shock wave interacts with the R22 bubble, reflection and diffraction of the shock wave occur on the bubble interface as well as wave transmission through the bubble interface. To better describe the flow patterns observed in Figure 10.4, a schematic flow organization is proposed in Figure 10.5.

When the incident shock wave hits the upstream interface (UI) of the bubble, a part of the pressure jump is transmitted inside the bubble while another part is reflected upstream. Let us mention that this reflection of the incident shock wave on the upstream bubble interface (UI) has been omitted in this schematic view but is clearly visible in front of the bubble in Figure 10.4. The incident shock wave passing in Air around the bubble is diffracted along the bubble surface while the refracted shock wave (RR) moves inside the bubble. This refracted shock wave interacts with the downstream bubble interface (DI), creating both a shock wave transmitted inside Air (TR) downstream the bubble and a reflected shock wave moving upstream inside the bubble. As the speed of sound of R22 is lower than in Air, the transmitted shock wave (TR) finally stays upstream of the incident shock wave (INC) (See Figure 10.5). Finally, the diffracted shock wave reflects on the symmetry line creating two branches of the incident shock wave (DIF), mimicking branches of the diffracted shock wave coming from the lower and the upper sides of the bubble, crossing the symmetry plane as experimentally recorded [HS87].

As the high-pressure jump imposed by the incident shock wave interacts with the density jump located at the bubble interface, Richtmyer–Meshkov instabilities are distinctly visible in Figure 10.4 along with the bubble interface. These instabilities are characteristic of the acceleration of an interface between two fluids at different densities.

Simulation have been run with and without the proposed modified OSMP scheme introduced in chapter 8. A comparison of the temperature fields obtained with and without the proposed modification is presented in Figure 10.6. Without the proposed modification, spurious oscillations appear on the temperature field at the upstream interface of the R22 bubble (Figure 10.6) in the same way that observed with the one dimensional shock tube test in § 8.4.2. The new M-P criterion on  $\tilde{\alpha}_{N+1}$  with equations (8.15), and (8.16) cure these spurious oscillations, and improve the resolution of the mass

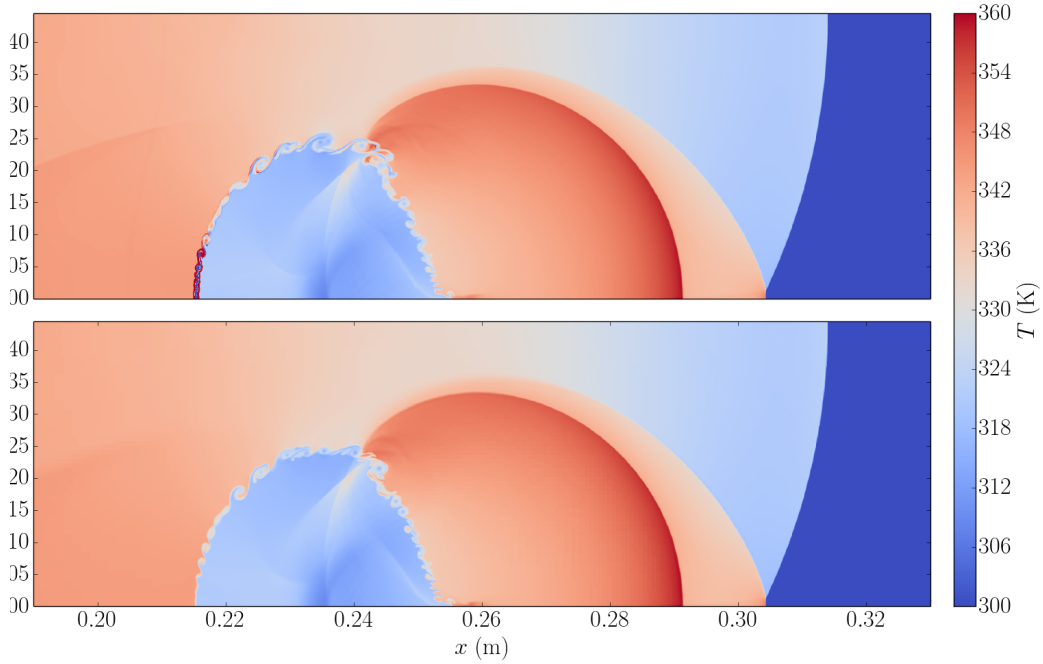


**Figure 10.6:** Temperature fields obtained with the 7<sup>th</sup>-order OSMP scheme with (at the bottom), and without (at the top) the proposed modification of the OSMP scheme.

fraction discontinuities. This confirms that the M-P condition on the supplementary invariant  $\tilde{\alpha}_{N+1}$  is needed to recover a stable solution with adapted values for the compressibility factors.

To validate present results for real gas flow, we compare them to experimental data coming from [HS87] on the  $x-t$  diagram (See Figure 10.7). To follow all the wave motions along time, we keep the same symbols like the ones used in the schematic view of flow patterns (See Figure 10.5). Although there is unavoidable variability in measurements, we can claim that a very good agreement is achieved by using the 7<sup>th</sup>-order MP scheme with the proposed modification on  $\tilde{\alpha}_{N+1}$ .

## 10.4 Conclusion

Multiresolution techniques are coupled with the previously described high-order numerical scheme in order to locally adapt the refinement with accuracy controlled using a threshold parameter  $\zeta$ . Such methods, already used in previous software, have proven their efficiency to give significant compression rates and gain in CPU time. Implementation in our work uses an iterative algorithm on tree data structure and guarantees a graded tree before each iteration of the numerical scheme. This implementation is very efficient but difficult to adapt for massive parallelization, which will limit us to realizing more extensive studies as described in the next. The efficient coupling between this multiresolution technique and our numerical method is illustrated with the example of a two-dimensional interaction between a shock and a bubble of dense gas that show efficient mesh adaptation and capture of the hydrodynamic instabilities like the Richtmyer-Meshkov instability on the edge of the bubble.

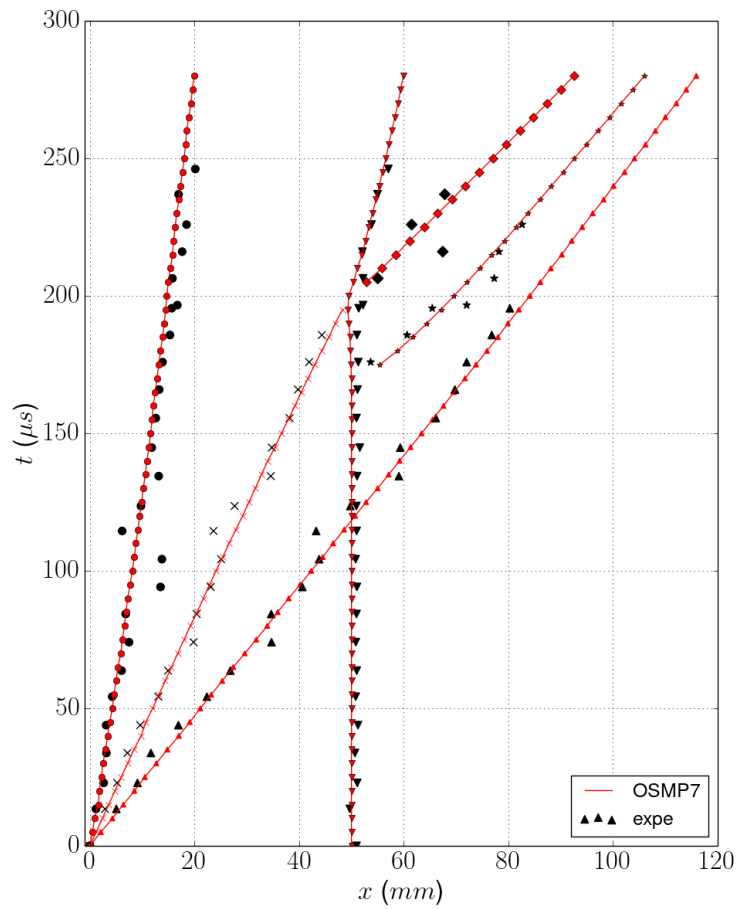


**Figure 10.7:**  $x - t$  diagram of the shock wave / R22 bubble interaction. Black dots are for experiments and lines with colored dots for simulations. Symbols related to the different waves are given in Figure 10.5.





# Immersed Boundary Method

## 11.1 Introduction

This chapter aims to describe the implementation of immersed boundaries in the computational volume to consider the impact of obstacles on the flow. Indeed, experimental devices such as those introduced in § 4.1.1 highlight the influence of obstacles on the flame acceleration phenomena and the condition of transition to detonation. Thus, numerous experimental [CD08], and numerical studies [GHO16][GOO07] realized in obstructed channels explore the influence of such geometries.

In order to consider solid obstacles inside the computational volume, an immersed boundary method has been implemented during the thesis. The advantage is adding boundary conditions on surfaces that are not necessarily aligned with the mesh. Thus there is no need to modify the computational mesh at the solid surface and allow us to use a cartesian mesh. The embedded solid is rigid and fixed in the computational domain in our studies. Thus no deformation or movement of the solid will impact the flow.

## 11.2 State of the art

Immersed Boundary Methods (IBM) have been initially introduced by Peskin [Pes72] in order to solve problematics of blood flow inside a heart with the necessity to consider fluid-structure interaction with elastic boundaries. Since then, numerous methods with integration of immersed boundary have been developed, a review of the main strategies have been realized in [MI05].

There are two major groups for IBMs methods, on the one hand, the *continuous forcing approach* with forcing function equivalent to source term integrated directly in the equations to enforce the boundary condition at the immersed boundary. On the other hand, the *discrete forcing approach* where boundary conditions are imposed through indirect means. This second method is not independent of the discretization but allows control of the conservation and stability properties, which is essential for compressible Navier Stokes computation, especially to capture shock waves interacting with solid.

Association between high-order numerical scheme and immersed boundary method for compressible flows have been investigated recently in [CHC11, BEBM18, KLM19, DZ21]. They generally required the integration of ghost cells inside the solid with an interpolation scheme to reproduce boundary conditions.

However, using only the ghost-cells approach may lead to non-conservative mass, momentum, and energy at the interface. This one is recovered using the Cartesian cut-cell approach, first introduced by Clarke et al [CSH86] for inviscid flows and later extended to viscous flows by Udaykumar et al. [USR96], and Ye et al. [YMUS99].

We use in this work the formalism described by Monasse et al. [MDM+12] and Puscas [PME+15] et al. that implement fluid-structure interaction using cut-cell finite volume approach and OSMP scheme for inviscid flows. The flux computation is realized by considering ghost cells inside the solid to reproduce the boundary conditions. Then, corrections are applied close to the boundary to achieve mass, momentum, and energy conservation.

Geometric considerations using the formalism of [MDM+12] allow describing cells crossed by solid called cut-cells and guarantee strict conservation of mass and energy. Specific treatments used to update the solution in the ghost cells, compute the exchange terms at the interface between solid and fluid and avoid numerical instabilities provoked by small cut cells are described in the following.

### 11.3 Integration of fluid-solid interface inside numerical solver

The integration of the embedded solid inside the numerical solver described in this work is done by adding three steps in the numerical solver described previously.

First, the geometrical configuration is computed, the entire solid cells and the cut cells by the embedded solid are isolated and described with geometrical parameters. The relevant quantities to integrate the embedded solid are described in § 11.3.1. In our simulations, the solid is fixed, then this step is required only at the beginning of the computation.

The second step consists of updating the ghost cells of the first layer of the solid cells before the computation of the Euler, and viscous operators integrated into the time operator splitting described in § 6. The method used for updating these ghost cells before each numerical operator and considering the direction of integration is described in § 11.3.2.

Finally, at the end of each iteration, the numerical integration of the cut-cells is recomputed using the computed flux, the geometrical parameters defined in the first step, and by adding the flux from the boundary. Particular treatment of the small cut-cells is also applied to avoid obtaining unstable integration when cell volume does not meet the CFL condition. This cut-cell finite-volume integration is described in § 11.3.3.

#### 11.3.1 Geometrical configuration

Close to the boundary, the geometrical configuration of the cut-cells is taken into account to compute the flux and guarantee local conservation.

Let  $C_{i,j,k}$  be a cut cell. Several geometric quantities are relevant to compute the numerical flux that are illustrated in Figure 11.1:

- The volume fraction,  $0 \leq \alpha_{i,j,k} \leq 1$  corresponds to the fraction of the cell occupied by the solid;
- The side area fractions  $0 \leq \kappa_{i\pm 1/2,j,k} \leq 1$ ,  $0 \leq \kappa_{i,j\pm 1/2,k} \leq 1$ ,  $0 \leq \kappa_{i,j,k\pm 1/2} \leq 1$ , corresponds to the fraction of each face of the mesh covered by the solid;
- The boundary area  $A_{i,j,k,\mathcal{F}}$  corresponds to the surface area of the face  $\mathcal{F}$  of the solid inside the mesh;
- The normal of each solid surface  $\mathbf{n}_{k,\mathcal{F}}$  of the face  $\mathcal{F}$  in the volume of fluid.

It can be noted that several faces can appear inside the mesh as illustrated in Figure 11.1 with their own values of area and corresponding normal vectors.

From a practical point of view, the resolution of these parameters and the configuration of the cut-cells are initialized at the beginning of the computation before the time iterations.

The algorithm introduced here operates on individual fluid grid cells, one at a time. The first part identifies the cut-cells, and the second part computes the polyhedron resulting from the intersection between the fluid grid cell  $C$  and each particle  $P$  composing the solid  $S$ .

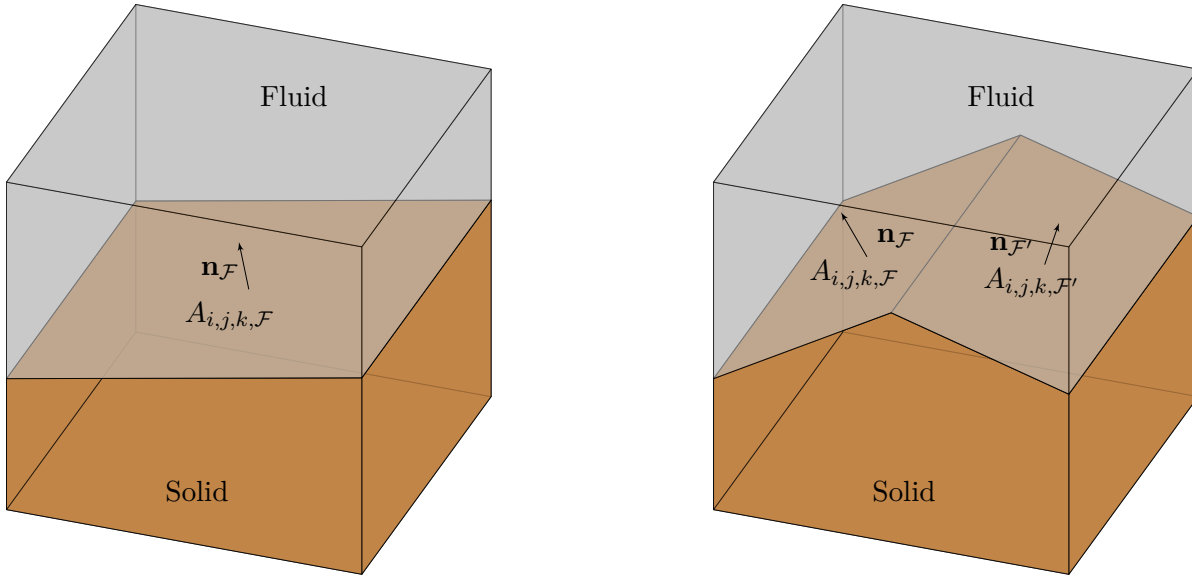


**Figure 11.1:** *Illustration of cut-cells intersected by one solid face for the left panel and two solid faces for the right panel*

1. Solid and cut cell are identified using the axis-aligned bounding boxes of the solid. A recursive algorithm on the graded tree described in Chapter 10 allows extracting the cells concerned quickly. However, such implementation implies that this algorithm does not work if the solid is not convex. In the case of a concave solid, we must then decompose it into a finite number of convex polyhedral particles.
2. The second part consists of obtaining in each cut cell the polyhedron formed by the intersection between the mesh cell and the immersed solid. The points of the polyhedron then correspond to:
  - the points of the cell present inside the solid;
  - the point of the solid present in the cell;
  - the intersection points between the edges of the cell and the solid;
  - in the case of a three-dimensional computation, we must add the intersection points of the edges of the solid with the faces of the cell.

The face of this polyhedron included on cell faces allow to compute the  $\kappa$ . The internal face not included on a cell face allow to extract the area  $A_{i,j,k,\mathbf{F}}$  and the normal  $\mathbf{n}_{\mathcal{F}}$ , and the volume of the polyhedron allow to obtain  $\alpha$ .

For the three-dimensional computation, the geometric tasks are handled using the Computational Geometry Algorithms (CGAL) Library. The three dimensions implementation is operational, although there are no such test cases in this work due to memory and calculation time issues, as we will discuss later.

### 11.3.2 Implementation of ghost cells inside the flow

The time operator splitting and the multidimensional splitting described in § 6 are run using ghost cells instead of solid cells to transcribe the impact of the boundary condition.

#### Interpolation of the symmetric point

The large stencil used in the OSMP7 scheme imposes to consider several layers of ghost cells inside the solid domain. Different strategies have been experimented to fill them. We choose to use here the values of the symmetric points of the ghost cell center across the boundary as a reference, as

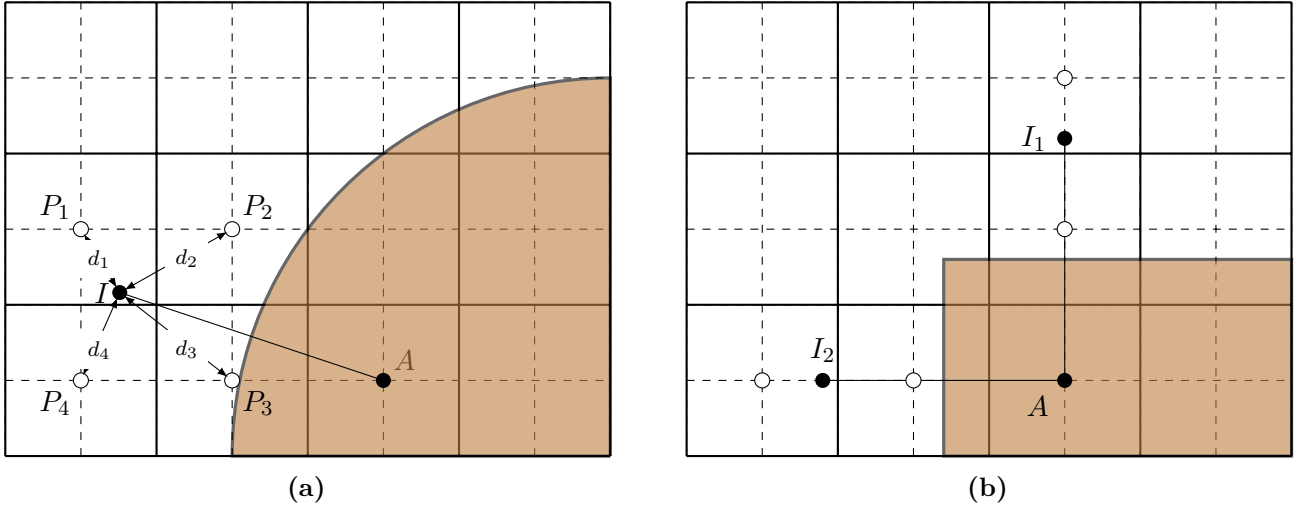


**Figure 11.2:** Schematic illustration of the interpolation of the symmetric point  $I$  of a ghost point  $A$  (left) in a general case (right) in the case of a sharp angle with distinction according to the integration direction

illustrated in Figure 11.2. This symmetric point does not necessarily correspond exactly to an existing fluid point because the boundary and the mesh are not always aligned. In that case, an interpolation is applied to estimate the value with more accuracy. This interpolation can be realized with various methods. We choose to reproduce here the strategy described in [CHC11] with a linear interpolation of variables  $\phi$  by using the values of the surrounding fluids points  $m$ :

$$\phi = \sum_m \omega_m \phi_m. \quad (11.1)$$

The weights  $\omega_m$  are computed with the inverse distance of the surrounding point  $\eta_m = 1/d_m^2$ , with  $d_m$  the distance to the symmetric point.

$$\omega_m = \delta_m \eta_m \left( \sum_k \delta_k \eta_k \right)^{-1}, \quad (11.2)$$

with  $\delta_k$  used to neglect the surrounding points inside the solid domain:

$$\delta_k = \begin{cases} 0 & \text{if point inside the solid,} \\ 1 & \text{otherwise.} \end{cases} \quad (11.3)$$

This interpolation is apply on values  $\rho Y_i$ ,  $u$ ,  $v$ ,  $w$ , and  $U$  instead of the conservative variables  $\mathbf{w}$  to avoid non-linear relations between variables.

Specific treatment is applied in the case of sharp angles to distinguish symmetric of the ghost cell according to the direction of integration of the numerical scheme. Indeed, the value of the ghost cell must be different according to the direction of integration during the multidimensional splitting scheme described in Chapter 6. The symmetric point considered to compute the ghost cell value will then be adapted close to an angle. The two distinct configurations according to the direction of integration are illustrated in Figure 11.2 in the case of a right angle corner.

Other interpolations methods to obtain value on the symmetric point with higher-order accuracy using, for example, polynomial approximation and Vandermonde matrix to estimate coefficients have been investigated [ZLL16, PHO+16]. However, the numerical simulations show that the order obtained at the boundary with our four-point interpolation is sufficient without using such methods and saves computational time.

## Boundary condition

The values of the ghost cells inside the solid domain depend on the condition imposed at the boundary. In the case of viscous flux, we use a no-slip velocity at the boundary, and the ghost cells are filled with the inverse velocity vector of the symmetric point:

$$\mathbf{u}_{ghost} = -\mathbf{u}_{sym}. \quad (11.4)$$

Without viscous flux, zero-normal condition at the solid body is imposed using a symmetric normal velocity at the boundary. The procedure we use to implement such zero-normal velocity condition is the same as the one used in [CHC11]. If we consider an arbitrary two-dimensional surface as shown in Figure 11.3, adiabatic walls with zero normal velocity conditions are enforced with:

1. Calculate the angle  $\theta$  between x-axis and velocity vector  $\mathbf{u}_{sym}$  of the symmetric point

$$\theta = \tan^{-1} \left( \frac{\mathbf{u} \cdot \vec{e}_y}{\mathbf{u} \cdot \vec{e}_x} \right). \quad (11.5)$$

2. Based on the quadrant in which  $\theta$  belongs, the angle is modify as:

$$\theta := (m + n)\pi + \theta, \quad \text{with} \quad m = \begin{cases} 0 & \text{if } 0 \leq \theta \leq \frac{1}{2}\pi, \\ 1 & \text{otherwise,} \end{cases}, \quad n = \begin{cases} 1 & \text{if } \frac{3}{2} \leq \theta \leq 2\pi, \\ 0 & \text{otherwise.} \end{cases} \quad (11.6)$$

3. Calculate  $\alpha$ , the angle between x-axis and the surface normal direction  $\mathbf{n}$ :

$$\alpha = \tan^{-1} \left( \frac{y_{sym} - y_{ghost}}{x_{sym} - x_{ghost}} \right). \quad (11.7)$$

4. Modify  $\alpha$  similar to  $\theta$  in step (3)

5. Calculate  $\gamma$  and  $\mathbf{u}_{ghost}$ :

$$\gamma = \pi + 2\alpha - \theta, \quad \mathbf{u}_{ghost} = |\mathbf{u}_{sym}| \begin{pmatrix} \cos(\gamma) \\ \sin(\gamma) \end{pmatrix}. \quad (11.8)$$

### 11.3.3 Finite volume integration of the cut-cells

At the end of the time iteration, the cut-cells will be corrected using the geometrical configuration by adapting the computed flux to the fluid interface, and boundary flux is added for each boundary face.

#### Conservative finite volume scheme

For a cut cell, we can reformulate the finite volume scheme using the Gauss theorem on a cut cell  $C_{i,j,k}$

$$\int_{t^n}^{t^{n+1}} \int_{\Omega_{i,j,k} \cap \Omega_F} \frac{\partial \mathbf{w}}{\partial t} dV dt + \int_{t^n}^{t^{n+1}} \int_{\partial(\Omega_{i,j,k} \cap \Omega_F)} \mathbf{F}(\mathbf{u}) \cdot \mathbf{n} dS dt = 0. \quad (11.9)$$

with  $\Omega_{i,j,k} \cap \Omega_F$  the intersection between the mesh and the volume of the solid and  $\partial(\Omega_{i,j,k} \cap \Omega_F)$  the wetted surface of the cut-cell. Considering the volume average of the conservating variables on the cut-cell

$$\mathbf{w}_{i,j,k} = \frac{1}{(1 - \alpha_{i,j,k})V_{i,j,k}} \int_{\Omega_{i,j,k} \cap \Omega_F} \mathbf{w} dx dy dz, \quad (11.10)$$

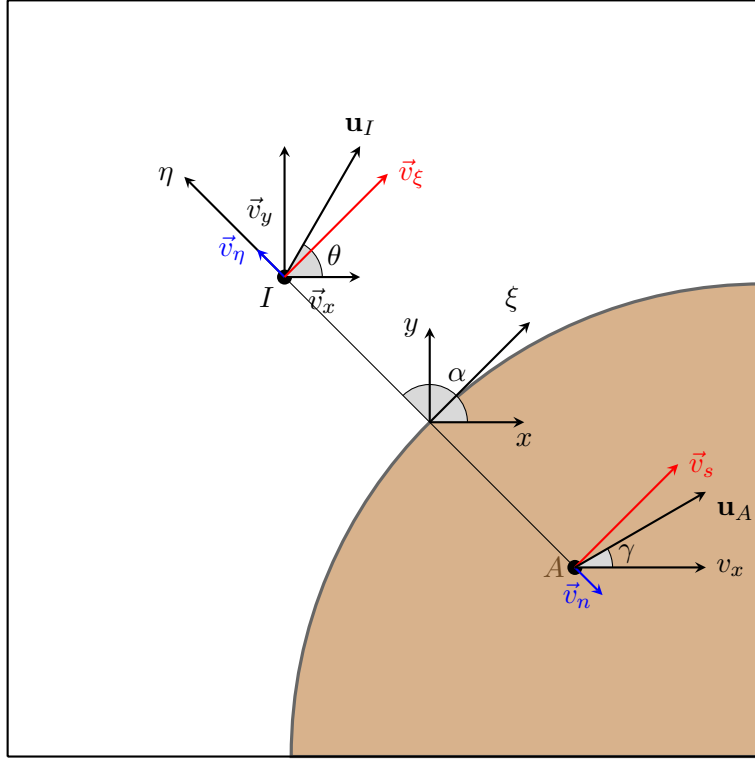


**Figure 11.3:** Schematic view for implementation of zero normal gradient of velocity at the solid surface.

we obtain the finite volume formulation

$$\begin{aligned}
(1 - \alpha_{i,j,k})\mathbf{w}_{i,j,k}^{n+1} &= (1 - \alpha_{i,j,k})\mathbf{w}_{i,j,k}^n \\
&+ \frac{\Delta t}{\Delta x_i} \left[ (1 - \kappa_{i-1/2,j,k})\mathbf{f}_{i-1/2,j,k} - (1 - \kappa_{i+1/2,j,k})\mathbf{f}_{i+1/2,j,k} \right] \\
&+ \frac{\Delta t}{\Delta y_j} \left[ (1 - \kappa_{i,j-1/2,k})\mathbf{f}_{i,j-1/2,k} - (1 - \kappa_{i,j+1/2,k})\mathbf{f}_{i,j+1/2,k} \right] \\
&+ \frac{\Delta t}{\Delta z_k} \left[ (1 - \kappa_{i,j,k-1/2})\mathbf{f}_{i,j,k-1/2} - (1 - \kappa_{i,j,k+1/2})\mathbf{f}_{i,j,k+1/2} \right] \\
&+ \frac{\Delta t}{V_{i,j,k}} \Xi_{i,j,k}.
\end{aligned} \tag{11.11}$$

The computation of the flux  $\mathbf{f}$  at the interface corresponds to the sum of the flux across each interface of the cell computed all along the time iteration step using ghost cells inside solid cells. It contains the contribution of the Euler and viscous operator and the different directions of integration included in the splitting scheme described in 6. The terms  $\Xi_{i,j,k}$  refer to the flux computed across the solid interface.

### Interface exchange term

In (11.11), the term  $\Xi_{i,j,k}$  corresponds to the flux exchanged between the solid and the fluid.

We suppose we can have multiple faces inside each cell, the flux  $\Xi_{i,j,k}$  across the solid interface of the cell then correspond to the sum of all the individual contributions of each interface  $ele$  inside the computational cell:

$$\Xi_{i,j,k} = \sum_{ele} \Xi_{ele}. \tag{11.12}$$

For the Euler operator, there is no material transfer, and the numerical flux at the interface is computed from the value of the pressure extrapolated at the solid interface. This extrapolation is made by using the evolution of the pressure several points along the normal to the face obtained by interpolation on the neighboring fluid points just as described for the computation of the ghost cell by symmetric point in §11.3.2.

For the viscous operator,

$$\Xi_{\mathcal{F}} = \mathcal{A}_{\mathcal{F}} \mathbf{n}_{\mathcal{F}} \begin{pmatrix} 0 \\ \vdots \\ 0 \\ \sigma_{\mathcal{F}} \mathcal{A}_{\mathcal{F}} \mathbf{n}_{\mathcal{F}} + P_{\mathcal{F}} \\ \lambda_{wall} \Delta T \end{pmatrix}, \quad (11.13)$$

with  $\sigma_{\mathcal{F}}$  the viscous strain tensor at the wall similar to (5.4) is computed at the interface with the hypothesis of zero-velocity boundary condition at the solid surface as done in the work of Dragojlovic et al. [DND06].

$$\sigma = \mu_{wall} \left( \nabla \mathbf{u} + \nabla^t \mathbf{u} - \frac{2}{3} (\nabla \cdot \mathbf{u}) \mathbb{I} \right). \quad (11.14)$$

The value of the pressure  $P_{\mathcal{F}}$ , and temperature  $T_{\mathcal{F}}$  on the surface are extrapolated with the value interpolated on the normale of this face. We consider in our simulations three points respectively located at  $0.5\Delta x$ ,  $1.5\Delta x$ , and  $2.5\Delta x$  on the normal of each face to compute a polynomial extrapolation. In the case of low resolution, which does not properly capture the boundary layer, this extrapolation method can also be adapted by considering a few points. Finally, dynamic viscosity  $\mu_{wall}$  and thermal conductivity  $\lambda_{wall}$  are computed from the thermodynamic state obtained on the face.

### Treatment of the small cut cells

An additional difficulty with this cut-cell finite volume approach is the creation of very small cut-cells by integrating an arbitrary solid in the regular mesh. Since the Courant number is inversely proportional to the cell dimension, the CFL stability condition becomes too restrictive to adapt the time step to the size of the smallest cut-cells.

Different methods have been developed in the literature to avoid such numerical instabilities without dramatically increasing computational time with so-called cell-merging [YMUS99], cell-linking [KAK03], or flux redistribution method [HKAH06].

In order to avoid excessive small time steps, we employ the flux redistribution strategy initially developed in [HKAH06]. This method mixes the fluid in small cells with neighboring cells we call *targeted* cells. This mixing procedure is applied when the volume fraction  $\alpha_{i,j,k}$  of the cell exceeds a threshold value that we took in our computations at  $\alpha_{th} = 0.5$ . The targeted cells are the neighboring cells that do not exceed this threshold value.

Then the conservative quantities of the corresponding cells are updated by:

$$(1 - \alpha_{i,j,k}^{n+1}) \mathbf{w}_{i,j,k}^{n+1} = \left( (1 - \alpha_{i,j,k}^{n+1}) \mathbf{w}_{i,j,k}^{n+1} \right)^o + \sum_{trg} \mathbf{M}_{i,j,k}^{trg}; \quad (11.15a)$$

$$(1 - \alpha_{trg}^{n+1}) \mathbf{w}_{trg}^{n+1} = \left( (1 - \alpha_{trg}^{n+1}) \mathbf{w}_{trg}^{n+1} \right)^o - \mathbf{M}_{i,j,k}^{trg}. \quad (11.15b)$$

with the subscript  $o$  corresponds to the conservative variable previously computed with (11.11). The exchange of conservative quantities  $\mathbf{M}_{i,j,k}$  from the problematic small cell  $\mathcal{C}_{u,j,k}$  to the targeted cells  $\mathcal{C}_{trg}$  is computed as:



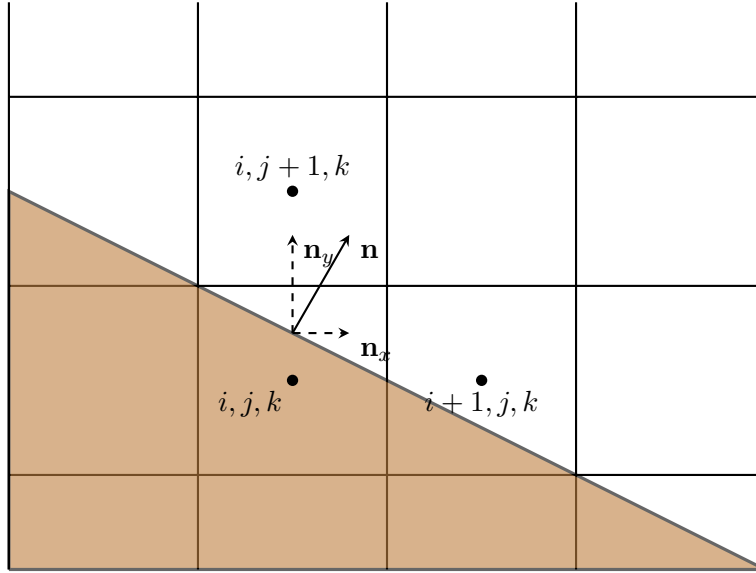


**Figure 11.4:** Small cut cells  $C_{i,j,k}$  and its two targeted cells  $C_{i,j+1,k}$  and  $C_{i+1,j,k}$

$$\mathbf{M}_{i,j,k} = -\mathbf{M}^{trg} = \frac{\beta_{i,j,k}^{trg}}{2 - \alpha_{i,j,k} - \alpha_{trg}} [(\alpha_{trg} \mathbf{w}_{trg}) \alpha_{i,j,k} - (\alpha_{i,j,k} \mathbf{w}_{i,j,k}) \alpha_{trg}], \quad (11.16)$$

where the  $\beta_{i,j,k}^{trg}$  are the weights associated to each targeted neighboring cells. We choose to apply to the targeted cell weight based on the normal direction  $\mathbf{n}_{i,j,k}$  of the internal face of the small cut cell as illustrated in the Figure 11.4:

$$\beta_{i,j,k}^{trg} = \left| \left( \sum_{ele} \mathbf{n}_{ele} \right) \cdot \mathbf{n}_{i,j,k}^{trg} \right|^2. \quad (11.17)$$

where  $\mathbf{n}_{i,j,k}^{trg}$  corresponds to the normal direction of the interface between the small cell and the targeted cell. To ensure consistency, the weights are normalized in order to respect:

$$\sum_{trg} \beta_{i,j,k}^{trg} = 1. \quad (11.18)$$

## 11.4 Numerical results

The developed immersed boundary method is used to compute 2D flow around geometric structures. First a cylinder is placed in a uniform free-stream with Reynolds number  $Re_D = 40$  and  $Re_D = 200$  to consider respectively steady and unsteady with periodic vortex shedding flow regimes. Those classical test cases usually served as validation cases immersed boundary implementation.

A shock/boundary interaction is also realized corresponding to the so-called Schardin's problem investigating the shock wave diffraction over a finite wedge the interaction with the tip vortices.

### 11.4.1 Flow around a cylinder at different Reynolds

We test here the computation of subsonic flows around an immersed infinite circular cylinder at different Reynolds numbers. The cylinder has a diameter  $d = 2$  cm. The computational domain has a  $L_y = 10d$  transverse dimension and a  $L_x = 40d$  streamwise dimension (Figure 11.5). The cylinder is positioned at the coordinates  $(0.2, 0)$ . The left boundary corresponds to a subsonic inflow with imposed velocity  $U_\infty$  and temperature  $T_0$ , and the right boundary condition is a subsonic non-reflecting

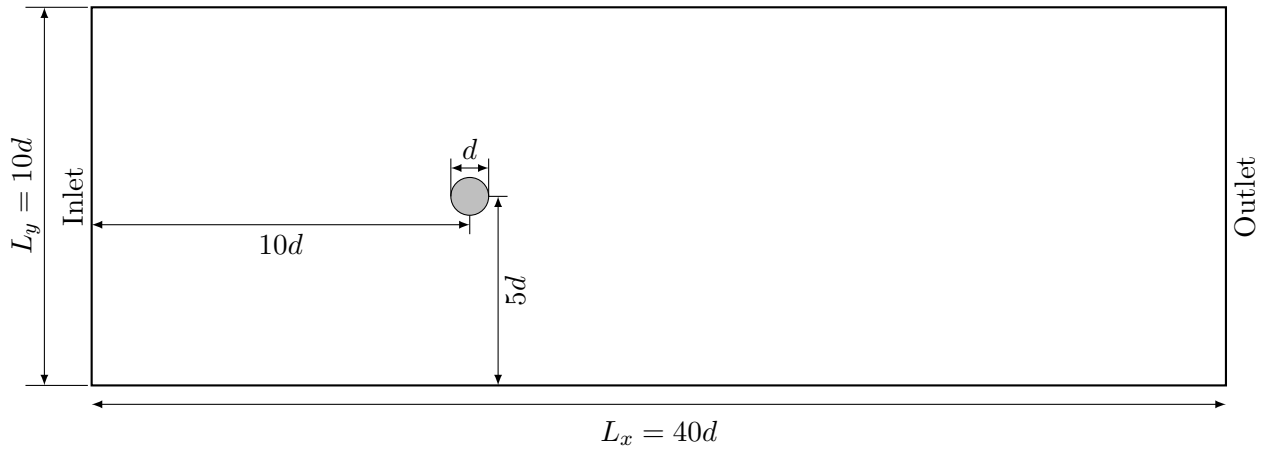


**Figure 11.5:** Sketch of the computational domain for subsonic flow around a cylinder

outflow with static pressure at infinity  $p_\infty$  set at atmospheric pressure. Those boundary conditions are set using the Navier Stokes Characteristic Boundary Conditions (NSCBC) strategy described in [PL92]. The choice of such lateral boundary conditions and the length of the computation domain of 40 diameters must avoid their influence on the flow around the cylinder. Finally, slip boundary conditions are imposed at the bottom and the top by applying symmetric conditions on the velocity.

The multiresolution method for adaptive mesh refinement as described in Chapter 10 is used in the simulation. The computational mesh is composed of 8 tree structures along the streamwise direction and two in the transverse direction. The trees are composed of eight grid levels corresponding to a smallest grid size of  $\Delta x = 0.39$  mm which corresponds expressed with the cylinder diameter respectively to  $\Delta x = d/25$  and  $\Delta x = d/50$ . This refinement gives converged values for the tested coefficients. The cylinder is approximated with 180 points read at the initialization of the computation to calculate the geometry of the cut-cells. The Figure 11.6 represents the volume fraction  $\alpha$  of the cut cells occupied by the solid for the coarse grid (with seven levels trees). Cells with volume fraction less than 0.5 will follow the mixing procedure described in § 11.3.3.

### Computation with $Re = 40$

Computation is performed with Reynolds numbers  $Re = \rho U_\infty d / \mu_l = 40$  and  $Re = 200$ , where  $\mu_l$  is the dynamic viscosity of the fluid. The mixture corresponds to Air with  $Y_{O_2} = 0.233$  and  $Y_{N_2} = 0.767$ . The free-stream velocity  $U_\infty$  is set to 15 m/s and the density  $\rho$  to 1 which correspond to a Mach number of  $Ma = 0.04$  small enough to not have compressible effects and be comparable to the simulations performed using incompressible solvers. The value of the constant dynamic viscosity is adapted to the value of the Reynolds number.

The force on the cylinder is given by the sum of the pressure and wall-shear stress on the surface of the cylinder:

$$F_{\mathcal{F}} = -p_{\mathcal{F}} + \tau_{\mathcal{F}}. \quad (11.19)$$

The expression of the drag coefficient  $C_D$  and lift coefficient  $C_L$  reads:

$$C_D = \frac{2F_D}{\rho U_\infty^2 d} i, \quad \text{and} \quad C_L = \frac{2F_L}{\rho U_\infty^2 d}, \quad (11.20)$$

with the drag and lift force  $F_D$  and  $F_L$  computed by integration of respectively the x-component and the y-component of the total force on the cylinder surface:

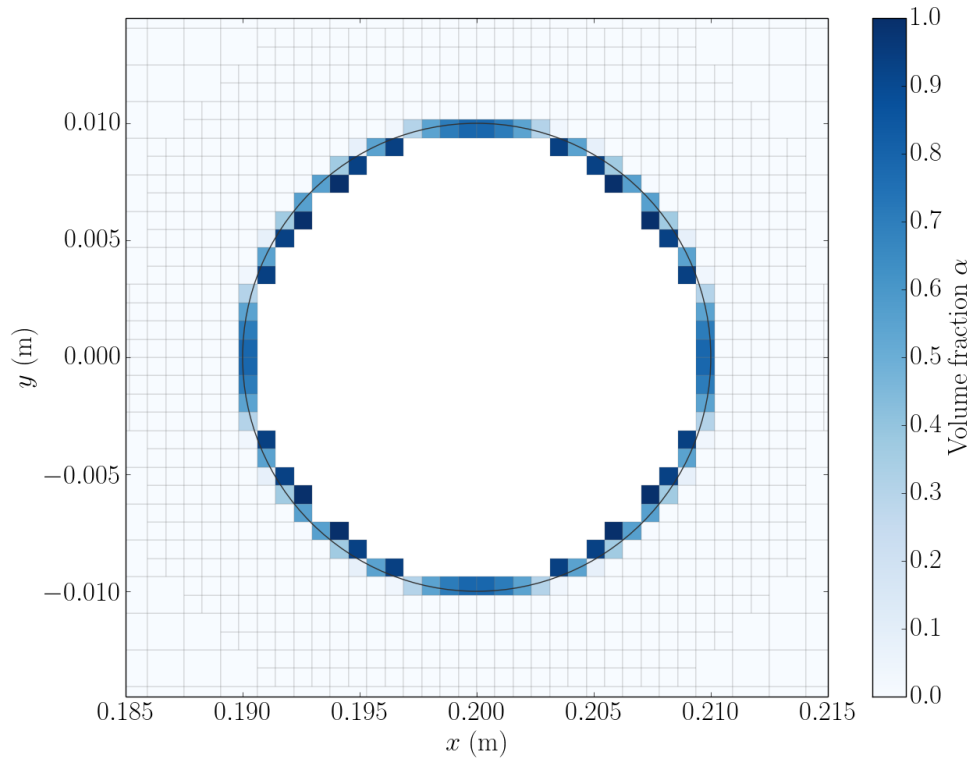


**Figure 11.6:** Volume fraction of cut cells around immersed cylinder with initial mesh with seven levels of refinement.

	$L/d$	$a/d$	$b/d$	$\theta$	$C_D$
De Palma et al. [DdPN06]	2.28	0.71	0.60	$53.8^\circ$	1.55
Gautier et al. [GBL13]	2.24	0.71	0.60	$53.6^\circ$	1.49
Di Mascio et al. [DZ21]	2.25	0.71	0.59		1.49
Khalili et al. [KLM19]	2.22	0.72	0.59	$53.1^\circ$	1.52
This work	2.17	0.712	0.587	$51.6^\circ$	1.75

**Table 11.1:** Physical parameters of the flow pattern around a circular cylinder at  $Re = 40$ : wake length  $L/d$ , location and recirculation centre  $(a,b)$ , separation angle  $\theta_s$  and drag coefficient  $C_D$

$$F_D = - \oint F_{\mathcal{F}}^x dx \quad \text{and} \quad F_L = - \oint F_{\mathcal{F}}^y dy. \quad (11.21)$$

Experimentally, the periodic vortex shedding first appears for Reynolds numbers around 50. For smaller Reynolds numbers, the flow is found to be steady. Results for the steady regime of Reynolds number  $Re_D = 40$  is shown in Figure 11.7 with the pressure field and the velocity component contours for the two grid levels.

The pair of attached, steady, symmetric vortices behind the cylinder has specific dimensions that can be compared to the precedent experimental and numerical studies. Figure 11.8 presents the usual physical parameters observed for such configuration with the wake length  $L$  and the recirculation center  $(a,b)$ . Table 11.1 reports this measured value and the computed value of the drag coefficient  $C_D$  with a comparison of results published in the literature.

At this point, the  $C_D$  value steps aside from the reference values. The reason for such differences in the drag coefficient value is still being investigated (error in implementation, computation of the viscous

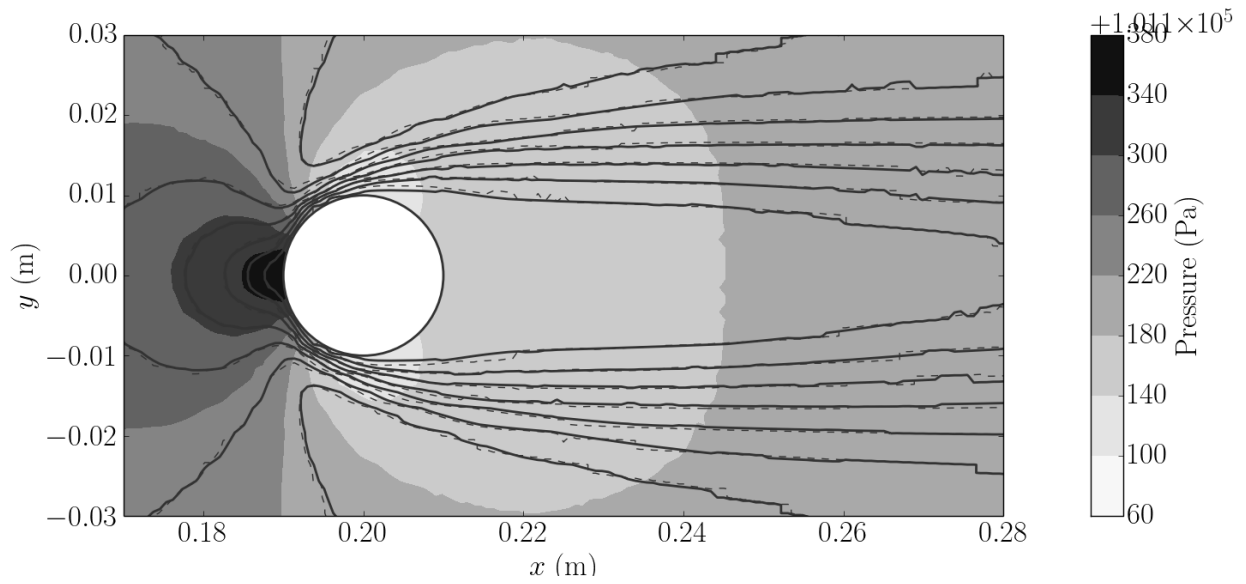


**Figure 11.7:** Pressure field at the finest level and velocity component computed on the seven levels grid (dashed lines) and the eight levels grid (solid lines) for  $Re = 40$

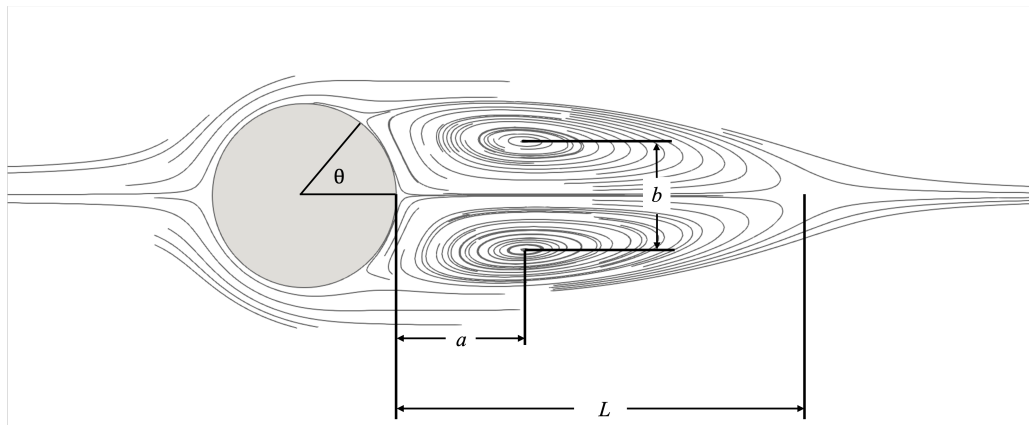


**Figure 11.8:** Physical parameters of the flow pattern for steady flow used in Table 11.1

tensor...). We are still working on improving the estimation of the boundaries values to update these values with consistent results.

### Computation with $Re = 200$

With more important Reynolds, the flow becomes unsteady and periodic shedding vortex are generated behind the cylinder. Figure 11.9 shows snapshots of the vorticity at different times.

The Strouhal number  $St$  is defined as the dimensionless frequency at which the vortices are shed downstream of the cylinder:

$$St = f_{st} \frac{d}{U_{\infty}}, \quad (11.22)$$

with  $f_{st}$  the vortex shedding frequency. This frequency is deduced from the Fourier transform of the temporal evolution of the transverse velocity behind the cylinder.

The computed Strouhal number  $St$  and the drag coefficients  $C_D$  and lift coefficients  $C_L$  are reported in Table 11.2.

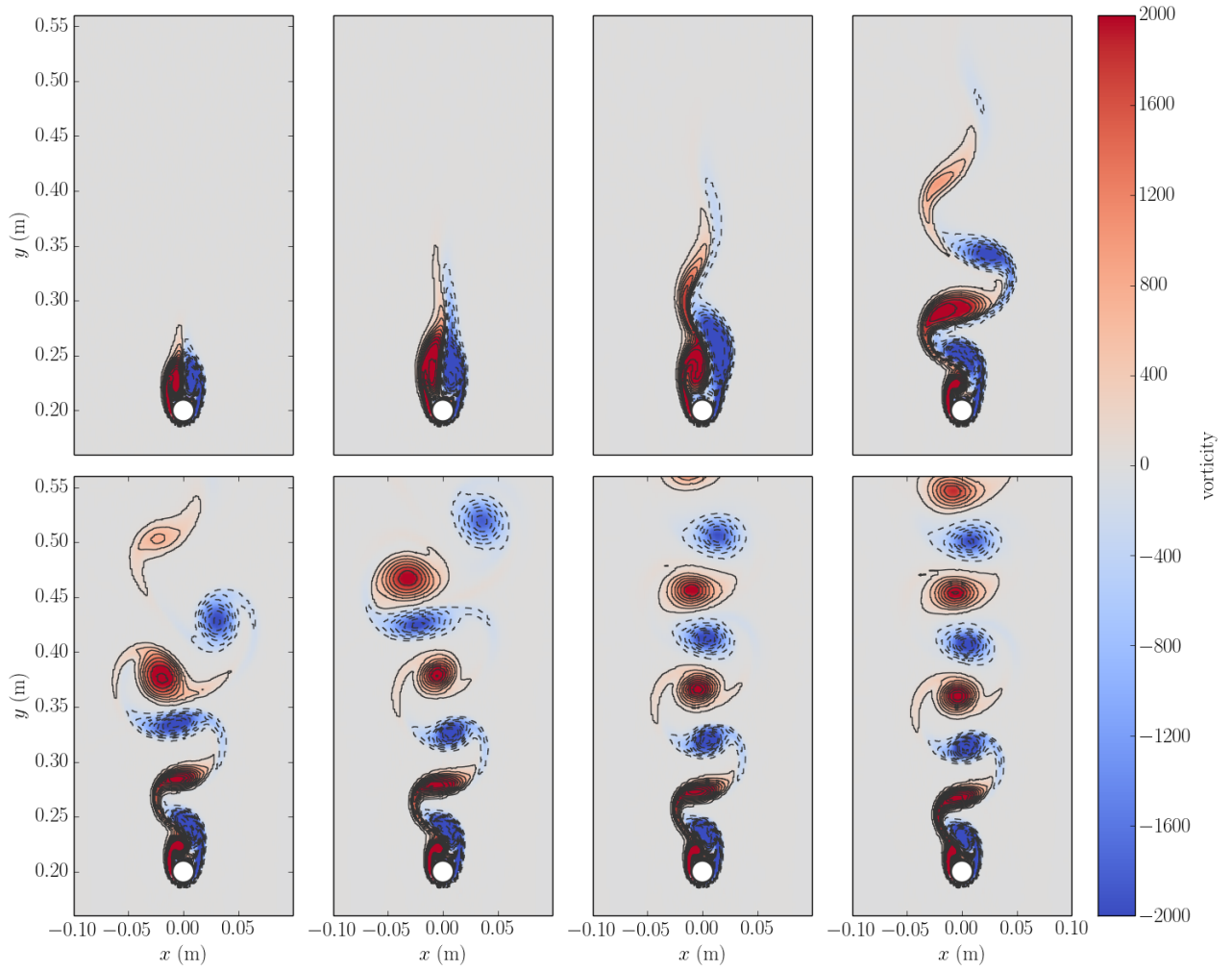


**Figure 11.9:** Vorticity contours from left to right at  $t = 5$  ms,  $t = 10$  ms,  $t = 15$  ms,  $t = 20$  ms,  $t = 25$  ms,  $t = 30$  ms,  $t = 40$  ms, and  $t = 50$  ms

	$St$	$C_D$	$C_L$
Linnick [LF05]	0.197	$1.34 \pm 0.044$	$\pm 0.69$
De Palma et al. [DdPN06]	0.190	$1.34 \pm 0.045$	$\pm 0.68$
Khalili et al. [KLM19]	0.191	$1.29 \pm 0.042$	$\pm 0.64$
This work	0.191	$1.714 \pm 0.0668$	$\pm 0.883$

**Table 11.2:** Unsteady flow past at circular cylinder at  $Re = 200$ : Strouhal number  $St$ , drag coefficient  $C_D$ , and lift coefficient  $C_L$ .

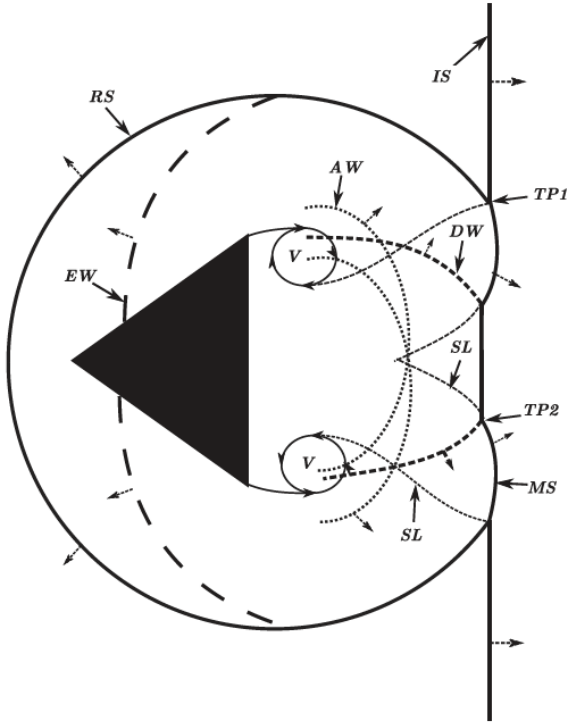


**Figure 11.10:** Description of the various waves arising in the Schardin's problem. AW: accelerated wave, DW: decelerated shock-wave, EW: expansion wave, IS: incident shock-wave, MS: Mach stem, RS: reflected shock-wave, SL: slip layer, TP1 and TP2: triple points, V: vortex. (issued from [BEBM18])

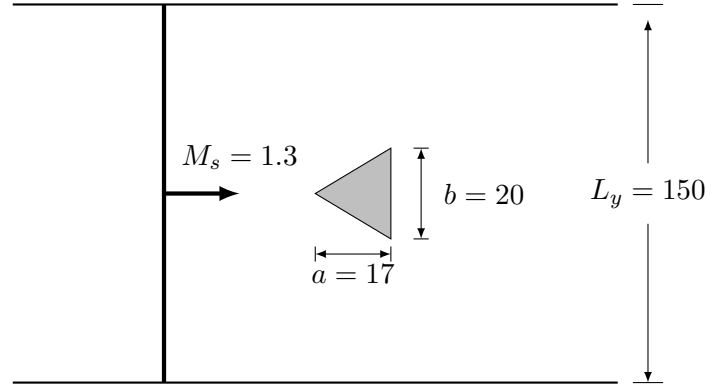


**Figure 11.11:** Schematic diagram of Schardin's problem, all the dimension are in mm

Similar to the previous results, our values for the integral of the force on the cylindre is overestimated.

#### 11.4.2 Shock wave interaction with two dimensional wedge

This test case consists of the impingement of a planar shock wave on an infinite two-dimensional wedge. It corresponds to an experimental device realized by Schardin [Sch57] in 1957. A Mach 1.30 shock interacts with a wedge and generates multiple compressible structures with Mach stems and triples points, reflected and scattered shocks, and vortices behind the wedge. This simulation is reproduced from [CC00] that also provides the experimental values. Figure 11.10 is a schematic diagram of various waves appearing in the problem with multiple Mach stems, triple points, reflected (attenuated and accelerated) shocks, slip-lines, and vortices.

The static pressure and temperature of the low-pressure side are taken 0.05 MPa and 300 K, respectively. The mixture is Air with  $Y_{O_2} = 0.233$  and  $Y_{N_2} = 0.767$ . The top and bottom correspond to slip walls, non-reflective boundary conditions are set on the inlet and the outlet.

Figure 11.11 display the computational domain, the time  $t = 0$  corresponds to the contact of the shock wave with the front vertice of the wedge. The computational mesh is composed of  $4 \times 3$  tree structures. We perform the simulation with different grids from eight to ten maximum levels of trees corresponding to cells of size  $\Delta x = 0.19$  mm for the 8th level,  $\Delta x = 97 \mu\text{m}$  for the 9th level, and  $\Delta x = 49 \mu\text{m}$  for the 10th level.

The general waves structure is well recovered in all refinement cases. Figure 11.12 compared the triple point (TP1) and (TP2) and locus vortex core (V) trajectories obtained with experimental and values of literature. Their evolution is in good agreement with previous results. Compressible flow-field characteristics are well-captured.

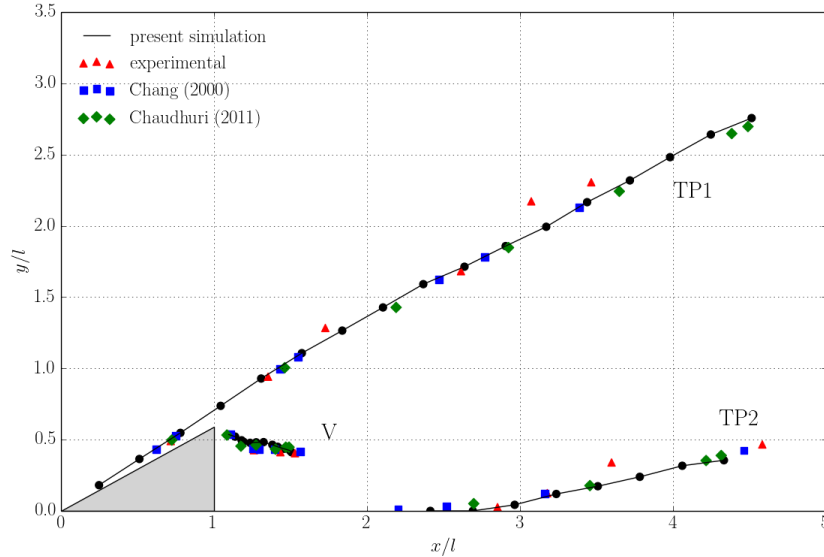


**Figure 11.12:** Comparison of triple point trajectory and locus of the vortex center

However, the small vortices generated behind the vertices and visible on the experimental results require refinement of order 10 to be observed. Figure 11.13 displays a sequence of Schlieren snapshots that illustrates the flow evolutions.

Instantaneous numerical shadowgraph picture at  $t = 151 \mu\text{s}$  is compared with the experimental shadowgraph reported in [CC00] on Figure 11.14.

## 11.5 Conclusion

Immersed Boundary Methods are integrated into the numerical scheme working on a cartesian mesh to consider complex geometry formed by obstacles in the flow. The implementation is based on the Cartesian cut-cell approach described in [MDM<sup>+</sup>12] and [PME<sup>+</sup>15] to guarantee the strict conservation of the conservative values. Then, the initialization of the cut-cell geometric configuration is realized at the initialization of the computation. A set of ghost cells is updated before each integration scheme according to the boundary conditions to apply the different high-order operators. Then a final integration of the cut cells is realized at the end of the time step to adapt the cut-cell conservative values using the interface exchange term.

The current implementation has been tested with a standard test case involving flow around the cylinder at different Reynolds and shock wave interaction with a two-dimensional wedge. The results obtained are consistent with physical observations, but with overestimated drag and lift coefficient is noticed for now.

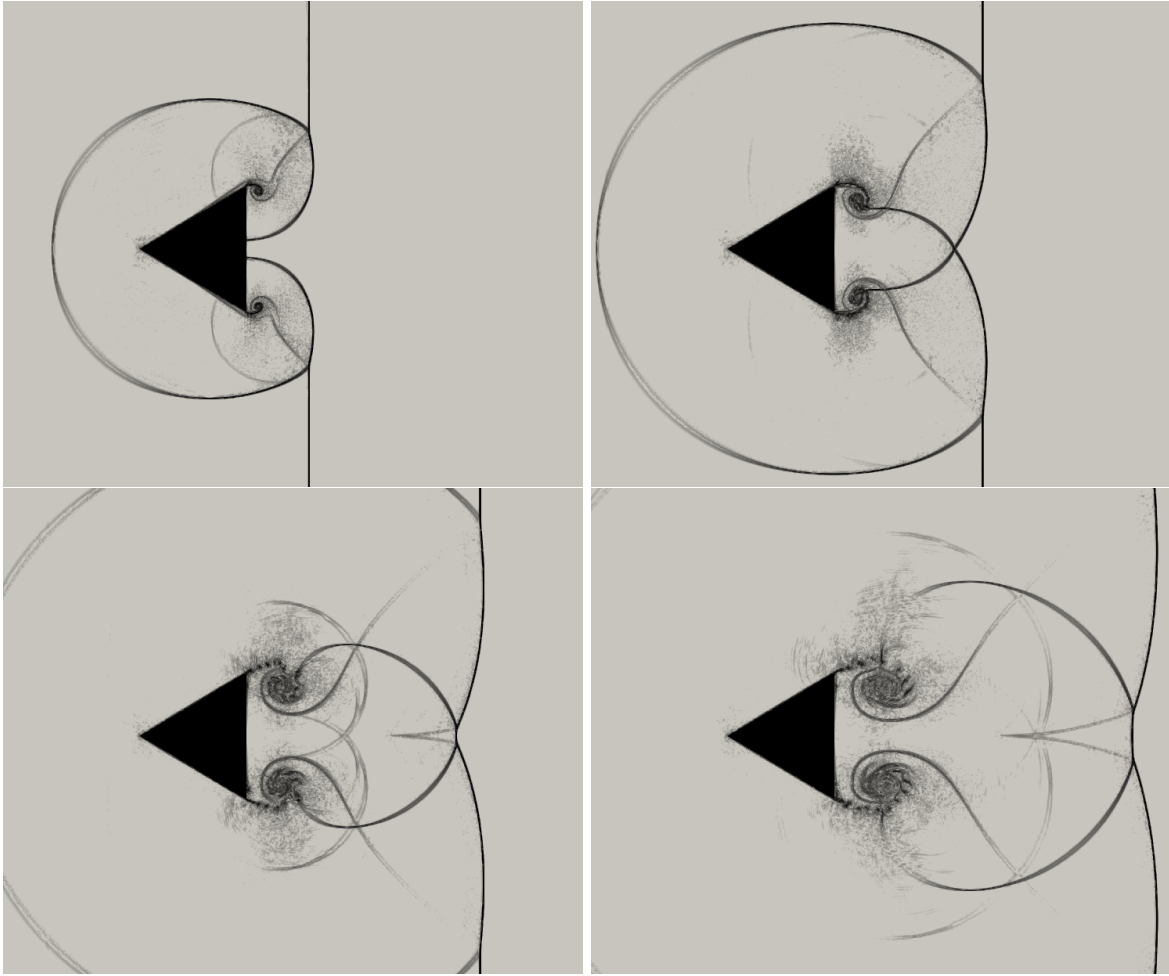


**Figure 11.13:** *Schlieren snapshots from top left to bottom right at  $t = 60 \mu s$ ,  $t = 90 \mu s$ ,  $t = 120 \mu s$ , and  $t = 150 \mu s$*

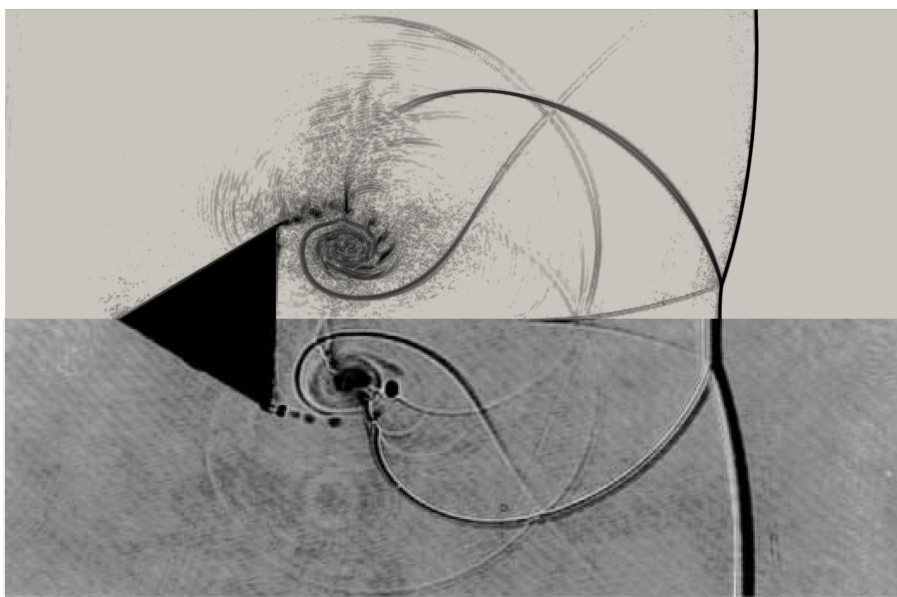


**Figure 11.14:** *Comparison of numerical shadowgraph (top-half) and experimental shadowgraph [CC00] (bottom-half) at  $151 \mu s$*





# In Situ Adaptive Tabulation (ISAT) for Multi-Scale Reaction Waves

As we will see in the applications in Part IV, the calculation of the different steps of the flame acceleration from the initial instabilities to the calculation of the detonation requires an important refinement. Despite the use of multiresolution methods, large meshes and small-time steps are required to correctly capture the phenomena impacting the flame acceleration, especially for three-dimensional calculations. To deal with those important CPU time, we had implemented OpenMP directives to share the memory between different processors and perform parallel computations. Another way considered to improve the numerical performance of the simulation is to use some chemistry acceleration method.

In our simulation with hydrogen combustion, we deal with 11 species and 39 reactions. With the time splitting strategy described in chapter 6, and especially with the Radau5 solver, which uses a time-stepping strategy based on jacobian computation and sub-iterations, the computational time used by the reaction operator can become very high.

Multiple strategies have been studied to cope with the cost of detailed kinetics simulations: Identification of Low-Dimensional Manifolds (IDLM [MP92] and REDIM [BM07]), flamelet models (FPV [PM04], FGM [Oij02]), Analytical Reduced Chemical mechanism (ARC [Pep08])... Since detailed chemistry for hydrogen simulation involved a limited number of species, the In Situ Adaptive Tabulation (ISAT) method built dynamic tabulation for stiff reaction operator seems to be quite adapted to our cases.

In this chapter, we discussed the performance of the ISAT computational time reduction strategy and the approximation introduced by such methods for the case of one and two-dimensional detonation.

## 12.1 In Situ Adaptive Tabulation (ISAT)

The ISAT method consists of building a dynamic table that stores a list of recorded points to quickly retrieve an estimation of a non-linear system like, in our case, the reactive terms solution. It has been initially described by Pope [Pop97] and since used in multiple configurations. It has been first adapted for homogeneous or quasi-homogeneous systems resulting in a computation time speedup factor of several orders of magnitude, but it has also been tested with transient phenomena like in internal combustion engine simulations [CJLD11, RLL<sup>+</sup>14, WZZ<sup>+</sup>17] or in detonation front simulation [DFC07, WDL18] with still good speedup factors. LES of flame acceleration and DDT with hydrogen flame mixture have also been tested [EMSM15]. They are often combined with other dimension reduction techniques and skeletal mechanisms when using a high number of reactions. However, this is not necessary here with hydrogen chemistry that involves a limited number of species.

We have based our implementation on the ISAT-CK7 algorithm available in open-source in [PHL<sup>+</sup>12].

This algorithm has been adapted to our test cases and linked to our computational code. The main guidelines of the ISAT-CK7 algorithm are summarized here. A more precise description of its implementation is available on [HE17].

### 12.1.1 Description of the approximation

We consider a set of variables to describe the local thermodynamic state. Along the reaction time-step  $\Delta t_{reac}$ , the computation of the reaction corresponds to an isochore transformation that preserves the internal energy. To characterize the thermodynamic state, we will then use the vector of variables:

$$\Phi = (U, \rho, Y_1, \dots, Y_{ns}). \quad (12.1)$$

We denote  $R(\Phi)$  the thermodynamic state obtained after the time step  $\Delta t_{reac}$  from an initial state  $\Phi$ .

The objective of the ISAT method is to obtain a fast approximation of the thermodynamic state of local points based on pre-recorded points while guaranteeing a tolerance criterion  $\epsilon_{tol}$ .

A linearized mapping makes the approximation from a recorded point. Let  $\Phi^q$  a point close to a pre-existing point  $\Phi^o$  in the tabulation.

$$\Phi^q = \Phi^o + \delta\Phi. \quad (12.2)$$

The approximation of the thermodynamic state  $R(\Phi^q) = \Phi^q(t + \Delta t_{reac})$  is then obtained using a linearized approximation computed with:

$$R(\Phi^q) = R(\Phi^o) + \frac{\partial R(\Phi^o)}{\partial \Phi^o} \delta\Phi + \mathcal{O}(|\delta\Phi|^2). \quad (12.3)$$

In order to control the error made by the linearized mapping, a *tolerance criteria*  $\epsilon_{tol}$  is applied on the results of  $R(\Phi^q)$ . An *Ellipsoid of accuracy* (EOA) based on the tolerance criteria is associated with each tabulated point. This EOA of a recorded point  $\Phi^o$  is described by the matrix  $\mathbf{M}$  such as:

$$\epsilon_{tol}^2 = \delta\Phi^T \mathbf{M} \delta\Phi, \quad (12.4)$$

At the initialization of a new point, the EOA is defined by:

$$\mathbf{M} = \mathbf{A}^T \mathbf{B}^T \mathbf{B} \mathbf{A}, \quad (12.5)$$

with  $\mathbf{A} = \frac{\partial R(\Phi^o)}{\partial \Phi^o}$  the sensitivity matrix and  $\mathbf{B}$  the scaling matrix applied to normalized the terms of the thermodynamic state. This region of accuracy is sketched in Figure 12.1.

Since reactive terms are non-linear terms, the local final thermodynamic state  $R(\Phi^q)$  can respect the tolerance criterion and yet be outside of the EOA of the recorded point  $\Phi^o$ . In that case, the EOA associated with the recorded point  $\Phi^o$  is enlarged to enclose the new point  $\Phi^q$  while keeping a minimum volume for the ellipsoid centered on  $\Phi^o$ . This growth algorithm is illustrated in Figure 12.1.

In our implementation, we have added a distance limit with the closest recorded point to avoid creating a very large EOA. Such issue has indeed been met with initially recorded points in the non-reactive zone that create initially too large EOA and inhibit the mixture's auto-ignition that must be recorded with new points.

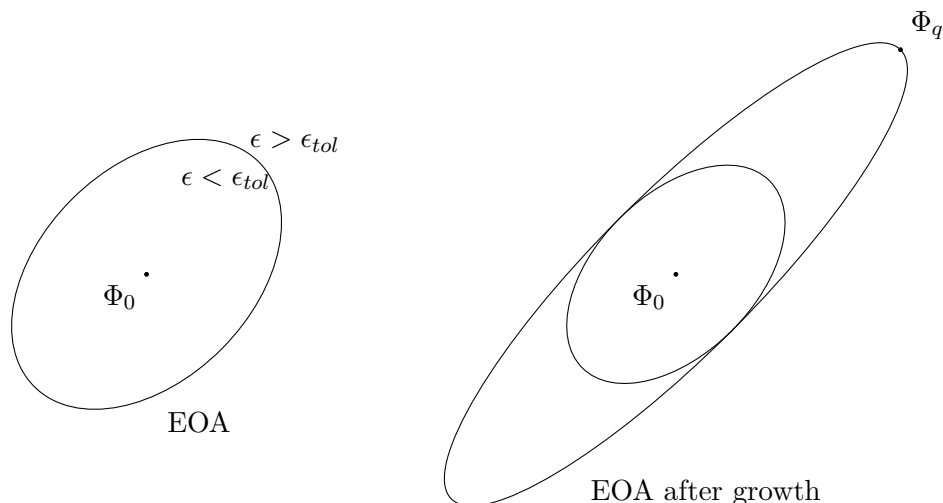


**Figure 12.1:** Schematic diagram of the region of accuracy and its growth

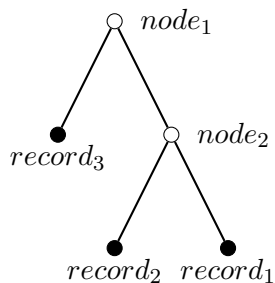


**Figure 12.2:** binary tree

### 12.1.2 Construction of the table

A point of the ISAT table *record* is thus constituted of its initial state  $\Phi^o$ , its final state  $R(\Phi^o)$ , its sensitivity matrix to carry out the linear approximation, and its EOA to guarantee the respect of the tolerance criterion and which can evolve during the time.

In order to quickly browse the tabulated points, they are arranged in a binary tree (Figure 12.2).

The leaves of the binary tree are the recorded point. The nodes of the tree contain a vector  $v$  and a scalar  $a$  that divides the region in two such as described in the following.

When the reaction operator of a new vector of thermodynamic variable  $\Phi^q$  must be computed, the first step of the algorithm is to find the closest record in the table. Then the algorithm browses the successive nodes until they obtain a leaf. When  $v^T \cdot \Phi^q < a$ , the following selected node is the left one, when  $v^T \cdot \Phi^q > a$ , the following selected node is the right one.

Once the closest point is found, if the new point is inside the EOA, the linear approximation (12.3) is performed, we call this event *retrieval*.

If the point is outside the EOA, the direct integration is performed to obtain  $R(\Phi^q)$ . We test if its solution respects the tolerance criteria,  $\|R(\Phi^q) - R(\Phi^o)\| < \epsilon_{tol}$ :

- if the criteria is met, the EOA of the recorded point is grown, we call this event *growth*.
- else, the point must be added to the table. The sensitivity matrix and the initial EOA are computed using (12.5) and a new node is created to split the recorded point and the new point with:

$$v = \Phi_r - \Phi_l \quad \text{and} \quad a = v^T \left( \frac{\Phi_l + \Phi_r}{2} \right), \quad (12.6)$$

This event is called *addition*.

In practice, the ISAT-CK7 algorithm can use several binary trees. In that case, the addition of a new point is performed successively on each tree to balance the tree’s size. A more significant number of tables yield slower retrieve times, but smaller tables reduce the time needed to build the table. The optimal value of the table is then problem-dependent.

## 12.2 Integration into the numerical scheme

### 12.2.1 Adaptation of the time operator splitting

Implementing the In Situ Adaptive Tabulation requires applying a fixed time-step for the reactive computation. The integration of this method in the splitting time scheme (6.12) requires that this time step respect the stability conditions imposed by the Euler and viscous operators.

To avoid being limited by this time step fixed at the initial time. Another strategy can also be used by using a larger reactive time-step  $\Delta t_{reac}$  and performing sub-iterations of convection and diffusion that respect stability criterion between each reaction operator:

$$w_j^{n+1} = \mathcal{L}_{\Delta t_{reac}/2}^R \left( \sum_k L_{\Delta t_k}^V L_{\Delta t_k}^E \right) L_{\Delta t_{reac}/2}^R w_j^n, \quad (12.7)$$

with  $k$  the index of the iterations until we obtain  $\sum_k \Delta t_k = \Delta t_{reac}$ .

However, in that case, the control of the accuracy is no longer totally under control since the splitting error could be degraded. It is probably possible to keep the second order of accuracy on the splitting time scheme. Indeed, control of the splitting error with such scheme introducing sub-iterations has been investigated by Duarte in [Dua11] by measuring the error dynamically with smaller reactive time steps. However, this method is not implemented here, and this scheme then introduced an uncertainty on the splitting error.


### 12.2.2 Application to transient compressible phenomena

Performance of ISAT is directly related to the time used to store the points and the number of retrievals obtained from these stored points that we can measure with the *retrieval ratio*. In the case of Low Mach number flow, the speedup factor of the original algorithm is very high. However, with compressible flow cases, the risk is to deteriorate the retrieval ratio due to the multiplication of thermodynamic states.

Some memory issues may also occur, which can, however, be contained using deletion mechanisms to avoid large tables such as applied in [DFC07] and adapted them with synchronization between tables when using parallelism as described in [WDL18]. In the literature, existing applications of ISAT tables with very dynamic phenomena such as detonation simulation generally reduce the computation of the points of the table by simplifying the original algorithm. For example, standard-size EOA around the recorded points allow to avoid the time-consuming computation of the sensitivity matrix [WDL18]. However, such simplification makes it impossible to control the tolerance error accurately as with the original algorithm. We chose in this work to keep the complete original algorithm with computation of the sensitivity matrix and adapted EOA. Our objective is then to determine if using ISAT in configuration with flame acceleration and transition to detonation can obtain significant CPU time consumption while keeping a relevant tolerance error.

## 12.3 Numerical simulation of gaseous detonation

We check the performances of the ISAT algorithm with one-dimensional and two-dimensional configurations involving gaseous detonation.

$T_I = 298 \text{ K}$ $u_I = 0 \text{ m/s}$ $p_I = 0.066 \text{ atm}$	$M=2.165$ 	$T_{II}$ $u_{II}$ $p_{II}$
-----------------------------------------------------------------------------	------------------------------------------------------------------------------------------------	----------------------------------

**Figure 12.3:** Ignition by a reflected shock wave, test case configuration

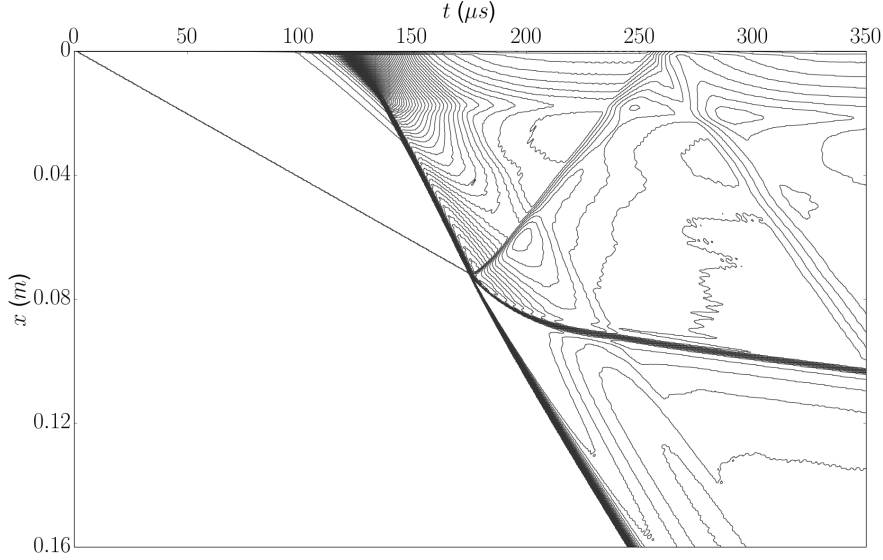


**Figure 12.4:** Isolines of temperature. Distinction of the different waves with the reflection wave, the transmission wave, the reflection and the detonation wave

### 12.3.1 Ignition and creation of detonation front by a shock wave reflection

This case corresponds to the experiment performed by Oran et al. [OYBC82] with the ignition of a mixture using a reflected shock wave. At the beginning a  $M = 2.165$  shock is initiated in a  $2\text{H}_2/\text{O}_2/7\text{Ar}$  mixture at 298 K and 0.066 atm (see Figure 12.3). The shock hits the left wall and reflects by increasing the temperature up to 1026 K and pressure up to 1.27 atm, which is sufficient to auto-ignite the mixture and create a detonation flame front.

The mesh comprises 12 trees with a maximum of seven levels leading to a maximum grid of 1536 points. At the left wall, zero gradients for conservative values and zero velocity are imposed. The solution is obtained through the original OSMP7 scheme. The direct integration of detailed kinetics is obtained using the Radau5 solver with a relative tolerance of  $10^{-3}$  and an absolute tolerance of  $10^{-10}$ . The simulation is purely compressible without diffusion terms.

### 12.3.2 Application without ISAT

Figure 12.4 presents the isolines of temperature in the time/distance plane obtained without using ISAT tabulation. The (abscissa) represents the time (starting from the shock reflection), and the ordinate represents the distance to the reflection location. The history of the temperature is then recorded. Reflection wave is visible at  $t = 0 \text{ s}$  with one isoline moving at  $M = 2.165$ . Auto-ignition produced reactive wave with isolines visible from  $100 \mu\text{s}$  that produce a first detonation wave that will catch up with the reflective wave.

Results can be compared to the experimental recording time-resolved schlieren photography (Figure 12.5) of the shock waves performed in [OYBC82], and various reproductions of this test case in the literature [OYBC82, IJK<sup>+</sup>, GTE17].

As the velocity of the detonation front is faster than the reflected shock wave, the present simulation predicts that a collision between the two waves takes place at  $t = 189.5 \mu\text{s}$ . This time is close

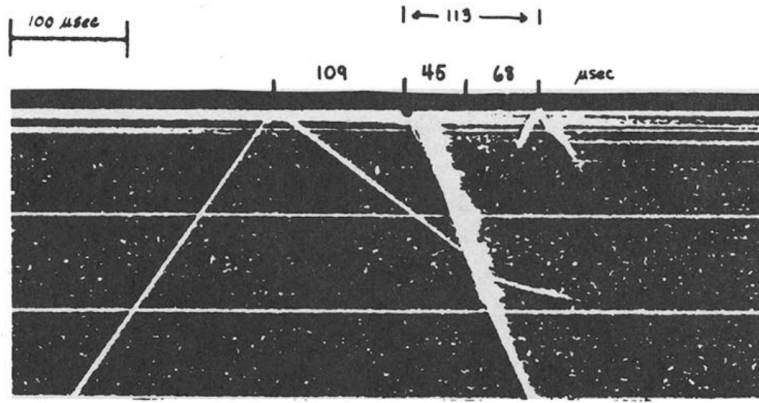


**Figure 12.5:** *Schlieren photograph with relative times marked [OYBC82]*

to numerical results in the literature that found collision after  $180 \mu s$  with another kinetic model. However, there is an apparent disagreement with individual times annotated in Figure 12.5. But, as specified in [OYBC82], "There is some ambiguity (about  $5 \mu s$ ) in determining these quantities from the original schlieren photograph".

After the collision, we observe the formation of three other waves: a contact discontinuity, a transmitted detonation front that will accelerate until the Chapman-Jouguet velocity, and a second reflected shock wave that again hits the wall at  $t = 280 \mu s$ . Those formations are also visible in the experimental results.

### 12.3.3 Application with ISAT

This computation is performed again using the ISAT-CK7 algorithm. In order to run the computation, we have to fix values for the reactive time step  $\Delta t_{react}$  and the tolerance criteria  $\epsilon_{tol}$ . Visual comparisons between profiles obtained with different integration time steps and tolerance criteria are reproduced in Figure 12.6. The comparison stays visual because discontinuity makes the calculation of errors difficult. We see that increasing the reaction time step implies an important error in the ignition time.

We choose a constant time-step for the integration of the reaction of  $10^{-7}s$ , which is close to the CFL condition. The tolerance  $\epsilon_{tol}$  is fixed at  $10^{-3}$ . Figure 12.7 shows the isolines of temperature obtained with this configuration. The results are close to the reference case without ISAT.

The ISAT table is reproduced in Figure 12.8. There are here eight binary trees that receive the new points successively. The modification of the number of trees does not impact the time consumption in this case.

A profiling study is performed to evaluate the computational efficiency of the ISAT strategy for this case involving large temporal evolution.

In the first case, we construct the ISAT table on a full mesh without using the adaptive mesh refinement strategy on a grid of 1536 points. The ISAT table then ultimately contains 38 759 recorded points with 88 788 growth EOA events along with 27 067 392 evaluations, which means that the table provided the final value 99.5% of the time. Compared to a simulation with the same fixed time step of  $t_{react} = 0.1 \mu s$ , the speed-up ratio for the computation of the reaction operator is 11.3, and the global acceleration of the simulation is 3.9. However, compared to the original case, with variable time step determined by the CFL, we obtain a speed-up ratio is reduced to 8.01 for the reaction operator and 2.76 for the total acceleration of the simulation.

Moreover, the computational time gain is also reduced using the multiresolution adaptive refinement since the number of cells in a homogeneous area is automatically reduced already prevail redundant use of the reaction solver. Using Harten criteria of  $\varsigma = 10^{-3}$ , the table retrieves directly the value only 95 % of the time, and the speed-up ratio drops to 1.9 for the reactive operator and 1.37 for the

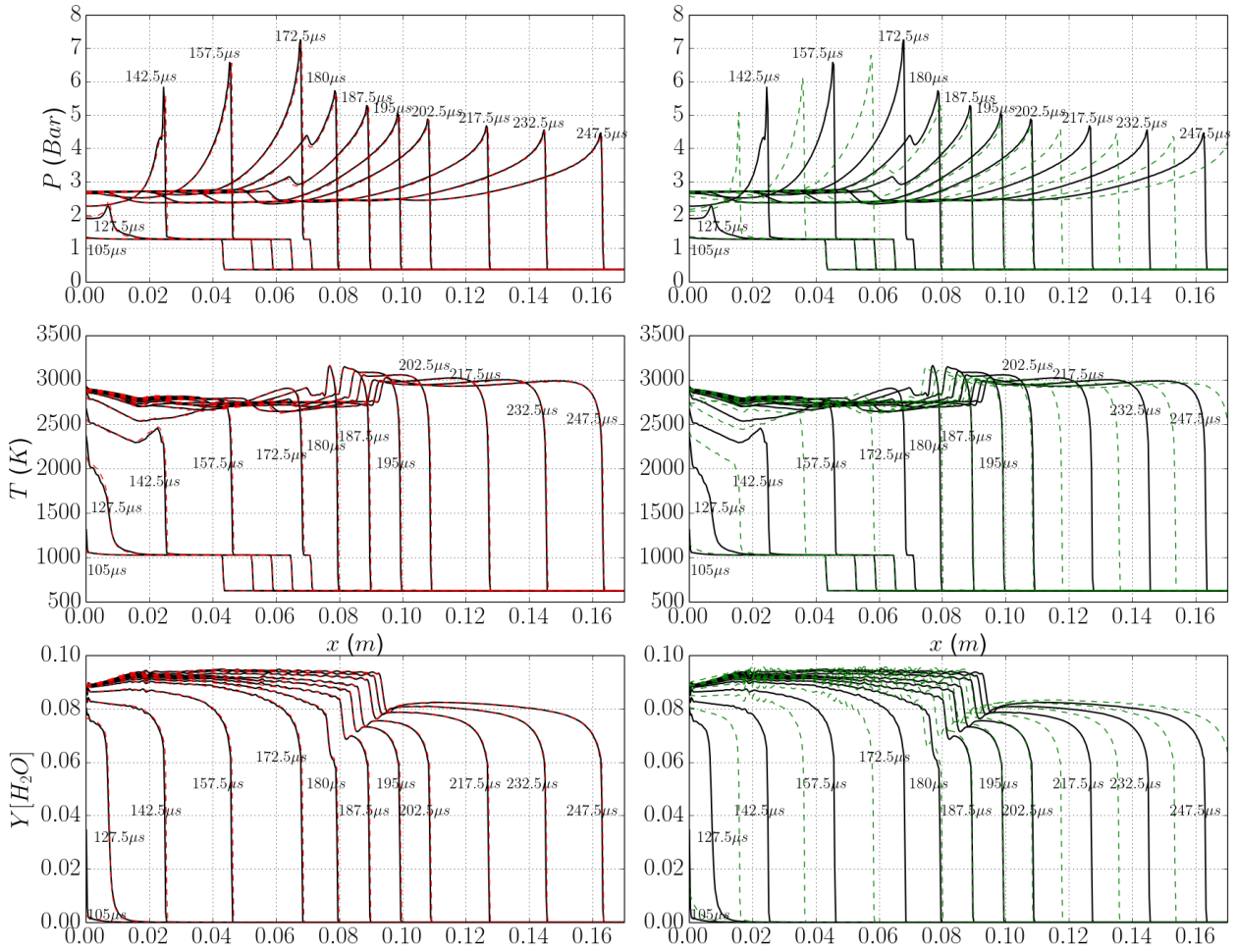


**Figure 12.6:** Comparison with various parameters of tolerance and time-step using in the ISAT-CK7 algorithm. In black solid line: reference result without ISAT; in red dashed line on the left figure:  $\epsilon_{tol} = 10^{-2}$  and  $\Delta t_{reac} = 10^{-7}$  s; in green dashed line on right figure:  $\epsilon_{tol} = 10^{-3}$ ,  $\Delta t_{reac} = 2 \cdot 10^{-7}$  s

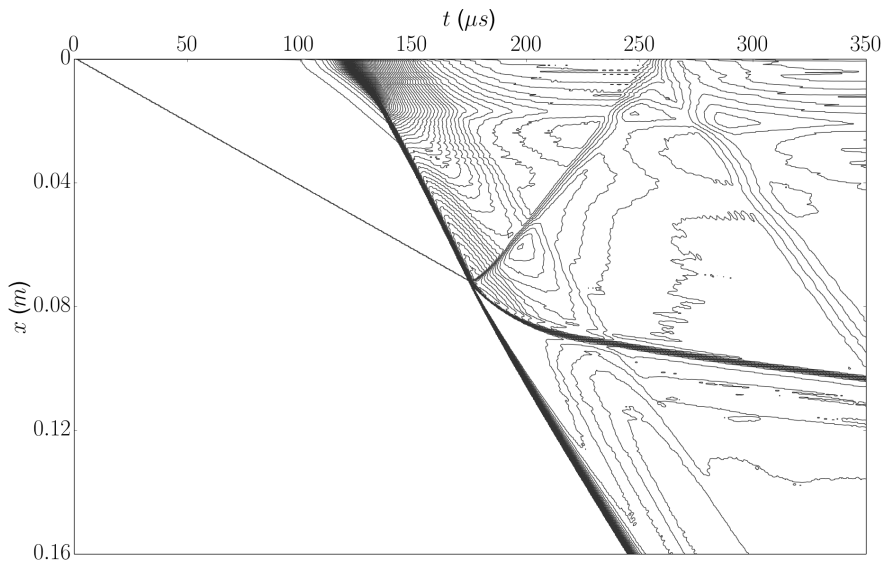


**Figure 12.7:** Isolines of temperature with ISAT-CK7 algorithm. Results are close to the reference results 12.4



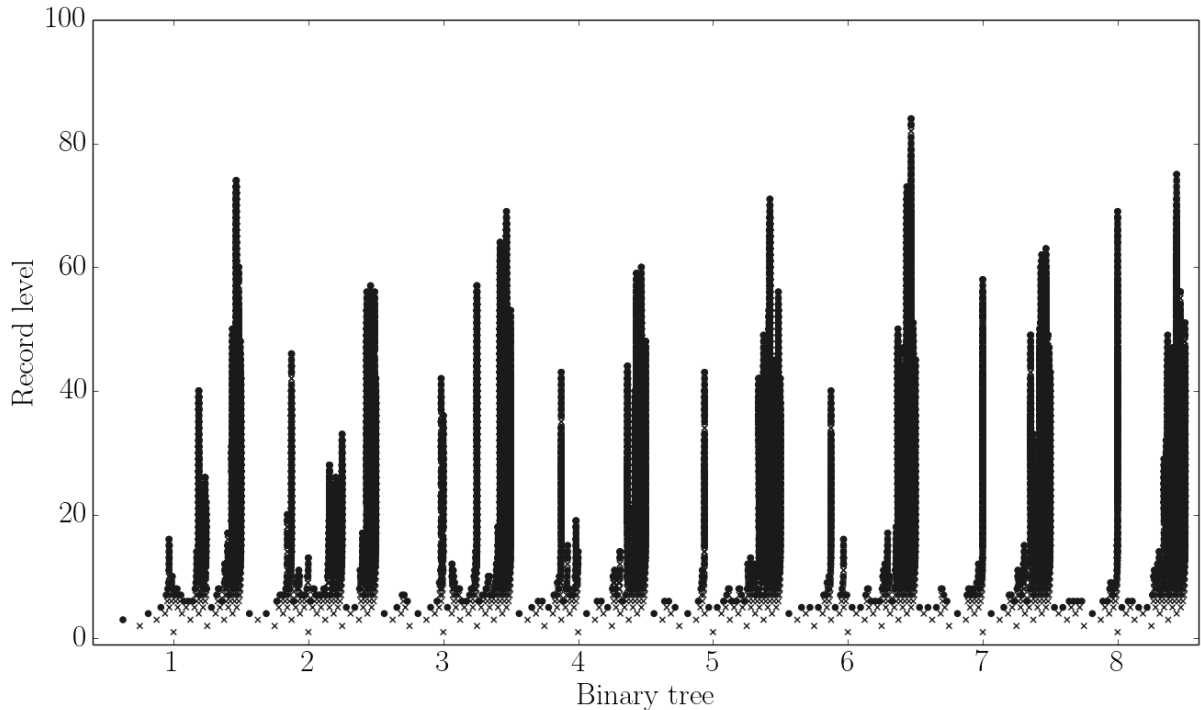


**Figure 12.8:** Representation of the ISAT binary trees with the 38 759 recorded points. The cross correspond to the nodes and the bullets corresponds to the recorded points

total simulation compared to the original numerical scheme. The association between mesh refinement and the ISAT algorithm is not well suited since, in the regular region, the ISAT table creates small variations that can increase the number of cells.

### 12.3.4 Two dimensional detonation front

We test the ISAT method for the computation of a two-dimensional detonation front. The objective is to observe cellular structures described in § 2.2.3. Same initial mixture  $2\text{H}_2/\text{O}_2/7\text{Ar}$  than in the one-dimensional case is applied with  $T = 298$  K and  $p = 0.066$  atm for the unburnt gas.

The computational profile is a rectangle  $L_x \times L_y = 150$  mm  $\times$  60 mm composed of  $5 \times 2 = 10$  trees with a maximum level of refinement of eight leading to a maximum grid of 655 360 grids.

The ZND profile of the mixture is computed with the AGATH solver and applied to initialize the computation. The Chapman-Jouguet velocity is imposed in the fresh gases to keep a fixed detonation front. In addition, a sinusoidal variation of the velocity is applied in the region ahead the precursor shock-wave to disturb the detonation front and start the development of cellular detonation. Computation is realized with and without the ISAT-CK7 algorithm. The constant time-step for the integration of the reaction is set to  $10^{-7}$  s, and the tolerance  $\epsilon_{tol}$  is fixed at  $10^{-3}$ .

Parallelization of the computation with OpenMP directives is realized. We use six different threads that impose to use six independent ISAT tables, which increases the number of recorded points and reduces the ISAT method's performance.

Even with the parallelization and adaptive mesh refinement, the ISAT algorithm's computation stays very efficient for this fixed detonation front since the observed condition is rather stable in time. A computational time gain of 17.24 is observed for the computation of the reaction.

However, with this weak detonation wave, the ISAT method drastically reduces the vorticity of the detonation front, and the characteristic detonation cells are not visible anymore on the computation. The tabulation has a stabilizing effect compared to the standard computation, even by applying a stronger perturbation to disturb the ZND detonation front (Figure 12.9).

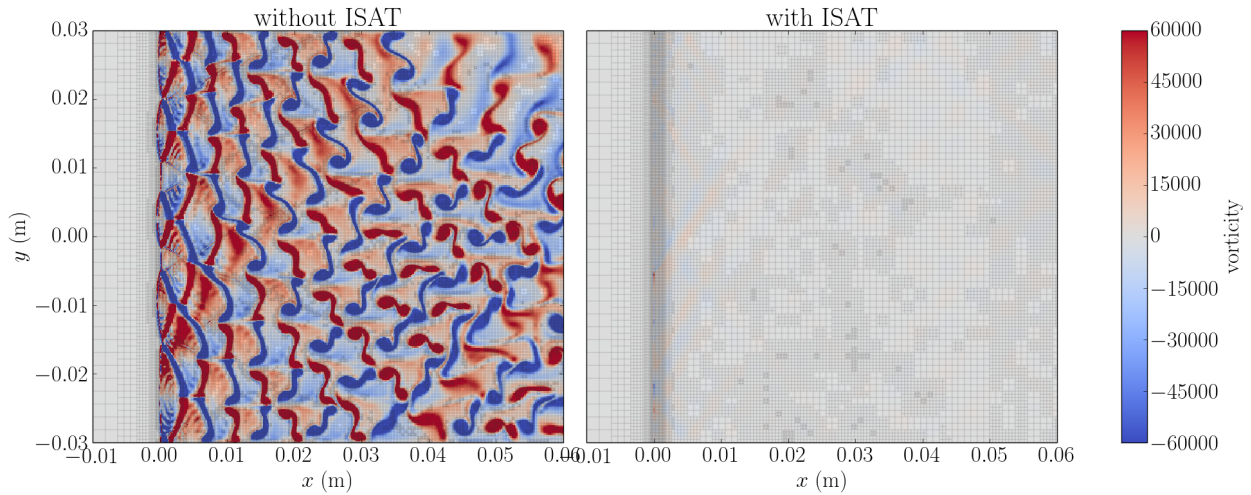


**Figure 12.9:** *Vorticity inside a two-dimensional detonation front in  $2H_2/O_2/7Ar$  initially at 6.67 kPa and 298 K at left (without ISAT), right (with ISAT)*

This effect probably comes from the attenuation of the small perturbations in the induction length that suppose to trigger the instabilities in the detonation front. Those perturbations probably need smaller tolerance criteria  $\epsilon_{tol}$  to be captured, but it imposes to lose computation gain compared to the reference without ISAT.

## 12.4 Concluding remarks

The association between ISAT methods and the adaptive mesh refinement methods is not always adequate. In smooth parts of the solution, it can generate some variations that increase the number of cells. Conversely, the ISAT method also implies difficulties in capturing small perturbations that can be significant, like those inside the induction length of detonation fronts.

This method also needs some optimization to be used with parallel computation. The ISAT algorithm and the management of the trees are not easily parallelizable and impose to increase the number of recorded points by using specific trees for each thread. Some algorithms to synchronize and prune the different trees can allow to reduce the number of points and obtain smaller tables but are not implemented here.

Although some tests are conclusive, we do not have enough experience using this method in our application cases. In this work, we use detailed hydrogen chemistry that does not have a prohibitive number of reactions. However, one can imagine greater usefulness for other types of detailed chemistry. Moreover, at the beginning of this work, the computational time required by the reactive part was the most limiting time compared to the other operators. The computation of the reactive part has been greatly improved by a better vectorization and a better parallelization which makes it less essential to use the ISAT algorithm described here.



## Part IV

# Applications Framework



# Introduction

Part I introduced the main steps of the flame acceleration process. A specific numerical solver has been developed in Part II and some additional numerical tools are presented in Part III. This present part aims to apply our numerical solver on realistic acceleration and detonation case simulations.

The part is split into two chapters. First, we performed a selection of academic test cases in Chapter 13 on laminar flame and detonation front with one and two-dimensional simulations. These tests allow to validate the transport models and the chemical mechanism of Mevel as well as to establish the mesh resolution required to capture the main mechanisms at successive steps of the flame acceleration described in part I.

Chapter 14 presents two extensive simulations. First, the propagation of a  $\text{H}_2$ /air detonation wave inside a porous medium. Attenuation and re-amplification of the  $\text{H}_2$ /air detonation front are observed with two geometrical configurations that influence diffraction of the initial front. Finally, the second test case reproduces two configurations of the GraVent acceleration tube experiments with and without  $\text{H}_2$  concentration gradient.



## Validation test cases

This chapter aims to verify the capability of our solver coupled to the chemical mechanism of Mével [MJL<sup>+</sup>09] to reproduce the main characteristic of hydrogen flames. First, we reproduce chemical properties such as the laminar flame speed or the ignition delay time; then, transport models are tested on the development of hydrodynamic instabilities that drives the first steps of the acceleration flame process. Finally, the properties of the detonation front are studied with the development of unstable modes in one dimension and the formation of detonation cells in two dimensions.

### 13.1 Fundamental combustion properties of hydrogen flame

This section aims to verify if the chemical mechanism of Mével [MJL<sup>+</sup>09] and multicomponent transport models are well suited to characterize fundamental hydrogen combustion properties such as the laminar flame speed without stretch ( $S_l^0$ ), the profile of the laminar flame, and the auto-ignition delay. Those properties are essential to adequately capture the acceleration steps of the flame from the laminar deflagration to the transition to detonation. Moreover, we make additional tests to estimate the resolution needed to properly represent the laminar profile with our high-order scheme.

#### 13.1.1 Laminar flame characteristics

The chemical kinetics of hydrogen oxidation has been well studied for the last decades. Laminar flame speeds  $S_l$  of hydrogen and air at standard temperature and pressure have been measured over a wide range of equivalence ratios. Different methods have been used experimentally for determining this parameter with spherical bomb method [AHF97, LCP03, DHD14], burner stabilized flame method [WL85, GJ72], or particle tracking velocimetry [PBO10]. The difficulty for these experimental devices is to reproduce the idealized case of steady laminar flame since actual flames are affected by heat losses, stretch, and flame instabilities. In particular, values below an equivalence ratio of 0.5 are difficult to capture because of the Darreus-Landau and thermo-diffusive instabilities and must be fitted numerically. Thus, data on  $S_l$  generally vary according to the experimental method.

The evaluation of the laminar flame profile is initialized by computing a hydrogen flame profile with the AGATH library. The computation is performed in a computational domain extended between -2 mm and 10 mm with a fixed front flame. With the AGATH solver, the profile is computed using a very fine refinement (with  $\Delta x = 1 \mu\text{m}$ ) for which the profile is converged.

The reaction is computed with the hydrogen chemical mechanism of Mével described in appendix B.4. Transport properties were evaluated using the multicomponent diffusion model and considering thermal diffusion (Soret effect).



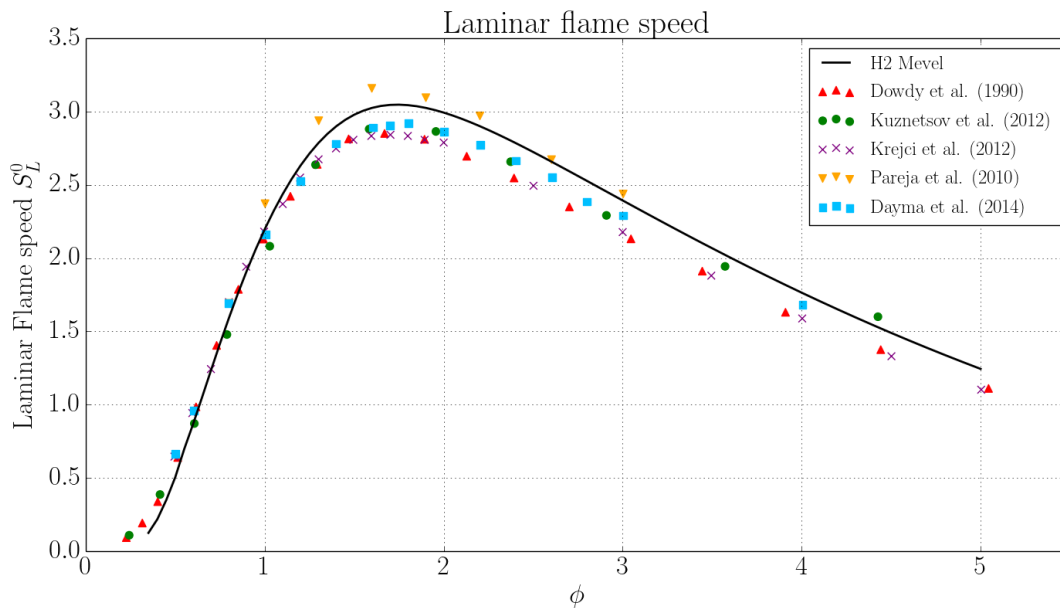


**Figure 13.1:** Laminar flame speed of  $H_2$ /air at atmospheric condition ( $P = 1 \text{ atm}$ ;  $T = 298 \text{ K}$ ) at different equivalence ratios

### Laminar flame speed

Figure 13.1 shows the laminar flame speed obtained with the chemical mechanism of Mével for a mixture  $H_2$ /Air at atmospheric conditions compared to the experimental data on a range  $[0.5 - 5]$  of equivalence ratio. The position of the maximum flame speed is well predicted, and its value is between the extreme values measured experimentally.

We also evaluate the impact on the laminar flame speed of the diffusion model described in § 5.1.2. Figure 13.2 presents laminar flame speed computed using mixture-averaged formulation (5.10) or computed without Soret effect. The absence of the Soret effect significantly impacts the flame profile of the laminar flame speed and must be considered in the simulation. In the same way, the mixture-averaged model (5.10) overestimates the laminar flame speed compared to the detailed multi-component transport model of Dixon-Lewis [DLC68].

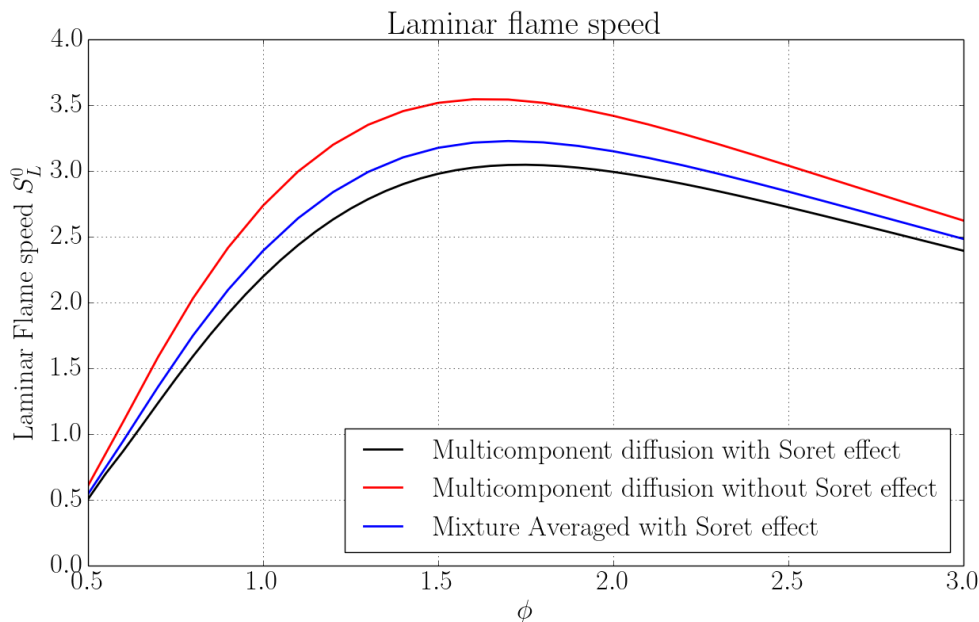
### Laminar profile

Figure 13.3 details the profile of the mass fraction of OH and the velocity for a fixed flame with stoichiometric  $H_2$ /Air flame at the atmospheric conditions.

This profile computed with AGATH on a computational domain of 1.2 cm is used as the initial condition in our solver to validate the capability of our solver to reproduce the same results and evaluate its performances using a coarser grid.

Outlet boundary conditions are defined using Navier-Stokes Characteristic Boundary Conditions (NSCBC) method. A subsonic non-reflective outflow condition is imposed using the Local One-Dimensional Inviscid (LODI) formalism described in [PL92] to infer the amplitude variation carried by the incoming characteristic acoustic wave  $\lambda_N = u - c_s$ . Pressure at infinity is imposed to relax to atmospheric pressure at the outlet using the formalism of the subsonic non-reflecting outflows.

As described in Chapter 6, reactive terms are solved using the Radau5 solver. The compressible effects have very limited influence on the laminar flame profile; thus, the order of the OSMP scheme used in this simulation has no impact significant impact on the final results that depends mainly of the viscous and diffusive terms. However, the time step's limitation due to the stability CFL condition imposed by the compressible operator implies a very accurate computation with the second-order Runge Kutta solver used for the viscous and diffusive operators.



**Figure 13.2:** Laminar flame speed of  $H_2$ /air at atmospheric condition ( $P = 1 \text{ atm}$ ;  $T = 298 \text{ K}$ ) at different equivalence ratios with various transport models

Figure 13.3 presents the modification of the profile after 1 ms of simulation for various refinements. The profile is correctly reproduced until  $\Delta x = 31.3 \mu\text{m}$  corresponding to seven cells in the laminar flame thickness  $\delta_l$  defined as the thermal flame thickness, and five cells in the reaction zone thickness  $\delta_R$  which is close to laminar flame thickness with stoichiometric hydrogen flame. With such refinement, an error of 2% is made on the laminar flame speed compared to the converged profile.

The thickness of the flame front is the area requiring the maximum refinement; strong species gradients allow multiresolution methods to capture this area efficiently. Thus, on the calculation of a laminar flame profile, the variation of the Harten criterion does not show any influence on the profile with efficient reduction of the mesh size. A Harten criterion fixed at  $\zeta = 0.5$  allows cell number reduction of 95% by removing all cells outside the flame thickness. However, as indicated by 10.12, the effective comparison with a threshold depends on the overall maximum detail that will increase when compressible phenomena with shock waves are involved. With interaction with the Chapman-Jouguet detonation wave, the threshold parameter is set to maximum to avoid defining inside the front flame.

### 13.1.2 Ignition delay

An additional fundamental characteristic of a mixture is its ignition delay time  $\tau_{igni}$ . Especially, this parameter impacts the detonation regime where the shock precursor auto-ignites the mixture and in the transition to detonation with the auto-ignition of hot spots.

Experimentally, this property is usually measured by shock tube experiments. Because of the difficulty due to viscous, heat transfer, and thermo-diffusive instability, the ignition delay times are often measured on a highly diluted mixture with a monoatomic gas to minimize these effects.

Figure 13.4 compares experimental results of [KMV<sup>+</sup>13] to ignition delay time computed with the hydrogen chemical mechanism of Mével for various different temperatures. The equivalence ratio of the  $H_2/O_2$  reaction is 0.5, and the mixture is diluted in Argon. Reaction terms are solved using the Radau5 solver. The ignition delay time is defined as the time corresponding to the maximum gradient of the OH radical.

Some results in the literature are also available for stoichiometric  $H_2$ /Air mixtures without dilution, as performed by Snyder et al. [SA65], Slack [Sla77] and [Gra66]. Computed ignition delay times are compared with these measurements in Figure 13.5 at 1 and 2 atm. The experimental data present good

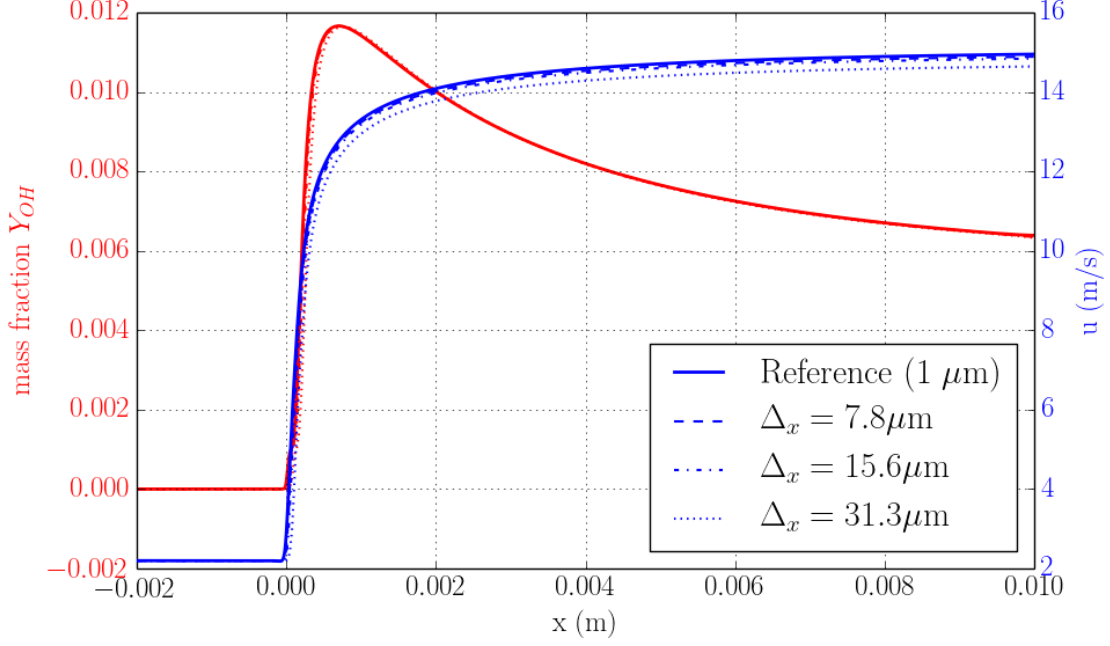


**Figure 13.3:** *Stoichiometric laminar flame  $H_2$ /air profile with various resolution*

agreement between them and with the computation for a temperature around 950-1000 K. Only these data are considered for validation. Below these values, the times involved are beyond our simulations' characteristic times.

## 13.2 Hydrodynamic and thermodiffusive instabilities

In this section, we reproduce a simulation of hydrogen laminar flame instability to evaluate the capability of our solver to properly reproduce the first step of the flame acceleration with the chemical mechanism of Mével.

As described in § 3.1.3, stability of the flame front is characterized by the Markstein length  $L_M$ . Experimentally, Markstein's lengths are evaluated using explosion spheres. In a spherical expanding flame, if there is no tangential velocity and the curvature of the flame corresponds to the stretch rate  $\mathbb{K}$  of the flame. Equation (3.3) then becomes:

$$S_l = S_l^0 - L_M \mathbb{K}, \quad (13.1)$$

with

$$\mathbb{K} = \frac{1}{A} \frac{dA}{dt}, \quad (13.2)$$

where  $A$  consists of the points that stay on the flame surface.

Another estimation of the Markstein length  $L_M$  considering the effects of volumetric heat loss given by Law [LAW06] used in more recent studies gives:

$$\left( \frac{S_l}{S_l^0} \right)^2 \ln \left( \frac{S_l}{S_l^0} \right) = -2 \frac{L_M \mathbb{K}}{S_l^0}. \quad (13.3)$$

For a spherical flame of radius  $R_f$ , the stretch rate  $\mathbb{K}$  is given by:

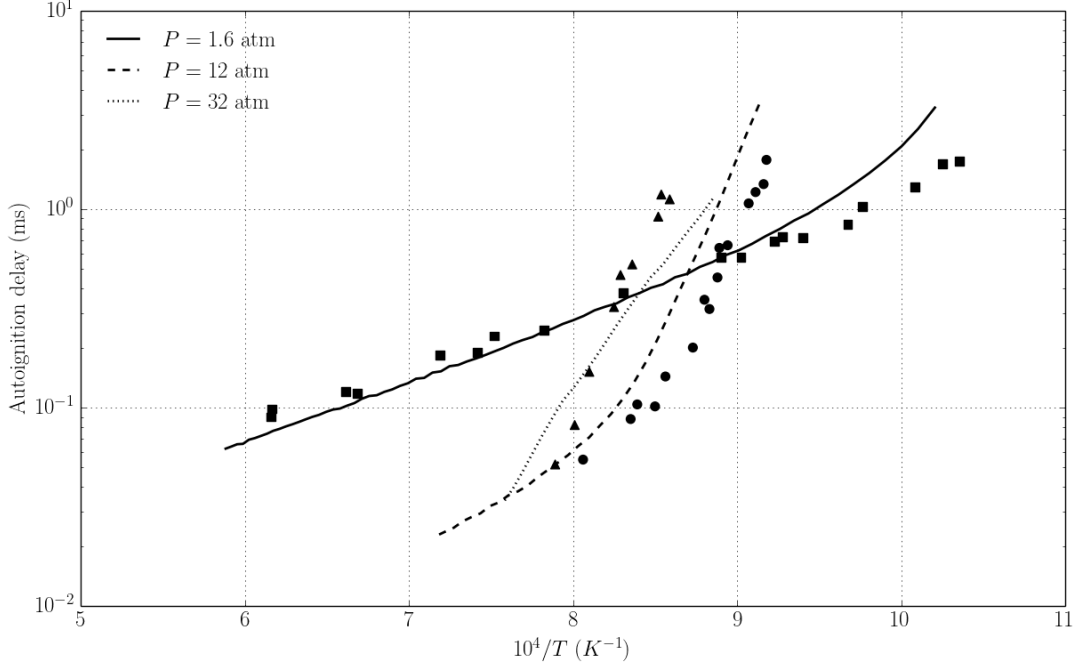


**Figure 13.4:** Comparison of the ignition delay time with Krejci et al. experimental results [KMV<sup>+</sup>13] for various pressures and for mixtures of  $H_2/O_2$  (98% dilution in Ar, equivalence ratio = 0.5)

$$\mathbb{K} = 2 \frac{V_S}{R_f}, \quad (13.4)$$

with  $V_S$  the velocity of the flame surface. Test cases performed in this work are computed in two dimensions. We choose to reproduce an analogous numerical experiment in two dimensions instead of three by considering the expansion of an infinite  $H_2$ /Air cylindrical flame at atmospheric pressure and temperature of the fresh gas at 298 K. In this case, the stretch rate becomes:

$$\mathbb{K} = \frac{V_S}{R_f}. \quad (13.5)$$

The initial solution is applied by interpolating the laminar flame profile computed by the AGATH solver on the radius of the cylinder. The initial bubble has a radius of 7 mm. We performed simulations

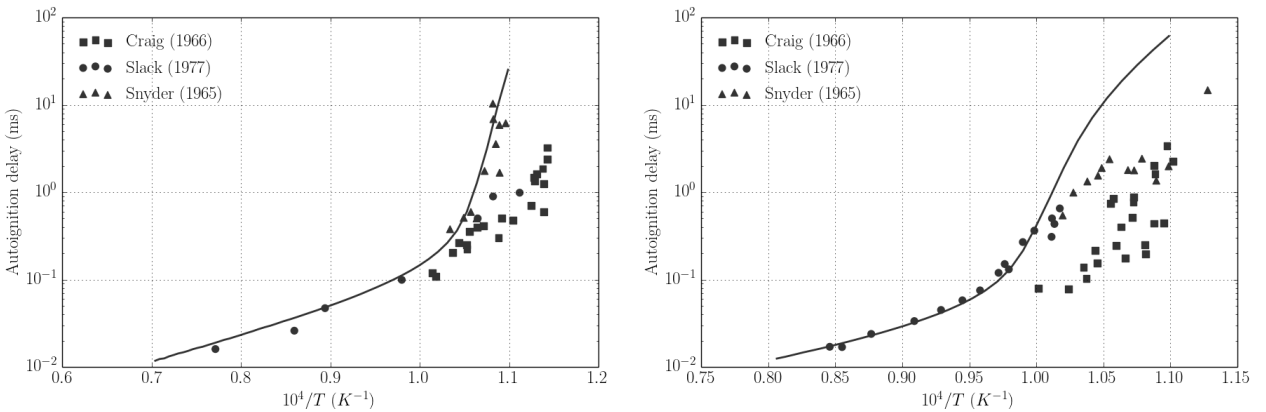


**Figure 13.5:** Evolution of the ignition delay time for stoichiometric  $H_2$ /air mixture at  $P = 1$  atm (left) and  $P = 2$  atm (right)

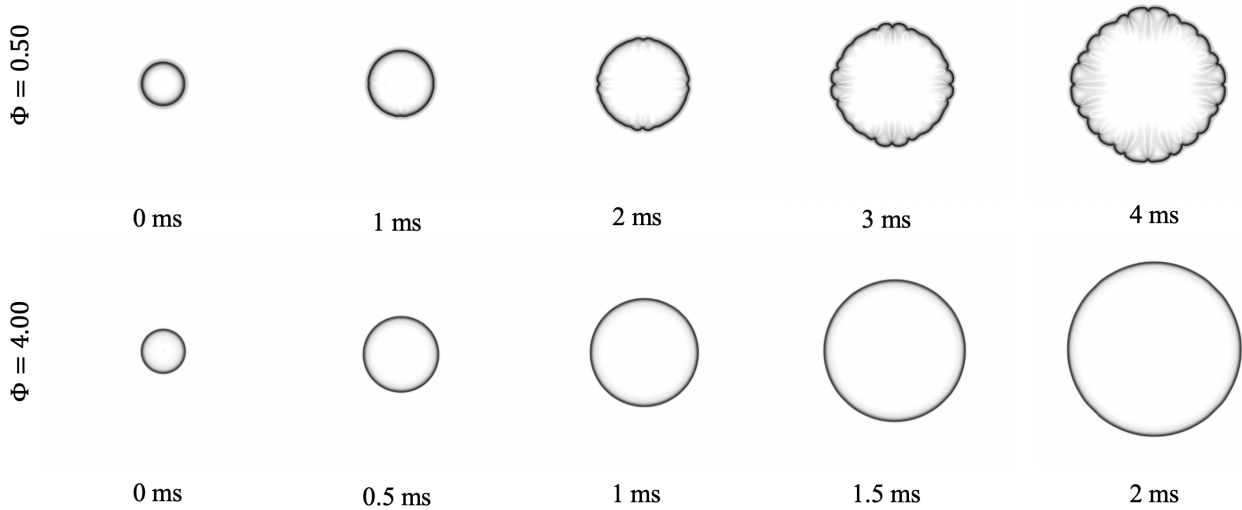


**Figure 13.6:** *Schlieren image of expanding cylindrical  $H_2$ /air flame at  $P = 1$  atm and  $T = 298$  K computed with  $|\Delta\rho|$*

with various equivalence ratios from  $\Phi = 0.5$  to  $\Phi = 4$  to reproduce stable and unstable fronts.

The computational domain consists of a square of 0.1 m side. We use a grid resolution of  $39.0 \mu\text{m}$ , corresponding to between 5 and 10 points in the laminar flame thickness depending on the equivalence ratio. As we saw with the laminar flame profile, this resolution is at the limit of refinement to capture the laminar flame profile properly. Harten criterion is set to  $\zeta = 0.1$ , sufficient to capture the flame profile without significant compressible effects.

As previously made in the one-dimensional laminar profile computations, the reactive terms are solved with the Radau5 solver, and the species diffusion terms are computed using the multicomponent diffusion model.

Figure 13.6 presents the evolution across time of cylindrical laminar flame with equivalence ratio of  $\Phi = 0.5$  and  $\Phi = 4$  that correspond respectively to unstable and stable case. In accordance with the theory, the lean flame produces instabilities. Across time, with the diminution of the stretch, the Peclet number increases, and more unstable wavelengths are developed.

Zero derivatives values are set for the conservative variables at the domain limits. These boundary conditions are not totally non-reflective and induce some perturbations in pressure that trigger the thermo-diffusive instabilities with some small pressure variation that propagates in the computational volume. The first perturbation visible for  $\Phi = 0.5$  also results from the reflection on the closer faces.

Extraction of Markstein number using (13.3) is presented Figure 13.7, the results are consistent with the experimental measurement realized in [DSTW91, AHF97, SSSL99, HZZ<sup>+</sup>06].

## 13.3 Detonation simulation

### 13.3.1 ZND detonation properties

As described in chapter 2, the structure of steady, one-dimensional computation of detonation profiles is performed using the ZND model described by the system of equations (2.10).

This subsection presents characteristic reaction time/length scales, activation energies, and thermal energies calculated for one-dimensional detonations propagating at  $V_{CJ}$ .

Characteristic length and time of detonation profiles can be chosen in many different ways. We consider here  $l_{1/2}$ , the half-reaction length defined as in [SS00] as the distance from the shock to the maximum temperature gradient location.

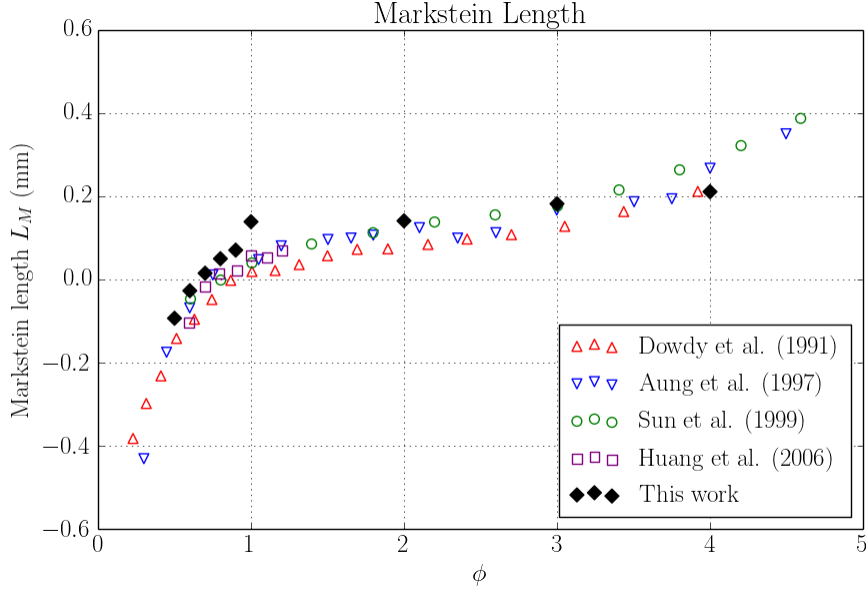


**Figure 13.7:** Computed Markstein lengths  $L_M$  from present simulations versus the stoichiometric ratio for  $H_2$ /air mixture at  $P = 1$  atm and  $T = 298$  K compared to experimental measurements from Dowdy et al. [DSTW91], Aung et al. [AHF97], Sun et al. [SSHL99] and Huang et al. [HZZ+06]

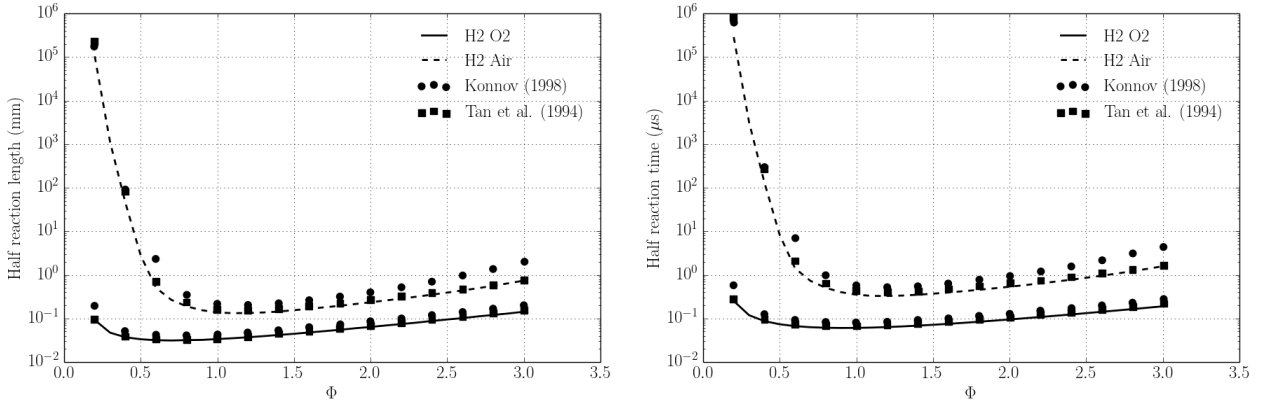


**Figure 13.8:** Hydrogen detonation characteristic reaction scales and time (half reaction length at left, and half reaction time at right) versus equivalence ratio with initial conditions of 295K and 1 bar.

Figure 13.8 presents the half-reaction length  $l_{1/2}$  and time obtain with the chemical mechanism of Mével for  $H_2$ /Air and  $H_2$ /O<sub>2</sub> detonation ZND profile initially at 295 K and 1 bar with various equivalence ratios. We propose a comparison with a similar study realized by Schultz and Shepherd in [SS00] using however two other hydrogen mechanisms [TDC+94, KON98].

Assuming that the induction time  $\tau_i$ , corresponding then to the time to obtain the maximum thermicity  $\dot{\sigma}_{\max}$  using (2.11) from the post-shock state, has an Arrhenius form, i.e.

$$\tau_i = A\rho_{VN}^n \exp\left(\frac{E_a}{R_{gas}T_{VN}}\right), \quad (13.6)$$

the normalized effective activation energy  $\Theta$  in the induction process may be determined by:

$$\Theta = \frac{E_a}{RT_{VN}} = \frac{1}{T_{VN}} \frac{\ln(\tau_2) - \ln(\tau_1)}{\frac{1}{T_2} - \frac{1}{T_1}}. \quad (13.7)$$

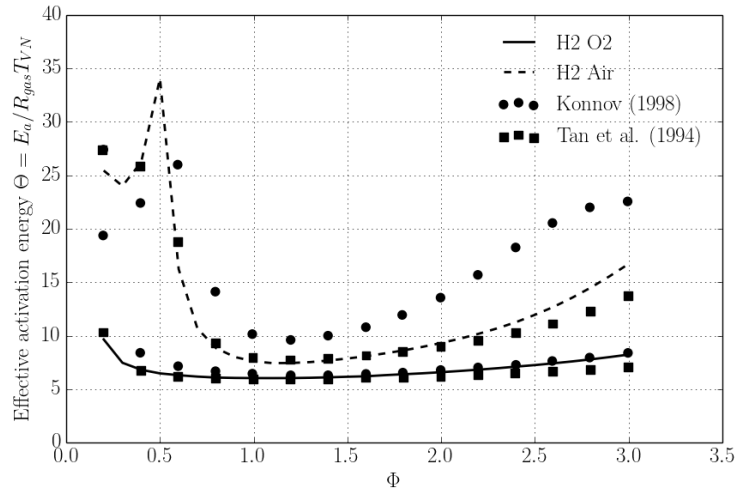


**Figure 13.9:** *Hydrogen detonation effective activation energy parameter  $\Theta$  versus equivalence ratio with initial conditions of 295K and 1 bar*

Conditions for the states one ( $T_1, \tau_1$ ) and two ( $T_2, \tau_2$ ) are obtained by considering the effect of a change in the shock velocity by 1% on the Chapman-Jouguet velocity  $u_{CJ}$ .

The normalized effective activation energy  $\Theta$  obtained with the chemical mechanism of Mével with various equivalence ratios are presented Figure 13.9. Values of the activation energy for  $H_2/O_2$  mixtures are close to the other hydrogen mechanisms. However, the impact of the dilution and especially with  $H_2/Air$  mixture gives non-linear variations with similar effects but with important differences between the different chemical mechanisms.

### 13.3.2 One-dimensional unstable detonation

As explained in § 3.2.2, the stability of the detonation has a strong impact on the behavior of the detonation front, especially the capability of the detonation to propagate across geometrical obstacles without quenching with the quasi-detonation regime.

As described in § 2.2.2, depending on the initial conditions and mixture properties, one-dimensional detonation can be inherently unstable, which will result in the generation of pulsations of the post-shock pressure and variations of the detonation front velocity. We reproduce here typical pulsating one-dimensional detonation modes with the detailed  $H_2-O_2$  chemical mechanism of Mével and compare results to the literature.

The mixture has an initial pressure  $p_0 = 1$  atm and an initial temperature  $T_0 = 298$  K.

We express in this section the induction length  $\Delta_I$  as the distance between the shock and the maximum of thermicity  $\dot{\sigma}_{max}$  and the reaction length  $\Delta_R$  as the Chapman-Jouguet velocity  $u_{CJ}$  divided by the maximal thermicity:

$$\Delta_R = \frac{u_{CJ}}{\dot{\sigma}_{max}}. \quad (13.8)$$

Figure 13.10 presents the 1-D detonation modes for mixtures with different argon dilution. A ZND profile is initiated with AGATH solver and propagated along the computational volume where we register the maximum pressure history  $p_s$  corresponding to the post-shock pressure.

Simulations are performed using a maximum refinement of  $\Delta x = 0.488 \mu m$  corresponding to about 60 cells in the induction length.

The pulsation frequency depends on the stability properties with a multiplication of the oscillation modes as instability increases until chaotic mode with an infinite unstable period orbit. In our results

**Table 13.1:** Values of detonation parameters computed for mixture at  $T_0 = 298\text{ K}$  and  $P_0 = 1\text{ atm}$  with hydrogen chemical mechanism of Mével

Mixture	$\Delta_I$ (mm)	$\Delta_R$ (mm)	$\Theta$	$\chi$	Mach
$2\text{H}_2 + \text{O}_2 + 25\%\text{Ar}$	$2.95 \times 10^{-2}$	0.116	4.97	1.26	5.22
$2\text{H}_2 + \text{O}_2 + 30\%\text{Ar}$	$2.95 \times 10^{-2}$	0.126	4.86	1.14	5.20
$2\text{H}_2 + \text{O}_2 + 35\%\text{Ar}$	$2.99 \times 10^{-2}$	0.138	4.76	1.03	5.18
$2\text{H}_2 + \text{O}_2 + 40\%\text{Ar}$	$3.14 \times 10^{-2}$	0.154	4.67	0.95	5.15
$2\text{H}_2 + \text{O}_2 + 50\%\text{Ar}$	$3.51 \times 10^{-2}$	0.205	4.51	0.77	5.08
$2\text{H}_2 + \text{O}_2 + 3.76\text{N}_2$	0.108	0.402	7.53	2.02	4.85

presented in Figure 13.10, no oscillation is visible with 50% Ar dilution, one oscillation mode is visible after destabilization for 40% Ar and 35% Ar, two modes for 30% Ar, and multiple modes for 25% Ar. We notice that the transition between these modes of perturbation is registered at lower dilution with the  $\text{H}_2$  chemical mechanism of Mével than with the San Diego mechanism [SW14] following results of Han et al. [HWL19].

The results from Figure 13.10 are obtained without viscous term. By applying the Navier Stokes equation for the 25% Ar case (Figure 13.11), no significant discrepancies appear in the amplitude and the frequency of the pulsation oscillations. We can only notice that the transient destabilizing period is faster for the same condition. Then the diffusive effects are moderate on the pulsating characteristic of a detonation.

The characteristic detonation values for the different dilution of Argon in stoichiometric  $\text{H}_2\text{-O}_2$  mixture are shown in table 13.1. We measure the value of the stability parameter  $\chi$  (2.13) proposed by Ng et al. [NRH<sup>+</sup>05] that allows distinguishing stable cases from unstable cases at a value close to one, which also seems to be consistent for the other operating points with various initial pressures.

The stoichiometric mixture  $\text{H}_2/\text{Air}$  that will be used in Chapter 14 shows a highly unstable behavior. The detonation mode for this mixture is not presented here since, with the strong pulsating detonation, the minimum temperature decays below the chain branching crossover temperature. This mechanism of detonation extinction is visible only in one dimension. For unstable detonations in two or three dimensions, instability creates a transverse shock that maintains the detonation propagation.

Unfortunately, the grid refinement required to capture these instabilities is very severe for the simulation cases we want to perform. We captured converged perturbation with 30 cells in the induction length for the unstable case. Above ten cells in the induction length, unstable behavior is not captured anymore. Such required refinement is excessive to apply on large simulations. The ability to correctly reproduce interaction between detonation front and boundary conditions could be impacted.

### 13.3.3 Two-dimensional unstable detonation

As done in one dimension in the previous section, we examine here various stability regimes ranging from weak to highly unstable detonations in two dimensions. The main difference between those regimes is the wave-front dynamics and the evolution of cellular patterns. We saw that some relation had been empirically established between the induction length and the size of the detonation cells [GED00, NJL07]. The pulsating instability that disturbs the induction zone observed in one dimension with the San Diego mechanism [SW14] results in a significant variation in the cellular pattern in two dimensions.

Many numerical studies have already observed detonation structures in two dimensions and tried to characterize the feature of cellular detonations. Regimes of detonation instability from weak cells to irregular cells are obtained by increasing the energy release, and the scaled activation energy  $\Theta = E_a/R_{gas}T_{VN}$  using one-step Arrhenius reaction model [BM92, GDO99]. The irregular structures



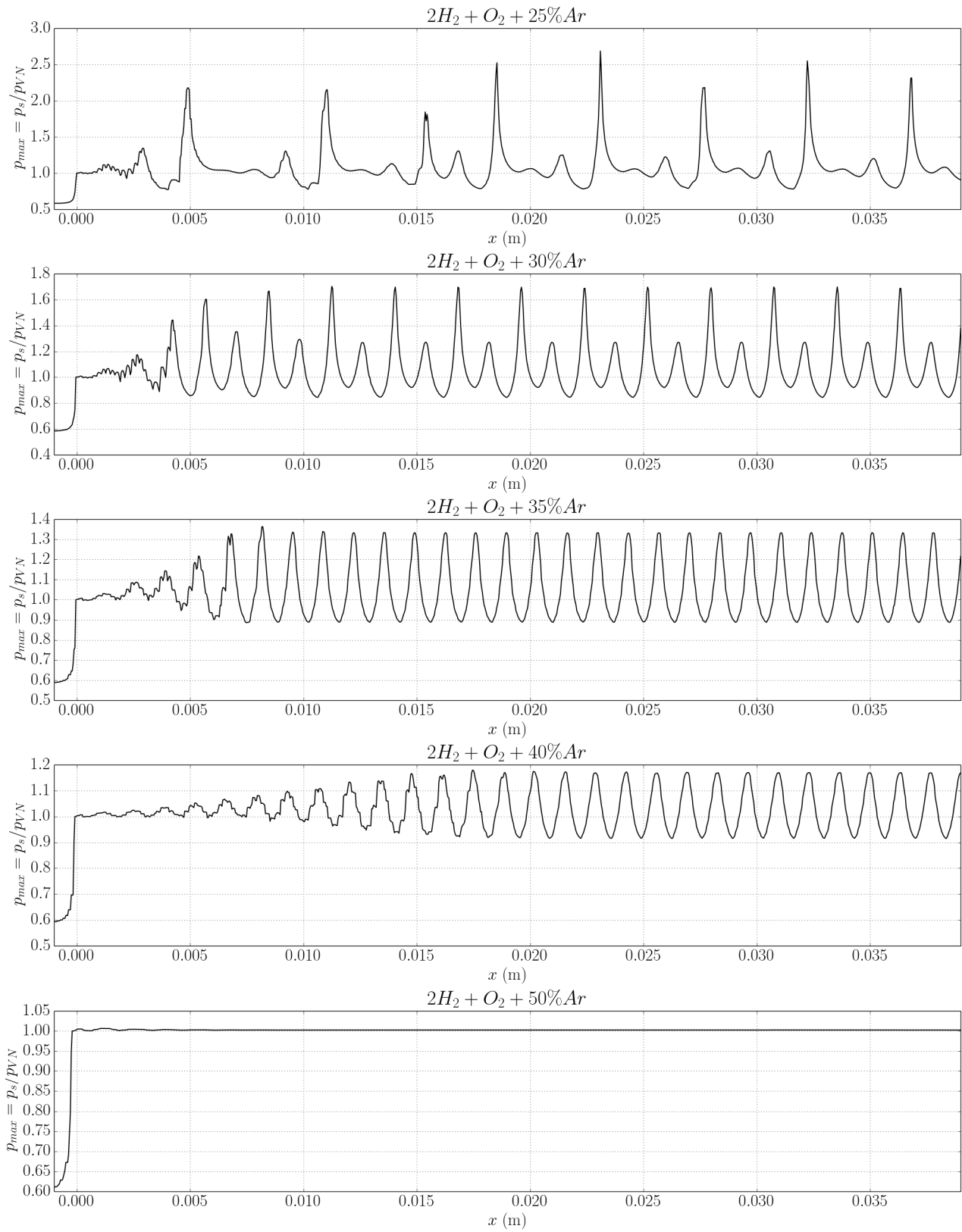


**Figure 13.10:** Maximum pressure histories for different Ar dilutions

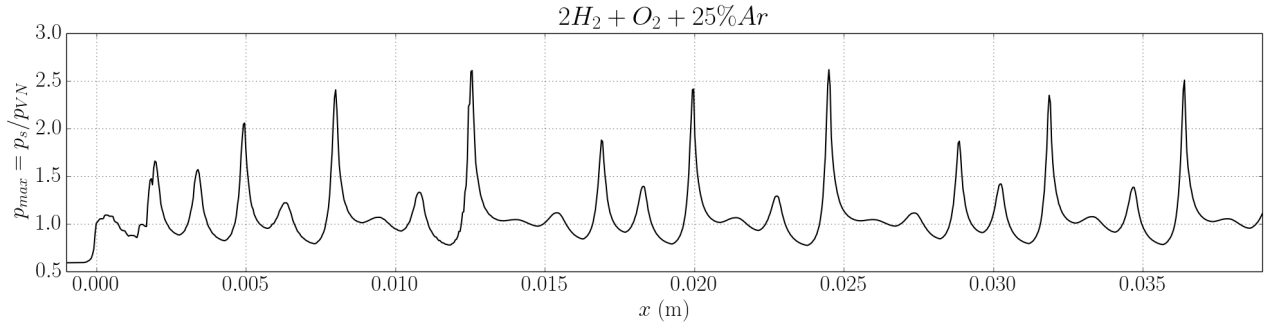


**Figure 13.11:** *Maximum pressure histories for 25% Ar dilutions with Navier Stokes equations*

are characterized by higher pressures at triple points and a higher frequency of appearance and disappearance of these points. Significant turbulent structures are also developing in the wake of the detonation front.

As observed in one dimension, detailed thermodynamic and chemical kinetic models play an important role. Taylor et al. [TKGO13] performed simulation of propagating detonation with detailed kinetic  $H_2$ -Air and  $H_2$ - $O_2$ -Ar with different refinement levels until high resolution of  $2.441 \mu\text{m}$  corresponding to 50 cells in the half-reaction length. With unstable detonation, as the grid resolution is increased, the regularity of the cellular pattern degenerates. Taylor et al. also raised some issues on the conditions behind the flame front and the time scale of the phenomena involved. Indeed, the time scale of molecular vibrational relaxation approaches the ignition delay times in the shocked material that can contradict the hypothesis of equilibrium chemical kinetic mechanism and might explain differences with experiments.

Three-dimensional numerical simulations of detonation front have already been performed [WSHN13] and have not shown qualitative differences with 2D results with however intrinsic phenomena like spinning detonation.

The required numerical grid resolution to capture the detonation structure correctly has also been discussed. Impact of the diffusion and hydrodynamic instabilities are observed with very high resolution [MM11, MMR12, CDLM17] with resolution from 25 cells per half-reaction length for regular cells to more than 300 cells per half-reaction length for irregular structures. However, despite the instability seeming to impact the detonation structure with an enhancement of the mixing rate, such detail does not affect the global behavior and the Chapman-Jouguet velocity. Choi et al. [CMY08] then indicate the smaller requirement to solve detonation cell structure based on the scaled activation energy  $\epsilon_i$  and the pre-exponential factor from 2 cells per half-reaction length for a regular structure to 15 for a highly unstable detonation.

The crucial point for the simulation of such detonation structure is the use of integration methods with low numerical diffusion. Our numerical scheme is then applied on a weakly unstable and highly unstable two-dimension detonation front to investigate the grid resolution we need to apply to reproduce the characteristic cellular structures and capture instabilities in the induction length.

We performed simulations of 2D detonation waves with both stoichiometric  $H_2/O_2$  mixtures without dilution and diluted with 40% Argon with pressure and temperature of the fresh gases  $p_0 = 0.2 \text{ atm}$  and  $T_0 = 298 \text{ K}$ . Corresponding stability parameters  $\chi$  for those mixtures are 1.38 and 0.59, corresponding respectively to an unstable regime and a very stable regime according to the neutral stability parameter we found close to  $\chi = 1$ .

A ZND wave structure computed with the AGATH solver is initially set on the computational volume. The ZND wave is initially inclined in the transverse direction with a linear variation of 20 cells in the vertical direction to provide flow disturbance and trigger the first instabilities.

We choose a computational domain height of  $L_y = 2 \text{ cm}$  with symmetric conditions on the top and bottom boundaries to observe a few detonation cells without attenuation. Simulation is performed

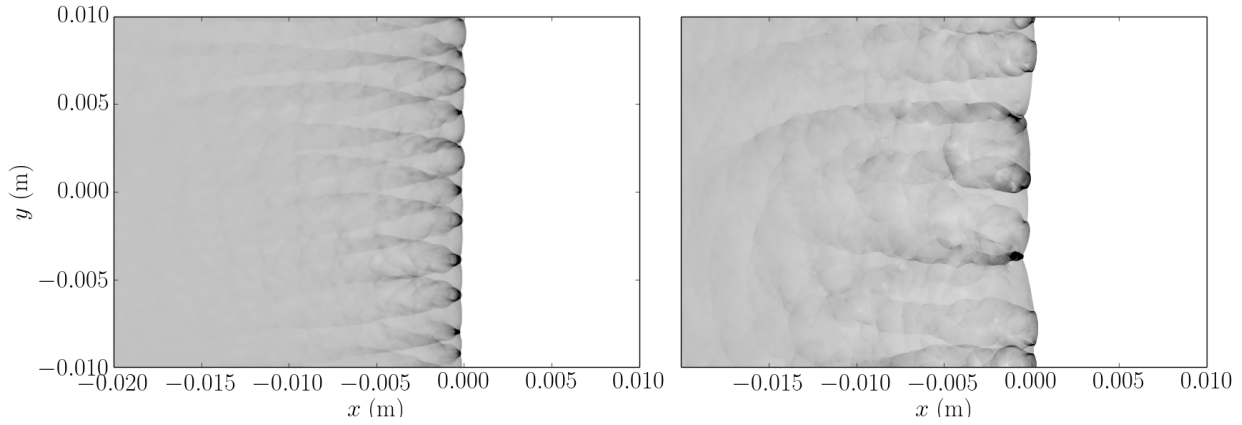


**Figure 13.12:** Pressure contours for detonation front with  $2H_2-O_2$  mixture with 40% Ar dilution (left) and no dilution (right).

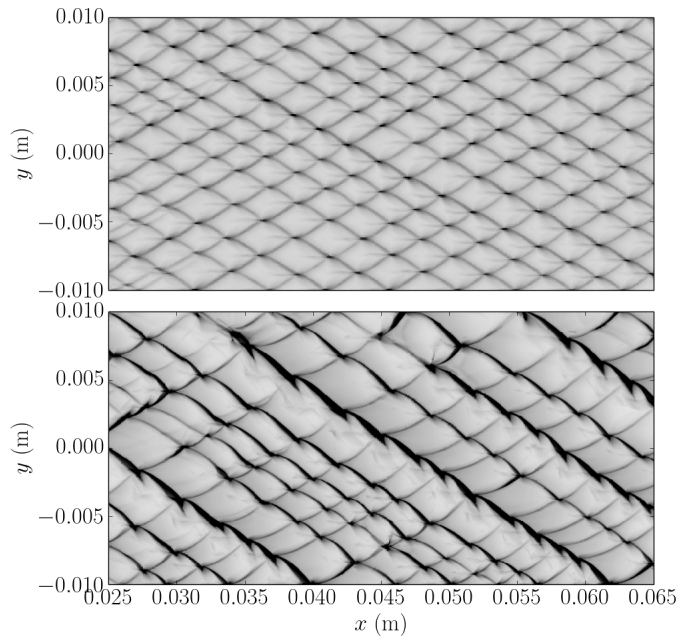


**Figure 13.13:** Numerical smoke foil records for  $2H_2-O_2$  mixture with 40% Ar dilution (up) and no dilution (down).

using the adaptive mesh refinement with the finest grid resolution of  $39 \mu\text{m}$  for the stable diluted case and  $19 \mu\text{m}$  for the unstable case corresponding respectively to 5 and 10 cells over the half-reaction length. Refinement in the unstable case is higher than for the weak case because five cells into the half-reaction length were insufficient to observe instability in the front. Ten cells over the half-reaction length seem necessary to observe the instability in the induction length induced by variation of ignition time and pockets of unreacted gas in the induction zone. This criterion is close to Choi's refinement recommendations [CMY08].

The first part of the solution is computed with a fixed detonation wave to create instabilities. Then, we transcript the solution in the laboratory frame to register the maximum pressure corresponding to the recorded position of the triple points along time to reproduce the results of a soot foil.

Figure 13.12 shows the front of the detonation wave with the transverse waves that induced triple point with local overpressure. A regular structure is obtained with the 40% Ar diluted case compared to the very unstable front observed with the stoichiometric non-diluted mixture.

Figure 13.13 shows the numerical smoke-foil records obtained by registering the maximum pressure

along time corresponding to the location of the triple points. Characteristic detonation cells are observed with a regular aspect in the 40% Ar diluted case and a more irregular aspect in the non-diluted one.

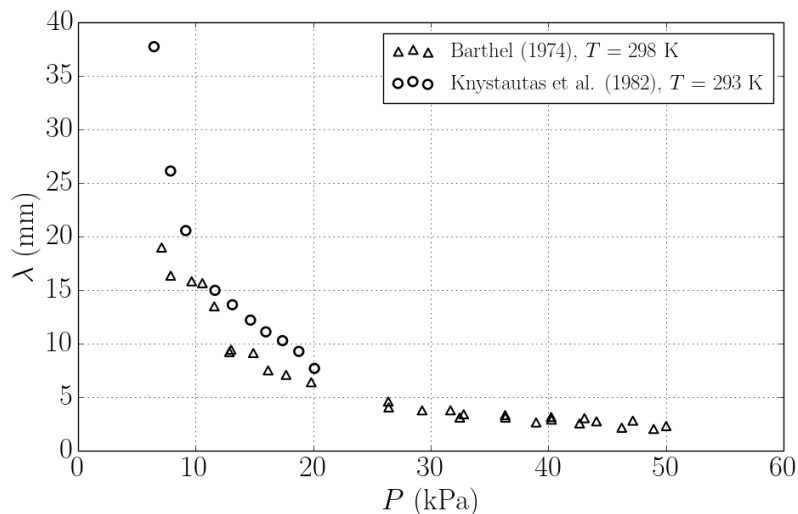


**Figure 13.14:** Detonation cell size for  $2H_2-O_2$  at various initial pressure measured experimentally by Barthel [Bar74] and Knystautas et al. [KLG82].

Detonation cell size for  $2H_2/O_2$  mixture with no dilution is compared to the experimental values reproduced in Figure 13.14. At  $P = 0.2$  atm, detonation cell size can be evaluated close to 4 mm, which is lower than experimental values. Such underestimation can be issued by many factors like an insufficient resolution, the chemical mechanism, the size of the transverse direction of the computational domain that can act as a waveguide, or detonation deficits and lowering of temperature in the experiments [XW21].

In the diluted case with 40% Argon, the size of the cells did not correspond to the experimental value, which measure cells of about 0.6 cm [Bar74]. It is explained by the very long time for appearance and disappearance of the triple point with such a weakly stable detonation. Thus, the cells observed in such simulation strongly depend on the perturbations we imposed initially. Then, we succeed to produce any kind of cell size, depending on the initial perturbation imposed, which is conserved over time.

## 13.4 Conclusion

The standard test cases presented in this chapter allow us to evaluate the performance of the chemical mechanism of Mével and the models used for our simulations. Our solver effectively captures the essential phenomena that compose the different stages of flame acceleration and the transition to detonation. Laminar flame velocities, thermo-diffusive and hydrodynamic instabilities, and flame front properties are well recovered.

However, the reproduction of specific properties such as those corresponding to the instability of the detonation fronts sometimes requires a critical refinement that demands greater computational resources to undertake more extensive simulations.



# Hydrogen flame acceleration simulations

## 14.1 Attenuation and re-initiation of detonation front with porous medium

This first application case presents a mechanism of detonation attenuation by a porous medium and the re-initiation due to wave reflection.

### 14.1.1 Overview

As described in § 3.2.2, the presence of obstacles in the flow generates a velocity deficit leading to quasi-detonations regimes or quenching of the detonation front. Using a porous medium reinforces this phenomenon by attenuating the transverse wave or, like in this case, with a volumetric expansion of the gases behind the leading shock wave. When the velocity deficit becomes too important, the auto-ignition behind the leading shock wave is no longer fast enough to maintain the detonation front structure, and the detonation is quenched. Passive methods using porous coatings lead to energy dissipation that destroys the detonation wave's cellular structure by absorbing the transverse waves. Interaction between detonation waves and perforated plates can also be used to slow down and quench the detonation front.

However, when detonation diffracts behind an obstacle, re-initiation of a detonation can occur as observed in experimental devices [Mak93, BLCM<sup>+</sup>13, SWP<sup>+</sup>17] and numerical simulations [RM11, Max16]. Transverse wave reflections produced by the obstacles behind diffraction waves amplify the incident shock strength and can re-initiate the detonation. Moreover, eddy mixing of shocked gases with combustion products probably significantly impacts the re-initiation mechanism by increasing reaction rates and leading to hot spot re-ignition behind the Mach shock.

Radulescu et al. [RM11] addressed numerical investigations of the mechanism of re-initiation after the interaction with a column of cylinders with an acetylene-oxygen detonation wave using Euler formulation. This result indicates that several shock reflections must be required to accelerate the leading shock wave to re-initiate the detonation sufficiently. In order to address eddy mixing impact, Maxwell [Max16] used LES investigation without succeeding in precisely reproducing the number of shock reflections when detonation re-initiation occurs.

We present in this section a simulation similar to [RM11] performed with a H<sub>2</sub>/Air detonation wave. The objective is to reproduce the re-initiating process of a detonation front and observe these mechanisms that are also involved in the onset of detonation.

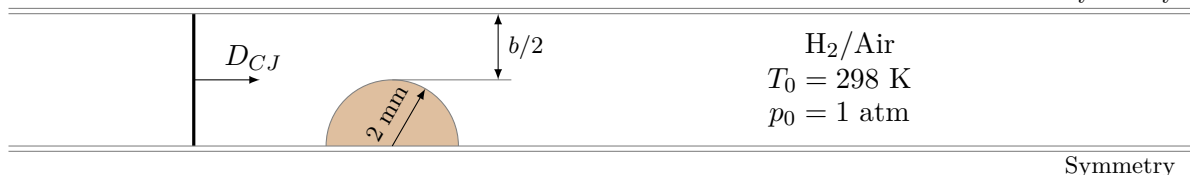


**Figure 14.1:** Schematic representation of initial condition and boundaries for simulation of detonation interaction with porous medium

### 14.1.2 Numerical Results

Figure 14.1 presents a schematic representation of the computational domain. The length of the computation domain is  $L_x = 8 \times 10^{-2}$  m. A solid cylinder of 2 mm radius with an adiabatic no-slip boundary condition is placed at 5 mm from the inlet surface. Symmetric conditions are considered at the top and the bottom boundaries to reproduce an infinite column of cylinders by focusing only on one half-cylinder. Different heights of the domain will be tested corresponding to a variation of  $b$ , the pore size between two adjacent cylinders.

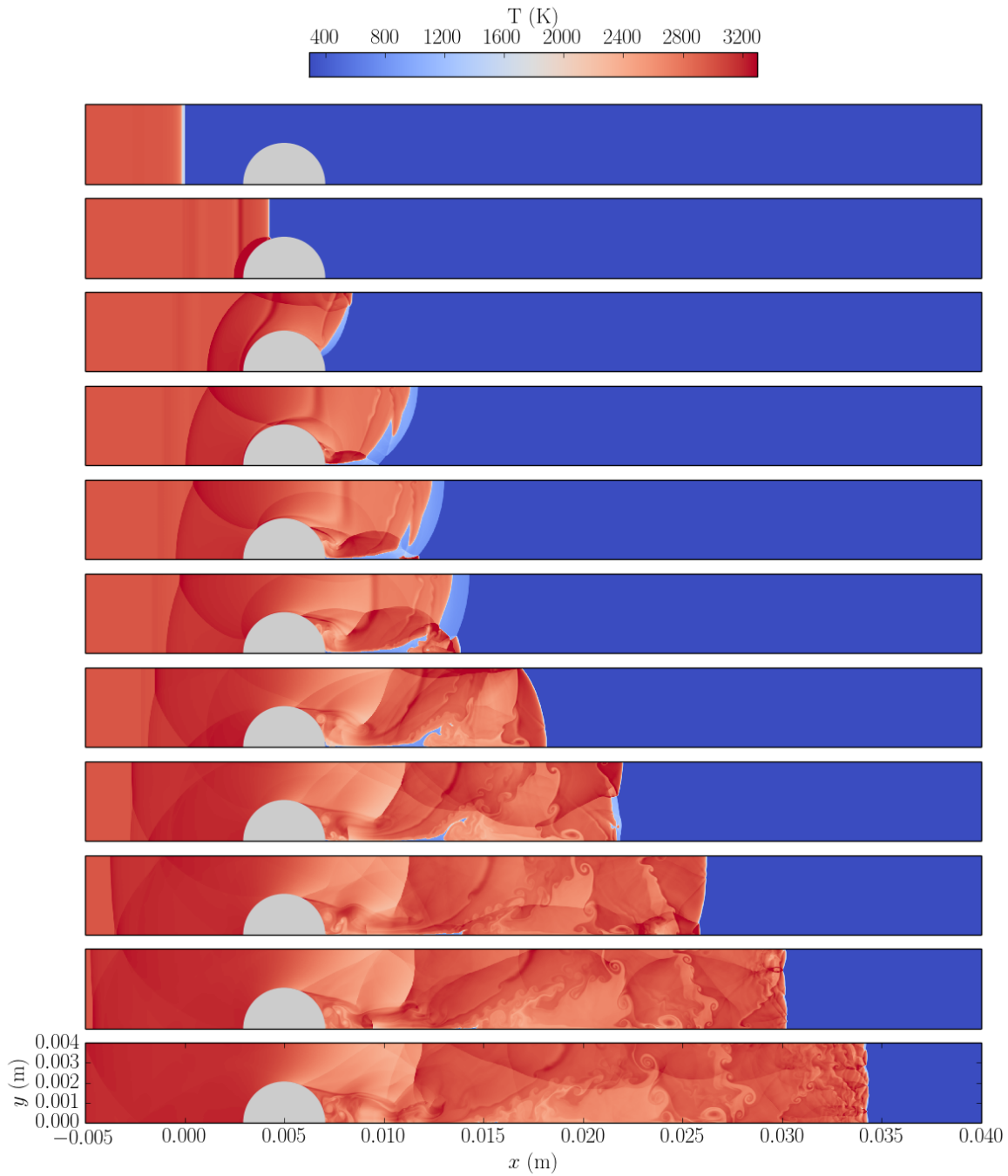
We consider a two-dimensional configuration with a stoichiometric  $\text{H}_2/\text{Air}$  mixture using the detailed  $\text{H}_2$  Mevel mechanism. Initial mixture is set to atmospheric condition with  $p_0 = 1$  atm and  $T_0 = 298$  K. A ZND profile computed with the AGATH solver is initiated upstream of the obstacle at  $x = 0$  mm. The half-reaction length computing for the detonation front is  $l_{1/2} = 0.134$  mm. Simulation is performed using the adaptive mesh refinement; we consider a maximum resolution of  $\Delta x = 15.6 \mu\text{m}$  corresponding to eight cells into the half-reaction length. The Harten criterion for adaptive refinement is set to  $\zeta = 0.01$ .

Figure 14.2 and Figure 14.3 represent the evolution of the temperature field, respectively, and the velocity of the precursor shock wave recorded on the top and bottom boundaries for a pore size of  $b = 4$  mm corresponding to  $30 l_{1/2}$ . Diffraction of the detonation front around the cylinder decouples the leading shock and the reactive front. A hot spot is created at the first shock reflection that auto-ignites the mixture. An overdriven detonation wave is initiated inside the unburned gas pocket that re-initiates the detonation. A second overdriven detonation wave is visible after the second reflection along the top boundary before the formation of a standard detonation at the Chapman-Jouguet velocity in the longitudinal direction.

Figure 14.4 presents the comparison between simulation at  $t = 9 \mu\text{s}$  with and without viscous terms. The re-ignition inside the unburnt gas seems to be slightly faster with viscous simulation due to the increase of reaction rate by the mixing process, but the global behavior of the simulation stays similar.

Another simulation is undertaken with a pore size reduced to  $b = 15l_{1/2}$  which is close to the detonation cell  $\lambda$ . The detonation cell size is generally considered as a limit for the quenching of the detonation front in an obstacle-filled tube. Temperature field evolution and velocity distribution at the top and bottom boundaries are presented respectively in Figure 14.5 and Figure 14.6. The diffraction around the cylinder leads to a significant slow down of the reaction front. Successive reflection waves between the top and the bottom boundaries re-ignite the mixture and accelerate the detonation front but do not give a self-sustained detonation with a velocity deficit of 25% compared to the theoretical Chapman-Jouguet velocity. The post-shock temperature also increases step by step until a significant hotspot occurs at  $t = 35 \mu\text{s}$  after the eighth wave reflection that re-established the detonation wave. Condition for a strong ignition from shock wave focusing such as described in § 3.2.1 have then been achieved at this point.

Thus, we reproduced with a hydrogen detonation front the phenomena observed experimentally [Mak93] and numerically [RM11, Max16] with acetylene. Propagation of quasi-detonation is reproduced; eddy mixing impacts the propagation velocity but is not decisive for the reinitiation of the detonation.



**Figure 14.2:** Temperature field evolution illustrating the detonation re-initiation with  $b = 30 l_{1/2}$ . Successive time at  $t = 0, 2, 4, 6, 7, 8, 10, 12, 14 \mu\text{s}$ ; temperature scale is between 298 K (blue) and 3500 K (red).



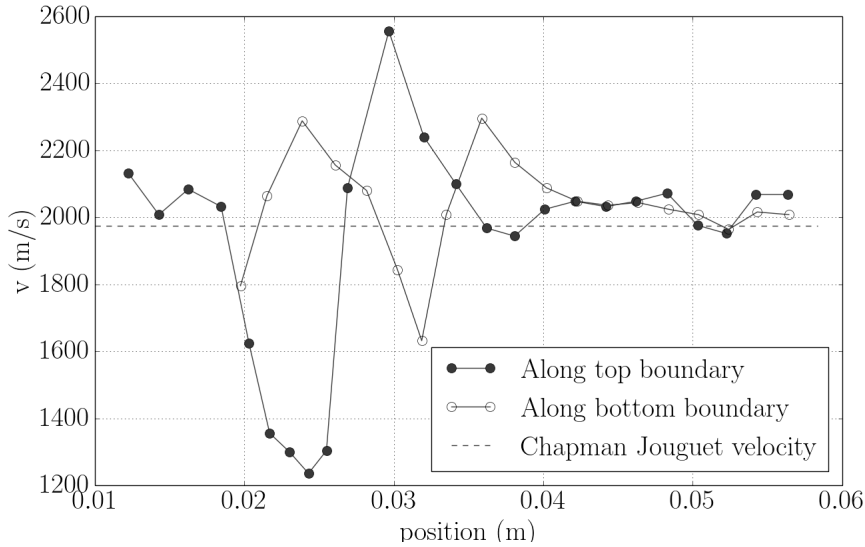


**Figure 14.3:** Velocity of the precursor shock-wave recorded along the top and bottom boundaries for a pore size  $b = 30l_{1/2}$

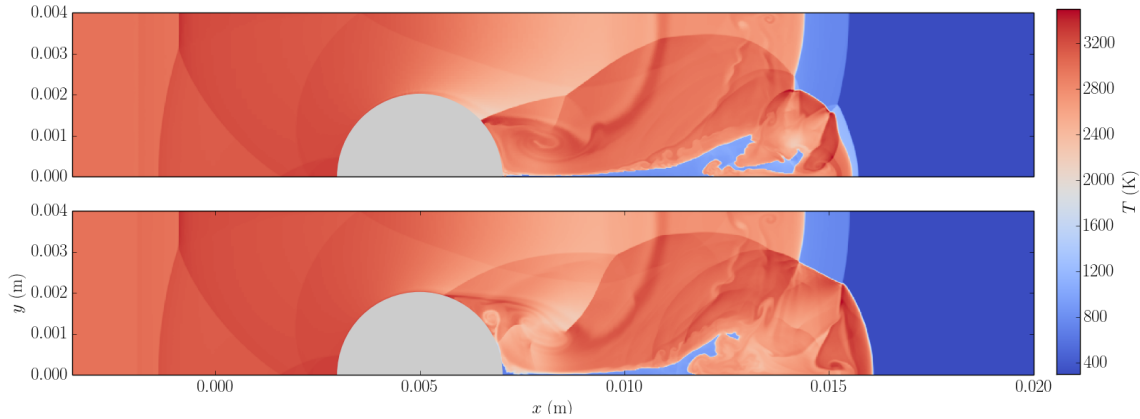


**Figure 14.4:** Temperature field obtained with Euler equations (at the top) and with Navier-Stokes equations (at the bottom) at  $t = 9 \mu\text{s}$

## 14.2 Acceleration tube configuration of the "GraVent" Technische University of Munich facility

Based on the previous analysis of the different phenomena, we try to perform here real-world scenarios of flame acceleration based on the DDT experiments of the Gradients and Venting ("GraVent") facility [BKH<sup>+</sup>16]. The experimental results are available in the open-source database (<https://www.mw.tum.de/td/forschung/ddt/>). This experimental device, described in § 4.1.1 allows imposing concentrations gradients in  $\text{H}_2$  perpendicular to the main direction of explosion front propagation, thus termed "transverse concentration gradients".

### 14.2.1 Experimental and Numerical setup

The tube consists of a horizontal rectangular channel measuring  $5.4 \text{ m} \times 0.3 \text{ m} \times 0.06 \text{ m}$ . We consider for our simulations the geometrical configuration BR60hS300 according to the denomination used in the Database. Seven horizontal flat obstacles are installed on the first part of the tube. They are placed in between  $x = 0.25 \text{ m}$  and  $x = 20.5 \text{ m}$  of the ignition plate with an obstacle spacing of  $0.3 \text{ m}$ . Each obstacle has a thickness of  $0.012 \text{ m}$  and a height of  $0.018 \text{ m}$ , corresponding to a blockage ratio of 60%.

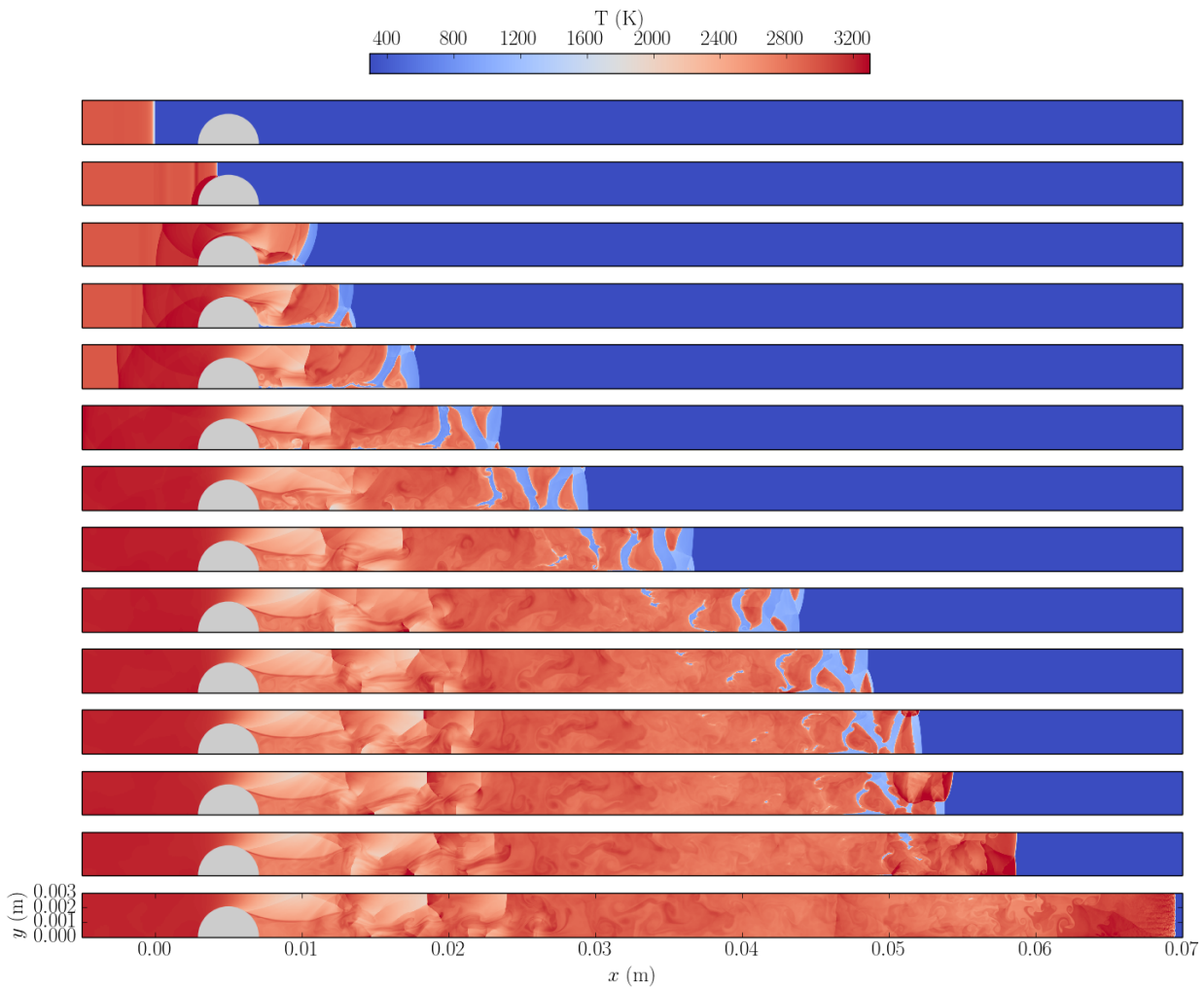


**Figure 14.5:** Temperature field evolution illustrating the detonation re-initiation with  $b = 15 l_{1/2}$ . Successive time at  $t = 0, 2, 6, 8, 11, 15, 19, 24, 29, 32, 34, 35, 37, 42 \mu\text{s}$ ; temperature scale is between 298 K (blue) and 3500 K (red).

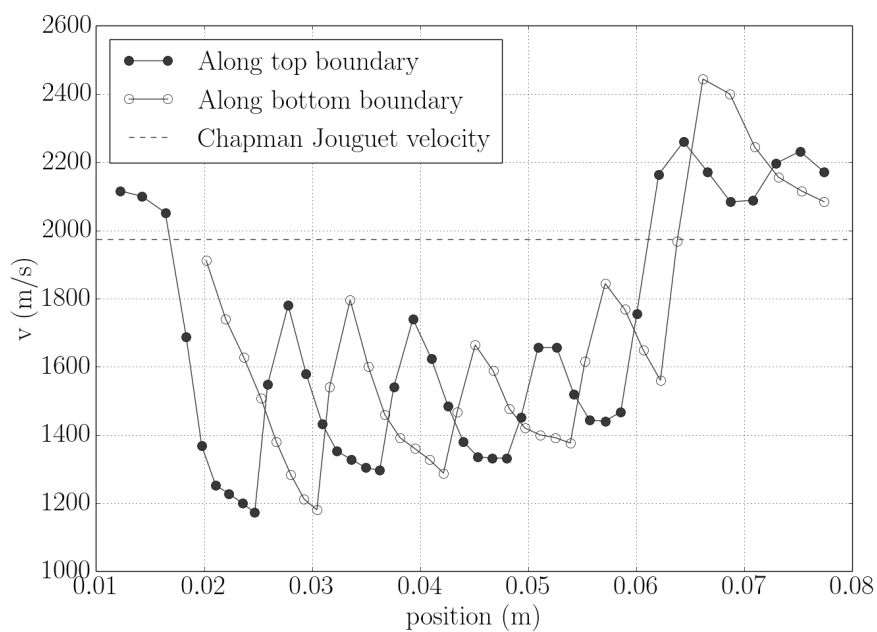


**Figure 14.6:** Velocity of the precursor shock-wave recorded along the top and bottom boundaries for a pore size  $b = 15l_{1/2}$

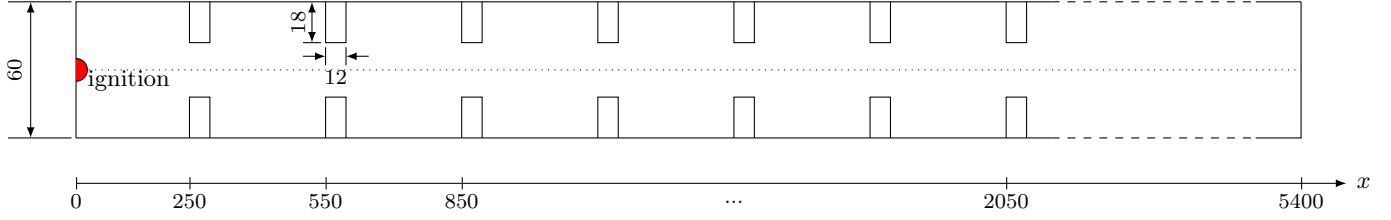


**Figure 14.7:** Schematic of the explosion channel in the obstructed configuration (BR60); Dimensions in (mm)

Hydrogen is injected through several nozzles located at the top wall. Vertical concentration gradients are initially generated, whereas the horizontal concentration gradients are negligible. Slopes of the gradient are controlled using the diffusion time  $t_d$  between  $H_2$  injection and ignition. The hydrogen distributions have been experimentally and numerically measured with the good agreement after  $t_d > 5$  s [VES12]. The mixture can be considered homogeneous for diffusion times  $t_d > 30$  s, whereas lower diffusion time results in an inhomogeneous concentration gradient profile with a typical S-shaped diffusion curve. The concentration profiles are described with four-order polynomials determined by Ettner [Ett12] by CFD simulation and transcript in Appendix A of [Boe15]. These profiles are used to initialize conditions for the simulations.

Ettner et al. [EVS14] have performed simulations of this acceleration tube with a combination of the PISO scheme for the low Mach simulation part and the HLLC solver once the combustion-induced flow has been developed. One step Arrhenius law is used for the chemistry, and Sutherland correlation is used for the transport properties. With the same solver, Wang et al. [WW17] reproduce the simulation of the experiment with higher refinement and custom chemistry. More recently, Khodadadi et al. [KHBW19] performed new simulations of the experimental devices with a similar numerical solver using the HLLC scheme and detailed hydrogen reaction of Ó Conaire [OCCS+04].

Two simulations are performed here in two dimensions with and without concentration gradient. The computational volume then has a length  $L_x = 5.4$  m. Without concentration gradient, the symmetric condition is imposed at the middle of the tube, which gives a height of  $L_y = 0.03$  m. With concentration gradient initialized, symmetric condition is no longer valid and the height is  $L_y = 0.06$  m. Except for the upper symmetric condition without concentration gradient, all the boundary conditions correspond to an adiabatic no-slip wall. Obstacles are set into the computational domain with a position corresponding to the experimental facilities by using an IBM described in Chapter 11.

We solve the Euler operator with a seventh-order OSMP7 scheme in time and space. Transport term used the Multicomponent description expressed in § 5.1.2. Detailed chemistry uses the H2 Mevel mechanism. Reactive source terms are solved using the Radau5 solver with a relative tolerance of  $1 \times 10^{-3}$  and an absolute tolerance of  $1 \times 10^{-10}$ .

Initially, the fluid is at rest at a temperature of 293 K and a pressure of 1 bar. We used a real gas configuration with a mixture of 79 % of  $N_2$  and 21 % of  $O_2$  in Air leading to, respectively, mass fraction  $Y_{Air} = 0.767$  and  $Y_{O_2} = 0.233$ . The mole concentration of the dihydrogen  $X_{H_2}$  is taken at 0.3, corresponding to  $Y_{H_2} = 0.029$  close to the stoichiometric condition. The inhomogeneous mixture simulation is initialized with the concentration profile after  $t_d = 10$  s corresponding to a molar concentration between 24.8 % vol and 34.5 % vol, corresponding to  $\Phi = 0.79$  and  $\Phi = 1.26$  respectively, approximated by the polynomial:

$$X_{H_2}(y) = -306.5 \cdot y^4 - 1002 \cdot y^3 + 92.3 \cdot y^2 - 0.2002 \cdot y + 0.2476. \quad (14.1)$$

This concentration profile is reproduced in Figure 14.8.

The ignition location is placed at the center of the ignition plate (the left end-wall) at  $x = 0$  m and

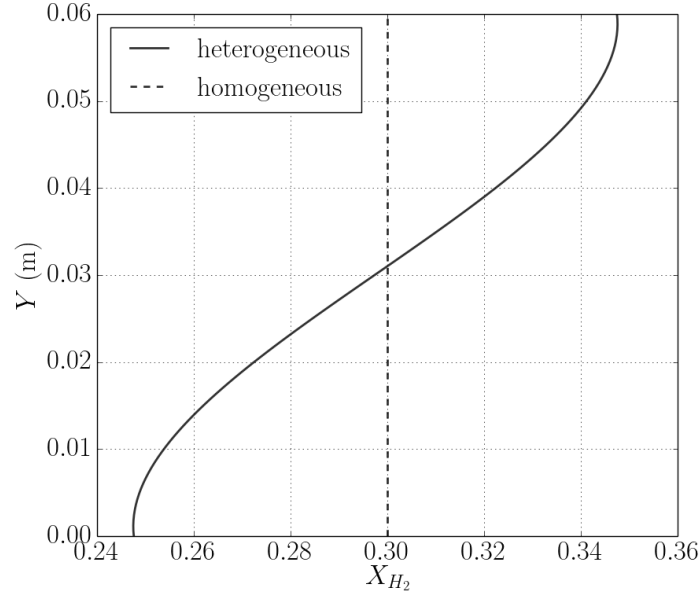


**Figure 14.8:** *Transverse  $H_2$  concentration profile in the inhomogeneous case at the initial condition*

$y = 0.03$  m by imposing a temperature of 2400 K at initial pressure in a patch of cells with a radius of 10 mm.

Simulations are performed on a structured grid using the adaptive mesh refinement method described in chapter 10. At the finest cell level, the mesh resolution is  $\Delta x = 29.3 \mu\text{m}$  with ten levels of refinement. This resolution leads to a maximum of 188 734 680 cells in the computational volume for the homogeneous case and 377 487 360 for the inhomogeneous case. However, the adaptive refinement with the Harten criterion  $\zeta = 0.1$  contains the number of effective cells below 2% of these theoretical maxima.

The finest resolution of the mesh corresponds to 7 cells inside the laminar flame thickness and between 4 and 5 cells inside the half-reaction length for detonation front at the initial atmospheric condition. According to the requirements defined in the previous Chapter 13, this resolution is sufficient in the first steps of the flame acceleration but is too limited to capture the detonation instability and the detonation diffraction phenomenon could hence be not properly captured. Moreover, the increase of the pressure along time in front of the flame shortened the characteristic length of the detonation and reduced the performance of the simulation again. However, a more important refinement was not affordable for our computational resources considering the performance of our numerical implementation.

Indeed, the poor ability of our code for parallelization, especially concerning the graduation of the tree, has not allowed conducting these two simulations up to the end. First drafts of the computations are presented here, which go through the first steps of the flame acceleration with homogeneous and inhomogeneous mixtures. Current results simulation provided the formation of a fast deflagration, but the transition to detonation has not been reached yet. However, we demonstrate with the current results, consistent with experimental observations and the previous simulations, the ability of our numerical methods to reproduce the flame acceleration process.

## 14.2.2 Numerical results

We present the first results obtained with the 30%  $H_2$ /Air mixture with a homogeneous and an inhomogeneous mixture in the obstructed channel (BR60).

Figure 14.9 shows flame speed data from experiments and the current results of the simulation with homogeneous and inhomogeneous initial conditions. The velocity is computed by using the maximal

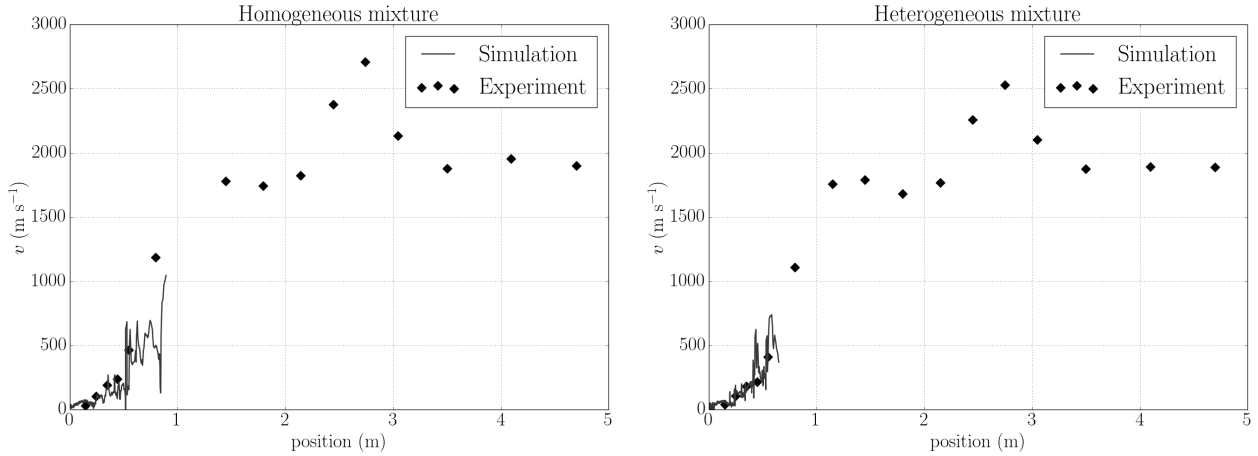


**Figure 14.9:** Comparison of the flame velocities with experimental data for homogeneous mixture (left) and inhomogeneous mixture (right)

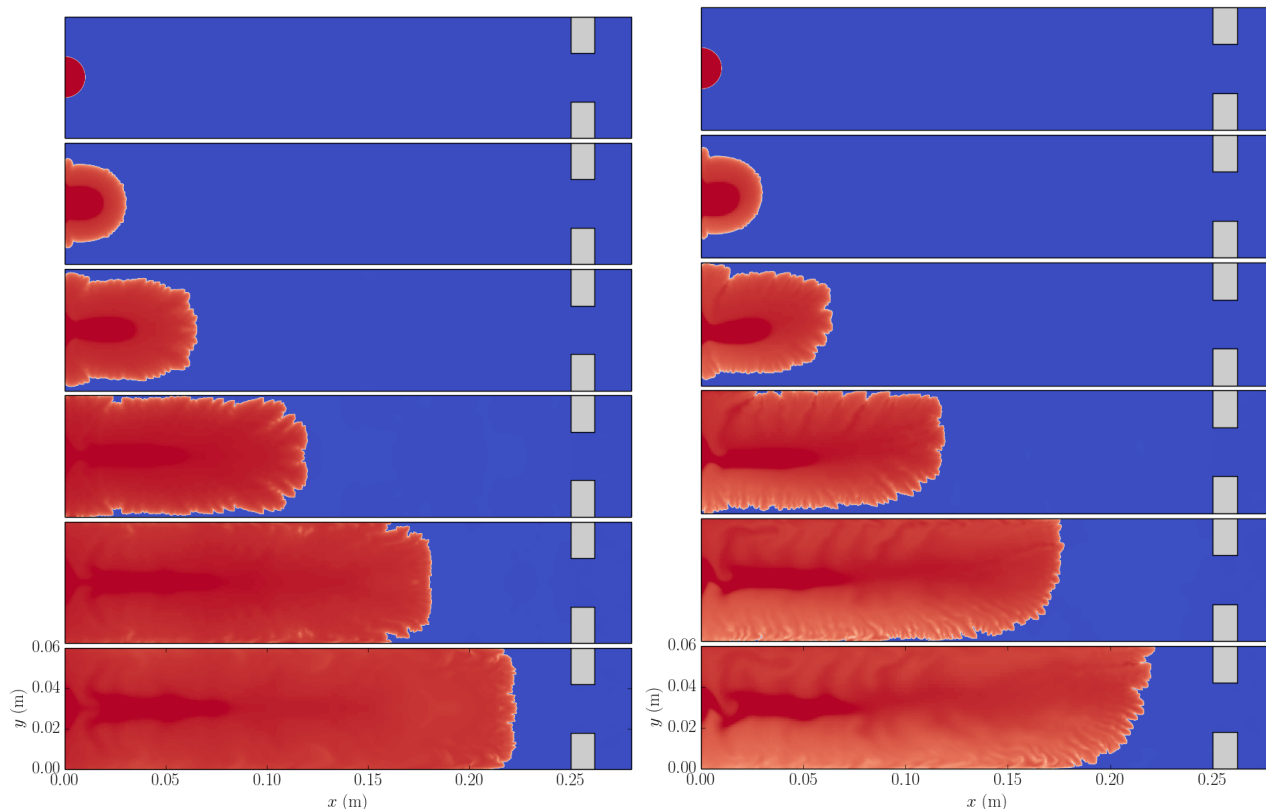
position of the front flame in the acceleration tube along time. Significant variations observed are induced by the dynamic structure in the flow and the influence of the obstacles that produce slow down and acceleration. At this time, the flame is in a fast turbulent deflagration with a velocity close to the burnt gas sound speed, which means that the transition to detonation might be imminent. Indeed, in the experiment, the velocity rises close to the Chapman-Jouguet velocity, which corresponds to  $1\,974\text{ m}\cdot\text{s}^{-1}$  under atmospheric conditions. An excellent agreement is obtained for the first steps of the flame acceleration with an inhomogeneous mixture. The velocity for the homogeneous mixture is slightly underestimated, maybe because of the impact of the symmetry condition as discussed in the following.

Figure 14.10 presents the evolution of both flames from 0 ms to 5 ms until the first obstacle, corresponding to the low Mach regime of deflagration. A distinct difference is visible between homogeneous and inhomogeneous cases. The flame front is inclined in the gradient mixture and propagates slowly in the lean mixture at the channel bottom since the laminar flame velocity is low. Smaller cellular structures are also discernible in the poorest region in accordance with the diminution of the Markstein length with the  $\text{H}_2$  concentration.

Figure 14.11 presents the evolution of the flame in between the first two obstacles. Vortices in the wake of the obstacles significantly influence flame behavior. Interaction between vortex and flame front created pockets of unburnt gas. Reactions in these pockets induce local expansion of the mixture, impacting the flow in two ways with acceleration in the propagation tube and reverse flows that go upstream of the tube. The velocity of the leading front (Figure 14.9) is then punctuated by small-scale successive discontinuous accelerations due to local expansion. The vicinity of the obstacles increases the pressure and decreases the speed downstream to produce powerful acceleration with expansion across the orifice.

We notice that the flame acceleration in our simulation is stronger for the inhomogeneous case in this section. This important flame acceleration for the inhomogeneous case comes from the more important mixing produced by large vortices. The largest dynamic structures that impact the front flame for the inhomogeneous case are the height of the channel. The formation of large pockets of unburnt gas visible in Figure 14.11 provokes gas expansions that increase the pressure in front of the front flame, positively impacting acceleration. In the homogeneous case, the structures are rather of the order of the height of the obstacles, also because the symmetry probably constrains them. The impossibility of producing larger dynamic structures can explain the small underestimation of the flame velocity compared to the experiment.

Figure 14.12 presents the density field as the flame passes through the second obstacle in the inhomogeneous mixture. This picture shows the different phenomena described so far. Many instabilities have



**Figure 14.10:** Temperature field in between the left end plate and the first obstacle for the homogeneous mixture (left), with symmetry applied at  $y = 0.03$  m, and inhomogeneous mixture (right) in the low Mach regime. Successive times at  $t = 0, 1, 2, 3, 4, 5$  ms; temperature scale is between 293 K (blue) and 3000 K (red).

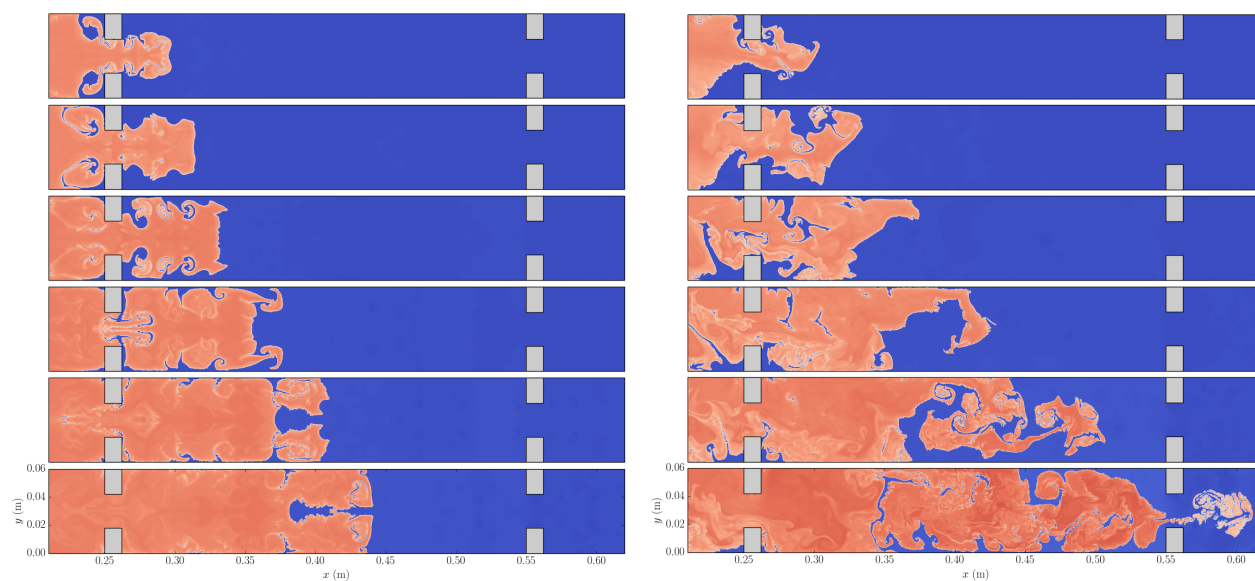


**Figure 14.11:** Temperature field in between the first two obstacles for homogeneous mixture (left), with symmetry applied at  $y = 0.03$  m and inhomogeneous mixture (right) in the fast deflagration regime. Successive times at  $t = 6, 6.25, 6.5, 6.75, 7, 7.25$  ms; temperature scale is between 293 K (blue) and 3000 K (red).

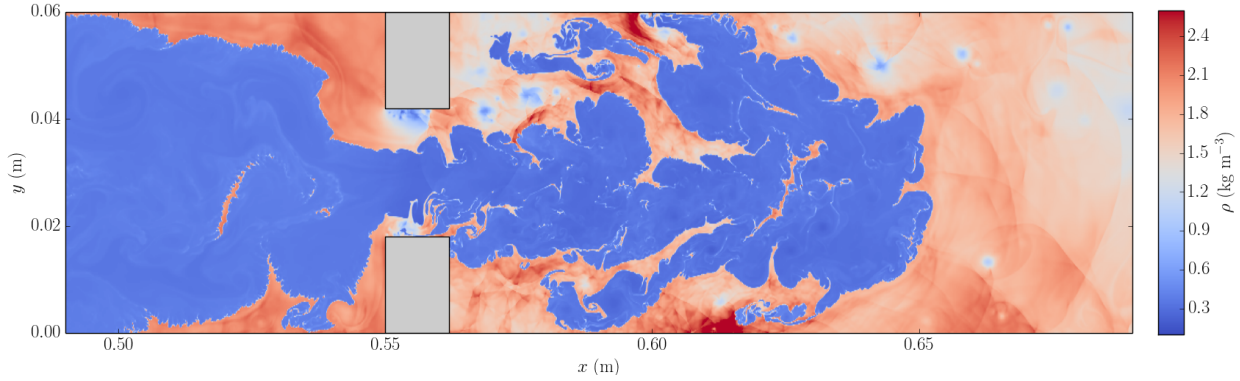


**Figure 14.12:** *Density field through the second obstacle for inhomogeneous mixture  $t = 7.34$  ms*

wrinkled the flame front from thermo-diffusive to Kelvin Helmholtz’s instabilities during interactions with pressure gradients. The vortices generated by the obstacles interact with the flame front and create a pocket of fresh gas that will expand.

As illustrated in Figure 14.13, most of the vorticity is produced downstream of the flame front. The baroclinic production term  $(\nabla\rho \times \nabla P)/\rho^2$  represent the vorticity generation. The surface fluctuation wrinkles of the density gradient are no longer aligned with the pressure gradient, producing Richtmyer Meshkov instability at the flame front.

Figure 14.14 presents the temperature and pressure field as the flame passes through the third obstacle in the homogeneous mixture. Powerful acceleration is generated by the expansion of the gas after the obstacle, illustrated by the pressure decrease. After the obstacle, strong compressible effects significantly influence the flame front, leading to favorable conditions for a transition to a detonation regime. First, reflected waves on the top and bottom boundaries increase the temperature that can produce auto-ignition and transition similar to the detonation re-initiation observed in § 14.1. Then, powerful acoustic waves are also generated upstream of the flame front and amplify the precursor pressure wave along time. This phenomenon seems to correspond to some self-reinforcement mechanisms such as described in § 3.2.1 which can lead to a transition to detonation if the reactive wave and the pressure wave coalesce.

Figures 14.15 and 14.16 show a closer view of the flame front itself. Figure 14.15 presents the density field and the mesh obtained at  $t = 8.68$  ms with the homogeneous mixture, which illustrates the effectiveness of multiresolution techniques in accurately capturing the flame front and compressional waves propagating through the computational volume. Figure 14.16 shows the mass fraction of the  $\text{HO}_2$  radical. It allows illustrating the refinement of the flame front, which is quite enough with seven cells into the front flame to capture the detailed chemical reaction properly according to the criteria determined in § 13.1.

### 14.3 Conclusion

Numerical studies have been conducted to investigate the flame acceleration process and the transition from deflagration to detonation.

First, attenuation of a hydrogen detonation front across a column of cylinders is presented. Quasi-detonation regime is reproduced numerically. According to the pore size of the porous medium, one or several shock reflections are required to retrieve conditions for re-initiation of the detonation.

Then, we present the simulation of the first steps of the flame acceleration process in an acceleration tube. This simulation reproduces the experimental device of the Technische University of Munich. It shows reasonable good agreement with theory and experimental measurement despite the incomplete simulation due to the excessive resource demand of the simulation. The initial laminar and turbulent

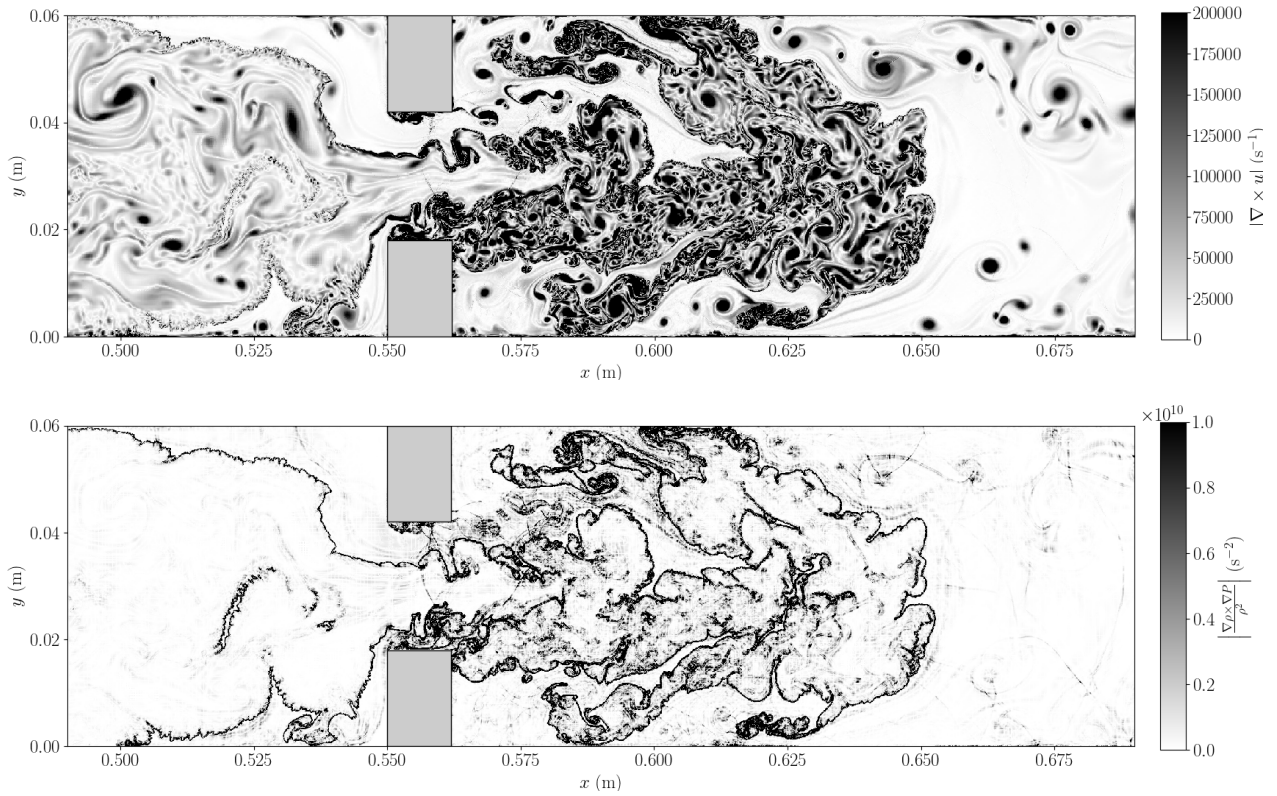


**Figure 14.13:** Vorticity field (top) and baroclinic production (bottom) through the second obstacle for inhomogeneous mixture  $t = 7.34$  ms

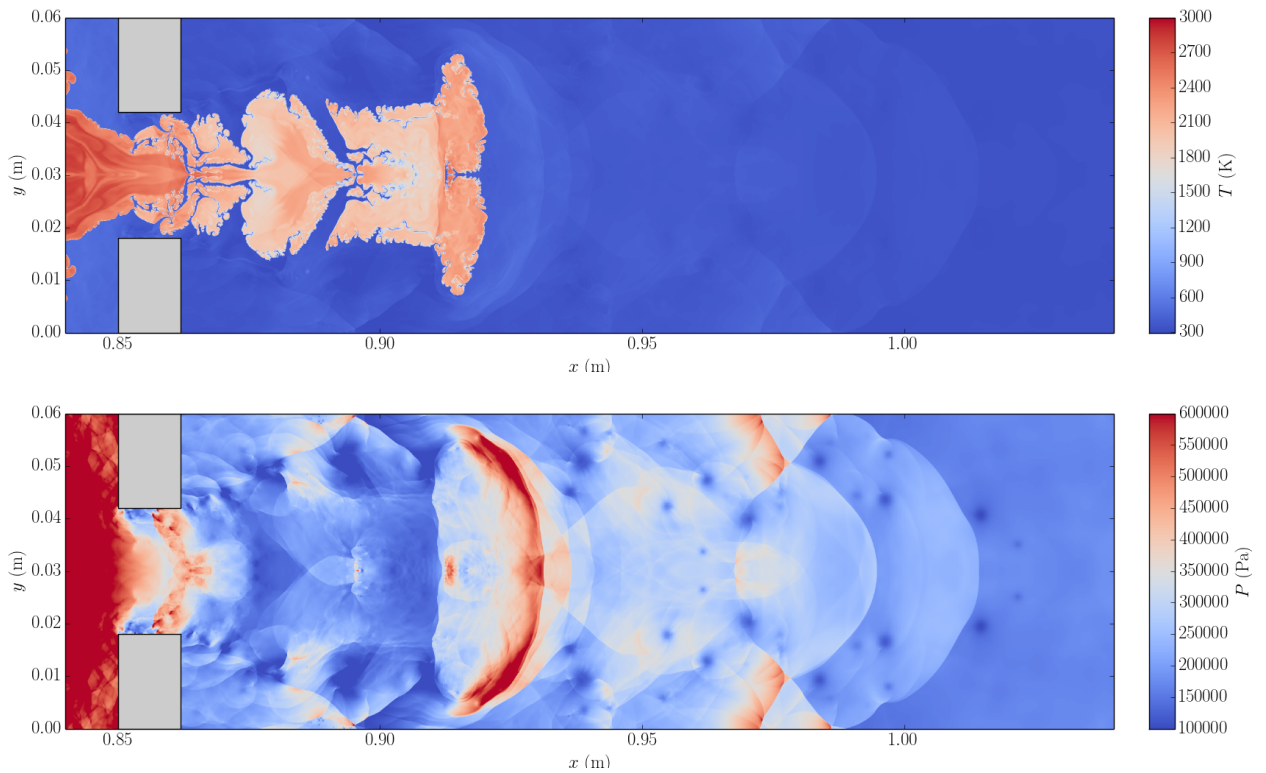


**Figure 14.14:** Temperature field (top) and pressure field (bottom) through the third obstacle for homogeneous mixture at  $t = 8.68$  ms, with symmetry applied at  $y = 0.03$  m



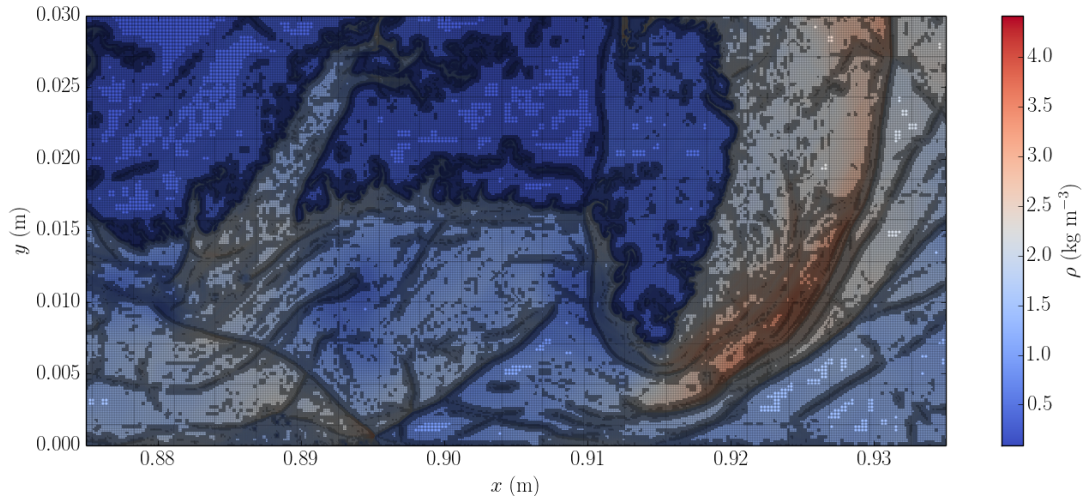


**Figure 14.15:** *Density field with mesh in the front flame for homogeneous mixture at  $t = 8.68$  ms*

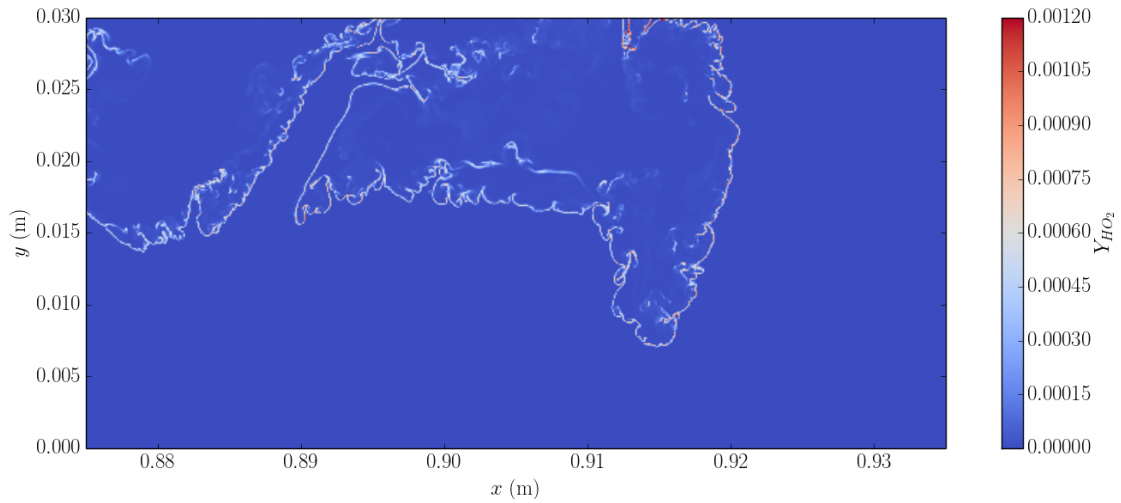


**Figure 14.16:** *Mass fraction of  $HO_2$  in the front flame for homogeneous mixture at  $t = 8.68$  ms*

deflagration regimes are observed with the homogeneous and heterogeneous mixture. Generation of vorticity and hydrodynamic instability through baroclinic torque have been highlighted. At the current last time of our simulations, compressible effects have become strongly significant; reflected shock waves producing small-scale vortices on the flame shear layer and new Richtmyer Meshkov instability. Reflected shock waves propagating in the domain and continuous amplification of the precursor pressure wave in front of the flame could correspond to some onset of detonation but are not strong enough to initiate this transition for now.

# General Conclusion and Prospects

## Summary

This thesis aims to propose a set of high-resolution methods to predict the phenomena occurring in the flame acceleration process and the transition to detonation. This subject is of interest in energy management and for various industries involving hydrogen. It is also being linked for several decades to nuclear safety issues, especially with the accidents at Three Miles Island and Fukushima, where hydrogen explosions endangered the integrity of the reactors.

The field of research applied to the evolution of a flame front in a confined environment involves various physical mechanisms ranging from thermo-diffusive instabilities impacting a laminar flame to the formation of onset of detonation and the behavior of a detonation front in a rough or porous medium. Over the last few decades, experimental studies have been carried out to identify the influence of such mechanisms, particularly using flame acceleration tubes. These experiments highlight the influence of some parameters as the presence of obstacles or concentration gradients, and allow the establishment of a set of empirical criteria. However, the various physical phenomena influencing the behavior of the flame are difficult to isolate properly, and the use of such criteria remains limited to correctly anticipating the evolution of a flame front in a complex environment.

The progress of numerical methods and simulation capacities can address these issues in the future. However, numerical methods dedicated to such simulation must overcome several limitations to faithfully reproduce highly compressible phenomena involving a wide spectrum of time and characteristic sizes with chemical and hydrodynamic length scales. The work presented here addresses these numerical issues and proposes a high-resolution numerical solver dedicated to resolving the flame acceleration process at the successive steps of its evolution until the transition to detonation.

We initially based our numerical setup on two existing tools: the AGATH library, which provides a flamelet library to compute chemical source terms and transport and thermodynamic model, and the MR\_CHORUS solver, which provides an efficient high-order compressible numerical scheme called the OSMP scheme. The MR\_CHORUS solver also includes multiresolution tools for adaptive mesh refinement that deal with multi-scales structures in space using a suitable local refinement. Developments have been realized to complete these numerical tools and adapt them to the problematics of flame acceleration.

The first part of these developments concerns the numerical scheme used:

- The MR\_CHORUS solver used a splitting operator to treat convection and diffusion operators with dedicated integration schemes. This initial integration scheme has been extended for multicomponent mixture, especially introducing diffusion operators using Multicomponent Dixon-Lewis diffusion coefficients. The scheme has also been completed by introducing a reactive operator using a Strang splitting scheme and solved with an implicit Radau5 solver to properly implement stiff source terms and use this solver with a wide range of time scales.
- For the resolution of the Euler operator, the OSMP scheme has been extended to work with multicomponent mixtures with convex state laws. In the context of hydrogen combustion, this scheme is then adapted to treat mixtures with temperature-dependent heat capacities that reproduce the variation of the vibrational and rotational energy of the molecular species with

temperature. This OSMP scheme presents a very low numerical diffusion and efficiently captures shocks, contact waves, and hydrodynamic instabilities. This work has led to a publication in the Journal of Computational Physics [LVK+22].

- However, in multidimensional cases, the OSMP scheme, based on the Roe solver, is sensitive to the so-called carbuncle instabilities near strong shock waves and a fortiori near detonation fronts. Several correction methods for Riemann solvers presented in the literature have been tested and extended to the OSMP scheme. Correction terms associated with a carbuncle sensor are proposed to correct these numerical instabilities, but further investigations may still be necessary to evaluate the real impact of these methods.

The numerical scheme was also completed with several numerical approaches to address some constraints encountered during the flame acceleration simulations.

- Immersed boundary methods have been added to allow considering solids of any shape in the flow despite the use of structured meshes. Specific geometric approaches, interpolation methods, and the use of ghost cells are proposed to associate the immersed boundary method with the high-order numerical scheme with strict conservation of mass and energy.
- In Situ Adaptive Tabulation (ISAT) methods have been tested to improve the computational performance of the reactive source terms. However, the gains obtained with hydrogen chemistry and simulations using multiresolution mesh adaptative methods were insufficient to integrate this approach in our simulations. The attenuation of instabilities, in particular in the detonation fronts, also limits the relevance of this type of method.

With these numerical tools, reference test cases are proposed to reproduce the main phenomena involved in flame acceleration and to evaluate the models used and the numerical needs, notably concerning the refinement required to capture them.

Classical one-dimensional shock-tube simulations and shock-bubble interaction studies have been conducted to underline the efficiency of our multicomponent OSMP scheme to capture the hydrodynamic instabilities.

We consider the hydrogen chemical mechanism developed by R. Mével, which has been previously used for detonation simulations. Fundamental properties such as the laminar flame velocity and the auto-ignition delay are well reproduced with this chemical mechanism. However, a precise multicomponent diffusion model is necessary to properly approximate the laminar velocity and thermo-diffusive instabilities. Cylindrical flames are used to evaluate the Markstein number obtained with these models. Finally, one-dimensional and two-dimensional detonation front simulation reproduces the instability phenomena related to the  $\chi$  parameter. Some refinement requirements have also been extracted from these simulations. Good behavior of the detonation front is then obtained with more than ten cells in the half-reaction length.

Finally, more complete simulations are proposed in this work with the interaction of a detonation front with a porous medium and the reproduction of the flame acceleration process in the GraVent acceleration tube of the TUM with and without concentration gradient. The first simulation presents an attenuation and a re-initiation of a detonation front that illustrates the capabilities of our numerical tools to reproduce the evolution of the detonation front properly. The initiation condition of a detonation from local shock wave focusing is illustrated in these tests case.

The second simulation presents the first stage of the flame acceleration in an acceleration tube and highlights the influence of the main phenomena identified as impacting the flame acceleration. The impact of the roughness of the tube and concentration gradients are illustrated. Local explosion in pockets of unburnt gas and production and growth of acoustic waves in front of the flame front, identified as potential onset of detonation, are reproduced. However, this simulation has not yet been completed entirely and does not reach the transition to detonation due to the lack of computational resources and efficiency of the numerical implementation.

The simulation tools developed in this work are therefore functional; they allow, as initially sought, precise monitoring of the behavior of a flame at different stages of its evolution. It has been tested on different test cases and can be extended to other configurations such as those studied experimentally. For example, it is possible to investigate new operating points, test the influence of parameters such as the Markstein number or the diffusion of species, reproduce critical extinction conditions, transition to detonation, simulate the interaction with porous walls or the ignition of pressurized H<sub>2</sub> jet release...

## Outlook

The numerical software described in this work has proven its capability to simulate the flame acceleration process as desired. However, several issues need additional investigations.

- Concerning carbuncle instability, the choice of the correction method used here is not entirely satisfactory. First, the analysis proposed in the Chapter 9 can be improved for cases with large stencils by using a more complete Jacobian. Indeed, the one used only considers the perturbations on the two neighboring cells of the face where the flux is calculated. Second, a correct evaluation of the corrections for the carbuncle requires establishing a clear distinction between the physical instabilities from the numerical instabilities.
- A dynamic chemistry tabulation method (ISAT) was presented but not used in the test cases. Indeed, this approach is not sufficiently effective for our configurations with hydrogen flames that present not complex enough chemistry and too significant evolutions over time. However, these methods may be relevant for other chemical mechanisms involving a larger number of reactions. A more thorough analysis of the error introduced by the tabulation is then necessary to determine its impact on the global error of the simulation and its interaction with the multiresolution methods, which can strongly impact the mesh refinement. Other techniques can also be used to describe the chemistry at lower cost with tabulation methods, reduction methods like ARC [Pep08], or recent deep learning methods adapted to stiff PDE like Stiff-PINN [JQS<sup>+</sup>21].
- A severe current limitation concerns the computational time obtained. The OSMP scheme and the multiresolution methods are proven to be efficient for CPU time consumption. However, the required refinement and the computational volume in the test case configurations impose better numerical code optimization and diminution of computational time. For such purposes, different tracks can be considered:
  - The use of adaptive splitting time steps approaches such as described in [Dua11] to increase the time steps while controlling the splitting error.
  - Large eddy simulation approach with subgrid-scale models and thickened flame front model can be used to obtain a more efficient simulation despite additional approximations that could impact the development of some instabilities and the onset of detonation that must be evaluated properly.
  - More globally, a better implementation of the code, more efficient memory management, and parallelization tools are needed. This last point is difficult with the current implementation of the code, which uses recursive functions on the refinement trees. However, current initiatives such as SAMURAI<sup>1</sup> are implementing mesh management methods with multiresolution tools to be parallelized efficiently.

Our numerical software has been tested in this work with one- and two-dimensional configurations. The numerical scheme and algorithmic features such as the immersed boundary also work with three-dimensional configurations. Validation of such configurations could become possible once the computational time issues are resolved and increase the possibilities of studies.

---

<sup>1</sup>SAMURAI: Structured Adaptive mesh and Multi-Resolution based on Algebra of Intervals <https://hpc-math-samurai.readthedocs.io>.

Finally, this software can also be completed with new functionalities. The integration of immersed walls can be done with dynamic walls by using fluid-structure coupling methods as in [MDM<sup>+</sup>12, PME<sup>+</sup>15] to reproduce the forces applied to the walls and the deformations generated. The high-resolution methods presented can also be extended to other research fields, such as atmospheric reentries or thermonuclear explosions of supernovas.

**Part V**

**Appendix**



# Hyperbolic system of Conservation Laws

This appendix provides mathematical properties of a general 1D hyperbolic system of conservation laws. We defined, in particular, the notion of weak solution and entropy conditions useful to guarantee the physical consistency of our scheme. Then, we present the Riemann problem and its resolution in the case of a non-linear system of hyperbolic system. The Riemann problem is introduced in the finite volume scheme. Numerical flux with an approximation of the Riemann problem allows convergence, with particular conditions, to the real physical solution.

## A.1 Mathematical background

### A.1.1 One-dimensional Conservation Laws

An hyperbolic system of conservation laws corresponds to a time dependent system of partial differential equations. We consider in this section only one space dimension that coincides with the directional splitting procedures. Then the hyperbolic system takes the form:

$$\frac{\partial}{\partial t} \mathbf{U}(x, t) + \frac{\partial}{\partial x} \mathbf{F}(\mathbf{U}(x, t)) = 0. \quad (2)$$

with  $\mathbf{U} : \mathbb{R} \times \mathbb{R}^+ \rightarrow \Omega$  with  $\Omega$  an open subset of  $\mathbb{R}^m$  with  $m$  the number of equations in this system.  $\mathbf{U}$  is then a vector with  $m$  components composed by conserved quantities or state variable corresponding to (5.1) in the case of fluids dynamics problem.  $F : \Omega \rightarrow \mathbb{R}^m$  is the flux function.

Cauchy problem designed the association of such system of conservation law with an initial condition  $U(x, t = 0) = U_0(x)$  for each variable  $x \in \mathbb{R}$ .

We consider  $\mathbf{A}$  the  $m \times m$  Jacobian matrix of the flux fonction.

$$\mathbf{A}(U) = \left( \frac{\partial \mathbf{F}_i(\mathbf{U})}{\partial_j \mathbf{U}} \right)_{1 \leq i, j \leq m}. \quad (3)$$

The system (6.2) is said to be *hyperbolic* if for each value of  $u$ , the matrix  $\mathbf{A}(U)$  is diagonalizable and its eigenvalues  $\lambda_1, \dots, \lambda_m$  are real.

Considering perturbations around a constant state and linearizing the system of equation, we can express (6.2) in the quasi-linear form with:

$$\frac{\partial}{\partial t} u(x, t) + \mathbf{A}(u) \frac{\partial}{\partial x} u(x, t) = 0. \quad (4)$$

Mathematical analysis of such hyperbolic systems has been extensively developed in the literature. Extensive description of their properties are available in [Lev92, LeV02, EG96]. We present in this chapter two main mathematical difficulties that have been identified for such systems. The first one concerns the development of singularity, leading at a finite time to a discontinuous solution that does not satisfy the PDE at all points since the derivatives are not defined at discontinuities. Manifestation



of such development in the fluids dynamics is the formation of shock waves in compressible flow corresponding to discontinuities in pressure and temperature and contact discontinuities where density and entropy jumps occurs. The *weak solution* has been developed to deal with the non-regularity of the solution.

The second one concerns the possible non-uniqueness of the solution. There is indeed more than one weak solution to the conservation law with the same initial data. However, only one corresponds to a physically relevant solution. Vanishing viscosity methods are introduced to consider a physical solution with an inherent viscosity that tends to zero. For gas dynamics, we can also consider the second law of thermodynamics, which states that entropy is nondecreasing and that this entropy must increase through a shock. This entropic condition is sufficient to specify a unique solution, and this notion can be generalized for other systems of conservation laws.

### A.1.2 Scalar case

We provide the first definitions by considering the scalar case. The Cauchy problem for the function  $u(x, t) \in \mathbb{R}$  becomes:

$$\begin{cases} \partial_t u + \partial_x(f(u)) = 0 & t \geq 0, x \in \mathbb{R}, \\ u(x, 0) = u_0(x) & x \in \mathbb{R}. \end{cases} \quad (5)$$

#### Characteristic curves

The characteristic curves are defined as the curves in the  $t - x$  plane along which the PDE becomes an Ordinary Differential Equation (ODE). In this case, the characteristic curves  $X = X(t)$  satisfy the ODE :

$$\frac{dX}{dt} = a(u(t, X(t))) = f'(u). \quad (6)$$

If  $u_0 \in C^1(\mathbb{R})$  and  $f \in C^2(\mathbb{R})$ ,  $u$  is constant along the characteristic curves. Indeed, considering  $v(t) = u(t, X(t))$  we retrieve the quasi-linear form of (5):

$$v'(t) = \partial_t u + \frac{dX}{dt} \partial_x u = 0. \quad (7)$$

For example, in the advection case, where  $a$  is a scalar constant, if  $u_0 \in C^1(\mathbb{R})$  the unique solution  $C^1$  from  $\mathbb{R}^+ \times \mathbb{R}$  in  $\mathbb{R}$  of the Cauchy problem is:

$$u(t, x) = u_0(x - at), \quad x \in \mathbb{R}, \quad t \geq 0. \quad (8)$$

So we have a unique solution signal  $u_0(\xi)$  traveling along the  $x$ -axis at a constant velocity  $a$ .

In the nonlinear case, characteristic curves from different initial values will travel at various velocities and possibly intersect. Such situations result in the creation of discontinuities inside the solution since at a specific point in the  $x - t$  space, solutions can be multievaluated which is not admissible.

#### Weak solution

To deal with discontinuities in the solution of the hyperbolic system, we need to use the weak form of the Cauchy problem. Thus, a function  $u(x, t)$  is said to be a weak solution of the Cauchy problem if  $\forall \phi \in C_0^\infty(C)$ , with  $C$  compact in  $\mathbb{R} \times \mathbb{R}^+$

$$\int_0^{+\infty} dt \int_{-\infty}^{\infty} dx \left[ \frac{\partial \phi}{\partial t} u + \frac{\partial \phi}{\partial x} f(u) \right] + \int_{-\infty}^{+\infty} \phi(x, 0) u_0(x) dx = 0, \quad (9)$$

where  $\mathcal{C}_0^\infty(C)$  represents the set of functions that are infinitely differentiable in  $C$  and equal to zero outside.

In this case, it is proved in [EG96] that a piecewise  $\mathcal{C}^1$  function  $u$  is a weak solution of (9) if and only if :

1.  $u(x, t)$  is a classical solution of the Cauchy problem where  $u \in \mathcal{C}^1$
2.  $u$  satisfied the Rankine-Hugoniot conditions along the discontinuities, i.e. for a discontinuities propagating at a speed  $v_D$  and with  $u_l$  the left state and  $u_r$  the right state around the discontinuity, it must satisfy:

$$v_D(u_l - u_r) = f(u_l) - f(u_r). \quad (10)$$

### Entropy conditions

However a weak solution of the Cauchy problem verifying the two conditions (9) and (10) is not necessarily unique. In order to represent physically admissible solution, we consider the limit of the viscous-perturbed conservation law as the viscosity  $\epsilon \rightarrow 0^+$ :

$$\frac{\partial u}{\partial t} + \frac{\partial f(u)}{\partial x} = \epsilon \frac{\partial^2 u}{\partial x^2}, \quad (11)$$

According to [Lev92], this solution is related to a convex entropy function  $\eta(u)$  and the associated entropy flux  $\psi(u)$ . Entropy function gives an additional conservation law for smooth solutions that becomes an inequality for discontinuous solution.

A weak solution of the problem (9) is said entropy-satisfying if it satisfy the entropy condition

$$\frac{\partial \eta(u)}{\partial t} + \frac{\partial \psi(u)}{\partial x} \leq 0, \quad (12)$$

for all the entropy couples  $(\eta(u), \psi(u))$ .

If  $u_0 \in L^\infty(\mathbb{R})$ , so the Cauchy problem has a unique entropy-satisfying solution  $u \in L^\infty(\mathbb{R}^+, \mathbb{R})$

In this case, a piecewise  $\mathcal{C}^1$  function  $u$  is a entropy-satisfying weak solution of (9) if and only if :

1.  $u(x, t)$  is a classical solution of the Cauchy problem where  $u \in \mathcal{C}^1$
2.  $u$  satisfied the inequality across discontinuities

$$v_D[\eta(u_R) - \eta(u_L)] \geq \psi(u_R) - \psi(u_L). \quad (13)$$

### Resolution of the Riemann problem

The Riemann problem is a classical problem that will intervene in the numerical finite volume methods used in our simulations. It corresponds to the Cauchy problem with particular discontinuous initial conditions:

$$\begin{cases} \frac{\partial u}{\partial t} + a(u) \frac{\partial u}{\partial x} = 0, & -\infty < x < \infty, t > 0, \\ u(x, 0) = u_0(x) = \begin{cases} u_L & x < 0, \\ u_R & x > 0. \end{cases} \end{cases} \quad (14)$$

with  $a(u) = f'(u)$ . The Riemann problem has a self-similar structure. Then the solution depends only on  $\xi = x/t$

$$u(t, x) = v\left(\frac{x}{t}\right) = v(\xi), \quad t > 0. \quad (15)$$

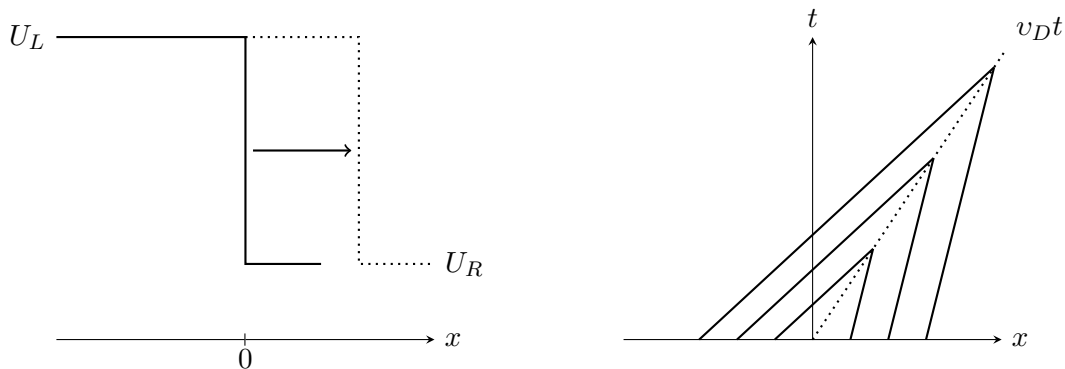


**Figure 17:** Solution (left) and characteristic waves (right) for a shock wave

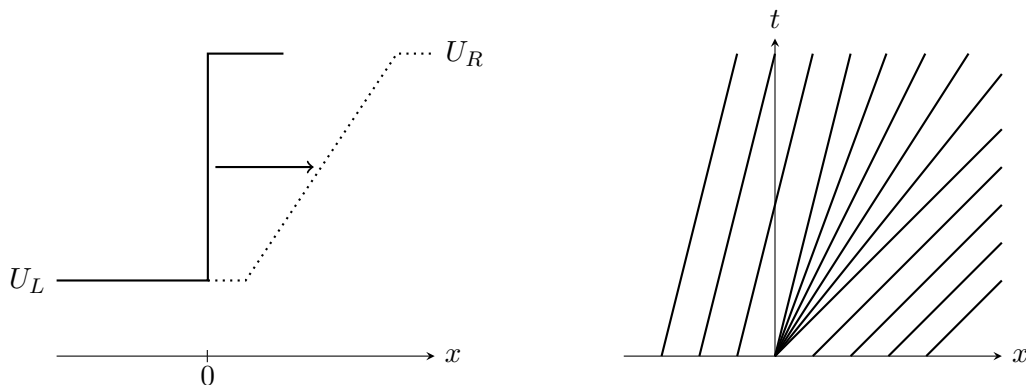


**Figure 18:** Solution (left) and characteristic waves (right) for a rarefaction wave

We consider here that  $a(u)$  is a monotone function of  $u$ , which means that  $f(u)$  is convex (or concave) function of  $u$ . In that case, there is two possible solutions for the evolution of the discontinuity depending on the relation between  $u_L$  and  $u_R$ .

- $a(u_L) > a(u_R)$ : the solution corresponds to a shock wave with a speed  $v_D$  determined by the Rankine-Hugoniot condition (10),

$$v_D = \frac{f(u_L) - f(u_R)}{u_L - u_R}; \quad (16)$$

- $a(u_L) < a(u_R)$ : the entropy condition (13) does not allow entropic discontinuities and the solution corresponds to a smooth self-similar solution connecting  $u_L$  and  $u_R$  called rarefaction wave:

$$w(\xi, u_L, u_R) = \begin{cases} u_L & \frac{x}{t} \leq a(u_L), \\ a^{-1}(\xi) & a(u_L) \leq \frac{x}{t} \leq a(u_R), \\ u_R & \frac{x}{t} \geq a(u_R). \end{cases} \quad (17)$$

The two possible solutions with a growing function  $a(u)$  are illustrated in the figures 17 and 18.

We notice that monotonicity of the characteristic speed  $a(u)$  is essential to characterized the behavior of the solution  $u(x, t)$ . If  $a(u)$  is not monotone, then some transition between a shock wave and a rarefaction wave is possible and solution of the Riemann solver becomes much more complex.

### A.1.3 Hyperbolic Systems of conservation laws

We now consider a hyperbolic system of conservation law expressed in its conservative formulation (6.2).

## Linear case

In the linear case, the flux expression becomes  $F(U) = \mathbf{A}U$  with  $\mathbf{A}$  a constant  $m \times m$  Jacobian matrix. This specific case will intervene in the definition of the Roe solver introduced in §7.1 which consists in a linearization of the Euler hyperbolic system.

Since we consider an hyperbolic system,  $\mathbf{A}$  is diagonalizable with real eigenvalues, we denote the right eigenvectors  $\mathbf{K}^{(i)}(\mathbf{U})$ ,  $i = 1, m$  of the matrix  $\mathbf{A}$  corresponding to the eigenvalues  $\lambda_i(\mathbf{U})$ ,  $i = 1, m$

$$\mathbf{A} = \mathbf{K}\mathbf{\Lambda}\mathbf{K}^{-1}, \quad (18)$$

where  $\mathbf{\Lambda} = \text{diag}(\lambda_1, \lambda_2, \dots, \lambda_m)$

We define a new set of lineary independent characteristic variables  $\mathbf{W} = (w_1, \dots, w_n)^T$  such as  $d\mathbf{W} = \mathbf{K}^{-1} d\mathbf{U}$

Direct substitution into equation (6.2) gives the characteristic form of the conservation laws:

$$\mathbf{W}_t + \mathbf{\Lambda}\mathbf{W}_x = 0. \quad (19)$$

Thus we obtain a linear combination of  $m$ -independent advection equations with characteristic speed defined by the eigenvalues  $\lambda_k$ , therefore, applying the characteristic method:

$$\mathbf{U}(X, t) = \sum_{i=1}^m \mathbf{K}^{-1(i)T} \mathbf{U}_0(x - \lambda_i t) \mathbf{K}^{(i)}, \quad (20)$$

In the case of a system strictly hyperbolic, which means that the eigenvalues ( $\lambda_k$ ) are such that  $\lambda_1 < \lambda_2 < \dots < \lambda_p$  we have a superposition of the left and right states in the eigenvector space. Indeed if we consider the decomposition of the initial state:

$$\mathbf{U}_L = \sum_{i=1}^m \alpha_i \mathbf{K}^{(i)}, \quad \mathbf{U}_R = \sum_{i=1}^m \beta_i \mathbf{K}^{(i)}. \quad (21)$$

Then the solution  $\mathbf{U}(x, t)$  at any point  $(x, t)$  became:

$$\begin{aligned} \mathbf{U}(x, t) &= \mathbf{U}_L + \sum_{\lambda_i < x/t} (\beta_i - \alpha_i) \mathbf{K}^{(i)} \\ &= \mathbf{U}_R - \sum_{\lambda_i \geq x/t} (\beta_i - \alpha_i) \mathbf{K}^{(i)} \end{aligned} \quad (22)$$

$\mathbf{U}(x, t)$  depends on the value at  $m$  particular points  $X - \lambda^p t$  for  $p = 1, \dots, m$ . This set of point corresponds to the domain of dependence  $\mathcal{D}(x, t)$  of the point  $(x, t)$ :

$$\mathcal{D}(\bar{x}, \bar{t}) = \{x = \bar{x} - \lambda_i \bar{t}, i = 1, \dots, m\}. \quad (23)$$

The size of the domain of dependence at a fixed time  $\tau$  is then bounded by the maximal eigenvalues of the system corresponding to the maximal velocity of the propagation of the information in space.

## The nonlinear case

We extend here the definitions and properties described previously to nonlinear hyperbolic systems in order to solve entirely the Riemann problem. In this case, the Jacobian matrix  $\mathbf{A}(\mathbf{u})$  is a function of the state variable  $\mathbf{u}$ . The characteristic curves, associated with the eigenvalues  $\lambda_k$  depend on the local state and are not necessarily straight lines anymore:

$$\frac{dX}{dt} = \lambda_k(\mathbf{u}(t, X(t))). \quad (24)$$

We call  $\lambda_k$ -field the characteristic field corresponding to the part of the solution relative to the  $k^{\text{th}}$  eigenvalue  $\lambda_k$ :

- a  $\lambda_k$ -field is said to be linearly degenerate (LD) if

$$d_U \lambda_k(\mathbf{U}) \cdot \mathbf{K}^{(k)}(\mathbf{U}) = 0, \quad \forall \mathbf{U} \in \mathbb{R}^m; \quad (25)$$

- a  $\lambda_k$ -field is said to be genuinely nonlinear (GNL) if

$$d_U \lambda_k(\mathbf{U}) \cdot \mathbf{K}^{(k)}(\mathbf{U}) \neq 0, \quad \forall \mathbf{U} \in \mathbb{R}^m. \quad (26)$$

In the scalar case with  $m = 1$ , we have  $\lambda(u) = a(u) = f'(u)$ , the characteristic field is then GNL if and only if  $a(u)$  does not vanish, i.e. if  $a(u)$  is strictly convex or a strictly concave function. Equivalently, a LD characteristic field corresponds to a constant velocity  $a(u) = a$ .

When  $m > 1$ , in an analogous way, if a hyperbolic system is convex, which implies that the eigenvalues  $\lambda_k(U)$  are monotone, then each  $\lambda_k$ -field is either GNL or LD.

## Riemann invariants and simple waves

Each  $\lambda_k$ -field is associated to  $k$ -Riemann invariants which are the functions  $g^{(k)}(\mathbf{U})$  such as:

$$\nabla_U g^{(k)}(\mathbf{U}) \cdot \mathbf{K}^{(k)}(\mathbf{U}) = 0, \quad \forall \mathbf{U} \in \mathbb{R}^m. \quad (27)$$

We note that if the  $\lambda_i$ -field is LD, then  $\lambda(u)$  is a Riemann invariant.

We define the integral curves corresponding to the curves in the phase space  $(u_1, \dots, u_m)$  tangent to the eigenvectors.

The  $k$ -invariants of Riemann are constant along the integral curves of the  $\lambda_k$ -field. Therefore, there are  $m - 1$  Riemann invariants with linearly independent gradients for each  $\lambda_k$ -fields. An unspecified  $k$ -Riemann invariant can be decomposed into a combination of  $m - 1$  linearly independent invariants.

In order to treat solutions with uniform zone, we introduce the notion of  $k$ -simple waves. A smooth solution on a domain  $D$  of  $\mathbb{R} \times \mathbb{R}^+$  is called a  $k$ -simple wave if  $g^{(k)}(\mathbf{u}(x; t))$  is constant in  $D$  for any  $k$ -Riemann invariant  $g^{(k)}$ . Such waves correspond to the area of the  $x - t$  space sharing boundary with a uniform zone.

Then since the  $k$ -Riemann invariants are constant along the integral curves, the values of  $\mathbf{u}$  in a  $k$ -simple wave are restricted to only one integral curve of  $\mathbf{r}_k$ . Moreover, in the case  $\mathbf{u}$  is a  $k$ -simple wave, since the solution is in the same integral curve, it can be proved as in [EG96] that the characteristic curves of the  $\lambda_k$ -field (24) are straight lines along with  $\mathbf{u}$  is constant.

This property is essential for solving the Riemann problem for a convex hyperbolic system of equations. Indeed, rarefaction waves are  $k$ -simple waves. It implies that the description of rarefaction wave made in (A.1.2) is a continuous weak solution and is still valid in the nonlinear case. In the Figure (18), the straight lines in the rarefaction fan correspond to the characteristic curves of the  $\lambda_k$ -field.

## Shock waves and contact discontinuities

In case of discontinuous solutions between two states  $u_L$  and  $u_R$ , the Rankine Hugoniot jump condition (10) must still be satisfied.

- If the  $\lambda_k$ -field is GNL, it corresponds to a *k-shock wave*. Just as in the linear case, those *k-shock* curve are admissible if they satisfy an entropy condition. For a GNL nonlinear field, the Lax's entropy condition sets that the jump between the left state  $u_L$  and the right state  $u_R$  is admissible only if:

$$\lambda_k(u_L) > v_D > \lambda_k(u_R), \quad (28)$$

with  $v_D$  the speed of the shock wave.

The characteristic curves of the  $\lambda_k$ -field intersect the shock wave as time advances, just as in the scalar case illustrated in 17. In the general case, the Lax entropy conditions are equivalent to the entropy condition for weak shock. However as it is proven in [EG96], in the case of the gas dynamics, the Lax entropy conditions coincide with the physical entropy condition.

- In the case the  $\lambda_k$ -field is LD, then a admissible weak solution is  $v_D = \lambda_k(u_L) = \lambda_k(u_R) = \bar{\lambda}_k$  that is called a *k-contact discontinuity*.

## Resolution of the Riemann problem

We are now able to solve the Riemann problem for a convex hyperbolic system (6.2).

$$\begin{cases} \frac{\partial}{\partial t} U(x, t) + \frac{\partial}{\partial x} F(U(x, t)) = 0, & -\infty < x < \infty, \quad t > 0, \\ u(x, 0) = u_0(x) = \begin{cases} u_L & x < 0, \\ u_R & x > 0. \end{cases} \end{cases} \quad (29)$$

Theorem given in [EG96] states that if the hyperbolic system is convex, all the  $\lambda_k$ -fields are either GNL or LD. Then, in the case of a strictly hyperbolic system (6.2), the Riemann problem has a weak solution with  $m-1$  constant states separated by rarefaction waves, admissible shock waves and contact discontinuities. Moreover, a weak solution of this kind is unique.

Let  $U_L$  be the left state, we summarize the possibilities for the right states  $U_R$  to be separated from  $U_L$  by a *k*th characteristic curve

- if  $\lambda_k$ -field is GNL then there is two possibilities:
  - The entropy condition (Lax entropy condition) is satisfied and there is a *k-shock* wave traveling with speed  $v_D$  that respect the Rankine Hugoniot conditions (10),
  - The shock is not admissible and  $U_L$  and  $U_R$  are separated with a rarefaction wave, a self-similar *k-simple* wave along with there is  $m-1$  constant *k-Riemann* invariants lineary independent and straight *k-characteristic* curves.
- if the  $\lambda_k$ -field is LD: then  $\lambda^{(k)}$  is a *k-Riemann* invariant wave. Thus, the *k*th characteristic curves behave like a linear one with  $\lambda^k(U_L) = \lambda^k(U_R)$ .

We note that in the case of a non strictly hyperbolic system, so with multiple eigenvalues. The  $\lambda_k$ -field associated with multiple eigenvalues can only be LD as it is the case in the Euler system.

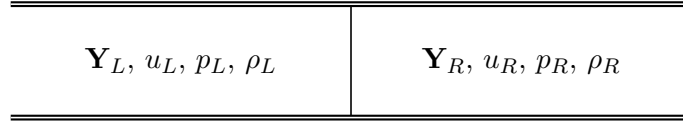


**Figure 19:** Schematic representation of the initial state in a shock tube.

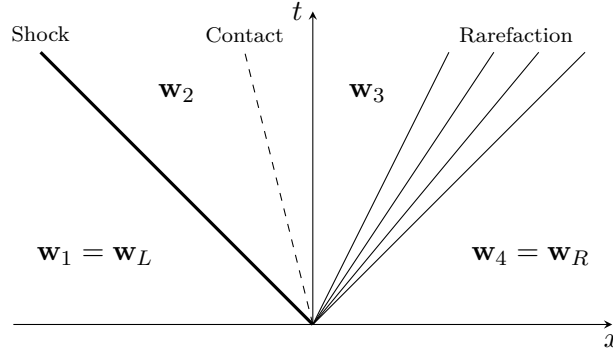


**Figure 20:** Structure of the solution of the Riemann problem in the  $x-t$  plane for the one-dimensional Euler equations in which the left wave is a shock wave and the right wave is a rarefaction wave.

## A.2 Riemann problem and Godunov solver for 1D Euler equations with mixtures of ideal gases with temperature-dependent heat capacities

For the Euler equation, the Riemann problem corresponds to the shock tube problem with two states on either side of a diaphragm removed initially. The initial condition is illustrated in Figure 19.

We consider the one-dimensional case, then for the  $x$ -axis :

$$\begin{cases} \frac{\partial \mathbf{w}}{\partial t} + \mathbf{A}(\mathbf{w}) \frac{\partial \mathbf{w}}{\partial x} = \mathbf{0}, & -\infty < x < \infty, t > 0, \\ \mathbf{w}(x, 0) = \mathbf{w}_0(x) = \begin{cases} \mathbf{w}_L & x < 0, \\ \mathbf{w}_R & x > 0. \end{cases} \end{cases} \quad (30)$$

### A.2.1 Resolution of the Riemann problem

Three different characteristic waves are associated with the three elementary waves solution. The characteristic field  $\lambda_0$  corresponding to the eigenvalue  $v$  is linearly degenerated, the two others  $\lambda_-$  and  $\lambda_+$  corresponding to  $v - c$  and  $v + c$  and are genuinely non-linear with the hypothesis of convexity of the equation of state.  $\lambda_0$  is then a contact discontinuity; the two others will either be a rarefaction wave or a shock wave. A representation of the three characteristic waves in the  $x-t$  plane is illustrated in Figure 20 corresponding to the solution with  $\lambda_-$  a shock wave and  $\lambda_+$  a rarefaction wave.

#### Rarefaction wave

Let us suppose  $\lambda_+$  be a rarefaction wave. Then  $\lambda_+$  is a simple wave, and there is conservation of the Riemann invariant corresponding to the characteristic variables relative to the other fields. Then we have:

$$\begin{cases} c_s^2 d\rho_i - Y_i dp = 0, & 1 \leq i \leq n_s, \\ dp - \rho c_s du = 0. \end{cases} \quad (31)$$

By the addition of the  $n_s$  first equations, we found the classical characteristic variables associated with the density:

$$c_s^2 d\rho - dp = 0 \quad (32)$$

and combined in the equation we can use  $d\rho_i = Y_i d\rho + \rho dY_i$  which finally gives us  $dY_i = 0$

Thus, the composition of the mixture does not change across a rarefaction wave, and the gas function  $R(\mathbf{Y}) = R_R$  is constant. Then the heat capacity ratio only depends of the temperature  $\gamma(T, \mathbf{Y}) = \gamma_R(T)$ .

Using the perfect gas law (5.34), we have:

$$\frac{dp}{p} = \frac{d\rho}{\rho} + \frac{dT}{T}. \quad (33)$$

With (32) and  $c_s^2 = \gamma(T)p/\rho$ , we obtain:

$$\frac{dp}{p} = \frac{\gamma_R(T)}{\gamma_R(T) - 1} \frac{dT}{T}. \quad (34)$$

Integrating this relation, we obtain a parametrization of the rarefaction wave based on the temperature:

$$p(T, \mathbf{w}_R) = p_R \exp \left( \int_{T_R}^T \frac{\gamma_R(\alpha)}{\gamma_R(\alpha) - 1} \frac{d\alpha}{\alpha} \right). \quad (35)$$

In a same way, the velocity in the rarefaction wave can be parametrized with the temperature. Combining (31), (32) and (33), we have:

$$du = \frac{\sqrt{R_R \gamma_R(T)} dT}{\gamma_R(T) - 1 \sqrt{T}}. \quad (36)$$

Then, the value of the velocity inside the rarefaction wave became:

$$u(T, \mathbf{w}_R) = u_R + \int_{T_R}^T \frac{\sqrt{R_R \gamma_R(\alpha)} d\alpha}{\gamma_R(\alpha) - 1 \sqrt{\alpha}}. \quad (37)$$

### Shock curve

Let us suppose  $\lambda^-$  is a shock curve. The Rankine Hugoniot condition (10) must then be satisfied. we call  $v$  the velocity of the fluid in the referential of the compression wave where the shock is fixed. The jump conditions across the discontinuity became:

$$\begin{cases} \rho_L v_L = \rho_2 v_2 = m, \\ \rho_L v_L^2 + p_L = \rho_2 v_2^2 + p_2, \\ m \left( h_L + \frac{1}{2} v_L^2 \right) = m \left( h_2 + \frac{1}{2} v_2^2 \right), \\ m Y_{L,1} = m Y_{2,1}, \\ \dots \\ m Y_{L,n_s} = m Y_{2,n_s}. \end{cases} \quad (38)$$

If  $m = 0$ , the discontinuity is a contact wave. In that case, pressure and velocity are constant:

$$p_L = p, \quad v_L = v. \quad (39)$$

If  $m \neq 0$ , the discontinuity is a shock wave. The Lax-entropy condition states that to obtain such a shock curve with entropy increasing, then:



$$v_L - c_{s,L} \geq 0 \geq v - c_s. \quad (40)$$

It means that the flow is supersonic ahead of the shock and subsonic behind it.

As in a rarefaction wave, the composition of the mixture remains constant across a shock wave, and the heat capacity ratio only depends on temperature  $\gamma(T, \mathbf{Y}) = \gamma_L(T)$

The first relation of (38) gives:

$$u_L^2 - u^2 = -(p_L - p) \left( \frac{1}{\rho_L} + \frac{1}{\rho} \right); \quad (41)$$

$$h_L - h = -\frac{1}{2}(u_L^2 - u^2) = \frac{1}{2}(p_L - p) \left( \frac{1}{\rho_L} + \frac{1}{\rho} \right). \quad (42)$$

we also have

$$v_L^2 = 2(h - h_L) \frac{(\rho/\rho_L)^2}{(\rho/\rho_L)^2 - 1}; \quad (43)$$

$$v^2 = 2(h - h_L) \frac{1}{(\rho/\rho_L)^2 - 1}. \quad (44)$$

For the shock wave, we also have a parametrization with the temperature  $T$ . Using the perfect gas law (5.34) and (42) we obtain the quadratic equation:

$$\zeta^2 - 2b\zeta - c = 0, \quad (45)$$

where  $\zeta = \rho/\rho_L = \sqrt{b^2 + c} + b$  and  $b = \frac{h-h_L}{R_L T} + \frac{1}{2} \left( \frac{T_L}{T} - 1 \right)$  and  $c = \frac{T_L}{T}$ .

Among the roots of 45, the condition  $\zeta > 0$  allows only one physical condition

In the laboratory framework, with the equations (43) and (44), the velocity of the shock is:

$$v_D = u_L - v_L = v_L - \sqrt{2(h - h_L) \frac{\zeta^2}{\zeta^2 - 1}}, \quad (46)$$

and

$$u = v + v_D = u_L - \sqrt{\frac{2(h - h_L)}{\zeta^2 - 1}}(\zeta - 1). \quad (47)$$

Figure 21 illustrated the intersection of the characteristic curves in the  $(u, p)$  plane

### A.2.2 Godunov solver

The Godunov solver is a finite-volume method that approximated the solution at the time  $t_{n+1}$  from the time  $t_n$  solving the exact Riemann problem at the intersection of each cell. To solve the Riemann problem, we need to determine the nature of the characteristic waves  $\lambda^{(+)}$  and  $\lambda^{(-)}$ . Based on the continuity of the pressure  $p^*$  and the velocity  $u^*$  across the contact wave, the GNL curves must intersect in the  $(u, p)$  plane as illustrated in Figure 21.

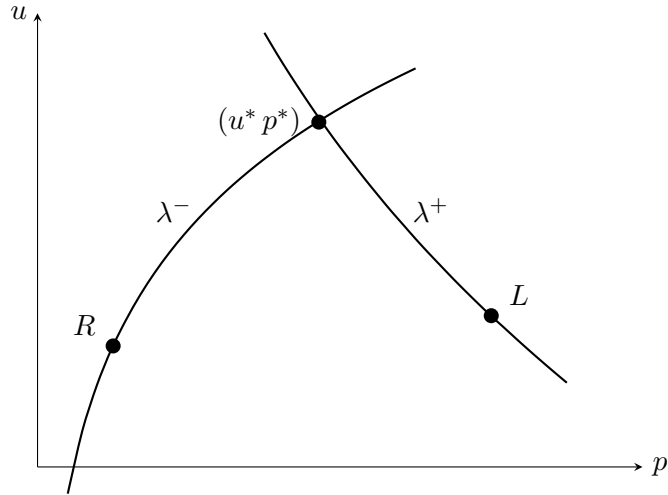


**Figure 21:** Determination of the nature and intersection of the characteristic curves of shock wave  $\lambda^-$  and rarefaction wave  $\lambda^+$  in the  $(u, p)$  plane

$$\begin{cases} u_L(T_L^*, \mathbf{w}_L) = u_R(T_R^*, \mathbf{w}_R), \\ p_L(T_L^*, \mathbf{w}_L) = p_R(T_R^*, \mathbf{w}_R). \end{cases} \quad (48)$$

The resolution of this nonlinear system is made with a Newton Raphson procedure on the parametrized variable  $T$ . The temperature  $T_L^*$  and  $T_R^*$  are obtained with this iterative process, and the complete Riemann problem can be solved using the description of the shock tube problem.

Solution of the state at the intersection  $x_{i+1/2}$  allow to compute the Euler flux (5.3). There are two possibilities, either this state corresponds to one of the constant states of the Riemann problem in the shock-tube problem, or the intersection is inside the rarefaction wave. In this last case, since the rarefaction wave is a simple wave, the characteristic wave is a straight line in the  $x - t$  plane, and the state at the intersection corresponds to the vertical line. Then, the temperature at the intersection is such as (37) gives a zero velocity, and the solution is also solved with an iterative Newton-Raphson procedure.

The solution of the Godunov solver is consistent, and by definition, entropy satisfying, so it converges to the physical, entropy satisfying solution of the conservation laws [HLL83]. Then, it can be used to obtain reference results. However, in this formulation, the Godunov solver is only first-order accurate in time and space. Moreover, solving the Riemann problem at each cell interface is generally too expensive in terms of CPU time since it requires multiple integrations and involves an iterative procedure. Approximate Riemann solvers and higher-order methods are usually preferred like the HLLC solver presented in Appendix A.2.2 and the Roe solver presented in §7.1.



# The HLLC Riemann solver

The HLLC solver has been built in several steps. The initial approach is the HLL approach [Dav88, Ein88] which is a two waves approximation. In order to apply it on the Euler solver, which needs to consider three characteristics waves, modification has been proposed in [TSS94].

## B.3 HLL solver

We consider again the structure of the exact solution of the Riemann problem described in A.2. Let  $t$  be a chosen time. The exact solution of the Riemann problem is then contained in the control volume  $[x_L, x_R] \times [0, t]$  with condition  $x_L \leq t\lambda_{\min}$  and  $x_R \geq t\lambda_{\max}$  to stop time step before superposition of domain of dependence. Considering the integral form of the conservation law, we obtain:

$$\int_{x_L}^{x_R} \mathbf{w}(x, T) dx = \int_{x_L}^{x_R} \mathbf{w}(x, 0) dx + \int_0^T \mathbf{f}^E(\mathbf{w}(x_L, t)) dt - \int_0^T \mathbf{f}^E(\mathbf{w}(x_R, t)) dt. \quad (49)$$

Applying the Riemann initial condition, integral form (49) became :

$$\int_{x_L}^{x_R} \mathbf{w}(x, t_2) dx = x_R \mathbf{w}_R - x_L \mathbf{w}_L + T(\mathbf{f}_R^E - \mathbf{f}_L^E). \quad (50)$$

This equation is called the "consistency condition".

By splitting the integral on the left-hand side into three integrals, we also obtain

$$\begin{aligned} \int_{x_L}^{x_R} \mathbf{w}(x, T) dx &= \int_{x_L}^{TS_L} \mathbf{w}(x, T) dx + \int_{TS_L}^{TS_R} \mathbf{w}(x, T) dx + \int_{TS_R}^{x_R} \mathbf{w}(x, T) dx, \\ &= \int_{TS_L}^{TS_R} \mathbf{w}(x, T) dx + (TS_L - x_L) \mathbf{w}_L + (x_R - TS_R) \mathbf{w}_R. \end{aligned} \quad (51)$$

By using (50), we obtain:

$$\mathbf{w}^{hll} = \frac{1}{T(S_L - S_R)} \int_{TS_L}^{TS_R} \mathbf{w}(x, T) dx = \frac{S_R \mathbf{w}_R - S_L \mathbf{w}_L + \mathbf{f}_L^E - \mathbf{f}_R^E}{S_R - S_L}. \quad (52)$$

The solution in the intermediary state  $\tilde{U}(x, t)$  consists of a single state  $\mathbf{U}^{hll}$  separated from data states by two waves of speeds  $S_L$  and  $S_R$

$$\tilde{U}(x, t) = \begin{cases} \mathbf{w}_L & \text{if } \frac{x}{t} \leq S_L, \\ \mathbf{w}^{hll} & \text{if } S_L \leq \frac{x}{t} \leq S_R, \\ \mathbf{w}_R & \text{if } \frac{x}{t} \geq S_R, \end{cases} \quad (53)$$

with

$$\mathbf{U}^{hll} = \frac{S_R \mathbf{U}_R - S_L \mathbf{U}_L + F_L - F_R}{S_R - S_L}. \quad (54)$$

Using this approximation of the intermediary state inside two waves, we also have:

$$\mathbf{f}^{hll} = \mathbf{f}_L^E - S_L \mathbf{w}_L - \frac{1}{T} \int_{TS_L}^0 \mathbf{w}(x, T) dx = \mathbf{f}_L^E + S_L (\mathbf{w}^{hll} - \mathbf{w}_L), \quad (55)$$

$$= \mathbf{f}_R^E - S_R \mathbf{w}_R - \frac{1}{T} \int_0^{TS_R} \mathbf{w}(x, T) dx = \mathbf{f}_R^E + S_R (\mathbf{w}^{hll} - \mathbf{w}_R). \quad (56)$$

The corresponding HLL intercell flux for the approximate Godunov method is then given by:

$$\mathbf{F}_{i+\frac{1}{2}}^{hll} = \begin{cases} \mathbf{F}_L & \text{if } 0 \leq S_L, \\ \mathbf{F}^{hll} & \text{if } S_L \leq 0 \leq S_R, \\ \mathbf{F}_R & \text{if } 0 \geq S_R, \end{cases} \quad (57)$$

with

$$\mathbf{F}^{hll} = \frac{S_R \mathbf{F}_L - S_L \mathbf{F}_R + S_L S_R (\mathbf{U}_R - \mathbf{U}_L)}{S_R - S_L} \quad (58)$$

## B.4 HLLC Approximate Riemann Solver

In order to add the influence of the contact wave associated with the multiple eigenvalues  $\lambda_i = v$ , Toro, Spruce and Speares [TSS94] add to the previous description the wave of speed  $S_*$  and two different intermediary states  $w_{*L}$  and  $w_{*R}$ .

$$\begin{aligned} w_{*L} &= \frac{1}{S_* - S_L} \int_{TS_L}^{TS_*} w(x, T) dx; \\ w_{*R} &= \frac{1}{S_R - S_*} \int_{TS_*}^{TS_R} w(x, T) dx. \end{aligned} \quad (59)$$

With the consistency condition (50) we obtain:

$$\left( \frac{S_* - S_L}{S_R - S_L} \right) w_{*L} + \left( \frac{S_R - S_*}{S_R - S_L} \right) w_{*R} = w^{hll}. \quad (60)$$

The HLLC approximate Riemann solver becomes

$$\tilde{\mathbf{U}}(x, t) = \begin{cases} \mathbf{w}_L & \text{if } \frac{x}{t} \leq S_L, \\ \mathbf{w}_{*L} & \text{if } S_L \leq \frac{x}{t} \leq S_*, \\ \mathbf{w}_{*R} & \text{if } S_* \leq \frac{x}{t} \leq S_R, \\ \mathbf{w}_R & \text{if } \frac{x}{t} \geq S_R, \end{cases} \quad (61)$$

$$\mathbf{F}_{i+\frac{1}{2}}^{hllc} = \begin{cases} \mathbf{F}_L & \text{if } 0 \leq S_L, \\ \mathbf{F}_{*L} & \text{if } S_L \leq 0 \leq S_*, \\ \mathbf{F}_{*R} & \text{if } S_* \leq 0 \leq S_R, \\ \mathbf{F}_R & \text{if } 0 \geq S_R, \end{cases} \quad (62)$$

using the appropriate control volume we have

$$f_{*L}^E = f_L^E + S_L(w_{*L} - w_L); \quad (63)$$

$$f_{*R}^E = f_{*L}^E + S_*(w_{*R} - w_{*L}); \quad (64)$$

$$f_{*R}^E = f_R^E + S_R(w_{*R} - w_R). \quad (65)$$

$$(66)$$

At this point, the resolution of the HLLC solver impose to estimate the value of the wave speeds  $S_L$ ,  $S_*$  and  $S_R$ . Based on the Godunov resolution of the Riemann problem, Roe average eigenvalues are generally used for practical computations, and by taking for  $S_L$  and  $S_R$

$$S_L = \tilde{u} - \tilde{a}, \quad S_R = \tilde{u} + \tilde{a}, \quad (67)$$

with

$$\tilde{u} = \frac{\sqrt{\rho_L}u_L + \sqrt{\rho_R}u_R}{\sqrt{\rho_L} + \sqrt{\rho_R}}, \quad \tilde{a} = \left[ (\gamma - 1) \left( \tilde{H} - \frac{1}{2}\tilde{u}^2 \right) \right]^{1/2}, \quad (68)$$

with the enthalpy approximated as

$$\tilde{H} = \frac{\sqrt{\rho_L}H_L + \sqrt{\rho_R}H_R}{\sqrt{\rho_L} + \sqrt{\rho_R}}. \quad (69)$$

$S_*$  wave speed is estimated using pressure estimation:

$$\begin{aligned} p_{*L} &= p_L + \rho_L(S_L - u_L)(S_* - u_L); \\ p_{*R} &= p_R + \rho_R(S_R - u_R)(S_* - u_R). \end{aligned} \quad (70)$$

using the equality  $p_{*L} = p_{*R}$  we have

$$S_* = \frac{p_R - p_L + \rho_L u_L (S_L - u_L) - \rho_R u_R (S_R - u_R)}{\rho_L (S_L - u_L) - \rho_R (S_R - u_R)}. \quad (71)$$

The intermediary fluxes  $f_{*L}^E$  and  $f_{*R}^E$  are

$$F_{*K} = F_K + S_K(U_{*K} - U_K), \quad (72)$$

for  $K = L$  and  $K = R$  using the intermediate states  $U_{*K}$  computed as

$$U_{*K} = \rho_K \left( \frac{S_K - u_K}{S_K - S_*} \right) \begin{pmatrix} 1 \\ S_* \\ v_K \\ \frac{E_K}{\rho_K} + (S_* - u_K) \left[ S_* + \frac{p_K}{\rho_K(S_K - u_K)} \right] \end{pmatrix}. \quad (73)$$



# H2 Mével

	Reaction	$A$	$b$	$Ea$
(1)	$H_2 + M = H + H + M$ H <sub>2</sub> /2.5 H <sub>2</sub> O/12 N <sub>2</sub> /0.0	$4.57 \cdot 10^{19}$	-1.4	104380
(2)	$H_2 + AR = H + H + AR$	$5.84 \cdot 10^{18}$	-1.1	104380
(3)	$H_2 + O_2 = OH + OH$	$2.50 \cdot 10^{12}$	0.00	39000
(4)	$H + H + H = H_2 + H$	$3.20 \cdot 10^{15}$	0.00	0
(5)	$H + HO_2 = H_2O + O$	$3.00 \cdot 10^{13}$	0.00	1720
(6)	$O + H_2 = H + OH$	$5.08 \cdot 10^4$	2.67	6290
(7)	$O + O + M = O_2 + M$ H <sub>2</sub> /2.5 H <sub>2</sub> O/12 AR/0.0	$6.16 \cdot 10^{15}$	-0.50	0
(8)	$O + O + AR = O_2 + AR$	$1.89 \cdot 10^{13}$	0.00	-1788
(9)	$H + O_2 = O + OH$	$1.91 \cdot 10^{14}$	0.00	16439
(10)	$H + O_2( + M) = HO_2( + M)$ Low Troé [0.5 1 · 10 <sup>-30</sup> 1 · 10 <sup>30</sup> ] H <sub>2</sub> /2.5 H <sub>2</sub> O/12 AR/0.0	$1.48 \cdot 10^{12}$ $3.482 \cdot 10^{16}$	0.60 -0.411	0 -1115
(11)	$H + O_2( + AR) = HO_2( + AR)$ Low Troé [0.5 1 · 10 <sup>30</sup> 1 · 10 <sup>30</sup> ]	$1.48 \cdot 10^{13}$ $1.49 \cdot 10^{15}$	0.60 0.00	0 -1000
(12)	$H + O + M = OH + M$ H <sub>2</sub> /2.5 H <sub>2</sub> O/12 AR/0.75	$4.71 \cdot 10^{18}$	-1.00	0
(13)	$OH + H_2 = H_2O + H$	$2.16 \cdot 10^8$	1.51	3430
(14)	$H_2O + O = OH + OH$	$2.97 \cdot 10^6$	2.02	13400
(15)	$H_2O_2( + M) = OH + OH( + M)$ Low Troé [0.5 1 · 10 <sup>30</sup> 1 · 10 <sup>30</sup> ] H <sub>2</sub> /2.5 H <sub>2</sub> O/12 AR/0.0	$2.95 \cdot 10^{14}$ $1.20 \cdot 10^{17}$	0.00 0.00	48430 45500
(16)	$H_2O_2( + AR) = OH + OH( + AR)$ Low Troé [0.5 1 · 10 <sup>29</sup> 1 · 10 <sup>31</sup> ]	$2.95 \cdot 10^{14}$ $1.90 \cdot 10^{16}$	0.00 0.00	48430 43000
(17)	$OH + H + M = H_2O + M$ H <sub>2</sub> /2.5 H <sub>2</sub> O/12 AR/0.0	$2.21 \cdot 10^{22}$	-2.00	0
(18)	$OH + H + AR = H_2O + AR$	$8.41 \cdot 10^{21}$	-2.00	0
(19)	$HO_2 + O = O_2 + OH$	$0.33 \cdot 10^{14}$	0.00	0
(20)	$HO_2 + H = H_2 + O_2$	$1.66 \cdot 10^{13}$	0.00	823
(21)	$HO_2 + H = OH + OH$	$7.08 \cdot 10^{13}$	0.00	295
(22)	$HO_2 + OH = H_2O + O_2$	$2.89 \cdot 10^{13}$	0.00	-497
(23)	$HO_2 + HO_2 = H_2O_2 + O_2$ Duplicate	$4.20 \cdot 10^{14}$	0.00	11982
(24)	$HO_2 + HO_2 = H_2O_2 + O_2$ Duplicate	$1.30 \cdot 10^{11}$	0.00	-1629



(25)	$\text{H}_2\text{O}_2 + \text{O}=\text{OH} + \text{HO}_2$	$9.55 \cdot 10^6$	2.00	3970
(26)	$\text{H}_2\text{O}_2 + \text{H}=\text{H}_2\text{O} + \text{OH}$	$0.24 \cdot 10^{14}$	0.00	3970
(27)	$\text{H}_2\text{O}_2 + \text{H}=\text{HO}_2 + \text{H}_2$	$4.82 \cdot 10^{13}$	0.00	7950
(28)	$\text{H}_2\text{O}_2 + \text{OH}=\text{H}_2\text{O} + \text{HO}_2$	$1.00 \cdot 10^{12}$	0.00	0
	Duplicate			
(29)	$\text{H}_2\text{O}_2 + \text{OH}=\text{H}_2\text{O} + \text{HO}_2$	$5.80 \cdot 10^{14}$	0.00	9557
	Duplicate			

---

**Table 1:**  $\text{H}_2$  Mevel's detailed mechanism [MJL<sup>+</sup>09]

# Synthèse en français

## D.5 Introduction

### D.5.1 Contexte

Cette thèse s'inscrit dans le contexte de l'accélération de flamme hydrogène. L'hydrogène est un gaz très utilisé dans l'industrie avec une production s'élevant en 2020 à 90 Mt. Il est actuellement principalement utilisé en tant qu'agent chimique avec des applications diverses comme la désulfuration et l'hydrogénation du pétrole, la production d'ammoniac, généralement destiné à la production d'engrais chimiques, ou la production de méthanol. Il est également de plus en plus utilisé pour la réduction directe de l'oxyde de fer pour produire de l'acier et se substituer ainsi au coke de charbon généralement utilisé.

De plus, de nombreuses autres applications sont en cours de développement pour utiliser l'hydrogène en tant que vecteur énergétique dans des domaines comme le transport ainsi que pour la production et le stockage de l'énergie. Cette utilisation permet de se substituer aux hydrocarbures classiquement utilisés pour ce type d'applications. En effet, la consommation de l'hydrogène à travers une combustion ou une pile à combustible permet des performances similaires à celui obtenu avec des hydrocarbures plus courants tout en produisant quasi uniquement de la vapeur d'eau.

Cependant, ces nouvelles utilisations vont multiplier les intermédiaires et se rapprocher du consommateur final. Des problématiques de sécurité vont alors se poser concernant le stockage, le transport et l'utilisation de l'hydrogène.

En effet, le mélange hydrogène-air est un gaz très inflammable avec une plage d'inflammabilité très large, entre 4 % et 75 % de fraction volumique, ainsi qu'une énergie d'allumage très faible en comparaison à celles requises pour allumer un mélange d'hydrocarbures traditionnels (10 fois inférieure à la stoechiométrie par rapport à un mélange méthane-air).

La recherche sur le risque hydrogène a été très active, ces dernières décennies, dans le domaine de la sécurité nucléaire. En effet, un scénario accidentel très étudié correspond à la production accidentelle d'hydrogène dans une enceinte de réacteur par hydrolyse de l'eau lorsque le zirconium, l'alliage entourant les pastilles de combustible n'est plus immergé et réagit à haute température avec la vapeur d'eau. L'inflammation d'un mélange hydrogène-air peut alors mener à une explosion et mettre en péril l'intégrité des bâtiments. Un scénario qui a ainsi été observé lors des incidents nucléaires de Three Miles Island en 1979 et de Fukushima-Daiichi en 2011.

### D.5.2 Accélération de flamme et transition vers la détonation

Cette thèse se concentre sur l'étude du comportement après inflammation d'une flamme hydrogène dans un milieu prémélangé au sein d'une enceinte confinée ou semi-confinée. L'influence de la présence éventuelle d'obstacles le long de l'écoulement ainsi que de gradients de concentration en hydrogène tels que l'on peut en observer dans des scénarios de fuite d'hydrogène sont également étudiés.

On considère dans nos scénarios un allumage avec un faible apport d'énergie (sans explosif). La flamme présente alors initialement un comportement laminaire.

Dans un premier temps, les instabilités thermo-diffusives et de Darrieus-Landau vont perturber le front de flamme laminaire, provoquer des plissements et augmenter la surface de flamme ainsi que sa vitesse de propagation. La flamme va également induire un écoulement turbulent en amont de celle-ci qui, une fois développé, va interagir avec le front de flamme et accélérer la flamme à des vitesses de l'ordre d'une dizaine de mètres par seconde. A partir d'une certaine célérité du front de flamme, des phénomènes compressibles vont devenir prédominants dans le comportement de la flamme avec la production d'instabilités de type Richtmyer-Meshkov ou de Kelvin-Helmholtz lors de l'interaction entre le front de flamme et les ondes de compression. Une flamme dans ce régime peut ainsi atteindre des vitesses proches de la vitesse du son.

Arrivé dans ce dernier régime de déflagration rapide, caractérisé par des vitesses importantes et des phénomènes de compression important, certaines conditions locales peuvent conduire à un phénomène de transition du régime de déflagration au régime de détonation dans lequel la flamme est auto-allumée par une forte onde de choc en amont du front de flamme, présentant d'importante surpression et une vitesse de propagation supersonique.

Le processus d'accélération de flamme est donc influencé par de multiples critères différents. D'une part, par les propriétés physiques du mélange comme le nombre de Lewis  $Le$  ou la vitesse de flamme laminaire  $S_l^0$ . Egalement, par les propriétés géométriques du milieu avec l'impact des parois et des obstacles géométriques qui permettent généralement d'augmenter l'accélération et de générer des points chauds, potentiels précurseurs de la transition vers la détonation. Pour finir, le comportement de la flamme dépend des phénomènes de compression, de diffusion et de turbulence.

Des dispositifs expérimentaux ont été mis en place pour étudier ce phénomène, avec notamment des tubes d'accélération de flamme tels que le tube SSEXHY présent au CEA ou le tube GraVent, de l'Université de Munich que l'on reproduit numériquement dans ces travaux. Ces dispositifs consistent à allumer un gaz prémélangé à une des extrémités du tube puis observer grâce à leurs instrumentations composées de capteurs piézo-électriques et de photomultiplicateur la propagation du front de flamme et les phénomènes de compression. Le mélange initial à l'intérieur du tube peut varier en composition et en pression initiale, de plus, certains de ces dispositifs comme le tube GraVent permettent de produire des concentration de gradient initial pour observer leur influence sur le comportement de la flamme. L'influence d'obstacles obstruant partiellement le tube a également été largement étudié avec ces dispositifs.

Cependant, la compréhension des phénomènes d'accélération de flamme reste limitée du fait de la large variation d'échelles mise en jeu, des nombreux mécanismes influençant le comportement de la flamme, et des effets localisés et très non-linéaire, comme la transition vers la détonation, difficiles à observer expérimentalement. Ainsi, des simulations numériques précises complémentaires aux dispositifs expérimentaux sont nécessaires pour améliorer la compréhension de tels phénomènes.

Une simulation numérique suivant l'accélération d'une flamme dans un milieu confinée doit également répondre à un certain nombre de contraintes. Tout d'abord, elle doit gérer les larges variations d'échelles en espace et en temps intervenant dans ces calculs. En effet, l'objectif est d'observer le comportement d'un front de flamme, dont l'échelle caractéristique est de l'ordre du dixièmes de millimètre se propageant librement dans de grandes enceintes. De même, les échelles caractéristiques de temps sont très variables depuis les instabilités thermodynamiques aux termes réactifs très rapides. Les différentes étapes de l'accélération forment une très large gamme de vitesses de quelques mètres par seconde jusqu'à des vitesses hypersonique pour la détonation. De plus, les phénomènes compressibles parcourant le domaine de calcul créent des phénomènes dynamiques avec des discontinuités numériques produites par les ondes de choc qui doivent alors être propagées numériquement sans diffusion. Enfin, les phénomènes locaux comme la transition vers la détonation sont très localisés et très non-linéaires et ainsi complexes à capturer efficacement.

Différentes simulations de ces phénomènes ont été réalisées à partir du début des années 2000 avec notamment les premiers travaux de Khokhlov et Oran [KOT99]. Quelques outils numériques ont été développés avec des toolbox OpenFOAM comme rhoCentralFoam [ZZZ21] ou le solveur FAST

[[HOO16](#)]. Plusieurs méthodes numériques sont disponibles dans la littérature, ces simulations sont généralement effectuées avec des schémas compressibles de type Godunov (souvent le schéma HLLC) couplés à des méthodes de capture de chocs avec des méthodes de reconstruction de type MUSCL ou WENO pour résoudre les phénomènes compressibles. Les échelles résolues varient également avec des approches DNS ou LES. Malgré quelques exceptions récentes, la majorité de ce type de simulations utilise des modèles réactifs simples, avec une loi d'Arrhenius. Des méthodes d'adaptation de maillage sont généralement associées à ces solveurs numériques pour permettre de suivre les phénomènes compressibles.

Nous avons, au cours de ces travaux, développé un solveur destiné à résoudre les différentes étapes de l'accélération de flamme avec intégration de modèles physiques précis et d'une résolution haute fidélité pour les phénomènes compressibles. L'objectif est d'apporter une validation à chaque étape du processus d'accélération.

Ce solveur se base sur deux outils initiaux. D'une part, le solveur MR\_CHORUS, décrit dans [[TRB15](#)] est construit pour les écoulements compressibles mono-composant. Il dispose d'outils d'adaptation de maillage par multirésolution et un schéma compressible OSMP basé sur le schéma de Roe avec une très faible dissipation numérique. D'autre part, la librairie AGATH qui permet de calculer les propriétés thermodynamiques et de transport des mélanges multi-composants ainsi que la résolution des termes sources réactifs.

## D.6 Description du solveur numérique

### D.6.1 Equations et modèles

La résolution s'effectue avec l'application des équations de Navier-Stokes. On distingue trois opérateurs de convection, de diffusion/viscosité et de réaction. Ces différents opérateurs sont résolus indépendamment et sont intégrés en temps grâce à un schéma de splitting de Strang dans lequel on place l'opérateur de réaction, le plus raide, aux extrémités. Ainsi, chaque opérateur est résolu avec un solveur dédié.

La résolution des termes sources s'effectue avec un solveur implicite radau5 décrit dans [[HW96](#)], l'opérateur de viscosité et de diffusion est résolu avec un solveur Runge Kutta du second ordre. L'opérateur Euler est résolu avec le solveur OSMP avec une généralisation décrites par la suite pour fonctionner avec des mélanges multi-composants.

Différents modèles physiques sont également pris en compte dans les équations. Tout d'abord, une vitesse de diffusion  $V_i$  est ajoutée aux équations de conservation d'espèce avec un modèle multi-composants basé sur des coefficients de diffusion calculés à partir des méthodes de Dixon-Lewis [[DLC68](#)] avec l'aide de la librairie AGATH. Un terme correspondant à l'effet Soret décrivant la diffusion de chaque espèce induite par les gradients de température est également considéré.

La cinétique chimique est calculée à partir du mécanisme de Mével [[MJL+09](#)] composé de neuf espèces réactives et 38 réactions. Ce mécanisme a été construit pour fonctionner pour des cas de détonation, sur des plages de fonctionnement généralement peu explorées lors de la conception de tels mécanismes, il est basé en grande partie sur le modèle de Konnov, identifié pour donner une bonne approximation des temps d'auto-allumage sur ces points à haute pression et haute température.

### D.6.2 Schéma OSMP

Le schéma OSMP est utilisé pour approximer la solution des équations d'Euler hyperbolique et suivre l'évolution des discontinuités avec une dissipation numérique minimale.

Le schéma OSMP est basé sur le solveur approximé de Riemann de Roe décrit dans [[Roe81](#)] qui consiste à évaluer les états intermédiaires du problème de Riemann avec une combinaison linéaire des états gauche et droit. L'expression approximée de la matrice jacobienne du flux de Euler  $\tilde{\mathbf{A}}$  doit respecter

plusieurs contraintes définis par Roe qui permettent de converger vers une solution entropique des équations d'Euler hyperboliques, en particulier les relations de saut à travers l'interface.

$$\tilde{\mathbf{A}}(\mathbf{w}_L, \mathbf{w}_R)(\mathbf{w}_L - \mathbf{w}_R) = \mathbf{f}^E(\mathbf{w}_L) - \mathbf{f}^E(\mathbf{w}_R) \quad (74)$$

Afin de respecter ces différentes propriétés, on utilise généralement les opérateurs de moyenne de Roe.

L'expression du flux s'effectue avec les invariants de Riemann  $\tilde{\alpha}_k$  qui sont convectés le long des ondes caractéristiques  $(\tilde{u} - \tilde{c}, \tilde{u}, \tilde{u} + \tilde{c})$  correspondant aux valeurs propres de la matrice Jacobienne.

$$\tilde{\mathbf{f}}^E(\mathbf{U}_L, \mathbf{U}_R) = \frac{1}{2}(\mathbf{f}^E(\mathbf{U}_L) + \mathbf{f}^E(\mathbf{U}_R)) - \frac{1}{2} \sum_{k=1}^N \tilde{\alpha}_k \cdot |\tilde{\lambda}_k| \tilde{\mathbf{K}}^{(k)}, \quad (75)$$

Le schéma de Roe est un solveur de Riemann complet, qui permet de reproduire les trois ondes caractéristiques du problème de Riemann. Il converge vers la solution entropique, mais reste cependant d'ordre un en temps et en espace et va avoir tendance à diffuser les discontinuités. L'objectif du schéma OSMP décrit dans [DT04] est d'augmenter l'ordre global du schéma en temps et en espace avec une méthode de capture de choc pour capturer les discontinuités. Il consiste à augmenter l'ordre en temps et en espace des équations de convections appliquées aux invariants de Riemann grâce à une procédure de Lax-Wendroff. Cette augmentation s'effectue en une seule étape avec un stencil minimal ce qui est bénéfique pour le temps de calcul CPU. Cependant, cette méthode implique des oscillations parasites proches des discontinuités qui ne convergent pas vers la solution entropique. Afin de corriger ce phénomène, une condition dite de conservation de la monotonie (MP) est appliquée. Celle-ci se base sur une condition TVD classique qui permet de réduire localement avec un limiteur de flux l'ordre du schéma proche des discontinuités. La condition MP améliore cette condition en se basant sur un stencil de trois points afin de différencier les discontinuités numériques des extrema et permettre de ne pas écrêter ces derniers. Ainsi le flux OSMP à l'ordre  $p$  correspond à :

$$\tilde{\mathbf{f}}_{j+1/2}^E = \frac{1}{2} (\mathbf{f}_{j+1}^E + \mathbf{f}_j^E) - \frac{1}{2} \sum_{k=1}^N (\tilde{\alpha}_k^{M-P} |\tilde{\lambda}_k| \cdot \tilde{\mathbf{K}}^{(k)})_{j+1/2}, \quad (76)$$

avec  $\tilde{\alpha}_k^{M-P}$  les fonctions associées au limiteur de flux MP :

$$\tilde{\alpha}_k^{M-P} = \left[ \left( 1 - \phi_k^{pM-P} (1 - |\nu_k|) \right) \tilde{\alpha}_k \right]_{j+1/2}, \quad k \in [1, N]. \quad (77)$$

### D.6.3 Extension du schéma OSMP au mélanges de gaz avec un équations d'état convexe

Le solveur de Roe classique et a fortiori le schéma OSMP décrit précédemment s'appliquent à un gaz idéal mono-composant avec des capacités thermiques massiques constantes. L'objectif ici est d'appliquer le schéma OSMP dans des configurations de mélanges multi-composants avec d'importantes variations de température comme intervenant dans le phénomène de combustion. Le modèle thermodynamique couramment employé pour les calculs de combustion considère une variation des capacités thermiques de chaque élément avec la température. Leurs valeurs sont approximées par des polynômes dits de NASA dont les coefficients sont disponibles dans les bases de données tels que [Bur84].

Les exemples proposés pour l'accélération de flamme hydrogène utilisent ce formalisme, mais plus globalement le schéma construit ici s'applique à des mélanges de gaz dont l'équation d'état est convexe. Avec cette hypothèse, la matrice jacobienne du flux d'Euler va faire intervenir de nouvelles variables  $\chi_i, i = 1, \dots, n_s$  et  $\kappa$  correspondant aux facteurs de compressibilités :

$$\chi_i = \left. \frac{\partial p}{\partial \rho_i} \right|_{\rho_{k,k \neq i}, \tilde{\epsilon}}, \quad \text{and} \quad \kappa = \left. \frac{\partial p}{\partial \tilde{\epsilon}} \right|_{\rho_{i,i=1,\dots,n_s}}. \quad (78)$$

Ces facteurs de compressibilités interviennent également dans l'expression de la vitesse du son

$$c_s^2 = \left. \frac{\partial p}{\partial \rho} \right|_{s, N_i, i=1,\dots,n_s} = \sum_{i=1}^{n_s} \chi_i Y_i + \kappa h. \quad (79)$$

Afin d'appliquer le schéma de Roe et de respecter les relations de saut à travers une discontinuité (74), l'expression des moyennes de Roe permet d'obtenir une condition liant la variation de la pression, les fractions massique et l'énergie interne avec les facteurs de compressibilités :

$$\Delta p = \sum_{i=1}^{n_s} \tilde{\chi}_i \Delta \rho_i + \tilde{\kappa} \Delta \epsilon \quad (80)$$

Afin de respecter cette relation, plusieurs procédures sont décrites dans la littérature principalement considérant un gaz avec deux composants, nous appliquons ici à des mélanges multi-composants la méthode introduite par Montagné et al. [MYV89] consistant à effectuer une première prédiction des facteurs de compressibilités  $(\hat{\chi}_i, \hat{\kappa})$  avec une intégration sur un chemin entre l'état gauche et droit. Cette solution est ensuite projetée orthogonalement sur l'hyperplan défini par (80) dans l'espace de coordonnées :

$$\left( \frac{1}{\hat{\kappa}}, \left\{ \frac{\chi_i}{\hat{s}\hat{\kappa}}, i = 1, \dots, n_s \right\} \right), \quad (81)$$

$$\text{Avec } \hat{s} = \hat{c}^2 = \sum_{i=1}^{n_s} \chi_i \hat{Y}_i + \hat{\kappa} h$$

Cette solution permet de retrouver les propriétés du schéma de Roe, mais elle n'est que très peu contraignante sur le choix des valeurs des facteurs de compressibilités ce qui va être problématique pour l'extension du schéma à l'ordre élevé avec l'application du schéma OSMP. En effet, proche des variations de composition des mélanges, des artefacts numériques vont apparaître comme représenté avec un exemple de tube à choc de Sod Figure 22. Ces artefacts sont issus d'inconsistances sur le stencil du schéma OSMP entre l'évolution des fractions massiques des différents composants et l'approximation des facteurs de compressibilités obtenus avec la procédure de Vinokur et Montagné. Afin de contraindre plus efficacement le choix de ces facteurs de compressibilités, nous imposons une nouvelle condition de préservation de la monotonie sur la combinaison de facteurs de compressibilités apparaissant dans l'expression du flux d'énergie totale.

$$\tilde{\alpha}_{N+1} = \sum_{i=1}^{n_s} \tilde{\alpha}_i \left( \tilde{E}_c - \frac{\tilde{\chi}_i}{\tilde{\kappa}} \right) \quad (82)$$

Cette combinaison correspond à un invariant de Riemann associé à l'onde caractéristique portée par la vitesse  $\tilde{u}$ . D'un point de vue mathématique, cette nouvelle condition est équivalente à sélectionner une combinaison  $(\bar{\chi}_i, i = 1, \dots, n_s, \bar{\kappa})$  solution du système d'équations :

$$\begin{cases} \Delta p = \sum_{i=1}^{n_s} \bar{\chi}_{i,j+1/2} \Delta \rho_i + \bar{\kappa}_{j+1/2} \Delta \epsilon, \\ \tilde{c}_{s,j+1/2}^2 = \sum_{i=1}^{n_s} \bar{\chi}_{i,j+1/2} \tilde{Y}_{i,j+1/2} + \bar{\kappa}_{j+1/2} \tilde{h}_{j+1/2}, \\ \tilde{\alpha}_{N+1,j+1/2}^{M-P} = \sum_{i=1}^{n_s} \tilde{\alpha}_{i,j+1/2}^{M-P} \left( \tilde{E}_{c,j+1/2} - \frac{\bar{\chi}_{i,j+1/2}}{\bar{\kappa}_{j+1/2}} \right). \end{cases} \quad (83)$$

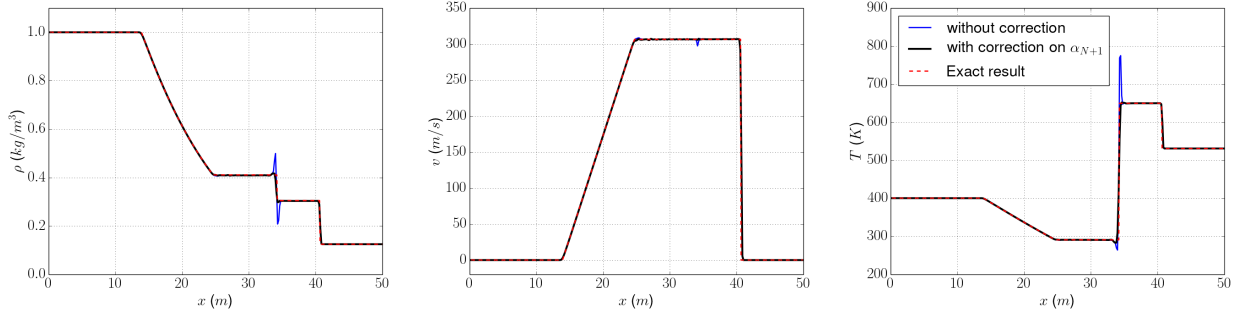


**Figure 22:** *Exemple de profils de densité, vitesse et température d'un tube de choc de Sod avec un mélange multi-composant avec et sans correction*

Ce système (83) correspond à un système linéaire composé de  $n_s + 1$  inconnues, l'existence d'une telle solution est alors garantie. L'unicité de la solution est obtenue dans le cas de deux espèces, une approximation est cependant conservée à travers l'estimation de la valeur de la vitesse du son  $\tilde{c}_s$  obtenue à partir de la première estimation dans la procédure de Vinokur et Montagné.

Cette généralisation du solveur OSMP a fait l'objet d'un article publié dans le Journal of Computational Physics [LVK+22].

Le schéma OSMP s'avère efficace pour obtenir des ordres élevés en ordre et en espace avec d'importantes variations d'espèces et est très peu diffusif proche des discontinuités. Cependant, des instabilités numériques peuvent apparaître proches des fortes ondes de choc avec plusieurs dimensions en espace comme observé lors des cas de simulation de détonation.

#### D.6.4 Phénomène de carbuncle

Les instabilités de choc de type carbuncle, nommées ainsi du fait de leur aspect, sont des instabilités numériques apparaissant lors de la perturbation d'une forte onde de choc alignée avec le maillage. La plupart des schémas approximatifs de Riemann ainsi que le schéma exact de Godunov lui-même sont sensibles à ce type de perturbation. Son origine semble provenir d'une dissipation insuffisante dans la direction transverse au choc sur les mailles en amont du choc.

Différentes études ont été menées pour caractériser et identifier les termes générant ces perturbations. Ainsi, plusieurs méthodes sont proposées dans la littérature pour traiter ces instabilités. Dans ces travaux, nous avons considéré trois propositions, l'une utilisant un solveur de Riemann rotatif [Ren03] pour ne plus considérer l'alignement entre le choc et le maillage, et les deux autres ajoutant un terme de dissipation supplémentaire avec un terme de vorticit  additionnel [CYBL18] ou en supprimant un terme li  à la variation de pression dans l'expression originale du flux [CHR+18b]. On applique  galement un senseur de d tonation tel que d crit dans [CHR+18a] afin de rep rer les mailles critiques pour l'apparition de ces instabilit s.

Aucune de ces m thodes ne pr sente une solution totalement id ale pour s'appliquer au sch ma OSMP. L'utilisation du solveur rotatif garanti de converger vers la solution faible des  quations d'Euler, mais celui-ci interf re avec le limiteur de flux du sch ma OSMP car ne s'int grant pas au stencil  largi. Les deux autres solutions peuvent ne pas remplir les conditions de stabilit s avec un large stencil et int grer des perturbations num riques du fait de la modification de l'expression du flux. Le choix a  t  fait dans les cas de calcul de recourir   l'ajout du terme de vorticit  additionnel.

### D.7 Algorithmie

Diff rentes m thodes algorithmiques ont  t   galement d velopp es dans ces travaux pour adapter le maillage dynamiquement, int grer des parois immerg es et tabul  dynamiquement la chimie pour gagner du temps CPU.

### D.7.1 Méthode d'adaptation de maillage

La première méthode décrite dans ce manuscrit concerne une méthode d'adaptation de maillage présente initialement dans le solveur MR\_CHORUS, utilisant des méthodes dites de multirésolution. Son fonctionnement se base sur l'utilisation d'un arbre décrivant les différents niveaux de raffinement locaux. Le calcul des flux entre chaque maille à partir des schémas numériques s'effectue au niveau des *feuilles*, sur le niveau le plus élevé dans l'arbre. Le choix d'augmenter ou diminuer le niveau de raffinement local est basé sur le calcul du *détail* retranscrivant la différence entre les valeurs des variables  $\rho Y_i$  sur les feuilles de l'arbre et celles obtenues par un opérateur de prédiction utilisant des extrapolations polynomiales depuis les mailles au niveau inférieur. A noter également que l'arbre doit également être gradué, c'est-à-dire permettre le calcul des feuilles virtuelles par l'opérateur de prédiction intervenant dans le stencil du schéma numérique et n'apparaissant pas dans l'arbre initial.

### D.7.2 Méthode de paroi immergées

L'intégration d'obstacles dans le volume de calcul s'effectue grâce à des méthodes dites de parois immergées, elles permettent de considérer des conditions aux limites dont les surfaces ne sont pas nécessairement alignées sur le maillage cartésien. On considère ici une méthode cut-cell pour garantir la conservation des variables de notre schéma.

Les cellules coupées par la paroi sont identifiées à l'initialisation du calcul et décrites par une description géométrique basée sur le volume occupé par le solide, les aires occupées sur chaque face de la maille et les normales et les aires des faces solide intérieures à la maille.

Les cellules fantômes présentes dans l'intérieur des parois sont calculées avec une interpolation et une pondération du point symétrique avec les mailles voisines.

Pour finir, afin de ne pas conserver une condition de stabilité CFL trop contraignante avec les cellules coupées, une redistribution du flux aux cellules voisines aux petites cellules coupées est mise en place.

### D.7.3 In Situ Adaptive Tabulation

Pour finir, nous présentons également une méthode de tabulation dynamique de la combustion. Nous avons testé cette méthode afin de réduire le temps de calcul CPU dédié à l'opérateur de réaction initialement très limitant. Une meilleure vectorisation du code a finalement permis de diminuer sensiblement son impact sur le temps de calcul global. La méthode ISAT [Pop97] permet de retrouver rapidement une estimation de la solution d'un système non-linéaire. Chaque nouveau point est enregistré et associé avec une matrice de sensibilité et un ellipsoïde de précision basée sur un critère de tolérance. Afin de rapidement retrouver le point le plus proche, un arbre binaire est parcouru. L'ellipsoïde peut être étendu dans le cas d'une variation suffisamment faible dans la zone considérée.

Son application a des cas de détonation avec notre mécanisme chimique indique plusieurs difficultés qui limitent les gains d'une telle méthode. D'une part, l'association avec les méthodes de raffinement de maillage n'est pas toujours adéquate, des petites variations étant créées dans les parties lisses de la solution, augmentant le nombre de mailles globale. A l'inverse, d'autres petites perturbations telles qu'apparaissant dans la longueur d'induction des fronts de détonation ne sont pas correctement capturées. Les gains de temps de calcul CPU obtenu pour la chimie détaillée d'hydrogène ne sont alors pas suffisants dans le cadre d'un cas d'accélération de flamme très transitoire pour justifier de l'utilisation de la méthode ISAT. Une chimie plus complexe avec un nombre plus important de réactions que dans notre cas pourrait cependant justifier le recours à cette stratégie.

## D.8 Résultats

Des calculs de validations sont présentés permettant d'évaluer les performances de notre solveur pour capturer les phénomènes essentiels du processus d'accélération de flamme.



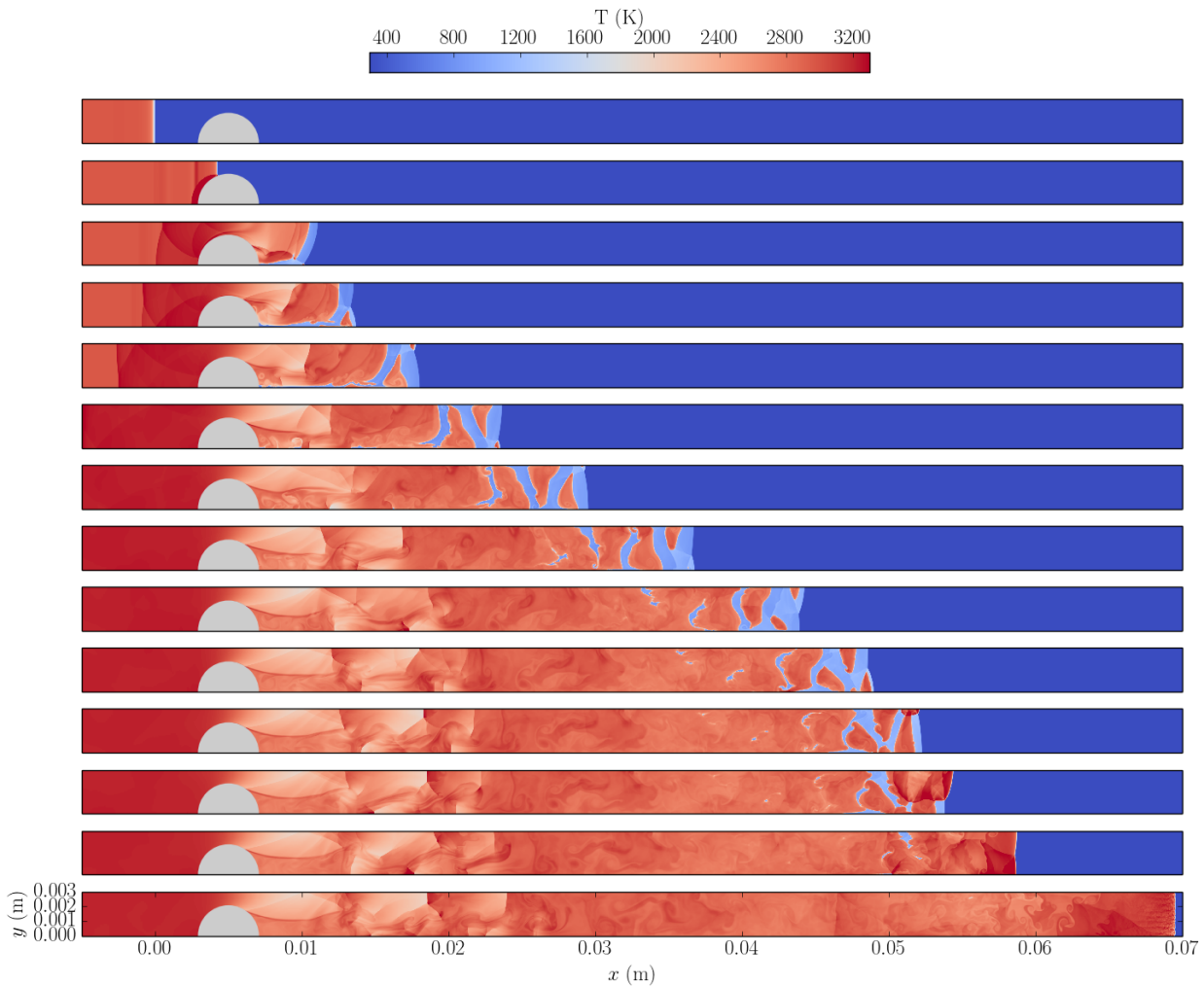


**Figure 23:** *Champ de température illustrant un régime de quasi-détonation et la réinitiation de la détonation après un milieu poreux avec la superposition d'ondes transverses*

Un modèle de chimie détaillée tel que le mécanisme de Mével et à un modèle de diffusion précis permet de reproduire la vitesse laminaire de flamme et les valeurs des longueurs de Markstein caractérisant l'instabilité du front de flamme laminaire. La capture des instabilités hydrodynamiques créées par les phénomènes compressibles s'avère très efficace grâce au schéma OSMP. Les fronts de détonation et leurs propriétés instables sont également reproduits à la condition d'appliquer un raffinement suffisant.

Pour finir, des simulations plus complètes sont proposées dans ce travail avec l'interaction d'un front de détonation avec un milieu poreux et la reproduction du processus d'accélération de la flamme dans le tube d'accélération GraVent de l'université de Munich avec et sans gradient de concentration. La première simulation présente une atténuation et une ré-initiation d'un front de détonation qui illustre les capacités de nos outils numériques à reproduire correctement l'évolution du front de détonation. La condition d'initiation d'une détonation à partir d'une focalisation locale de l'onde de choc est illustrée dans ces cas d'essais. On observe également la grande non-linéarité de ce phénomène puisqu'une onde de détonation se développe à partir d'un état critique (Figure 23) très similaire aux autres superpositions d'onde transverses ne déclenchant pas ce phénomène.

La deuxième simulation présente les premières étapes de l'accélération de la flamme dans un tube d'accélération et met en évidence l'influence des principaux phénomènes identifiés comme ayant un impact sur l'accélération de la flamme (Figure 24). L'impact de la rugosité du tube et des gradients de concentration est mis en évidence. L'explosion locale dans des poches de gaz non brûlé et la production et la croissance d'ondes acoustiques à l'avant du front de flamme, identifiées comme début potentiel de détonation, sont reproduites. Cependant, cette simulation n'est pas encore entièrement achevée et

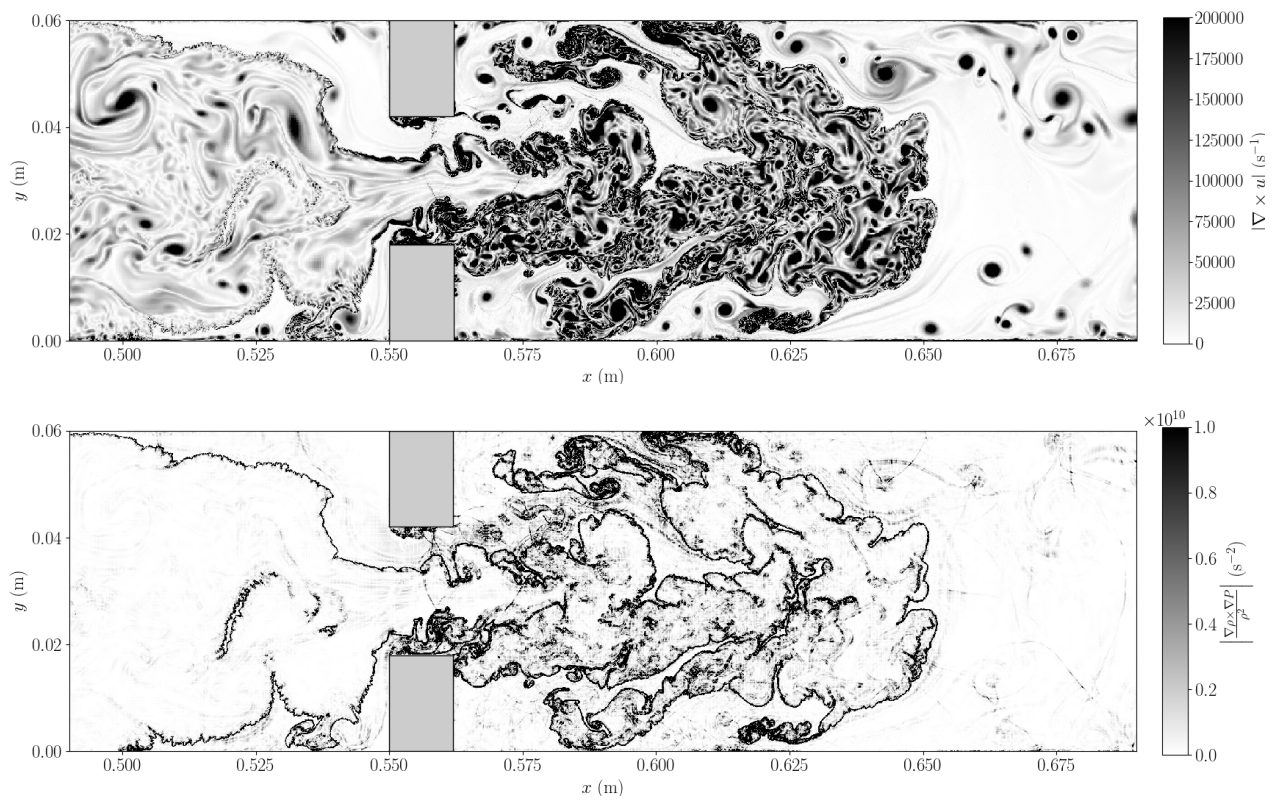


**Figure 24:** *Champ de vorticit  (haut) et de production barocline (bas) illustrant la perturbation du front de flamme et son acc l ration dans le tube d'acc l ration*

n'atteint pas la transition vers la d tonation en raison du manque de ressources de calcul et d'efficacit  de l'impl mentation num rique.



# Bibliography

- [Abg91] Rémi Abgrall. An extension of roe’s upwind scheme to algebraic equilibrium real gas models. *Computers & Fluids*, 19(2):171 – 182, 1991.
- [Abg96] Rémi Abgrall. How to prevent pressure oscillations in multicomponent flow calculations: A quasi conservative approach. *Journal of Computational Physics*, 125(1):150 – 160, 1996.
- [ABM02] R. Addabbo, J.K. Bechtold, and M. Matalon. Wrinkling of spherically expanding flames. *Proceedings of the Combustion Institute*, 29(2):1527–1535, 2002.
- [AHF97] K.T. Aung, M.I. Hassan, and G.M. Faeth. Flame stretch interactions of laminar premixed hydrogen/air flames at normal temperature and pressure. *Combustion and Flame*, 109(1):1–24, 1997.
- [Ahm16] Mohamed Saifelislam Abeelgadir Ahmed. *Run-Up Distance From Deflagration to Detonation In Fast Flames*. PhD thesis, University of Ottawa, 01 2016.
- [APS05] J.M. Austin, F. Pintgen, and J.E. Shepherd. Reaction zones in highly unstable detonations. *Proceedings of the Combustion Institute*, 30(2):1849–1857, 2005.
- [ATC17] Sina Arabi, Jean-Yves Trépanier, and Ricardo Camarero. A simple extension of roe’s scheme for real gases. *Journal of Computational Physics*, 329:16 – 28, 2017.
- [ATC19] Sina Arabi, Jean-Yves Trépanier, and Ricardo Camarero. A simple extension of roe’s scheme for multi-component real gas flows. *Journal of Computational Physics*, 388:178 – 194, 2019.
- [Aus03] Joanna Maria Austin. *The role of instability in gaseous detonation*. PhD thesis, California Institute of Technology, January 2003.
- [AWS02] A. Vesper, W. Breitung, and S.B. Dorofeev. Run-up distances to supersonic flames in obstacle-laden tubes. *J. Phys. IV France*, 12(7):333–340, 2002.
- [BA03] G. Billet and R. Abgrall. An adaptive shock-capturing algorithm for solving unsteady reactive flows. *Computers & Fluids*, 32(10):1473–1495, 2003.
- [Bar74] Harold O. Barthel. Predicted spacings in hydrogen-oxygen-argon detonations. *The Physics of Fluids*, 17(8):1547–1553, 1974.
- [BAVL10] Vitaly Bychkov, V’yacheslav Akkerman, Damir Valiev, and Chung K. Law. Influence of gas compression on flame acceleration in channels with obstacles. *Combustion and Flame*, 157(10):2008–2011, 2010.
- [BBHS16] L. R. Boeck, F. M. Berger, J. Hasslberger, and T. Sattelmayer. Detonation propagation in hydrogen–air mixtures with transverse concentration gradients. *Shock Waves*, 26:181–192, 2016.

- [BEBM18] Radouan Boukharfane, Fábio Henrique Eugênio Ribeiro, Zakaria Bouali, and Arnaud Mura. A combined ghost-point-forcing / direct-forcing immersed boundary method (ibm) for compressible flow simulations. *Computers & Fluids*, 162:91–112, 2018.
- [Bec00] Alberto Beccantini. *Upwind Splitting Schemes for Ideal Gases Mixtures with Temperature-Dependant Specific Heat Capacities*. PhD thesis, Université d’Evry, Evry-Val d’Essonne, 2000.
- [Bet42] H. A. Bethe. On the theory of shock waves for an arbitrary equation of state. Technical Report Serial No. NDRC-B-237, Office of Scientific Research and Development, Washington, DC, May 1942.
- [BH97] Barna L. Bihari and Ami Harten. Multiresolution schemes for the numerical solution of 2-d conservation laws i. *SIAM Journal on Scientific Computing*, 18(2):315–354, 1997.
- [BKH<sup>+</sup>16] Lorenz Boeck, Peter Katzy, Josef Hasslberger, Andreas Kink, and Thomas Sattelmayer. The " gravent ddt database ". *Shock Waves*, 26, 03 2016.
- [BLCM<sup>+</sup>13] R.R. Bhattacharjee, S.S.M. Lau-Chapdelaine, G. Maines, L. Maley, and M.I. Radulescu. Detonation re-initiation mechanism following the mach reflection of a quenched detonation. *Proceedings of the Combustion Institute*, 34(2):1893–1901, 2013.
- [BM87] J.K. Bechtold and M. Matalon. Hydrodynamic and diffusion effects on the stability of spherically expanding flames. *Combustion and Flame*, 67(1):77–90, 1987.
- [BM92] Anne Bourlioux and Andrew J. Majda. Theoretical and numerical structure for unstable two-dimensional detonations. *Combustion and Flame*, 90(3):211 – 229, 1992.
- [BM07] V. Bykov and U. Maas. The extension of the ildm concept to reaction–diffusion manifolds. *Combustion Theory and Modelling*, 11(6):839–862, 2007.
- [BMR91] Anne Bourlioux, Andrew J. Majda, and Victor Roytburd. Theoretical and numerical structure for unstable one-dimensional detonations. *SIAM Journal on Applied Mathematics*, 51(2):303–343, 1991.
- [BMS17] L.R. Boeck, R. Mével, and T. Sattelmayer. Models for shock-induced ignition evaluated by detailed chemical kinetics for hydrogen/air in the context of deflagration-to-detonation transition. *Journal of Loss Prevention in the Process Industries*, 49:731–738, 2017.
- [Boe15] Lorenz Boeck. *Deflagration-to-Detonation Transition and Detonation Propagation in H<sub>2</sub>-Air Mixtures with Transverse Concentration Gradients*. PhD thesis, Technische Universität München, 06 2015.
- [Bor85] R. Borghi. *On the Structure and Morphology of Turbulent Premixed Flames*, pages 117–138. Springer US, Boston, MA, 1985.
- [Bur84] Alexander Burcat. Thermochemical data for combustion calculations. *Combustion Chemistry*, pages 455–473, 01 1984.
- [CC94] Carey F. Cox and Pasquale Cinnella. General solution procedure for flows in local chemical equilibrium. *AIAA Journal*, 32(3):519–527, 1994.
- [CC00] Se-Myong Chang and Keun-Shik Chang. On the shock–vortex interaction in schardin’s problem. *Shock Waves*, 10(5):333–343, Nov 2000.
- [CCD11] Marcos Castro, Bruno Costa, and Wai Sun Don. High order weighted essentially non-oscillatory weno-z schemes for hyperbolic conservation laws. *Journal of Computational Physics*, 230(5):1766–1792, 2011.
- [CD08] G. Ciccarelli and S. Dorofeev. Flame acceleration and transition to detonation in ducts. *Progress in Energy and Combustion Science*, 34(4):499–550, 2008.

- [CDLM17] Xiaodong Cai, Ralf Deiterding, Jianhan Liang, and Yasser Mahmoudi. Adaptive simulations of viscous detonations initiated by a hot jet using a high-order hybrid weno-cd scheme. *Proceedings of the Combustion Institute*, 36(2):2725–2733, 2017.
- [CdW06] G. Ciccarelli and B. de Witt. Detonation initiation by shock reflection from an orifice plate. *Shock Waves*, 15(3):259–265, Jul 2006.
- [CG85] Phillip Colella and Harland M Glaz. Efficient solution algorithms for the riemann problem for real gases. *Journal of Computational Physics*, 59(2):264–289, 1985.
- [CHC11] Arnab Chaudhuri, Abdellah Hadjadj, and Ashwin Chinnayya. On the use of immersed boundary methods for shock/obstacle interactions. *Journal of Computational Physics*, 230(5):1731–1748, 2011.
- [CHR<sup>+</sup>18a] Zhiqiang Chen, Xudong Huang, Yu-Xin Ren, Zhifeng Xie, and Ming Zhou. Mechanism-derived shock instability elimination for riemann-solver-based shock-capturing scheme. *AIAA Journal*, 56(9):3652–3666, 2018.
- [CHR<sup>+</sup>18b] Zhiqiang Chen, Xudong Huang, Yu-Xin Ren, Zhifeng Xie, and Ming Zhou. Mechanism study of shock instability in riemann-solver-based shock-capturing scheme. *AIAA Journal*, 56(9):3636–3651, 2018.
- [CJLD11] Francesco Contino, Hervé Jeanmart, Tommaso Lucchini, and Gianluca D’Errico. Coupling of in situ adaptive tabulation and dynamic adaptive chemistry: An effective method for solving combustion in engine simulations. *Proceedings of the Combustion Institute*, 33(2):3057–3064, 2011.
- [CKMP03] Albert Cohen, Sidi Mahmoud Kaber, Siegfried Müller, and Marie Postel. Fully adaptive multiresolution finite volume schemes for conservation laws. *Math. Comput.*, 72(241):183–225, January 2003.
- [CL03] J. Chao and J. H. S. Lee. The propagation mechanism of high speed turbulent deflagrations. *Shock Waves*, 12(4):277–289, Jan 2003.
- [CMRR21] Frédéric Coquel, Claude Marmignon, Pratik Rai, and Florent Renac. An entropy stable high-order discontinuous galerkin spectral element method for the baer-nunziato two-phase flow model. *Journal of Computational Physics*, 431:110135, 2021.
- [CMY08] J. Choi, F. Ma, and Vigor Yang. Some numerical issues on simulation of detonation cell structures. *Combustion, Explosion, and Shock Waves*, 44:560–578, 09 2008.
- [Coh00] A. Cohen. *Wavelet methods in numerical analysis*, volume 7 of *Handbook of Numerical Analysis*. P.G. Ciarlet and J.L. Lions, editors, Elsevier, Amsterdam, 2000.
- [CPLP07] N. Chaumeix, S. Pichon, F. Lafosse, and C.-E. Paillard. Role of chemical kinetics on the detonation properties of hydrogen /natural gas/air mixtures. *International Journal of Hydrogen Energy*, 32(13):2216–2226, 2007. ICHS-2005.
- [CSH86] D. Keith Clarke, M. D. Salas, and H. A. Hassan. Euler calculations for multielement airfoils using cartesian grids. *AIAA Journal*, 24(3):353–358, 1986.
- [CW82] P. Clavin and F. A. Williams. Effects of molecular diffusion and of thermal expansion on the structure and dynamics of premixed flames in turbulent flows of large scale and low intensity. *Journal of Fluid Mechanics*, 116:251–282, 1982.
- [CYBL18] Shusheng Chen, Chao Yan, Lin Boxi, and Yan-su Li. A new robust carbuncle-free roe scheme for strong shock. *Journal of Scientific Computing*, 77:1–28, 11 2018.
- [Dah63] Germund G. Dahlquist. A special stability problem for linear multistep methods. *BIT Numerical Mathematics*, 3(1):27–43, Mar 1963.

- [Dah05] A.E. Dahoe. Laminar burning velocities of hydrogen–air mixtures from closed vessel gas explosions. *Journal of Loss Prevention in the Process Industries*, 18(3):152 – 166, 2005.
- [Dar38] G Darrieus. On the theory of slow combustion. *La Technique Moderne*, 30:18, 1938.
- [Dav88] S. F. Davis. Simplified second-order godunov-type methods. *SIAM Journal on Scientific and Statistical Computing*, 9(3):445–473, 1988.
- [dCE02] Julien de Charentenay and Alexandre Ern. Multicomponent transport impact on turbulent premixed h<sub>2</sub>/o<sub>2</sub> flames. *Combustion Theory and Modelling*, 6(3):439–462, 2002.
- [DDG<sup>+</sup>09] Ralf Deiterding, Margarete O. Domingues, Sonia M. Gomes, Olivier Roussel, and Kai Schneider. Adaptive multiresolution or adaptive mesh refinement? a case study for 2d euler equations. In *Multiresolution and Adaptive Methods for Convection-Dominated Problems*, pages 28–42, Paris, France, Jan 2009. Société de Mathématiques Appliquées et Industrielles (SMAI). Research Org.: Oak Ridge National Lab. (ORNL), Oak Ridge, TN (United States), Sponsor Org.: USDOE Office of Science (SC), Contract Number: DE-AC05-00OR22725.
- [DdPN06] P. De Palma, M.D. de Tullio, G. Pascazio, and M. Napolitano. An immersed-boundary method for compressible viscous flows. *Computers & Fluids*, 35(7):693–702, 2006. Special Issue Dedicated to Professor Stanley G. Rubin on the Occasion of his 65th Birthday.
- [DFC07] G. Dong, B. C. Fan, and Y. L. Chen. Acceleration of chemistry computations in two-dimensional detonation induced by shock focusing using reduced isat. *Combustion Theory and Modelling*, 11(5):823–837, 2007.
- [DHD14] Guillaume Dayma, Fabien Halter, and Philippe Dagaut. New insights into the peculiar behavior of laminar burning velocities of hydrogen–air flames according to pressure and equivalence ratio. *Combustion and Flame*, 161(9):2235–2241, 2014.
- [DKA<sup>+</sup>01] S.B. Dorofeev, M.S. Kuznetsov, V.I. Alekseev, A.A. Efimenko, and W. Breitung. Evaluation of limits for effective flame acceleration in hydrogen mixtures. *Journal of Loss Prevention in the Process Industries*, 14(6):583 – 589, 2001.
- [DLC68] Graham Dixon-Lewis and Thomas George Cowling. Flame structure and flame reaction kinetics ii. transport phenomena in multicomponent systems. *Proceedings of the Royal Society of London. Series A. Mathematical and Physical Sciences*, 307(1488):111–135, 1968.
- [DM04] Stéphane Descombes and Marc Massot. Operator splitting for nonlinear reaction-diffusion systems with an entropic structure : singular perturbation and order reduction. *Numerische Mathematik*, 97(4):667–698, Jun 2004.
- [DMG04] Michael Dumbser, Jean-Marc Moschetta, and Jérémie Gressier. A matrix stability analysis of the carbuncle phenomenon. *Journal of Computational Physics*, 197(2):647–670, 2004.
- [DND06] Zoran Dragojlovic, Farrokh Najmabadi, and Marcus Day. An embedded boundary method for viscous, conducting compressible flow. *Journal of Computational Physics*, 216(1):37 – 51, 2006.
- [Dor09] S.B. Dorofeev. Hydrogen flames in tubes: Critical run-up distances. *International Journal of Hydrogen Energy*, 34(14):5832–5837, 2009. 2nd International Conference on Hydrogen Safety.
- [DS10] Richard R. Dobbins and Mitchell D. Smooke. A fully implicit, compact finite difference method for the numerical solution of unsteady laminar flames. *Flow, Turbulence and Combustion*, 85(3):763–799, Dec 2010.

- [DSK<sup>+</sup>00] S. B. Dorofeev, V. P. Sidorov, M. S. Kuznetsov, I. D. Matsukov, and V. I. Alekseev. Effect of scale on the onset of detonations. *Shock Waves*, 10(2):137–149, May 2000.
- [DSTW91] David R. Dowdy, David B. Smith, Simon C. Taylor, and Alan Williams. The use of expanding spherical flames to determine burning velocities and stretch effects in hydrogen/air mixtures. *Symposium (International) on Combustion*, 23(1):325–332, 1991. Twenty-Third Symposium (International) on Combustion.
- [DT04] V. Daru and C. Tenaud. High order one-step monotonicity-preserving schemes for unsteady compressible flow calculations. *Journal of Computational Physics*, 193:563–594, 2004.
- [Dua11] Max Pedro Duarte. *Adaptive numerical methods in time and space for the simulation of multi-scale reaction fronts*. PhD thesis, Ecole Centrale Paris, 2011.
- [Dup] *Propagation of Detonation Waves in an Acoustic Absorbing Walled Tube*, pages 248–263.
- [DvW19] Fabian Denner and Berend G. M. van Wachem. Numerical modelling of shock-bubble interactions using a pressure-based algorithm without riemann solvers. *Experimental and Computational Multiphase Flow*, 1(4):271–285, 2019.
- [DXL<sup>+</sup>18] Xi Deng, Bin Xie, Raphaël Loubère, Yuya Shimizu, and Feng Xiao. Limiter-free discontinuity-capturing scheme for compressible gas dynamics with reactive fronts. *Computers & Fluids*, 171:1 – 14, 2018.
- [DZ21] Andrea Di Mascio and Stefano Zaghi. An immersed boundary approach for high order weighted essentially non-oscillatory schemes. *Computers & Fluids*, 222:104931, 2021.
- [EG96] Pierre-Arnaud Raviart (auth.) Edwige Godlewski. *Numerical Approximation of Hyperbolic Systems of Conservation Laws*. Applied Mathematical Sciences 118. Springer New York, 1996.
- [Ehl69] B.L. Ehle. *On Padé approximations to the exponential function and A-stable methods for the numerical solution of initial value problems*. PhD thesis, University of Waterloo, 1969.
- [Ein88] Bernd Einfeldt. On godunov-type methods for gas dynamics. *SIAM Journal on Numerical Analysis*, 25(2):294–318, 1988.
- [EMSM15] S. Emami, K. Mazaheri, A. Shamooni, and Y. Mahmoudi. Les of flame acceleration and ddt in hydrogen–air mixture using artificially thickened flame approach and detailed chemical kinetics. *International Journal of Hydrogen Energy*, 40(23):7395–7408, 2015.
- [Erp62] Jerome J. Erpenbeck. Stability of step shocks. *The Physics of Fluids*, 5(10):1181–1187, 1962.
- [Erp64] Jerome J. Erpenbeck. Stability of idealized one-reaction detonations. *The Physics of Fluids*, 7(5):684–696, 1964.
- [Ett12] Florian Anton Ettner. *Effiziente numerische Simulation des Deflagrations–Detonations–Übergangs*. PhD thesis, Technische Universität München, 10 2012.
- [EVS14] Florian Ettner, Klaus G. Vollmer, and Thomas Sattelmayer. Numerical simulation of the deflagration-to-detonation transition in inhomogeneous mixtures. *Journal of Combustion*, 2014:686347, May 2014.
- [FHA16] Lin Fu, Xiangyu Y. Hu, and Nikolaus A. Adams. A family of high-order targeted eno schemes for compressible-fluid simulations. *Journal of Computational Physics*, 305:333–359, 2016.



- [GBL13] R. Gautier, D. Biau, and E. Lamballais. A reference solution of the flow over a circular cylinder at  $re=40$ . *Computers & Fluids*, 75:103–111, 2013.
- [GBO21] Vadim N. Gamezo, Christian L. Bachman, and Elaine S. Oran. Flame acceleration and ddt in large-scale obstructed channels filled with methane-air mixtures. *Proceedings of the Combustion Institute*, 38(3):3521–3528, 2021.
- [GDO99] Vadim N. Gamezo, Daniel Desbordes, and Elaine S. Oran. Formation and evolution of two-dimensional cellular detonations. *Combustion and Flame*, 116(1):154–165, 1999.
- [GEB03] X.J. Gu, D.R. Emerson, and D. Bradley. Modes of reaction front propagation from hot spots. *Combustion and Flame*, 133(1):63–74, 2003.
- [GED00] A.I Gavrikov, A.A Efimenko, and S.B Dorofeev. A model for detonation cell size prediction from chemical kinetics. *Combustion and Flame*, 120(1):19–33, 2000.
- [GHO16] G.B. Goodwin, R.W. Houim, and E.S. Oran. Effect of decreasing blockage ratio on ddt in small channels with obstacles. *Combustion and Flame*, 173:16–26, 2016.
- [GJ72] R. Günther and G. Janisch. Measurements of burning velocity in a flat flame front. *Combustion and Flame*, 19(1):49–53, 1972.
- [GKC<sup>+</sup>12] Randall O. Gauntt, Donald A. Kalinich, Jeffrey N. Cardoni, Jesse Phillips, Andrew Scott Goldmann, Susan Y. Pickering, Matthew Francis, Kevin Robb, Larry J. Ott, Dean Wang, Curtis Smith, Shawn Germain, David Schwieder, and Cherie Phelan. Fukushima daiichi accident study : status as of april 2012. Technical report, United States, 2012. Research Org.: Sandia National Laboratories (SNL), Albuquerque, NM, and Livermore, CA (United States). Sponsor Org.: USDOE National Nuclear Security Administration (NNSA) Report Number: SAND2012-6173 Contract Number: AC04-94AL85000.
- [Gla88] P Glaister. An approximate linearised riemann solver for the euler equations for real gases. *Journal of Computational Physics*, 74(2):382 – 408, 1988.
- [GOO07] Vadim N. Gamezo, Takanobu Ogawa, and Elaine S. Oran. Numerical simulations of flame propagation and ddt in obstructed channels filled with hydrogen-air mixture. *Proceedings of the Combustion Institute*, 31(2):2463–2471, 2007.
- [GOO08] Vadim N. Gamezo, Takanobu Ogawa, and Elaine S. Oran. Flame acceleration and ddt in channels with obstacles: Effect of obstacle spacing. *Combustion and Flame*, 155(1):302–315, 2008.
- [Gra66] Roger R. Graig. A shock tube study of the ignition delay of hydrogen-air mixtures near the second explosion limit. Technical report, Air Force Aero-Propulsion Lab, Wright-Patterson, 1966. Technical report AFAPL-TR-66-74.
- [GS66] RALPH B. GILBERT and ROGER A. STREHLOW. Theory of detonation initiation behind reflected shock waves. *AIAA Journal*, 4(10):1777–1783, 1966.
- [GSH<sup>+</sup>13] J. Grune, K. Sempert, H. Haberstroh, M. Kuznetsov, and T. Jordan. Experimental investigation of hydrogen-air deflagrations and detonations in semi-confined flat layers. *Journal of Loss Prevention in the Process Industries*, 26(2):317–323, 2013. Selected Papers from the Eighth International Symposium on Hazards, Prevention, and Mitigation of Industrial Explosions (Yokohama, Japan, 5–10 September 2010).
- [GSv<sup>+</sup>15] S. Gupta, E. Schmidt, B. von Laufenberg, M. Freitag, G. Poss, F. Funke, and G. Weber. Thai test facility for experimental research on hydrogen and fission product behaviour in light water reactor containments. *Nuclear Engineering and Design*, 294:183–201, 2015.
- [GTE17] L.F. Gutiérrez Marcantoni, J. Tamagno, and S. Elaskar. rhocentralrffoam: An open-foam solver for high speed chemically active flows – simulation of planar detonations –. *Computer Physics Communications*, 219:209–222, 2017.

- [Har83] Ami Harten. High resolution schemes for hyperbolic conservation laws. *Journal of Computational Physics*, 49(3):357–393, 1983.
- [Har95] Ami Harten. Multiresolution algorithms for the numerical solution of hyperbolic conservation laws. *Communications on Pure and Applied Mathematics*, 48(12):1305–1342, 1995.
- [HC92] Longting He and Paul Clavin. Critical conditions for detonation initiation in cold gaseous mixtures by nonuniform hot pockets of reactive gases. *Symposium (International) on Combustion*, 24(1):1861–1867, 1992. Twenty-Fourth Symposium on Combustion.
- [HC94] Longting He and Paul Clavin. On the direct initiation of gaseous detonations by an energy source. *Journal of Fluid Mechanics*, 277:227–248, 1994.
- [HDH11] Zekai Hong, David F. Davidson, and Ronald K. Hanson. An improved h<sub>2</sub>/o<sub>2</sub> mechanism based on recent shock tube/laser absorption measurements. *Combustion and Flame*, 158(4):633–644, 2011. Special Issue on Kinetics.
- [HE17] J. D. Hedengren and T. F. Edgar. Storage and retrieval of optimal control, 2017.
- [HH83] Ami Harten and James M Hyman. Self adjusting grid methods for one-dimensional hyperbolic conservation laws. *Journal of Computational Physics*, 50(2):235–269, 1983.
- [HHLK76] A. Harten, J. M. Hyman, P. D. Lax, and B. Keyfitz. On finite-difference approximations and entropy conditions for shocks. *Communications on Pure and Applied Mathematics*, 29(3):297–322, 1976.
- [HK11] Ryan W. Houim and Kenneth K. Kuo. A low-dissipation and time-accurate method for compressible multi-component flow with variable specific heat ratios. *Journal of Computational Physics*, 230(23):8527–8553, 2011.
- [HKAH06] X.Y. Hu, B.C. Khoo, N.A. Adams, and F.L. Huang. A conservative interface method for compressible flows. *Journal of Computational Physics*, 219(2):553 – 578, 2006.
- [HLL83] Amiram Harten, Peter D. Lax, and Bram van Leer. On upstream differencing and godunov-type schemes for hyperbolic conservation laws. *SIAM Review*, 25(1):35–61, 1983.
- [HO87] Ami Harten and Stanley Osher. Uniformly high-order accurate nonoscillatory schemes. i. *SIAM Journal on Numerical Analysis*, 24(2):279–309, 1987.
- [HOO16] Ryan W. Houim, Alp Ozgen, and Elaine S. Oran. The role of spontaneous waves in the deflagration-to-detonation transition in submillimetre channels. *Combustion Theory and Modelling*, 20(6):1068–1087, 2016.
- [HS87] J.-F. Haas and B. Sturtevant. Interaction of weak shock waves with cylindrical and spherical gas inhomogeneities. *Journal of Fluid Mechanics*, 181:41–76, 1987.
- [HTERT04] R. Hilbert, F. Tap, H. El-Rabii, and D. Thévenin. Impact of detailed chemistry and transport models on turbulent combustion simulations. *Progress in Energy and Combustion Science*, 30(1):61 – 117, 2004.
- [HW96] Ernst Hairer and Gerhard Wanner. *Solving Ordinary Differential Equations II. Stiff and Differential-Algebraic Problems*, volume 14. Springer, Berlin, Heidelberg, 01 1996.
- [HWL19] Wenhui Han, Cheng Wang, and Chung K Law. Pulsation in one-dimensional h<sub>2</sub>-o<sub>2</sub> detonation with detailed reaction mechanism. *Combustion and Flame*, 200:242–261, 2019.
- [HZZ<sup>+</sup>06] Zuohua Huang, Yong Zhang, Ke Zeng, Bing Liu, Qian Wang, and Deming Jiang. Measurements of laminar burning velocities for natural gas–hydrogen–air mixtures. *Combustion and Flame*, 146(1):302–311, 2006.
- [IEA21] International Energy Agency IEA. Hydrogen, November 2021.

- [IJK<sup>+</sup>] K.-S. Im, S.-T. Joh, C.-K. Kim, S.-C. Chang, and C. Jorgenson. *Application of the CESE method to detonation with realistic finite-rate chemistry*.
- [JC13] C. Johansen and G. Ciccarelli. Modeling the initial flame acceleration in an obstructed channel using large eddy simulation. *Journal of Loss Prevention in the Process Industries*, 26(4):571–585, 2013.
- [Jou05] Jouguet. Sur la propagation des réactions chimiques dans les gaz. *Journal de Mathématiques Pures et Appliquées*, 1:347–425, 1905.
- [JQS<sup>+</sup>21] Weiqi Ji, Weilun Qiu, Zhiyu Shi, Shaowu Pan, and Sili Deng. Stiff-pinn: Physics-informed neural network for stiff chemical kinetics. *The Journal of Physical Chemistry A*, 125(36):8098–8106, Sep 2021.
- [KAD<sup>+</sup>98] M.S. Kuznetsov, V.I. Alekseev, S.B. Dorofeev, I.D. Matsukov, and J.L. Boccio. Detonation propagation, decay, and reinitiation in nonuniform gaseous mixtures. *Symposium (International) on Combustion*, 27(2):2241–2247, 1998.
- [KAK03] M.P. Kirkpatrick, S.W. Armfield, and J.H. Kent. A representation of curved boundaries for the solution of the navier–stokes equations on a staggered three-dimensional cartesian grid. *Journal of Computational Physics*, 184(1):1–36, 2003.
- [KAMD05] M. Kuznetsov, V. Alekseev, I. Matsukov, and S. Dorofeev. Ddt in a smooth tube filled with a hydrogen–oxygen mixture. *Shock Waves*, 14(3):205–215, Nov 2005.
- [KD19] Abhishek Kundu and Sudipta De. High resolution numerical simulation of a shock-accelerated refrigerant-22 bubble. *Computers & Fluids*, 193:104289, 2019.
- [KDE96] S.I. Kryuchkov, S.B. Dorofeev, and A.A. Efimenko. Critical conditions for detonation propagation through mixture with decreasing reaction rate. *Symposium (International) on Combustion*, 26(2):2965–2972, 1996.
- [KGO12] D. A. Kessler, V. N. Gamezo, and E. S. Oran. Gas-phase detonation propagation in mixture composition gradients. *Philosophical Transactions of the Royal Society A: Mathematical, Physical and Engineering Sciences*, 370(1960):567–596, 2012.
- [KHBW19] Reza Khodadadi Azadboni, Ali Heidari, Lorenz R. Boeck, and Jennifer X. Wen. The effect of concentration gradients on deflagration-to-detonation transition in a rectangular channel with and without obstructions – a numerical study. *International Journal of Hydrogen Energy*, 44(13):7032–7040, 2019.
- [KHW20] Reza Khodadadi Azadboni, Ali Heidari, and Jennifer X. Wen. Numerical studies of flame acceleration and onset of detonation in homogenous and inhomogeneous mixture. *Journal of Loss Prevention in the Process Industries*, 64:104063, 2020.
- [KJG11] M. Kuznetsov, T. Jordan, and J. Grune. Combustion regimes in a stratified layer of hydrogen - air mixture, Jul 2011.
- [KLG82] R. Knystautas, J.H. Lee, and C.M. Guirao. The critical tube diameter for detonation failure in hydrocarbon-air mixtures. *Combustion and Flame*, 48:63–83, 1982.
- [KLM19] M. Ehsan Khalili, Martin Larsson, and Bernhard Müller. High-order ghost-point immersed boundary method for viscous compressible flows based on summation-by-parts operators. *International Journal for Numerical Methods in Fluids*, 89(7):256–282, 2019.
- [KMV<sup>+</sup>13] Michael C. Krejci, Olivier Mathieu, Andrew J. Vissotski, Sankaranarayanan Ravi, Travis G. Sikes, Eric L. Petersen, Alan Kérmonès, Wayne Metcalfe, and Henry J. Curran. Laminar Flame Speed and Ignition Delay Time Data for the Kinetic Modeling of Hydrogen and Syngas Fuel Blends. *Journal of Engineering for Gas Turbines and Power*, 135(2), 01 2013. 021503.

- [KON98] A. A. KONNOV. Detailed reaction mechanism for small hydrocarbons combustion, release 0.4. <http://homepages.vub.ac.be/~akonnov/>, 1998.
- [Kon19] Alexander A. Konnov. Yet another kinetic mechanism for hydrogen combustion. *Combustion and Flame*, 2019.
- [KOO19] Carolyn R. Kaplan, Alp Ozgen, and Elaine S. Oran. Chemical-diffusive models for flame acceleration and transition-to-detonation: genetic algorithm and optimisation procedure. *Combustion Theory and Modelling*, 23(1):67–86, 2019.
- [KOT99] A.M. Khokhlov, E.S. Oran, and G.O. Thomas. Numerical simulation of deflagration-to-detonation transition: the role of shock–flame interactions in turbulent flames. *Combustion and Flame*, 117(1):323 – 339, 1999.
- [KRM<sup>+</sup>05] R. J. Kee, F.M Rupley, J.A Miller, M.E. Coltrin, J. F. Grcar, E. Meeks, H.K. Moffat, A.E. Lutz, G. Dixon-Lewis, M.D. Smooke, J. Warnatz, G.H. Evans, R.S. Larson, R.E. Mitchell, L.R. Petzold, W.C. Reynolds, M. Caracotsios, W.E. Stewart, P. Glarborg, C. Wang, O. Adigun, W.G. Houf, C.P. Chou, P. Miller, S.F. Ho, and D.J. Young. *CHEMKIN Release 4.0.2*. Reaction Design, San Diego, CA, 2005.
- [KSQH02] A K Kapila, D W Schwendeman, J J Quirk, and T Hawa. Mechanisms of detonation formation due to a temperature gradient. *Combustion Theory and Modelling*, 6(4):553–594, 2002.
- [KT02] Alexander Kurganov and Eitan Tadmor. Solution of two-dimensional riemann problems for gas dynamics without riemann problem solvers. *Numerical Methods for Partial Differential Equations*, 18(5):584–608, 2002.
- [Lan44] L D Landau. Propagation d’un front de flamme. *Acta Physicochim. USSR*, 19:77, 1944.
- [Lar91] B Larrouturou. How to preserve the mass fractions positivity when computing compressible multi-component flows. *Journal of Computational Physics*, 95(1):59 – 84, 1991.
- [LAW06] C. K. LAW. Propagation, structure, and limit phenomena of laminar flames at elevated pressures. *Combustion Science and Technology*, 178(1-3):335–360, 2006.
- [LCP03] N Lamoureux, N Chaumeix, and C.-E Paillard. Laminar flame velocity determination for h<sub>2</sub>–air–he–co<sub>2</sub> mixtures using the spherical bomb method. *Experimental Thermal and Fluid Science*, 27(4):385–393, 2003. Second Mediterranean Combustion Symposium.
- [Lee08] John H. S. Lee. *The Detonation Phenomenon*. Cambridge University Press, The Edinburgh Building, Cambridge CB2 8RU, UK, 2008.
- [Lev92] R. J. Leveque. *Numerical Methods for Conservation Laws*. Springer, 2nd edition edition, 1992.
- [LeV02] Randall J. LeVeque. *Finite Volume Methods for Hyperbolic Problems*. Cambridge texts in applied mathematics. Cambridge University Press, 1 edition, 2002.
- [LF05] Mark N. Linnick and Hermann F. Fasel. A high-order immersed interface method for simulating unsteady incompressible flows on irregular domains. *Journal of Computational Physics*, 204(1):157–192, 2005.
- [Lio00] Meng-Sing Liou. Mass flux schemes and connection to shock instability. *Journal of Computational Physics*, 160(2):623–648, 2000.
- [LJN13] John H.S. Lee, Anne Jesuthasan, and Hoi Dick Ng. Near limit behavior of the detonation velocity. *Proceedings of the Combustion Institute*, 34(2):1957–1963, 2013.
- [LKO22] Xiaoyi Lu, Carolyn R. Kaplan, and Elaine S. Oran. Predictions of flame acceleration, transition to detonation, and detonation propagation using the chemical-diffusive model. *Combustion and Flame*, 235:111705, 2022.

- [LKY78] J.H. Lee, R. Knystautas, and N. Yoshikawa. Photochemical initiation of gaseous detonations. *Acta Astronautica*, 5(11):971–982, 1978.
- [LLS90] Meng-Sing Liou, Bram Van Leer, and Jian-Shun Shuen. Splitting of inviscid fluxes for real gases. *Journal of Computational Physics*, 87(1):1–24, 1990.
- [LOC94] Xu-Dong Liu, Stanley Osher, and Tony Chan. Weighted essentially non-oscillatory schemes. *Journal of Computational Physics*, 115(1):200 – 212, 1994.
- [LR05] J. H. S. Lee and M. I. Radulescu. On the hydrodynamic thickness of cellular detonations. *Combustion, Explosion and Shock Waves*, 41(6):745–765, Nov 2005.
- [LV99] D Lanser and J.G Verwer. Analysis of operator splitting for advection–diffusion–reaction problems from air pollution modelling. *Journal of Computational and Applied Mathematics*, 111(1):201–216, 1999.
- [LVK<sup>+</sup>22] Luc Lecointre, Ronan Vicquelin, Sergey Kudriakov, Etienne Studer, and Christian Tenaud. High-order numerical scheme for compressible multi-component real gas flows using an extension of the roe approximate riemann solver and specific monotonicity-preserving constraints. *Journal of Computational Physics*, 450:110821, 2022.
- [LW60] Peter Lax and Burton Wendroff. Systems of conservation laws. *Communications on Pure and Applied Mathematics*, 13(2):217–237, 1960.
- [LZKD04] Juan Li, Zhenwei Zhao, Andrei Kazakov, and Frederick L. Dryer. An updated comprehensive kinetic model of hydrogen combustion. *International Journal of Chemical Kinetics*, 36(10):566–575, 2004.
- [Mak93] Aristidis Makris. *The propagation of gaseous detonations in porous media*. PhD thesis, McGill University, 1993.
- [Mal05] Fabrice Malet. *Etude expérimentale et numérique de la propagation de flammes prémélangées turbulentes dans une atmosphère pauvre en hydrogène et humide*. PhD thesis, Université d’Orléans, 2005. Thèse de doctorat dirigée par Paillard, Claude-Etienne et Chaumeix, Nabihia Cinétique chimique appliquée Orléans 2005.
- [MAR51] GEORGE H. MARKSTEIN. Experimental and theoretical studies of flame-front stability. *Journal of the Aeronautical Sciences*, 18(3):199–209, 1951.
- [Max16] Brian Maxwell. *Turbulent Combustion Modelling of Fast Flames and Detonations Using Compressible LEM-LES*. PhD thesis, University of Ottawa, 01 2016.
- [MDK85] W. Müller-Dietsche and G. Katzenmeier. Reactor safety research at the large scale facility hdr. *Nuclear Engineering and Design*, 88(3):241–251, 1985.
- [MDM<sup>+</sup>12] L. Monasse, V. Daru, C. Mariotti, S. Piperno, and C. Tenaud. A conservative coupling algorithm between a compressible flow and a rigid body using an embedded boundary method. *Journal of Computational Physics*, 231(7):2977 – 2994, 2012.
- [MI05] Rajat Mittal and Gianluca Iaccarino. Immersed boundary methods. *Annual Review of Fluid Mechanics*, 37(1):239–261, 2005.
- [MJL<sup>+</sup>09] R. Mével, S. Javoy, F. Lafosse, N. Chaumeix, G. Dupré, and C.-E. Paillard. Hydrogen–nitrous oxide delay times: Shock tube experimental study and kinetic modelling. *Proceedings of the Combustion Institute*, 32(1):359–366, 2009.
- [MKYD99] M. A. Mueller, T. J. Kim, R. A. Yetter, and F. L. Dryer. Flow reactor studies and kinetic modeling of the h<sub>2</sub>/o<sub>2</sub> reaction. *International Journal of Chemical Kinetics*, 31(2):113–125, Jan 1999.
- [MM61] L. Monchick and E. A. Mason. Transport properties of polar gases. *The Journal of Chemical Physics*, 35(5):1676–1697, 1961.

- [MM82] M. Matalon and B. J. Matkowsky. Flames as gasdynamic discontinuities. *Journal of Fluid Mechanics*, 124:239–259, 1982.
- [MM11] Y. Mahmoudi and K. Mazaheri. High resolution numerical simulation of the structure of 2-d gaseous detonations. *Proceedings of the Combustion Institute*, 33(2):2187–2194, 2011.
- [MMR12] Kiumars Mazaheri, Yasser Mahmoudi, and Matei I. Radulescu. Diffusion and hydrodynamic instabilities in gaseous detonations. *Combustion and Flame*, 159(6):2138 – 2154, 2012.
- [MO71a] J.W. Meyer and A.K. Oppenheim. Coherence theory of the strong ignition limit. *Combustion and Flame*, 17(1):65–68, 1971.
- [MO71b] J.W. Meyer and A.K. Oppenheim. On the shock-induced ignition of explosive gases. *Symposium (International) on Combustion*, 13(1):1153–1164, 1971. Thirteenth symposium (International) on Combustion.
- [MP89] Ralph Menikoff and Bradley J. Plohr. The riemann problem for fluid flow of real materials. *Rev. Mod. Phys.*, 61:75–130, Jan 1989.
- [MP92] U. Maas and S.B. Pope. Implementation of simplified chemical kinetics based on intrinsic low-dimensional manifolds. *Symposium (International) on Combustion*, 24(1):103–112, 1992. Twenty-Fourth Symposium on Combustion.
- [MVZ97] Lorenzo Mottura, Luigi Vigeveno, and Marco Zaccanti. An evaluation of roe’s scheme generalizations for equilibrium real gas flows. *Journal of Computational Physics*, 138(2):354 – 399, 1997.
- [MYV89] J.-L. Montagne, H. C. Yee, and M. Vinokur. Comparative study of high-resolution shock-capturing schemes for a real gas. *AIAA Journal*, 27(10):1332–1346, 1989.
- [MZG02] Bonnie McBride, Michael Zehe, and Sanford Gordon. Nasa glenn coefficients for calculating thermodynamic properties of individual species. *NASA*, 10 2002.
- [Ng05] Hoi Dick Ng. *The effect of chemical reaction kinetics on the structure of gaseous detonations*. PhD thesis, McGill University, 2005.
- [NJL07] Hoi Dick Ng, Yiguang Ju, and John H.S. Lee. Assessment of detonation hazards in high-pressure hydrogen storage from chemical sensitivity analysis. *International Journal of Hydrogen Energy*, 32(1):93–99, 2007.
- [NRH<sup>+</sup>05] H. D. Ng, M. I. Radulescu, A. J. Higgins, N. Nikiforakis, and J. H. S. Lee. Numerical investigation of the instability for one-dimensional chapman–jouguet detonations with chain-branching kinetics. *Combustion Theory and Modelling*, 9(3):385–401, 2005.
- [NS05] Mikhail Noskov and Mitchell D. Smooke. An implicit compact scheme solver with application to chemically reacting flows. *Journal of Computational Physics*, 203(2):700–730, 2005.
- [OCCS<sup>+</sup>04] Marcus Ó Conaire, Henry J. Curran, John M. Simmie, William J. Pitz, and Charles K. Westbrook. A comprehensive modeling study of hydrogen oxidation. *International Journal of Chemical Kinetics*, 36(11):603–622, 2004.
- [OG07] Elaine S. Oran and Vadim N. Gamezo. Origins of the deflagration-to-detonation transition in gas-phase combustion. *Combustion and Flame*, 148(1):4 – 47, 2007.
- [Oij02] J.A. Oijen, van. *Flamelet-generated manifolds : development and application to premixed laminar flames*. PhD thesis, Mechanical Engineering, 2002.
- [Oxo99] D. L. Chapman B.A. Oxon. Vi. on the rate of explosion in gases. *The London, Edinburgh, and Dublin Philosophical Magazine and Journal of Science*, 47(284):90–104, 1899.

- [OYBC82] E.S. Oran, T.R. Young, J.P. Boris, and A. Cohen. Weak and strong ignition. i. numerical simulations of shock tube experiments. *Combustion and Flame*, 48:135 – 148, 1982.
- [OZP<sup>+</sup>14] Carsten Olm, István Gy. Zsély, Róbert Pálvölgyi, Tamás Varga, Tibor Nagy, Henry J. Curran, and Tamás Turányi. Comparison of the performance of several recent hydrogen combustion mechanisms. *Combustion and Flame*, 161(9):2219–2234, 2014.
- [PBO10] Jhon Pareja, Hugo J. Burbano, and Yasuhiro Ogami. Measurements of the laminar burning velocity of hydrogen–air premixed flames. *International Journal of Hydrogen Energy*, 35(4):1812–1818, 2010.
- [PC88] PIERRE PELCE and PAUL CLAVIN. Influence of hydrodynamics and diffusion upon the stability limits of laminar premixed flames. In Pierre Pelcé, editor, *Dynamics of Curved Fronts*, pages 425–443. Academic Press, San Diego, 1988.
- [PD01] Maurizio Pandolfi and Domenic D’Ambrosio. Numerical instabilities in upwind methods: Analysis and cures for the “carbuncle” phenomenon. *Journal of Computational Physics*, 166(2):271 – 301, 2001.
- [Pep08] P. Pepiot. *Automatic strategies to model transportation fuel surrogates*. PhD thesis, Stanford University, 2008.
- [Pes72] Charles S Peskin. Flow patterns around heart valves: A numerical method. *Journal of Computational Physics*, 10(2):252–271, 1972.
- [PHL<sup>+</sup>12] S.B. Pope, V. Hiremath, S.R. Lantz, R. Zhuyin, and L. Lu. Isat-ck7: Fortran 90 libraries for the efficient implementation of combustion chemistry, 2012.
- [PHO<sup>+</sup>16] Vito Pasquariello, Georg Hammerl, Felix Orley, Stefan Hickel, Caroline Danowski, Alexander Popp, Wolfgang A. Wall, and Nikolaus A. Adams. A cut-cell finite volume – finite element coupling approach for fluid–structure interaction in compressible flow. *Journal of Computational Physics*, 307:670–695, 2016.
- [PI88] K. PEERY and S. IMLAY. *Blunt-body flow simulations*. Joint Propulsion Conferences. American Institute of Aeronautics and Astronautics, Jul 1988. 0.
- [PKL88] O. Peraldi, R. Knystautas, and J.H. Lee. Criteria for transition to detonation in tubes. *Symposium (International) on Combustion*, 21(1):1629–1637, 1988. Twenty-First Symposium (International on Combustion).
- [PL92] T. J. Poinso and S. K. Lele. Boundary conditions for direct simulations of compressible viscous flows. *Journal of Computational Physics*, 101:104–129, 1992.
- [PM04] CHARLES D. PIERCE and PARVIZ MOIN. Progress-variable approach for large-eddy simulation of non-premixed turbulent combustion. *Journal of Fluid Mechanics*, 504:73–97, 2004.
- [PME<sup>+</sup>15] Maria Adela Puscas, Laurent Monasse, Alexandre Ern, Christian Tenaud, Christian Mariotti, and Virginie Daru. A time semi-implicit scheme for the energy-balanced coupling of a shocked fluid flow with a deformable structure. *Journal of Computational Physics*, 296:241 – 262, 2015.
- [Pop97] S. B. Pope. Computationally efficient implementation of combustion chemistry using in situ adaptive tabulation. *Combustion Theory and Modelling*, 1(1):41–63, 1997.
- [PQVV00] Marica Pelanti, Luigi Quartapelle, L. Vigeveno, and Luigi Vigeveno. A review of entropy fixes as applied to roe’s linearization. Technical report, Politecnico di Milano, 2000.
- [Qui94] James J. Quirk. A contribution to the great riemann solver debate. *International Journal for Numerical Methods in Fluids*, 18(6):555–574, 1994.

- [Rad03] Matei Radulescu. *The propagation and failure mechanism of gaseous detonations: experiments in porous-walled tubes*. PhD thesis, McGill University, 2003.
- [R.E07] R.E.Henry. Tmi-2: A textbook in severe accident management, 11 2007.
- [Ren03] Yu-Xin Ren. A robust shock-capturing scheme based on rotated riemann solvers. *Computers & Fluids*, 32(10):1379 – 1403, 2003.
- [RGCM00] J.-Ch. ROBINET, J. GRESSIER, G. CASALIS, and J.-M. MOSCHETTA. Shock wave instability and the carbuncle phenomenon: same intrinsic origin? *Journal of Fluid Mechanics*, 417:237–263, 2000.
- [RL02] Matei I Radulescu and John H.S Lee. The failure mechanism of gaseous detonations: experiments in porous wall tubes. *Combustion and Flame*, 131(1):29–46, 2002.
- [RLL<sup>+</sup>14] Zhuyin Ren, Yufeng Liu, Tianfeng Lu, Liuyan Lu, Oluwayemisi O. Oluwole, and Graham M. Goldin. The use of dynamic adaptive chemistry and tabulation in reactive flow simulations. *Combustion and Flame*, 161(1):127–137, 2014.
- [RM11] MATEI I. RADULESCU and BRIAN McN. MAXWELL. The mechanism of detonation attenuation by a porous medium and its subsequent re-initiation. *Journal of Fluid Mechanics*, 667:96–134, 2011.
- [Rod17] Alexander V. Rodionov. Artificial viscosity in godunov-type schemes to cure the carbuncle phenomenon. *Journal of Computational Physics*, 345:308–329, 2017.
- [Roe81] P.L Roe. Approximate riemann solvers, parameter vectors, and difference schemes. *Journal of Computational Physics*, 43(2):357 – 372, 1981.
- [Roe85] P. L. Roe. Some contributions to the modelling of discontinuous flows. In *Large-Scale Computations in Fluid Mechanics*, pages 163–193, January 1985.
- [RSB13] Matei Radulescu, G. Sharpe, and Derek Bradley. A universal parameter quantifying explosion hazards, detonability and hot spot formation: The  $\chi$  number. pages 617–626, 01 2013.
- [SA65] Skinner GB. Snyder AD, Robertson J. Zanders DL. Shock tube studies of fuel-air ignition characteristics. Technical report, Monsanto Research Corporation, 1965. Technical report AFAPL-TR-65-93.
- [SBT<sup>+</sup>12] E. Studer, J. Brinster, I. Tkatschenko, G. Mignot, D. Paladino, and M. Andreani. Interaction of a light gas stratified layer with an air jet coming from below: Large scale experiments and scaling issues. *Nuclear Engineering and Design*, 253:406–412, 2012. SI : CFD4NRS-3.
- [Sca17] Roberta Scarpa. *Mécanisme d’accélération d’une flamme de prémélange hydrogène/air et effets sur les structures*. PhD thesis, Université d’Orléans, 2017.
- [Sch57] Professor H. Schardin. High frequency cinematography in the shock tube. *The Journal of Photographic Science*, 5(2):17–19, 1957.
- [SH97] A. Suresh and H.T. Huynh. Accurate monotonicity-preserving schemes with runge-kutta time stepping. *Journal of Computational Physics*, 136:83–99, 1997.
- [Shc40] KI Shchelkin. Influence of tube roughness on the formation and detonation propagation in gas. *Journal of Experimental and Theoretical physics*, 10(10):823–827, 1940.
- [SHC20] Qingguan Song, Yong Han, and Wei Cao. Numerical investigation of self-sustaining modes of 2d planar detonations under concentration gradients in hydrogen–oxygen mixtures. *International Journal of Hydrogen Energy*, 45(53):29606–29615, 2020.



- [sKKRK03] Sung soo Kim, Chongam Kim, Oh-Hyun Rho, and Seung Kyu Hong. Cures for the shock instability: Development of a shock-stable roe scheme. *Journal of Computational Physics*, 185(2):342–374, 2003.
- [Sla77] M.W. Slack. Rate coefficient for  $\text{h} + \text{o}_2 + \text{m} = \text{ho}_2 + \text{m}$  evaluated from shock tube measurements of induction times. *Combustion and Flame*, 28:241–249, 1977.
- [SMMT88] J.E. Shepherd, I.O. Moen, S.B. Murray, and P.A. Thibault. Analyses of the cellular structure of detonations. *Symposium (International) on Combustion*, 21(1):1649–1658, 1988. Twenty-First Symposium (International on Combustion).
- [SQ97] MARK SHORT and JAMES J. QUIRK. On the nonlinear stability and detonability limit of a detonation wave for a model three-step chain-branching reaction. *Journal of Fluid Mechanics*, 339:89–119, 1997.
- [SS00] E. Schultz and J. Shepherd. Validation of detailed reaction mechanisms for detonation simulation. Technical report, California Institute of Technology Pasadena, 2000.
- [SSHL99] C.J. Sun, C.J. Sung, L. He, and C.K. Law. Dynamics of weakly stretched flames: quantitative description and extraction of global flame parameters. *Combustion and Flame*, 118(1):108–128, 1999.
- [SSZ<sup>+</sup>17] Lisong Shi, Hua Shen, Peng Zhang, Deliang Zhang, and Chihyung Wen. Assessment of vibrational non-equilibrium effect on detonation cell size. *Combustion Science and Technology*, 189(5):841–853, 2017.
- [ST64] K.I. Shchelkin and Y.K. Troshin. *Gasdynamics of Combustion*. NASA TT-F. National Aeronautics and Space Administration, 1964.
- [ST95] Nickolay N. Smirnov and Michael V. Tyurnikov. Experimental investigation of deflagration to detonation transition in hydrocarbon-air gaseous mixtures. *Combustion and Flame*, 100(4):661–668, 1995.
- [SW14] Antonio L. Sánchez and Forman A. Williams. Recent advances in understanding of flammability characteristics of hydrogen. *Progress in Energy and Combustion Science*, 41:1–55, 2014.
- [Swe84] P. K. Sweby. High resolution schemes using flux limiters for hyperbolic conservation laws. *SIAM Journal on Numerical Analysis*, 21(5):995–1011, 1984.
- [SWP<sup>+</sup>17] Mohamed Saif, Wentian Wang, Andrzej Pekalski, Marc Levin, and Matei I. Radulescu. Chapman–jouguet deflagrations and their transition to detonation. *Proceedings of the Combustion Institute*, 36(2):2771–2779, 2017.
- [SY14] Zhijun Shen, Wei Yan, and Guangwei Yuan. A stability analysis of hybrid schemes to cure shock instability. *Communications in Computational Physics*, 15(5):1320–1342, 2014.
- [TBB01] Geraint Thomas, Richard Bambrey, and Caren Brown. Experimental observations of flame acceleration and transition to detonation following shock-flame interaction. *Combustion Theory and Modelling*, 5(4):573–594, 2001.
- [TD11] Christian Tenaud and Max Duarte. Tutorials on adaptive multiresolution for mesh refinement applied to fluid dynamics and reactive media problems. *ESAIM Proceedings*, 34, 12 2011.
- [TDC<sup>+</sup>94] Yewen Tan, Philippe Dagaut, Michel Cathonnet, Jean Claude Boettner, Jean Sylvain Bachman, and Patrick Carlier. Natural gas and blends oxidation and ignition: Experiments and modeling. *Symposium (International) on Combustion*, 25(1):1563–1569, 1994. Twenty-Fifth Symposium (International) on Combustion.

- [TEP17] TEPCO. The 5th progress report on the investigation and examination of unconfirmed and unresolved issues on the development mechanism of the Fukushima Daiichi nuclear accident. Technical report, 12 2017.
- [TKGO13] B.D. Taylor, D.A. Kessler, V.N. Gamezo, and E.S. Oran. Numerical simulations of hydrogen detonations with detailed chemical kinetics. *Proceedings of the Combustion Institute*, 34(2):2009–2016, 2013.
- [TLK91] A. Teodorczyk, J.H.S. Lee, and R. Knystautas. The structure of fast turbulent flames in very rough, obstacle-filled channels. *Symposium (International) on Combustion*, 23(1):735–741, 1991. Twenty-Third Symposium (International) on Combustion.
- [Tor09] Eleuterio Toro. *Riemann Solvers and Numerical Methods for Fluid Dynamics: A Practical Introduction*. 3. ed. Springer, Berlin, Heidelberg, 2009.
- [TPH20] Colin A.Z. Towery, Alexei Y. Poludnenko, and Peter E. Hamlington. Detonation initiation by compressible turbulence thermodynamic fluctuations. *Combustion and Flame*, 213:172–183, 2020.
- [TRB15] Christian Tenaud, Olivier Roussel, and Linda Bentaleb. Unsteady compressible flow computations using an adaptive multiresolution technique coupled with a high-order one-step shock-capturing scheme. *Computers & Fluids*, 120:111 – 125, 2015.
- [Tro79] J. Troe. Predictive possibilities of unimolecular rate theory. *Journal of Physical Chemistry*, 83:1, Jan 1979. Research Org.: Univ. Goettingen, Germany.
- [TSE91] G.O. Thomas, P. Sutton, and D.H. Edwards. The behavior of detonation waves at concentration gradients. *Combustion and Flame*, 84(3):312–322, 1991.
- [TSS94] E. F. Toro, M. Spruce, and W. Speares. Restoration of the contact surface in the hll-riemann solver. *Shock Waves*, 4(1):25–34, Jul 1994.
- [USR96] H. S. UDAYKUMAR, W. SHYY, and M. M. RAO. Elafint: A mixed eulerian–lagrangian method for fluid flows with complex and moving boundaries. *International Journal for Numerical Methods in Fluids*, 22(8):691–712, 1996.
- [VBA<sup>+</sup>10] Damir Valiev, Vitaly Bychkov, V’yacheslav Akkerman, Chung K. Law, and Lars-Erik Eriksson. Flame acceleration in channels with obstacles in the deflagration-to-detonation transition. *Combustion and Flame*, 157(5):1012 – 1021, 2010.
- [VES12] K. G. Vollmer, F. Ettner, and T. Sattelmayer. Deflagration-to-detonation transition in hydrogen/air mixtures with a concentration gradient. *Combustion Science and Technology*, 184(10-11):1903–1915, 2012.
- [VM90] Marcel Vinokur and Jean-Louis Montagné. Generalized flux-vector splitting and roe average for an equilibrium real gas. *Journal of Computational Physics*, 89(2):276 – 300, 1990.
- [VS65] V.V. Voevodsky and R.I. Soloukhin. On the mechanism and explosion limits of hydrogen-oxygen chain self-ignition in shock waves. *Symposium (International) on Combustion*, 10(1):279–283, 1965. Tenth Symposium (International) on Combustion.
- [vtI17] Bart S. van Lith, Jan H.M. ten Thijsse Boonkcamp, and Wilbert L. IJzerman. Embedded weno: A design strategy to improve existing weno schemes. *Journal of Computational Physics*, 330:529–549, 2017.
- [WDL18] Jintao Wu, Gang Dong, and Baoming Li. Parallel chemistry acceleration algorithms based on isat method in gaseous detonation computations. *Computers & Fluids*, 167:265–284, 2018.

- [WL85] C.K. Wu and C.K. Law. On the determination of laminar flame speeds from stretched flames. *Symposium (International) on Combustion*, 20(1):1941–1949, 1985. Twentieth Symposium (International) on Combustion.
- [Wol15] Erik Wolf. Chapter 9 - large-scale hydrogen energy storage. In Patrick T. Moseley and Jürgen Garcke, editors, *Electrochemical Energy Storage for Renewable Sources and Grid Balancing*, pages 129–142. Elsevier, Amsterdam, 2015.
- [WSHN13] Cheng Wang, Chi-Wang Shu, Wenhui Han, and Jianguo Ning. High resolution weno simulation of 3d detonation waves. *Combustion and Flame*, 160(2):447–462, 2013.
- [WW17] Chang-Jian Wang and Jennifer X. Wen. Numerical simulation of flame acceleration and deflagration-to-detonation transition in hydrogen-air mixtures with concentration gradients. *International Journal of Hydrogen Energy*, 42:7657–7663, 2017.
- [WZZ<sup>+</sup>17] Haiqiao Wei, Lei Zhou, Hua Zhou, Zhen Lu, Zhuyin Ren, and Graham M. Goldin. Toward efficient chemistry calculations in engine simulations through static adaptive acceleration. *Combustion Science and Technology*, 189(4):623–642, 2017.
- [XDS18] Huahua Xiao, Qiangling Duan, and Jinhua Sun. Premixed flame propagation in hydrogen explosions. *Renewable and Sustainable Energy Reviews*, 81:1988–2001, 2018.
- [XW21] Qiang Xiao and Chunshen Weng. Effect of losses on hydrogen–oxygen–argon detonation cell sizes. *Physics of Fluids*, 33(11):116103, 2021.
- [YMUS99] T. Ye, R. Mittal, H.S. Udaykumar, and W. Shyy. An accurate cartesian grid method for viscous incompressible flows with complex immersed boundaries. *Journal of Computational Physics*, 156(2):209–240, 1999.
- [Yos80] Norihiko Yoshikawa. *Coherent shock wave amplification in photochemical initiation of gaseous detonations*. PhD thesis, McGill University, 1980.
- [Zel80] Ya.B. Zeldovich. Regime classification of an exothermic reaction with nonuniform initial conditions. *Combustion and Flame*, 39(2):211–214, 1980.
- [ZLCZ16] Fan Zhang, Jun Liu, Biaosong Chen, and Wanxie Zhong. Evaluation of rotated upwind schemes for contact discontinuity and strong shock. *Computers & Fluids*, 134-135:11–22, 2016.
- [ZLL16] Chi Zhu, Haoxiang Luo, and Guibo Li. High-order immersed-boundary method for incompressible flows. *AIAA Journal*, 54:1–8, 05 2016.
- [ZLMS70] Ya. B. Zel’dovich, V. B. Librovich, G. M. Makhviladze, and G. I. Sivashinskii. On the onset of detonation in a nonuniformly heated gas. *Journal of Applied Mechanics and Technical Physics*, 11(2):264–270, Mar 1970.
- [ZZZ21] Ruixuan Zhu, Majie Zhao, and Huangwei Zhang. Numerical simulation of flame acceleration and deflagration-to-detonation transition in ammonia-hydrogen–oxygen mixtures. *International Journal of Hydrogen Energy*, 46(1):1273–1287, 2021.